

Radiometric Modeling of Mechanical Draft Cooling Towers
to Assist in the Extraction of their Absolute Temperature
from Remote Thermal Imagery

by

Matthew Montanaro

B.S. Physics, Rochester Institute of Technology, 2005

A dissertation submitted in partial fulfillment of the
requirements for the degree of Doctor of Philosophy
in the Chester F. Carlson Center for Imaging Science
Rochester Institute of Technology

May 2009

Signature of the Author _____

Accepted by _____
Coordinator, Ph.D. Degree Program Date

CHESTER F. CARLSON CENTER FOR IMAGING SCIENCE
ROCHESTER INSTITUTE OF TECHNOLOGY
ROCHESTER, NEW YORK

CERTIFICATE OF APPROVAL

Ph.D. DEGREE DISSERTATION

The Ph.D. Degree Dissertation of Matthew Montanaro
has been examined and approved by the
dissertation committee as satisfactory for the
dissertation required for the
Ph.D. degree in Imaging Science

Dr. Carl Salvaggio, Dissertation Advisor Date

Dr. Alfred J. Garrett

Dr. David W. Messinger

Dr. Edward C. Hensel

DISSERTATION RELEASE PERMISSION
ROCHESTER INSTITUTE OF TECHNOLOGY
CHESTER F. CARLSON CENTER FOR IMAGING SCIENCE

Title of Dissertation:

**Radiometric Modeling of Mechanical Draft Cooling Towers
to Assist in the Extraction of their Absolute Temperature
from Remote Thermal Imagery**

I, Matthew Montanaro, hereby grant permission to Wallace Memorial Library of R.I.T. to reproduce my thesis in whole or in part. Any reproduction will not be for commercial use or profit.

Signature

Date

Radiometric Modeling of Mechanical Draft Cooling Towers to Assist in the Extraction of their Absolute Temperature from Remote Thermal Imagery

by

Matthew Montanaro

Submitted to the
Chester F. Carlson Center for Imaging Science
in partial fulfillment of the requirements
for the Doctor of Philosophy Degree
at the Rochester Institute of Technology

Abstract

Determination of the internal temperature of a mechanical draft cooling tower (MDCT) from remotely-sensed thermal imagery is important for many applications that provide input to energy-related process models. The problem of determining the temperature of an MDCT is unique due to the geometry of the tower and due to the exhausted water vapor plume. The radiance leaving the tower is dependent on the optical and thermal properties of the tower materials (*i.e.*, emissivity, BRDF, temperature, etc.) as well as the internal geometry of the tower. The tower radiance is then propagated through the exhaust plume and through the atmosphere to arrive at the sensor. The expelled effluent from the tower consists of a warm plume with a higher water vapor concentration than the ambient atmosphere. Given that a thermal image has been atmospherically compensated, the remaining sources of error in extracted tower temperature due to the exhausted plume and the tower geometry must be accounted for. A temperature correction factor due to these error sources is derived through the use of three-dimensional radiometric modeling. A range of values for each important parameter are modeled to create a target space (*i.e.*, look-up table) that predicts the internal MDCT temperature for every combination of parameter values. The look-up table provides data for the creation of a fast-running parameterized model. This model, along with user knowledge of the scene, provides a means to convert the image-derived apparent temperature into the estimated absolute temperature of an MDCT.

"Be patient, for the world is broad and wide"

In Memoria di Mio Nonno,

Giuseppe Bonomo



Acknowledgements

Issac Newton famously said “If I have seen further it is only by standing on the shoulders of giants.” This statement captures the reality of my time at RIT. I would not have completed this degree if it were not for the continuous support of many people. I am extremely grateful to my advisor, Carl Salvaggio, for his guidance, patience, trust, and faith in me. I appreciate him taking me on as a student and for his constant support and encouragement. Al Garrett of the Savannah River National Laboratory (SNRL) sponsored the MDCT project on which this dissertation is based. His guidance and encouragement is very appreciated. Dave Messinger was always available for help and to guide me in the right direction. Ed Hensel graciously agreed to be on my committee. His suggestions were very helpful during the process. I would also like to acknowledge the U.S. Department of Energy for their sponsorship under contract number DE-AC09-96SR18500.

In addition to the committee members, there have been many others who have lent their help and expertise over the past few years. Joel Kastner and Zoran Ninkov, who along with Carl Salvaggio, encouraged me to pursue a graduate degree at the Center for Imaging Science (CIS). Jim Bollinger of the SRNL was very helpful in providing data sets that I requested. His guidance and encouragement is much appreciated. The entire MDCT staff at the SRNL obtained and provided data on the imaging and ground measurement campaign. Niek Sanders and Adam Goodenough have spent countless hours writing and debugging DIRSIG code that was used in this dissertation. Paul Lee and David Pogorzala took the time to give me a crash course in using DIRSIG when I first started my degree. Guy Ward and Peter Falise provided surplus MDCT construction materials. Christina Kucarak and Kyle Foster measured and recorded the spectral emissivities of the MDCT materials. Mike Metzler, Carol May, and Doug Ratay were very helpful in deciphering the NEFDS. Gail Anderson shared her MODTRAN expertise and answered many questions even when she was on vacation. Frank Padula shared his atmospheric and meteorological expertise. Steve LaLonde, Shawn Higbee, and Melissa Rura shared their expertise in multivariate statistics. Paul Mezzanini, Ryan Lewis, and Gurcharan Khanna kept the RIT Research Computing cluster running. Paul was always available to answer my many emails to him no matter what time it was. Jim Bodie maintained the CIS servers and workstations on which much of the calculations in this dissertation were performed on. I am thankful to the DIRS staff and students and to the RIT staff for all their help throughout my years at DIRS and at RIT.

I am indebted to Scott Brown for sharing his endless knowledge and expertise on the wide range of subjects that have come up in our conversations. I greatly appreciate his guidance and support. Mike Richardson, “my agent,” always looked out for me and was very encouraging and supportative. John Schott, “the Godfather,” was always there for advice and help although I am still afraid to look him in the eye for fear of turning to stone. I am grateful for the opportunity and privilege to have worked with him. Cindy Schultz, my “work mom,” has been a source of constant support throughout my time in graduate school. She kept me in line everyday and always laughed when I passed by her office on my many laps around the building. Aaron Gerace and Prudhvi Gurram started the program with me four years ago and have accompanied me on many of those laps. Over the years they have not only been a huge help but have also been a constant source of reason to scare off the clowns.

I have many friends outside of RIT who always ask me how my work is going and who always encourage me to continue. I am very thankful of my close friends who have been the quiet keepers of my sanity.

Lastly, I am very grateful of my parents, Nicola and Romea Montanaro, and of my brothers, Andrew, Christopher, and Patrick. I am very fortunate to have a family that has always been supportative in all of my endeavours. My parents, along with my grandparents, Antonio, Antonietta, Giuseppe, and Luisa, immigrated to the United States leaving their homes in the hillside towns of Italy. They have made many sacrifices to provide their children with a new world of opportunities. This degree is for them as much as it is for me.

Thank you to all of you,

Matt Montanaro

Rochester, New York

May 2009

Contents

Abstract	I
Table of Contents	IX
List of Figures	XV
List of Tables	XXI
Nomenclature	XXV
Acronyms	XXVII
1 Introduction	1
2 Objectives	3
2.1 Cooling Tower Basics	3
2.2 Mechanical Draft Cooling Tower Anatomy	5
2.3 MDCT Thermal Imagery	5
2.4 Analysis	12
2.5 Preliminary Variables	13
2.6 Summary	14
3 Theory	15
3.1 Self-Emitted Radiance	15
3.1.1 Blackbody Radiation	15
3.1.2 Directional Emissivity	16
3.2 Reflected Radiance	17
3.2.1 Bidirectional Reflectance Distribution Function	17
3.2.1.1 BRDF models	18
3.2.1.1.1 Lambertian Model	18
3.2.1.1.2 Ward Model	18
3.2.1.1.3 Torrance-Sparrow and Priest-Germer Models . . .	19
3.2.1.1.4 Beard-Maxwell Model and the NEFDS	20
3.2.1.1.5 Shell Target Model	20

3.2.2	Directional Hemispherical Reflectance	20
3.3	Conservation of Energy	21
3.4	Energy Paths Reaching a Sensor	22
3.4.1	Material Radiance	22
3.4.2	Atmospheric Effects	22
3.4.2.1	Atmospheric Transmission	23
3.4.2.1.1	Absorption	23
3.4.2.1.2	Scattering	24
3.4.2.1.3	Total Transmission	26
3.4.2.2	Atmospheric Emission	26
3.4.3	Governing Equation	27
3.5	Imaging System	28
3.5.1	Collection	28
3.5.2	Detection	30
3.5.2.1	Spatial Sampling	31
3.5.2.2	Temporal Sampling	31
3.5.2.3	Spectral Sampling	31
3.5.2.3.1	Band Effective Values	32
3.5.2.4	Noise	32
3.5.3	Calibration	33
3.6	Apparent Temperature	33
3.6.1	Planck Formula Inversion	34
3.6.2	Temperature-Radiance Look-Up Table	34
4	Background	37
4.1	Modeling Tools	37
4.1.1	MODTRAN	37
4.1.2	DIRSIG	39
4.2	Temperature Retrieval Methods	40
4.2.1	Atmospheric Compensation	40
4.2.1.1	Ground Truth	40
4.2.1.2	Single-Channel Method	41
4.2.1.3	Multi-Channel Method	42
4.2.1.4	Multi-Angle Method	43
4.2.1.5	MTI Sea Surface Temperature Retrieval	44
4.2.1.6	AAC Algorithm	45

4.2.1.7	ISAC Algorithm	46
4.2.1.8	Physics-Based Modeling	46
4.2.2	Temperature/Emissivity Separation	47
4.2.2.1	Reference Channel Method	48
4.2.2.2	Normalized Emissivity Method	48
4.2.2.3	Temperature/Emissivity Separation Algorithm	48
4.2.2.4	ARTEMIS Algorithm	50
4.2.3	Temperature Retrieval Summary	50
5	Methodology	51
5.1	Tower Leaving Radiance	51
5.1.1	Spectral Measurements of MDCT Materials	54
5.1.2	BRDF of NEFDS Materials	56
5.1.3	DIRSIG Model of Closed and Open Cavities	58
5.1.4	Effective Emissivity of Drift Eliminators	61
5.1.5	MDCT DIRSIG Rendering with BRDF Materials	65
5.1.6	MDCT Fan Blade Motion	68
5.1.7	Atmospheric Downwelled Radiance	72
5.1.8	Tower Leaving Radiance Summary	74
5.2	sensor-reaching Radiance	75
5.2.1	MODTRAN Simulation of Air Column	76
5.2.2	MODTRAN Simulation of MDCT Exhaust Plume	82
5.2.3	Sensitivity of Plume Gradient	86
5.2.4	sensor-reaching Radiance Summary	88
5.3	Approach	89
5.3.1	Overview	90
5.3.2	Physics Model	90
5.3.2.1	Tower Leaving Radiance with DIRSIG	90
5.3.2.1.1	DIRSIG Parameters	92
5.3.2.2	Plume Leaving Radiance with MODTRAN	93
5.3.2.2.1	MODTRAN Parameters	94
5.3.2.3	Physics Model Summary	94
5.3.3	Sensor Model	95
5.3.3.1	Region of Interest - Mixed vs. Cavity	96
5.3.4	Target Space Look-Up Table	97
5.3.5	Parameterized Model	97

5.4	Methodology Summary	98
6	Results	99
6.1	Physics Model Generation	99
6.2	Sensor Model and LUT Generation	100
6.2.1	Ideal Sensor	101
6.2.2	SC 2000 Inframetrics Sensor	103
6.2.2.1	SC 2000 Random Dataset	104
6.3	SRNL Data Set	106
6.3.1	Understanding the SRNL Data Set	107
6.3.2	Atmospheric Compensation	108
6.3.3	Actual Temperature Errors	112
6.3.4	Predicted Temperature Errors	114
6.3.5	Comparison of Atmospheric Uncertainties	123
6.3.6	Comparison of Sensor Spectral Response	128
6.3.7	Validity of Parameterized Model	133
6.3.8	Look-up Table Interpolation	135
6.4	Results Summary	140
7	Summary and Conclusions	141
7.1	Recommendations	143
A	Derivation of the Planck Blackbody Radiation Equation	145
A.1	Statistical Physics	145
A.2	Planck Distribution	146
A.3	Total Energy of the States	147
A.4	Planck Spectral Energy Density	149
A.5	Blackbody Spectral Exitance	149
A.6	Blackbody Spectral Radiance	151
A.7	Total Blackbody Radiated Power	151
A.8	Wavelength of Maximum Emission	152
B	Multiple Regression Analysis	155
B.1	Least-Squares Regression	155
B.2	Analysis of Variance	156
B.2.1	Sum of Squares	156
B.2.2	Mean Squares	157

B.2.3	Coefficient of Multiple Determination	157
B.2.4	F-Test	158
B.3	Aptness of the Fitted Model	158
B.3.1	Standardized Residuals vs. Fitted Responses	159
B.3.2	Normal Probability Plot of Standardized Residuals	159
C	Propagation of Uncertainties	161
C.1	Analytical Method	161
C.2	Empirical Method	162
D	Calculation of Effective Sky Temperature	163
E	Estimation of Plume Path Length	165
F	Precipitable Water in an Air Column	169
	Bibliography	171

List of Figures

1.1	Electromagnetic Spectrum	1
2.1	Mechanical draft cooling towers at the Savannah River Site.	3
2.2	Schematic drawing of a counter-flow MDCT	4
2.3	Location of ground-truth measurements taken by SRNL	6
2.4	SRNL 20may04D14 thermal image with mixed and cavity ROIs	8
2.5	SRNL 20may04e02 thermal image with mixed and cavity ROIs	9
2.6	SRNL 20may04e04 thermal image with mixed and cavity ROIs	10
2.7	SRNL 20jun05G09 thermal image with mixed and cavity ROIs	11
2.8	Preliminary variables affecting the apparent temperature recorded by a sensor of a MDCT.	14
3.1	Planck curves for a 5800 Kelvin and 300 Kelvin blackbody.	17
3.2	Ward diffuse and specular BRDF models.	19
3.3	Atmospheric scattering as a function of particle radius and incident radia- tion wavelength.	25
3.4	Atmospheric spectral transmission along a vertical space-to-ground path generated from a MODTRAN mid-latitude summer atmosphere.	26
3.5	Illustration of atmospheric emission as the sum of the emissions from each homogeneous layer.	27
3.6	Illustration of the blurring effect and sampling as radiance from a point source passes through an imaging system.	29
3.7	Airy disc pattern representing the PSF of a diffraction-limited circular aper- ture system.	30
4.1	Multispectral Thermal Imager (MTI) band locations	44
5.1	Diagram of a single photon path for an exposed object and a cavity object. .	52
5.2	Drift eliminator emissivity spectra of two separate physical locations on the material measured with a SOC-400 instrument.	54
5.3	Metal plate emissivity spectra of two separate physical locations on the ma- terial measured with a SOC-400 instrument.	54

5.4	Wood support emissivity spectra of two separate physical locations on the material measured with a SOC-400 instrument.	55
5.5	Plastic disc emissivity spectra of two separate physical locations on the material measured with a SOC-400 instrument.	55
5.6	NEFDS BRDF of weathered galvanized bare steel (NEF #0525UUUSTLa) measured at an illumination angle of 20°.	56
5.7	NEFDS BRDF of mildly weathered plastic tarp (NEF #1019UUUFABa) measured at an illumination angle of 20°.	56
5.8	NEFDS BRDF of weathered bare construction lumber (NEF #0404UUU-WOD) measured at an illumination angle of 20°.	57
5.9	NEFDS BRDF of weathered paint on insulation panel (NEF #0887UUUPNT) measured at an illumination angle of 20°.	57
5.10	DIRSIG simulation layout of a closed box and an open well	58
5.11	Results of the closed box DIRSIG simulation.	59
5.12	Results of the open well DIRSIG simulation.	59
5.13	Comparison between a photograph of MDCT drift eliminators and a CAD drawing of the drift eliminators.	62
5.14	Ward BRDF models used in the drift eliminator effective emissivity simulation.	63
5.15	CAD drawing of a counter-flow MDCT exterior view and interior view . . .	65
5.16	DIRSIG MDCT radiance images rendered with a diffuse Ward BRDF model and a specular Ward BRDF model.	66
5.17	Apparent temperature profiles across the fan stack opening of the MDCT for the diffuse Ward BRDF image and the specular Ward BRDF image. . . .	67
5.18	DIRSIG rendering of an MDCT looking into the fan stack opening with a one-pixel-wide ring drawn.	68
5.19	Square-wave signal representing the fan blade and cavity radiances at each pixel location in the ring at different times.	69
5.20	DIRSIG rendering of an MDCT with a stationary fan and a blurred rendering representing a rotating fan.	70
5.21	Temperature error from a 300 K object as a function of emissivity and MODTRAN standard atmospheric profile.	73
5.22	Illustration of the radiance from the tower passes through the exhaust plume to reach the sensor.	75
5.23	Atmospheric column representing the plume layer and the ambient atmosphere modeled in MODTRAN.	76

5.24	Schematic of the atmospheric layers assigned in MODTRAN. The first segment represents the exhaust plume while the second segment represents the rest of the air column. Standard atmospheric conditions are assigned to every layer except for those in the first segment where the air temperature and dew point temperature are varied.	78
5.25	Results of the MODTRAN plume mid-latitude summer simulation showing the temperature error between the material blackbody temperature and the sensor derived apparent temperature.	79
5.26	Results of the MODTRAN plume sub-arctic winter simulation showing the temperature error between the material blackbody temperature and the sensor derived apparent temperature.	80
5.27	Results of the MODTRAN plume-only mid-latitude summer simulation showing the temperature error between the material blackbody temperature and the sensor derived apparent temperature.	83
5.28	Results of the MODTRAN plume-only sub-arctic winter simulation showing the temperature error between the material blackbody temperature and the sensor derived apparent temperature.	84
5.29	Three plume gradient functions modeled in MODTRAN.	87
5.30	Illustration of the procedure to predict the MDCT temperature error.	89
5.31	Ward BRDF model assigned to the facets in the DIRSIG CAD model.	91
5.32	Illustration of atmospheric layers in MODTRAN used to model the moisture gradient in the plume.	93
5.33	High resolution DIRSIG image along with the mixed ROI and cavity-only ROI drawn for sensor angle of 0°	96
6.1	SRNL data set LWIR images.	106
6.2	Interpolated atmospheric profiles used in MODTRAN to correct the SRNL images.	109
6.3	Radiosonde station locations shown relative to SRS.	110
6.4	The actual and the predicted temperature error with uncertainty ranges for the 20may04D14 image. ROI, atmosphere, and sensor uncertainty is included in the error bars.	117
6.5	The actual and the predicted temperature error with uncertainty ranges for the 20may04E02 image. ROI, atmosphere, and sensor uncertainty is included in the error bars.	118

6.6	The actual and the predicted temperature error with uncertainty ranges for the 20may04E04 image. ROI, atmosphere, and sensor uncertainty is included in the error bars.	119
6.7	The actual and the predicted temperature error with uncertainty ranges for the 20jun05G09 image. ROI, atmosphere, and sensor uncertainty is included in the error bars.	120
6.8	The actual and the predicted temperature error with uncertainty ranges for the 20may04D14 image. The uncertainty ranges are for an atmospheric uncertainty of 0.1 K (top), 1.1 K (middle), and 2.2 K (bottom).	124
6.9	The actual and the predicted temperature error with uncertainty ranges for the 20may04E02 image. The uncertainty ranges are for an atmospheric uncertainty of 0.1 K (top), 1.1 K (middle), and 2.2 K (bottom).	125
6.10	The actual and the predicted temperature error with uncertainty ranges for the 20may04E04 image. The uncertainty ranges are for an atmospheric uncertainty of 0.1 K (top), 1.1 K (middle), and 2.2 K (bottom).	126
6.11	The actual and the predicted temperature error with uncertainty ranges for the 20jun05G09 image. The uncertainty ranges are for an atmospheric uncertainty of 0.1 K (top), 1.1 K (middle), and 2.2 K (bottom).	127
6.12	Comparison of an ideal, flat, unit spectral response and a realistic microbolometer spectral response in the longwave infrared region.	128
6.13	The actual and the predicted temperature error with uncertainty ranges for the 20may04D14 image using the microbolometer spectral response.	129
6.14	The actual and the predicted temperature error with uncertainty ranges for the 20may04E02 image using the microbolometer spectral response.	130
6.15	The actual and the predicted temperature error with uncertainty ranges for the 20may04E04 image using the microbolometer spectral response.	131
6.16	The actual and the predicted temperature error with uncertainty ranges for the 20jun05G09 image using the microbolometer spectral response.	132
6.17	Diagnostic plots indicating a lack-of-fit of the multiple linear regression model to the 20may04D14 mixed ROI LUT data.	133
6.18	The actual temperature errors and the predicted temperature errors based on a LUT nearest neighbor interpolation with uncertainty ranges for the 20may04D14 image.	136
6.19	The actual temperature errors and the predicted temperature errors based on a LUT nearest neighbor interpolation with uncertainty ranges for the 20may04E02 image.	137

6.20	The actual temperature errors and the predicted temperature errors based on a LUT nearest neighbor interpolation with uncertainty ranges for the 20may04E04 image.	138
6.21	The actual temperature errors and the predicted temperature errors based on a LUT nearest neighbor interpolation with uncertainty ranges for the 20jun05G09 image.	139
A.1	Photons escaping a blackbody cavity from a thin shell inside the cavity . . .	149
A.2	Spectral radiance for a blackbody at a temperature of 300 Kelvin	154
E.1	Comparison of the six atmospheric stability classes using the associated ambient temperature gradients in reference to dry and wet adiabatic lapse rates.	167
E.2	Gaussian plume model rendered in Matlab. The solid line represents the sensor line-of-sight. The exit air velocity is set to 10 m/s, stack height is 9 m, stack radius is 2 m, wind speed is 0.75 m/s, and the atmospheric stability is slightly unstable. The estimated path length through this plume is 6 m. .	168

List of Tables

1	Radiometric Terms	XXV
2	Acronyms	XXVII
2.1	SRNL 20may04D14 image ROI statistics.	8
2.2	SRNL 20may04D14 ground measured temperatures compared to the mean ROI temperatures.	8
2.3	SRNL 20may04D14 ground measurements collected at 02:06 EDT on 20 May 2004.	8
2.4	SRNL 20may04e02 image ROI statistics.	9
2.5	SRNL 20may04e02 ground measured temperatures compared to the mean ROI temperatures.	9
2.6	SRNL 20may04e02 ground measurements collected at 02:06 EDT on 20 May 2004.	9
2.7	SRNL 20may04e04 image ROI statistics	10
2.8	SRNL 20may04e04 ground measured temperatures compared to the mean ROI temperatures.	10
2.9	SRNL 20may04e04 ground measurements collected at 02:06 EDT on 20 May 2004.	10
2.10	SRNL 20jun05G09 image ROI statistics.	11
2.11	SRNL 20jun05G09 ground measured temperatures compared to the mean ROI temperatures.	11
2.12	SRNL 20jun05G09 ground measurements collected at 22:17 EDT on 20 June 2005.	11
5.1	Results of the DIRSIG drift eliminator effective emissivity simulations. . . .	64
5.2	Effective sky apparent temperatures for the standard MODTRAN atmo- spheres.	73
5.3	Parameter values for the MODTRAN plume simulations.	78
5.4	Parameter values for the plume-only MODTRAN simulations.	82
5.5	Apparent temperature errors for three plume gradient functions and for three plume lengths.	87
6.1	MDCT physics model parameters and associated modeling tools.	99

6.2	MDCT parameter values used for the target-space LUT.	100
6.3	Regression model parameter labels.	101
6.4	MDCT random parameter values	105
6.5	Radiosonde station information for the radiosonde profiles used to atmospherically compensate the SRNL images.	108
6.6	Original and the atmospherically-corrected image ROI temperatures for the SRNL 20may04D14 image.	111
6.7	Original and the atmospherically-corrected image ROI temperatures for the SRNL 20may04E02 image.	111
6.8	Original and the atmospherically-corrected image ROI temperatures for the SRNL 20may04E04 image.	111
6.9	Original and the atmospherically-corrected image ROI temperatures for the SRNL 20jun05G09 image.	111
6.10	Temperature uncertainties in the measured ground, ROI, sensor, and atmospheric variables	112
6.11	Temperature errors between the atmospherically-corrected mean ROI temperature and the measured ground-truth exit air temperature for the SRNL 20may04D14 image.	113
6.12	Temperature errors between the atmospherically-corrected mean ROI temperature and the measured ground-truth exit air temperature for the SRNL 20may04E02 image.	113
6.13	Temperature errors between the atmospherically-corrected mean ROI temperature and the measured ground-truth exit air temperature for the SRNL 20may04E04 image.	113
6.14	Temperature errors between the atmospherically-corrected mean ROI temperature and the measured ground-truth exit air temperature for the SRNL 20jun05G09 image.	113
6.15	Estimates of the sensor view zenith angle along with uncertainties. The angles were estimated by measuring the vertical and horizontal pixel diameters of the fan stack opening of each image.	115
6.16	Predictor estimates and uncertainties used in the 20may04D14 parameterized regression model	117
6.17	Comparison of the actual and predicted temperature errors for the 20may04D14 image. ROI, atmosphere, and sensor uncertainty is included.	117
6.18	Predictor estimates and uncertainties used in the 20may04E02 parameterized regression model	118

6.19	Comparison of the actual and predicted temperature errors for the 20may04E02 image. ROI, atmosphere, and sensor uncertainty is included.	118
6.20	Predictor estimates and uncertainties used in the 20may04E04 parameterized regression model	119
6.21	Comparison of the actual and predicted temperature errors for the 20may04E04 image. ROI, atmosphere, and sensor uncertainty is included.	119
6.22	Predictor estimates and uncertainties used in the 20jun05G09 parameterized regression model	120
6.23	Comparison of the actual and predicted temperature errors for the 20jun05G09 image. ROI, atmosphere, and sensor uncertainty is included.	120
6.24	Predictor estimates and uncertainties used in the 20may04D14 parameterized regression model	129
6.25	Comparison of the actual and predicted temperature errors for the 20may04D14 image using the microbolometer spectral response.	129
6.26	Predictor estimates and uncertainties used in the 20may04E02 parameterized regression model	130
6.27	Comparison of the actual and predicted temperature errors for the 20may04E02 image using the microbolometer spectral response.	130
6.28	Predictor estimates and uncertainties used in the 20may04E04 parameterized regression model	131
6.29	Comparison of the actual and predicted temperature errors for the 20may04E04 image using the microbolometer spectral response.	131
6.30	Predictor estimates and uncertainties used in the 20jun05G09 parameterized regression model	132
6.31	Comparison of the actual and predicted temperature errors for the 20jun05G09 image using the microbolometer spectral response.	132
6.32	Predictor estimates used in the 20may04D14 LUT nearest neighbor interpolation.	136
6.33	Comparison of the actual temperature errors and the predicted temperature errors based on a LUT nearest neighbor interpolation for the 20may04D14 image.	136
6.34	Predictor estimates used in the 20may04E02 LUT nearest neighbor interpolation.	137
6.35	Comparison of the actual temperature errors and the predicted temperature errors based on a LUT nearest neighbor interpolation for the 20may04E02 image.	137

6.36	Predictor estimates used in the 20may04E04 LUT nearest neighbor interpolation.	138
6.37	Comparison of the actual temperature errors and the predicted temperature errors based on a LUT nearest neighbor interpolation for the 20may04E04 image.	138
6.38	Predictor estimates used in the 20jun05G09 LUT nearest neighbor interpolation.	139
6.39	Comparison of the actual temperature errors and the predicted temperature errors based on a LUT nearest neighbor interpolation for the 20jun05G09 image.	139
E.1	Constants used in the calculation of the vertical and crosswind dispersion coefficients for the Gaussian plume model in an urban environment.	166
E.2	Description of the six atmospheric stability classes and the associated ambient temperature gradients.	166

Nomenclature

There is a strong emphasis on radiometry in this document. A list of common radiometric terms used here are presented in Table 1. Square brackets are used to represent physical units of variables and parameters. Wavelength units are in microns ($1 \mu m = 10^{-6} m$). Temperatures are in units of Kelvin $[K]$ ($K = ^\circ C + 273.15$). The following notations are equivalent, $[W/m^2/sr/\mu m] = [W/(m^2 sr \mu m)] = [W m^{-2} sr^{-1} \mu m^{-1}] = \left[\frac{W}{m^2 sr \mu m} \right]$.

Symbol	Units	Term
λ	μm	Wavelength of photon
T	K	Absolute temperature
T_{App}	K	Apparent temperature
$L(\theta, \phi, \lambda)$	$\frac{W}{m^2 sr \mu m}$	Spectral radiance in the θ, ϕ direction
$L(\theta, \phi)$	$\frac{W}{m^2 sr}$	Radiance in the θ, ϕ direction
$L_{BB}(\lambda, T)$	$\frac{W}{m^2 sr \mu m}$	Spectral blackbody radiance
$E(\lambda)$	$\frac{W}{m^2 \mu m}$	Spectral irradiance
$\Phi(\lambda)$	$\frac{W}{\mu m}$	Spectral radiant flux
$\rho'(\theta_i, \phi_i, \theta_r, \phi_r, \lambda)$	$\frac{1}{sr}$	Bidirectional Reflectance Distribution Function
$\rho(\theta, \phi, \lambda)$		Directional hemispherical reflectance
$\varepsilon(\theta, \phi, \lambda)$		Directional emissivity
$\alpha(\lambda)$		Spectral absorptivity or absorbance
$\tau(\lambda)$		Spectral transmission or transmittance
$L_{atm}(\theta, \phi, \lambda)$	$\frac{W}{m^2 sr \mu m}$	Spectral self-emitted atmospheric radiance
\hat{L}_λ	$\frac{W}{m^2 sr \mu m}$	Band effective spectral radiance
\hat{L}	$\frac{W}{m^2 sr}$	Band effective radiance
$R'(\lambda)$		Peak-normalized sensor spectral response
(θ_i, ϕ_i)		Incident zenith and azimuth angle
(θ_r, ϕ_r)		Reflected zenith and azimuth angle

Table 1: Summary of radiometric terms and units used in this document

Acronyms

A number of acronyms are used in this document for the sake of brevity in certain areas. A list of frequent acronyms used here are listed in Table 2.

Acronym	Meaning
BRDF	Bidirectional Reflectance Distribution Function
CAD	Computer Aided Drafting
DHE	Directional Hemispherical Emissivity
DHR	Directional Hemispherical Reflectance
EDT	Eastern Daylight Time (GMT - 4 hrs.)
DIRS	Digital Imaging and Remote Sensing Laboratory
DIRSIG	Digital Imaging and Remote Sensing Image Generation
DOE	Department of Energy
GSD	Ground Sampling Distance
GMT	Greenwich Mean Time
IFOV	Instantaneous Field of View
LWIR	Longwave Infrared (<i>approx.</i> 8 - 14 μm)
LUT	Look-up Table
MDCT	Mechanical Draft Cooling Tower
MODTRAN	MODerate spectral resolution TRANsmittance
MWIR	Midwave Infrared (<i>approx.</i> 3 - 5 μm)
NEFDS	Nonconventional Exploitation Factors Data System
PSF	Point Spread Function
RIT	Rochester Institute of Technology
RMS	Root Mean Squared
ROI	Region of Interest
SRNL	Savannah River National Laboratory
SRS	Savannah River Site
VNIR	Visible and Near-Infrared (<i>approx.</i> 0.4 - 1.1 μm)

Table 2: Summary of acronyms used in this document

Chapter 1

Introduction

If we knew what it was we were doing, it would not be called research, would it?

- Albert Einstein

The derivation of the absolute temperature of a material surface from remote thermal imagery is a complex process. Remote thermal imaging is necessary when it is impossible or impractical to obtain a direct temperature measurement of a material surface. Only photons that have been thermally emitted from the surface carry information about the temperature of that surface. However, this self-emitted signal from the surface is not the only signal entering a sensor. Signals from other background objects will enter the field of view of the sensor and will be detected. Furthermore, the temperature signal from the surface of interest will be altered by the optical properties of the surface and by its environment. Separating out these unwanted signals and effects is a painstaking process.

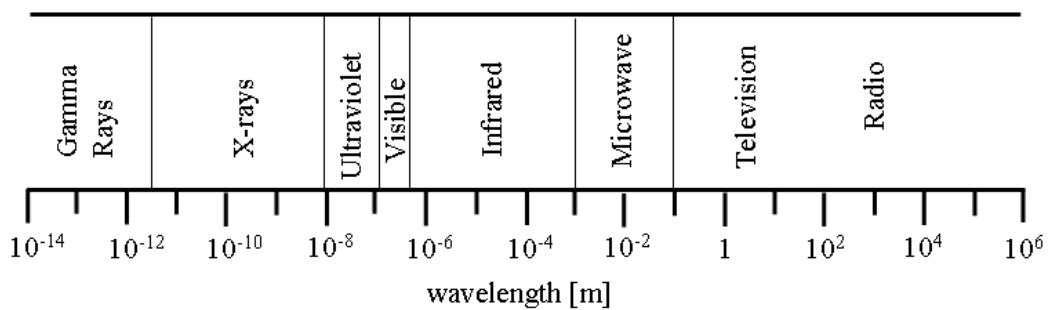


Figure 1.1: Electromagnetic radiation spectrum

The topic of remote sensing involves analyzing the signals, or photons, that are collected by a sensor. A photon contains a certain amount of energy depending on its wavelength. For a beam of photons, the rate at which its energy is propagating is known as the *radiant flux*, Φ , in units of energy per unit time, or *Watts* [1]. It is often convenient to express the energy flux that originates from a surface and into a particular direction. The radiometric term known as *radiance*, L , describes the flux per unit projected area per unit solid an-

gle [1]. The radiance when measured per wavelength has units of *Watts per square meter per steradian per micron*, $[W/m^2/sr/\mu m]$.

Although remote sensing may encompass the entire electromagnetic spectrum, only the infrared region will be utilized here. From the ultraviolet to the short-wave infrared (approximately $0.1 - 2 \mu m$), there will be several orders of magnitude more flux from the sun than from self-emission of objects at the Earth ambient temperature of 300 K. This spectral range is referred to as the *reflective* region and thermal or self-emitted flux is ignored. At longwave infrared (LWIR) wavelengths (approximately $8 - 14 \mu m$), there are several orders of magnitude more flux from self-emission than from reflected solar flux. This region is referred to as the *thermal* region [1]. The self-emitted radiation from objects at the ambient Earth temperature makes this spectral region ideal for determining the temperature of such objects. For this reason, the discussion and analysis in this document will be limited to this spectral region.

This document will present a detailed description of the problem, introduce the physics of thermal radiometry, provide an overview of previous approaches to remote temperature retrieval, propose a methodology to obtain the MDCT temperature from a remote thermal image, and reveal the results and conclusions of the research.

Chapter 2

Objectives

Knowledge of the absolute temperature of a surface is useful for a wide range of applications ranging from environmental to industrial to security. The objective of this project is to estimate the temperature of the air exiting a mechanical draft cooling tower (MDCT) through the use of remote thermal imagery. Knowledge of the temperature of the cooling towers is necessary for input into process models that yield information about the industrial processes that the cooling towers service. A visible and thermal image of such cooling towers is displayed in Figure 2.1.

A camera sensitive to the LWIR spectral region is used to observe the cooling tower. Each pixel in the resulting thermal image is converted into an apparent temperature, or image-derived temperature. *The apparent temperature of pixels inside the fan stack of the tower is to be correlated to the exit air temperature.*

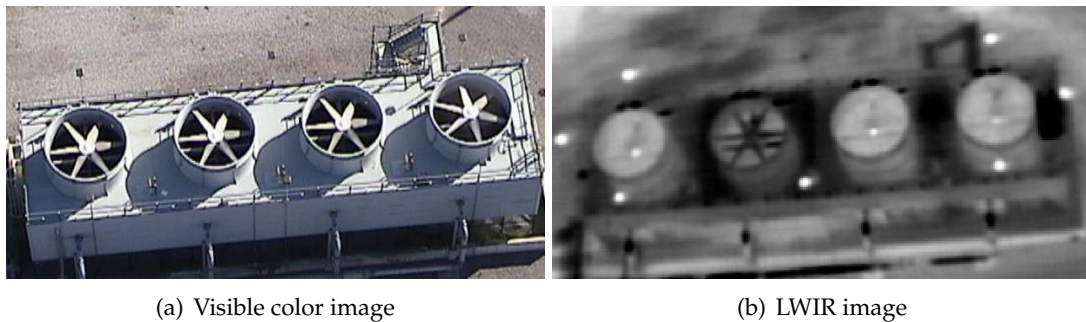


Figure 2.1: Mechanical draft cooling towers at the Savannah River Site.

2.1 Cooling Tower Basics

Industrial plants generate substantial amounts of excess heat. Water is a popular medium used to transport excess heat from an industrial process. Waste heat is absorbed by water having a cooler temperature than the process. This warm water must now either be discharged into a body of water, or cooled and recycled. In the latter method, a cooling

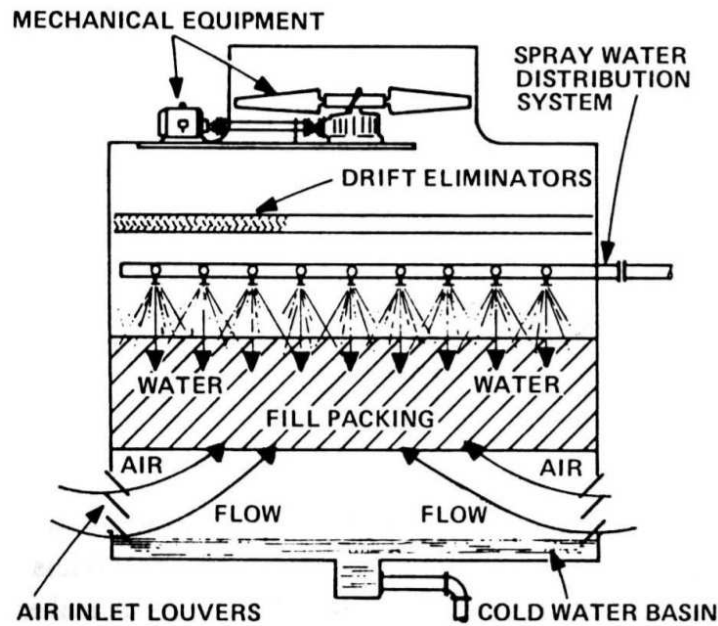


Figure 2.2: Schematic drawing of a counter-flow MDCT (Burger 1995 [2]).

tower is a standard option to recycle the water. In the cooling tower, the waste heat from the water is rejected into the atmosphere and the cooled water is recirculated through the system [2]. There are various types of cooling towers but all function on the same physics.

The basic principle governing the cooling of the water is evaporative cooling and the exchange of sensible heat. Water exposed to cooling air streams will release heat and evaporate. The penalty is the loss of water which is discharged into the atmosphere as hot moist water vapor. When the water is warmer than the ambient air, the air cools the water. Air gets warmer as it gains sensible heat of the water and the water is cooled as sensible heat is transferred to the air. The evaporative effect of the release of latent heat of vaporization also cools the water. Approximately 75% of the cooling is latent heat and 25% is due to sensible heat transfer [2].

Air becomes heated and saturated as it passes through the cooling tower. Atmospheric cooling is limited by the ambient wet bulb temperature. Wet bulb is determined from a psychrometric chart as the intersection of the ambient dry bulb temperature and the dew point temperature. Therefore, the wet bulb temperature is always between the dry bulb and dew point temperatures. Wet bulb is an indication of the evaporative potential of the atmosphere. The water cannot be cooled to a lower temperature than the wet bulb [2].

2.2 Mechanical Draft Cooling Tower Anatomy

The counter-flow variety of MDCT is presented here in detail since this type is widely used in industry and at the Savannah River Site (SRS). A schematic drawing of a counter-flow tower is shown in Figure 2.2. Water that has been heated through an industrial process is pumped to the top of the cooling tower. A water distribution system turns the heavy stream of water into light droplets as preparation to being cooled by the air stream. The water is sprayed onto a baffle material, called *fill*, that provides large water surface areas to facilitate heat transfer. Air enters the tower from below and contacts the water falling through the fill. The cooled water is collected at the base of the tower in a basin to be recirculated to the industrial plant. Moisture-laden air rises through the distribution plumbing and is exhausted out the stack of the tower. The flowing air will pick up mist and droplets and will carry them with the air flow out of the tower. Material known as *drift eliminators* is placed between the water distribution system and the tower stack to minimize the dispersal of entrained water droplets into the surrounding atmosphere. Drift eliminators are a series of baffles which cause air to gently change direction at least three times thereby obtaining greater surface contact to release water droplets [2]. A fan is situated in the stack to induce air flow through the tower. It is the presence of this fan that gives the MDCT its name.

The towers exist in one of three states. *Water on, fans on* refers to water flowing through the tower and the fan is operating to force air through the tower. *Water on, fans off* refers to water flowing through the tower but the fan is inactive. This is a so called “natural draft” mode in which air exits the fan stack opening through natural convection. The final state is *water off, fans off* in which the tower is not operating.

2.3 MDCT Thermal Imagery

The Savannah River National Laboratory (SRNL) recorded thermal imagery of the cooling towers at the Savannah River Site in the late spring of 2004 and 2005. The images were captured with an Inframetrics SC 2000 microbolometer thermal camera having a 7.6 - 13.5 μm spectral range, an instantaneous field of view (IFOV) of 1.4 milliradians, and a sensitivity of less than 0.1 K. The sensor was flying on board a helicopter at altitudes between 350 and 2000 feet (106.7 and 610 meters) above the ground. The output image is converted directly into a brightness, or apparent, temperature by the sensor.

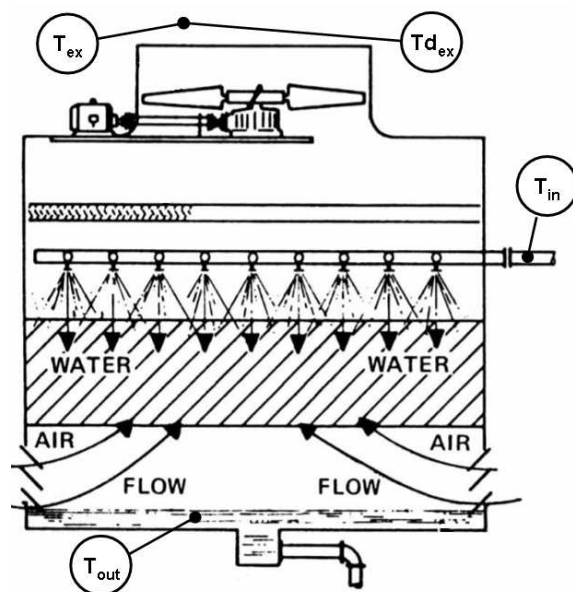


Figure 2.3: Location of ground-truth measurements taken by SRNL [2] [3].

Thermal images of the H-area and F-Area cooling units at SRS are presented in the following figures. Regions of interest (ROIs) were drawn for each tower and statistics across these regions were determined. The ROIs were first drawn to include the entire fan stack opening of the tower. This first set of ROIs simulate low spatial resolution imagery in which the ground sample distance (GSD) of the sensor is large enough to encompass the fan stack opening of the tower. A second set of ROIs were drawn in such a manner that avoided visible obstructions such as fan blades and internal support structures. Ground-truth measurements were taken nearly simultaneous with the airborne imagery. The exhaust air temperature exiting the cooling tower is T_{ex} . The exhaust is either forced out of the fan stack when fans are operating or it is expelled by natural convection when fans are off. This temperature was measured with a HOBO temperature sensor mounted on a metal pipe positioned about 0.5 meters inside the edge of the shroud by the motor that drives the fan. The corresponding dew point temperature of the exhaust air is Td_{ex} and was measured by the same HOBO in the same place. The temperature of the hot water coming into the tower is T_{in} while T_{out} is the average temperature of the cooled water collected in the basin at the base of the towers. The ambient air temperature T_{amb} , dew point temperature Td_{amb} , and pressure P were taken approximately two meters above the ground and five meters from the base of the towers [3]. Simultaneous wind speed and direction data is also available for each image. The wind measurements were obtained at heights of 4 meters and 60 meters.

Each data set presented here includes the original image with the ROIs overlaid. Brighter pixels represent higher apparent temperatures while darker pixels represent lower apparent temperatures. Each image has two sets of ROIs: one in which the ROI was drawn over the entire fan stack opening of the tower (ROI-1) and another in which the fans and other structures were avoided (ROI-2). A table of ROI statistics is included for each set of ROIs and another table contains the coincident measured ground data. All temperatures are displayed in Kelvin. The operating status of each tower in the image is also given along with a comparison of the ground measured exit air temperature and the mean ROI temperatures from the image. Ground temperature, pressure, and wind measurements are presented in the ground measurements table. The images were all collected at night and span observation altitudes of 350 to 2000 feet (106.7 to 610 meters).

SRNL 20may04D14 image (Night)

02:02 EDT 20 May 2004 at 500 ft. Towers are labeled F1 through F6 from right to left.

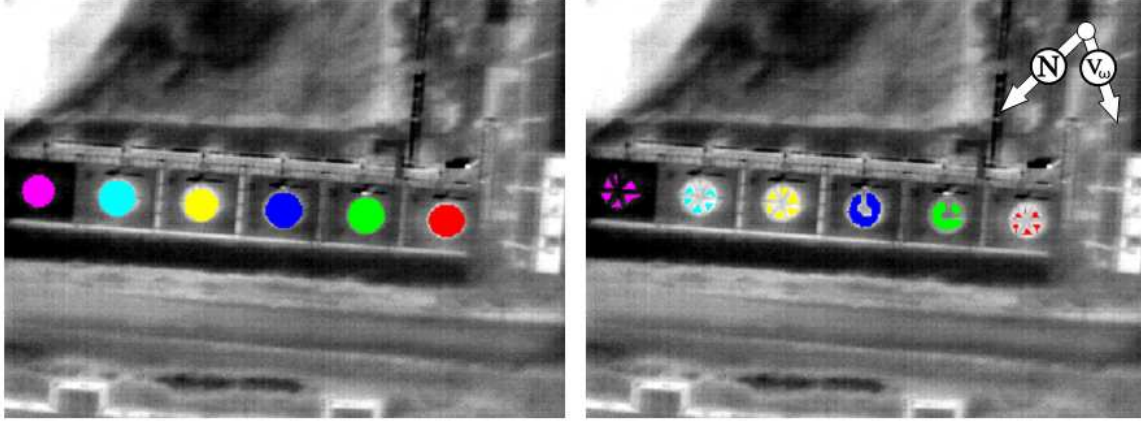


Figure 2.4: ROI-1 (left) and ROI-2 (right). The N arrow indicates the direction of north while the v_w arrow indicates the surface wind velocity direction. The GSD is approximately 0.22 m.

	ROI-1 Statistics [K]				ROI-2 Statistics [K]			
ID	Min	Max	Mean	St. Dev.	Min	Max	Mean	St. Dev.
F1	294.05	295.75	294.96	0.30	294.85	295.75	295.26	0.25
F2	293.15	294.55	293.89	0.25	293.45	294.55	294.01	0.22
F3	293.45	295.35	294.55	0.31	293.75	295.35	294.65	0.27
F4	294.65	296.15	295.33	0.32	294.75	296.15	295.50	0.29
F5	294.05	296.35	295.14	0.38	294.85	296.35	295.51	0.25
F6	291.35	292.85	292.03	0.28	291.85	292.85	292.27	0.18

Table 2.1: SRNL 20may04D14 image ROI statistics.

ID	Water/Fan	T_{ex} [K]	Td_{ex} [K]	$\bar{T}_{ROI-1} - T_{ex}$ [K]	$\bar{T}_{ROI-2} - T_{ex}$ [K]
F1	On/Off	295.55	295.45	-0.59	-0.29
F2	On/50%	294.25	294.15	-0.36	-0.24
F3	On/100%	294.75	294.35	-0.20	-0.10
F4	On/Off	295.65	295.45	-0.32	-0.15
F5	On/Off	296.75	296.75	-1.61	-1.24
F6	Off/Off	294.45	293.45	-2.42	-2.18

Table 2.2: Ground measured temperatures compared to the mean ROI temperatures.

T_{in} [K]	T_{out} [K]	T_{amb} [K]	Td_{amb} [K]	P [mb]	4m Wind [m/s]	60m Wind [m/s]
297.61	296.09	292.87	291.06	1011.39	0.48 @ 117.5°	4.86 @ 178.6°

Table 2.3: Ground measurements collected at 02:06 EDT on 20 May 2004.

SRNL 20may04e02 image (Night)

02:04 EDT 20 May 2004 at 1000 ft. Towers are labeled F1 through F6 from right to left.



Figure 2.5: ROI-1 (left) and ROI-2 (right). The N arrow indicates the direction of north while the v_w arrow indicates the surface wind velocity direction. The GSD is approximately 0.43 m.

	ROI-1 Statistics [K]				ROI-2 Statistics [K]			
ID	Min	Max	Mean	St. Dev.	Min	Max	Mean	St. Dev.
F1	294.45	295.35	294.88	0.22	294.45	295.35	294.99	0.21
F2	293.25	293.35	293.91	0.22	293.75	294.35	294.03	0.16
F3	294.05	294.95	294.53	0.24	294.15	294.95	294.59	0.20
F4	294.75	295.65	295.13	0.21	294.85	295.65	295.22	0.21
F5	294.65	295.65	295.13	0.26	294.95	295.65	295.28	0.18
F6	291.65	292.85	292.34	0.26	292.15	292.85	292.53	0.16

Table 2.4: SRNL 20may04e02 image ROI statistics.

ID	Water/Fan	T_{ex} [K]	Td_{ex} [K]	$\bar{T}_{ROI-1} - T_{ex}$ [K]	$\bar{T}_{ROI-2} - T_{ex}$ [K]
F1	On/Off	295.55	295.45	-0.67	-0.56
F2	On/50%	294.25	294.15	-0.34	-0.22
F3	On/100%	294.75	294.35	-0.22	-0.16
F4	On/Off	295.65	295.45	-0.52	-0.43
F5	On/Off	296.75	296.75	-1.62	-1.47
F6	Off/Off	294.45	293.45	-2.11	-1.92

Table 2.5: Ground measured temperatures compared to the mean ROI temperatures.

T_{in} [K]	T_{out} [K]	T_{amb} [K]	Td_{amb} [K]	P [mb]	4m Wind [m/s]	60m Wind [m/s]
297.61	296.09	292.87	291.06	1011.39	0.48 @ 117.5°	4.86 @ 178.6°

Table 2.6: Ground measurements collected at 02:06 EDT on 20 May 2004.

SRNL 20may04e04 image (Night)

02:07 EDT 20 May 2004 at 2000 ft. Towers are labeled F1 through F6 from right to left.



Figure 2.6: ROI-1 (left) and ROI-2 (right). The N arrow indicates the direction of north while the v_ω arrow indicates the surface wind velocity direction. The GSD is approximately 0.85 m.

	ROI-1 Statistics [K]				ROI-2 Statistics [K]			
ID	Min	Max	Mean	St. Dev.	Min	Max	Mean	St. Dev.
F1	294.65	295.05	294.82	0.14	294.65	295.05	294.83	0.14
F2	293.75	294.15	293.88	0.12	293.35	294.15	293.81	0.22
F3	293.85	294.45	294.22	0.17	293.55	294.75	294.24	0.29
F4	294.65	295.05	294.84	0.14	293.75	295.05	294.63	0.40
F5	294.45	294.85	294.68	0.14	294.45	294.85	294.70	0.11
F6	292.25	292.85	292.58	0.19	292.55	292.85	292.65	0.11

Table 2.7: SRNL 20may04e04 image ROI statistics

ID	Water/Fan	T_{ex} [K]	Td_{ex} [K]	$\bar{T}_{ROI-1} - T_{ex}$ [K]	$\bar{T}_{ROI-2} - T_{ex}$ [K]
F1	On/Off	295.55	295.45	-0.73	-0.72
F2	On/50%	294.25	294.15	-0.37	-0.44
F3	On/100%	294.75	294.35	-0.53	-0.51
F4	On/Off	295.65	295.45	-0.81	-1.02
F5	On/Off	296.75	296.75	-2.08	-2.05
F6	Off/Off	294.45	293.45	-1.87	-1.80

Table 2.8: Ground measured temperatures compared to the mean ROI temperatures.

T_{in} [K]	T_{out} [K]	T_{amb} [K]	Td_{amb} [K]	P [mb]	4m Wind [m/s]	60m Wind [m/s]
297.61	296.09	292.87	291.06	1011.39	0.48 @ 117.5°	4.86 @ 178.6°

Table 2.9: Ground measurements collected at 02:06 EDT on 20 May 2004.

SRNL 20jun05G09 image (Night)

22:17 EDT, 20 June 2005 at 350 ft. Towers are labeled H1 through H4 from right to left.

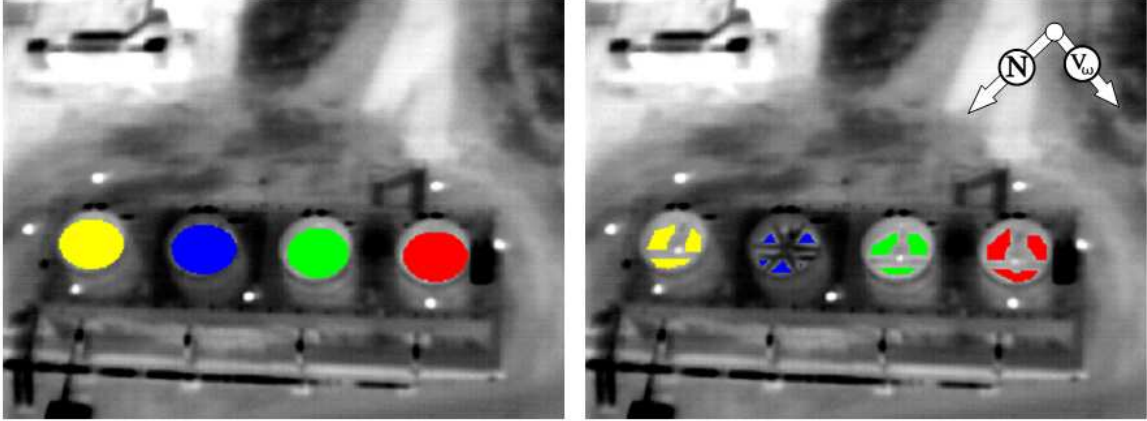


Figure 2.7: ROI-1 (left) and ROI-2 (right). The N arrow indicates the direction of north while the v_w arrow indicates the surface wind velocity direction. The GSD is approximately 0.15 m.

ID	ROI-1 Statistics [K]				ROI-2 Statistics [K]			
	Min	Max	Mean	St. Dev.	Min	Max	Mean	St. Dev.
H1	296.05	299.15	297.56	0.48	297.15	298.45	297.81	0.27
H2	296.35	301.45	297.70	0.46	297.35	298.25	297.86	0.21
H3	291.95	296.85	294.59	1.06	294.45	296.85	295.80	0.49
H4	295.75	300.15	297.45	0.54	296.65	298.35	297.64	0.29

Table 2.10: SRNL 20jun05G09 image ROI statistics.

ID	Water/Fan	T_{ex} [K]	Td_{ex} [K]	$\bar{T}_{ROI-1} - T_{ex}$ [K]	$\bar{T}_{ROI-2} - T_{ex}$ [K]
H1	On/On	297.16	297.12	0.40	0.65
H2	On/On	296.78	296.51	0.92	1.08
H3	On/Off	296.01	290.72	-1.42	-0.21
H4	On/On	296.39	294.99	1.06	1.25

Table 2.11: Ground measured temperatures compared to the mean ROI temperatures.

T_{in} [K]	T_{out} [K]	T_{amb} [K]	Td_{amb} [K]	P [mb]	4m Wind [m/s]	60m Wind [m/s]
299.66	295.46	296.39	293.17	1008.67	0.75 @ 91°	4.37 @ 104°

Table 2.12: Ground measurements collected at 22:17 EDT on 20 June 2005.

2.4 Analysis

The data presented in Figures 2.4 through 2.7 are representative of images obtained at night, at various collection altitudes, for various tower operating conditions, and for different view angles. The mean ROI temperatures, \bar{T}_{ROI-1} and \bar{T}_{ROI-2} , and the ground-measured exit air temperature, T_{ex} , are not equal. This difference must be accounted for. Several statements can be made about the data presented here.

For the nadir images (Figures 2.4 to 2.6), the temperature errors are all less than zero which means that the mean ROI temperature is less than the measured exit air temperature. This is expected since factors such as the emissivity, atmospheric effects, and blurring would tend to cause the apparent temperature to be less than the absolute temperature.

The magnitude of the temperature errors, $|\Delta T|$, is smaller in the *fans on* case than in the *fans off* case for all altitudes. The spinning fan forces the air inside the tower cavity out of the tower stack. Therefore the interior and exterior air are closer to being the same temperature. On the other hand, in the *fans off* case air is expelled from the tower through natural convection. As a consequence, the air exiting the tower stack is at a slightly lower temperature since it cools as it expands and rises. The $|\Delta T|$ is therefore larger for the *fans off* case than in the *fans on* case.

The magnitude of the temperature errors are smaller for ROI-2 than for ROI-1 for altitudes of 500 feet (152.5 m) and 1000 feet (305.0 m). This is expected because when the fan blades are avoided, as in ROI-2, the ROI contains pixels from the interior of the tower only. When the ROI does not avoid the fan blades, as in ROI-1, the ROI contains pixels from both the interior and exterior (fan blades) of the tower. The exterior pixels will have a lower apparent temperature since they will reflect a lower radiance from the sky and will be at a lower absolute temperature because of radiative cooling at night. Also, the ROI-1 and ROI-2 temperatures are roughly the same at an observation altitude of 2000 feet (610.0 m). The optical blur of the pixels at this higher altitude cause ROI-2 to behave as ROI-1 and therefore the apparent temperatures are roughly equal.

Lastly, $|\Delta T|$ increases for both ROIs as the observation altitude increases. This decrease in apparent temperature with increasing altitude is caused by the increase in atmospheric path.

The dataset also contains an image acquired at an oblique angle (Figure 2.7). For this scene, the temperature error is greater than zero for the *fans on* case but is less than zero for the *fans off* case. In other words, the apparent temperature is greater than the exit air temperature when the fans are operating. The opposite is true when the fans are not operating. The lower apparent temperature in the *fans off* case is expected since the emissivity, atmospheric radiance loss, etc. would decrease the sensor-reaching radiance and therefore yield a lower apparent temperature. This trend was observed in the nadir imagery. The higher apparent temperature for the *fans on* towers is most likely due to the motion of the fan. The fan motor drives a gearbox which in turn drives the fan blades. This gearbox was obscured by the fan hub in the nadir imagery. For the oblique image however, the gearbox is slightly exposed. The heat generated by friction within the gearbox causes its absolute temperature to increase. This contributes to an increase in sensor-reaching radiance which results in a higher apparent temperature.

The magnitude of the temperature error, $|\Delta T|$, is smaller for ROI-2 than for ROI-1 in the *fans off* case. As with the nadir images, when the fan blades are avoided, as in ROI-2, the ROI contains pixels from the warm interior of the tower only and does not contain cooler pixels from the exterior of the tower. Therefore, the apparent temperature is closer to the true exit air temperature for ROI-2 in the *fans off* case. Conversely, $|\Delta T|$ is greater for ROI-2 than for ROI-1 in the *fans on* case. Although the fan blades and internal structure were avoided as best as possible in ROI-2, some of the warmer pixels caused by the fan gearbox may have blurred into the cavity pixels. The cooler fan blade pixels are not included in the ROI. Therefore, the pixels in ROI-2 would have a warm bias which causes $|\Delta T|$ to be greater than the ROI-1 case.

2.5 Preliminary Variables

It is clear from the previous section that there are many factors that may affect the radiance reaching the sensor and therefore the derived exit air temperature. The thermal images of MDCTs provided an initial look at the factors that might be important in accurately determining the exit air temperature. The atmosphere will attenuate the radiance as it leaves the tower and travels to the sensor. In addition, the atmosphere will blur the signal reaching the sensor so that a given pixel will contain some radiance from its neighbors. The viewing geometry of the sensor also greatly affects the derived temperature. The altitude and view angle of the sensor defines the path length through the atmosphere. The ground sampling distance (GSD) of the sensor will influence whether the internal

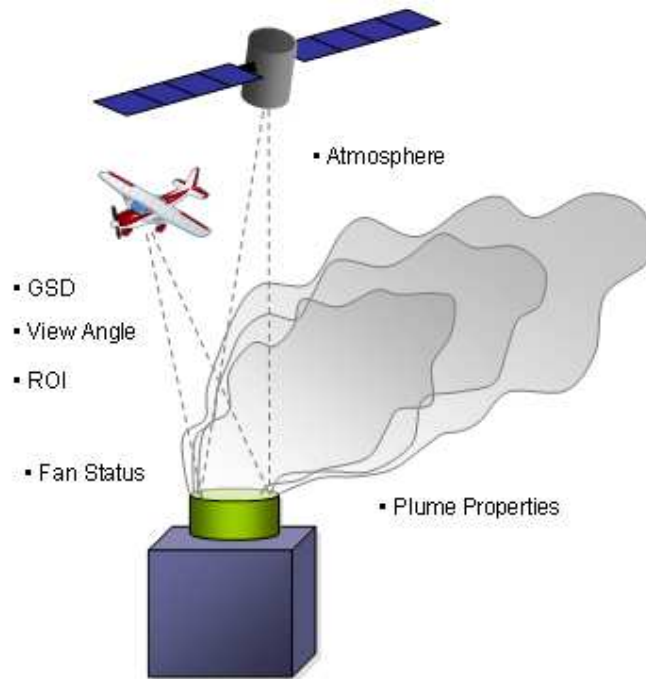


Figure 2.8: Preliminary variables affecting the apparent temperature recorded by a sensor of a MDCT.

structure is visible or if the entire fan stack opening is covered by a single pixel. The operating status of the fans determine the air flow through the tower which in turn affects the derived temperature. The ROI chosen will also determine what pixels are included in the temperature derivation.

2.6 Summary

To reiterate, the objective is to derive the exit air temperature of a MDCT from remote thermal imagery. The apparent temperature of the tower from the thermal image will be correlated to the exit air temperature. The temperature of the exhausted air is one of the required inputs into an energy-related process model.

In the following chapters, the physical phenomenology of the factors that affect the radiance reaching the sensor will be investigated. Constraints will then be placed on these variables and a method will be developed to correct for the error between the apparent temperature and measured exit air temperature of the MDCT.

Chapter 3

Theory

Remote sensing involves the gathering of information about a target of interest by analyzing the radiant energy emanating from that target. The energy detected by a sensor, however, is a collection of light from many sources traveling various paths to reach the sensor. Many of these paths are unrelated to the target of interest and the paths directly between the target and sensor are modified by the radiometric environment. The factors affecting the signal entering the sensor cannot be easily separated and therefore must be modeled or estimated in order to extract the desired information about the target of interest. An overview of temperature extraction from remote thermal imagery is presented in this chapter.

3.1 Self-Emitted Radiance

The amount of thermal energy contained in a material is represented by its absolute temperature, T , expressed in units of *Kelvin*. All materials have an absolute temperature above zero since all materials interact with their environment through the laws of thermodynamics. A material having an absolute temperature, T , will continuously radiate and absorb energy in order to reach thermal equilibrium with its environment.

3.1.1 Blackbody Radiation

An idealized surface in which all electromagnetic radiation is completely absorbed at all wavelengths and then re-radiated is known as a *blackbody*. These surfaces have the property that their absorptivity is unity while their reflectivity is zero. Max Planck derived an expression for the spectral radiance of a blackbody in 1901 (See Appendix A) [4]. The *Planck blackbody radiation equation* describes the spectral distribution of the emitted energy of a blackbody at temperature, T , into a solid angle above the blackbody surface. Planck's law is defined as

$$L_{BB}(\lambda, T) = \frac{2hc^2}{\lambda^5} \frac{1}{e^{hc/\lambda kT} - 1} \left[\frac{W}{m^2 sr \mu m} \right], \quad (3.1)$$

where:

h	Planck constant	$6.6256 \cdot 10^{-34} [J \cdot s]$
c	speed of light in vacuum	$2.9979 \cdot 10^8 [m/s]$
k	Boltzmann constant	$1.3807 \cdot 10^{-23} [J/K]$
λ	wavelength of emission	$[\mu m]$
T	absolute temperature	$[K]$.

The Planck equation is dependent on both the temperature of the object and on the wavelength of emission. The units of the variables and constants in equation (3.1) must be handled with care in order to arrive at the desired dimensions of $[W/m^2/sr/\mu m]$.

The relationship between the wavelength of peak emission of a blackbody and its temperature is *Wien's displacement law* stated as

$$\lambda_{peak} = \frac{2897.768 [\mu m K]}{T} [\mu m]. \quad (3.2)$$

The sun is approximately a blackbody at a temperature of 5800 Kelvin having a peak emission in the visible region (approximately $0.5 \mu m$). The average temperature of the Earth is about 300 Kelvin with a peak emission in the longwave infrared region (approximately $10 \mu m$). Most terrestrial emissive remote sensing is done in the longwave infrared since most objects on the Earth are near 300 Kelvin. The Planck distribution for blackbodies of different temperatures are shown in Figure 3.1.

3.1.2 Directional Emissivity

Ideal blackbodies do not exist in nature. Real objects are not perfect emitters and will therefore emit less radiance than a blackbody. The spectral emissivity, $\varepsilon(\lambda)$, is a measure of the effectiveness of an object as a radiator. The emissivity of a material at wavelength λ and temperature T is defined as the ratio of the radiation emitted by the material at that wavelength to the radiation emitted by a blackbody at the same temperature and wavelength [5]. For Lambertian surfaces, the emitted radiance is distributed equally into the hemisphere above the surface. The self-emission for Lambertian surfaces is defined as

$$L(\lambda, T) = \varepsilon(\lambda) L_{BB}(\lambda, T) \left[\frac{W}{m^2 sr \mu m} \right]. \quad (3.3)$$

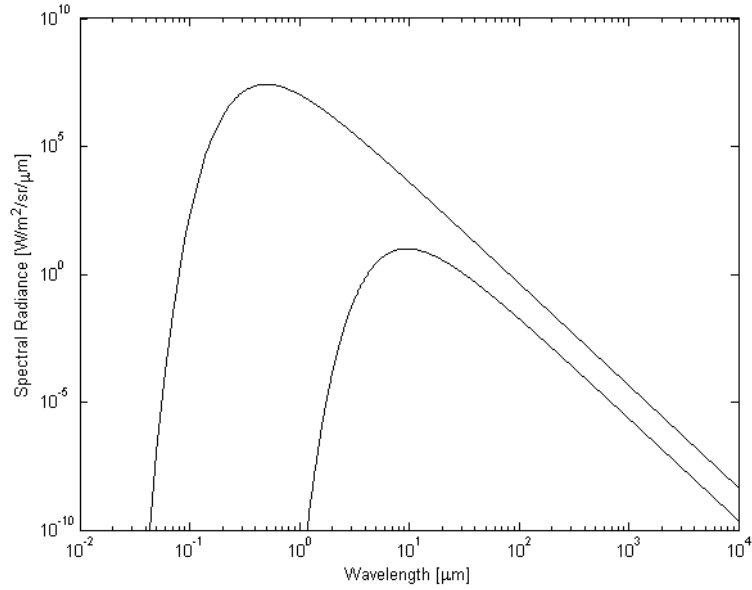


Figure 3.1: Planck curves for a 5800 Kelvin (top) and 300 Kelvin (bottom) blackbody.

Most materials are not Lambertian and will radiate more in some directions than in others. The emissivity term is modified to incorporate this dependence on view angle. The self-emission for non-Lambertian surfaces is then

$$L(\theta, \phi, \lambda, T) = \varepsilon(\theta, \phi, \lambda) L_{BB}(\lambda, T) \quad \left[\frac{W}{m^2 sr \mu m} \right] \quad (3.4)$$

where (θ, ϕ) indicate the direction of the sensor. The parameter $\varepsilon(\theta, \phi, \lambda)$ is known as the *directional emissivity*.

3.2 Reflected Radiance

Reflected radiance can be treated in a similar, complementary fashion to the self-emitted radiance. The reflectance properties of a surface describe how radiance from background sources is scattered into the hemisphere above the material surface. As with the self-emitted radiance, both the magnitude and directional distribution of the reflected radiance must be taken into account.

3.2.1 Bidirectional Reflectance Distribution Function

The reflectance of a surface generally depends on the illumination angle, the view angle, and the wavelength. This angular dependence is characterized by a *bidirectional reflectance distribution function (BRDF)*. It is defined as the ratio of the radiance, L , reflected from the

surface into the direction (θ_r, ϕ_r) to the irradiance, E , incident on the surface from direction (θ_i, ϕ_i) [1] and is written as

$$\rho'(\theta_i, \phi_i, \theta_r, \phi_r, \lambda) = \frac{L(\theta_r, \phi_r, \lambda)}{E(\theta_i, \phi_i, \lambda)} \left[\frac{1}{sr} \right]. \quad (3.5)$$

The BRDF describes the distribution of reflected radiance into the hemisphere from a given source geometry. It can be thought of as a probability distribution function for the reflected radiance in any direction [1].

3.2.1.1 BRDF models

The BRDF is a function of all combinations of the incident and reflected angles as well as wavelength. The large number of angles and wavelengths needed to fully describe the directional distribution makes measuring a BRDF a tedious process. As a result, models have been introduced that approximate a true BRDF with only a hand full of adjustable parameters. These parameters control the shape of the BRDF so that any range of a specular to a diffuse BRDF can be modeled.

3.2.1.1.1 Lambertian Model Probably the simplest BRDF model is the Lambertian model. A Lambertian, or diffuse, surface is one that reflects equally in all directions [1]. The model is written as

$$\rho'(\theta_i, \phi_i, \theta_r, \phi_r) = \frac{\rho}{\pi} \left[\frac{1}{sr} \right], \quad (3.6)$$

where ρ is the reflectance of the material. This model is often used for quick calculations when a “directional” BRDF is not necessary.

3.2.1.1.2 Ward Model The BRDF model described by Ward [6] adds a specular component to the Lambertian model. It is a mathematical model designed to approximate a true physical BRDF. The objective was to fit measured isotropic and anisotropic reflectance data with a simplistic formula with intuitively meaningful parameters. For an isotropic surface, the slope only varies in one dimension and is based on a Gaussian distribution. The BRDF of this case is modeled as

$$\rho'(\theta_i, \phi_i, \theta_r, \phi_r) = \frac{\rho_d}{\pi} + \frac{\rho_s}{\sqrt{\cos \theta_i \cos \theta_r}} \frac{e^{-\tan^2 \alpha / \sigma^2}}{4\pi\sigma^2} \left[\frac{1}{sr} \right], \quad (3.7)$$

where ρ_d is the diffuse reflectance, ρ_s is the specular reflectance, σ is the root-mean-square (RMS) of the surface slope (similar to surface roughness), and α is the angle between the

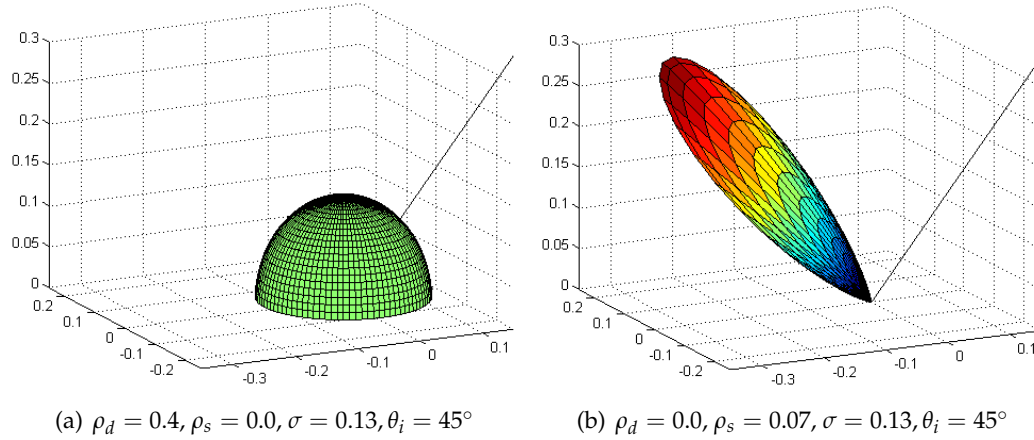


Figure 3.2: Ward BRDF model: diffuse (left) and specular (right). The thin line on the right hand side in the figures indicates the incident ray.

surface normal \vec{n} and vector \vec{n}' that bisects the incident and reflected rays. Ward notes that the reflectance values in equation (3.7) may have a spectral dependence and may vary as a function of angle so long as the sum of ρ_d and ρ_s is less than unity. The normalization factor is valid as long as σ is not much greater than 0.2. A proper normalization is necessary to ensure physically meaningful results [6]. The α and ϕ angles are determined by the geometry of the incident and reflected rays. The user is only responsible for providing estimates of ρ_d , ρ_s , and σ . A small value of σ corresponds to a narrow specular lobe, while a large value corresponds to a wide lobe. The Ward BRDF model is appealing due to its simplicity. However, the model and its input parameters are not based on any physical measurements. Figure 3.2 illustrates two Ward reflectance functions.

3.2.1.1.3 Torrance-Sparrow and Priest-Germer Models Torrance and Sparrow developed a BRDF model based on the microfacet theory [7]. A rough surface is modeled as a collection of tiny facets. The slopes of these microfacets are assumed to be randomly oriented according to a probability distribution. Each microfacet acts as a specular reflector that obeys the law of reflection so that reflection occurs in the plane of incidence and the reflected angle equals the incident angle. The reflectance of the microfacet is calculated from the Fresnel equations. Torrance and Sparrow also account for the effect of shadowing and masking of a facet by adjacent facets. See reference [7] for a complete description of the Torrance-Sparrow BRDF model.

Priest and Germer extended the Torrance-Sparrow model to provide a polarized bidirectional reflectance function [8]. The Priest-Germer model itself only provides the specular

component of the BRDF. It assumes that the polarized reflectance is due to specular reflection while the diffuse reflection is unpolarized. Like the Torrance-Sparrow model, the Priest-Germer model is based on the assumption that the rough surface of the material is a collection of tiny, specular, and randomly oriented microfacets. Refer to reference [8] for details of the Priest-Germer BRDF model.

3.2.1.1.4 Beard-Maxwell Model and the NEFDS The Beard-Maxwell model is also based on the microfacet theory in which reflection occurs at the first surface but adds a volumetric component in which scattering occurs beneath the surface [5] [9]. The model requires seven input parameters that adjust the scatter from the first surface and from beneath the surface. The number of free parameters in this model is large compared to the previously mentioned BRDF models. These parameters are based on actual measured data for real materials which allow the model to more accurately describe a BRDF. The Beard-Maxwell model serves as the basis for the Nonconventional Exploitation Factors Data System (NEFDS) [5]. The NEF database contains measured input parameters for several hundred materials. The Beard-Maxwell model along with NEF materials provide a powerful way to generate reflectance models from a few measured parameters for several hundred materials.

3.2.1.1.5 Shell Target Model Shell generalized the previously mentioned BRDF models in his Ph.D. dissertation in 2005 [10]. Shell decomposes these models into a general form to allow for polarization of the model based on the polarized Priest-Germer model. Shell splits the BRDF model into a specular and a volumetric component. The specular component results from specular scattering from the front surface via the Fresnel equations. The volumetric component results from subsurface scattering and is assumed to be completely depolarizing.

3.2.2 Directional Hemispherical Reflectance

The ratio of the total power reflected into the entire hemisphere by a surface to the power incident on the surface from a specified direction is the *directional hemispherical reflectance* (DHR). It is the integral of the BRDF over the entire hemisphere above a surface for a fixed incident angle. The directional hemispherical reflectance is

$$\rho(\theta_i, \phi_i, \lambda) = \int_{2\pi} \rho'(\theta_i, \phi_i, \theta_r, \phi_r, \lambda) \cos(\theta_r) d\omega_r, \quad (3.8)$$

where the integral is taken over all solid angles, $d\omega_r$, of the hemisphere. The DHR is a unitless quantity whose range of values are $0 \leq \rho \leq 1$. The DHR is also defined through the reciprocal relation as the ratio of the radiance reflected by a surface into direction (θ_r, ϕ_r) to the radiance uniformly incident on the surface from the entire hemisphere. The two definitions are equivalent so that $\rho(\theta_i, \phi_i, \lambda) = \rho(\theta_r, \phi_r, \lambda)$. If a material is isotropic, then the azimuthal dependence in equation (3.8) can be ignored,

$$\rho(\theta_i, \phi_i, \lambda) = \rho(\theta, \lambda). \quad (3.9)$$

Furthermore, if the angular dependence is ignored altogether, then the familiar reflectance of a material is $\rho(\lambda)$.

3.3 Conservation of Energy

When radiance is incident on an object, it may be absorbed, reflected, or transmitted. These phenomena are represented by the unitless quantities of absorptivity $\alpha(\lambda)$, reflectivity $\rho(\lambda)$, and transmittance $\tau(\lambda)$, respectively [1]. The conservation of energy requires that these quantities sum to unity so that all the incident radiance is accounted for:

$$\alpha(\lambda) + \rho(\lambda) + \tau(\lambda) = 1. \quad (3.10)$$

Kirchhoff's work in thermal radiation led to the conclusion that energy being absorbed at a particular wavelength must be equal to the energy emitted at that same wavelength for an object in thermal equilibrium. Therefore, the absorptivity is equal to the emissivity $\alpha(\lambda) = \varepsilon(\lambda)$ [11]. For an opaque object where transmission is zero, *Kirchhoff's law* is

$$\varepsilon(\lambda) + \rho(\lambda) = 1. \quad (3.11)$$

This relation can be generalized so that the angular dependence of the emissivity and reflectivity manifests itself,

$$\varepsilon(\theta, \phi, \lambda) + \rho(\theta, \phi, \lambda) = 1. \quad (3.12)$$

The quantities $\varepsilon(\theta, \phi, \lambda)$ and $\rho(\theta, \phi, \lambda)$ are the previously defined directional emissivity and directional hemispherical reflectance from Sections 3.1.2 and 3.2.2.

3.4 Energy Paths Reaching a Sensor

The radiance incident on a sensor has many components. These components come from a variety of sources and depend on the material optical properties and on the radiometric properties of the surrounding scene. Photons will be traced from the major energy paths entering the sensor to produce a generic equation describing the radiance at the sensor.

3.4.1 Material Radiance

In thermal remote sensing, information about the temperature of the target is of interest. This temperature information is carried by the self-emitted radiance term. It is a function of the Planck equation modified by the object's directional emissivity (see Section 3.1). Given that the emissivity is less than unity and through Kirchoff's relation, real material surfaces will also reflect radiance from the surround. The reflected background component is due to the self-emission from background sources due to the temperature of these sources. The reflected component depends on the BRDF of the material surface (see Section 3.2). The radiance leaving the surface of an object headed toward the sensor is written as

$$L(\theta, \phi, \lambda) = \varepsilon(\theta, \phi, \lambda)L_{BB}(\lambda, T) + \int_{2\pi} L_{bkgd}(\theta_i, \phi_i, \lambda) \rho'(\theta_i, \phi_i, \theta, \phi, \lambda) \cos(\theta_i) d\omega_i, \quad (3.13)$$

where the units are $[W/m^2/sr/\mu m]$. In the reflected term, the background radiance incident from direction (θ_i, ϕ_i) is weighted by the BRDF and solid angle in that direction and the integral is evaluated over the hemisphere above the surface. The emissive term is the familiar self-emission from equation (3.4). The angles (θ, ϕ) indicate the direction of the sensor. Note that the background radiance is a generic term representing all the surrounding radiation sources. These sources may include the sun, the sky, other objects, etc. For a uniform background, L_{bkgd} is independent of direction and is a constant of integration. The resulting integral is simply the directional hemispherical reflectance from equation (3.8) so the surface-leaving radiance reduces to

$$L(\theta, \phi, \lambda) = \varepsilon(\theta, \phi, \lambda)L_{BB}(\lambda, T) + \rho(\theta, \phi, \lambda)L_{bkgd}(\lambda) \left[\frac{W}{m^2 sr \mu m} \right]. \quad (3.14)$$

3.4.2 Atmospheric Effects

The radiance leaving the material surface must then propagate through the atmosphere to reach the sensor. The atmosphere may considerably modify this radiance along the line of sight to the sensor. The constituent gases and aerosols attenuate the signal by absorption

and scattering out of photons. This phenomenon is captured by the atmospheric transmission parameter, $\tau(\lambda)$. The atmospheric constituents also have a finite temperature and will emit their own self-emitted radiance in all directions, thereby adding to the apparent material radiance [5]. This radiance from the atmosphere may be reflected off the target, thereby contributing to the background radiance, L_{bgd} , or may enter the sensor directly.

3.4.2.1 Atmospheric Transmission

Atmospheric transmission refers to the loss of photons by a volume of atmosphere. It encompasses both the absorption and scattering out of photons.

3.4.2.1.1 Absorption Absorption refers to the removal of photons by a material through the conversion of electromagnetic energy to some other form of energy, usually thermal. It occurs when the energy (wavelength) of the incoming photon is sufficient to cause a rotational, vibrational, or electronic energy transition in a molecule present in the atmosphere. The molecule absorbs the photon and makes a quantum jump to a higher energy state. The molecule will quickly lose this excess energy through collisions with other molecules and return to its original energy state. The photon energies (wavelengths) that will be absorbed by a molecule depend on the transition energies between states of that molecule [11]. The amount of absorption by atmospheric gases is dependent on the quantity of the gas and on its temperature and pressure [5]. These discrete energy absorptions manifest themselves as discrete lines in the absorption spectrum of a gas. However, interactions between the gas molecules will cause perturbations in their energy states which results in broadening of the absorption lines. When the broadened lines are close to each other, they combine to form a continuum of absorption [1]. A typical gas absorption spectrum will therefore exhibit both discrete (molecular) and continuum absorption features. Major absorbers in Earth's atmosphere in the LWIR are O_3 , CO_2 , and H_2O .

The amount of absorption of a propagating beam of radiation in a given path length depends on the effective size and density of absorbing particles. The absorption cross section, $C_\alpha(\lambda)$, is a measure of the effectiveness of a particle as an absorber to a particular wavelength of radiation. The fractional amount of flux that is absorbed per unit length is defined as

$$\beta_\alpha(\lambda) = m C_\alpha(\lambda) \left[\frac{1}{m} \right] \quad (3.15)$$

where m is the number of particles per unit volume and $\beta_\alpha(\lambda)$ is known as the *absorption coefficient*. It is the fractional amount of flux lost to absorption per unit length [1].

For a horizontal layer of gas of infinitesimally small thickness, dz , the fractional amount of absorption through the layer is

$$d\alpha(\lambda) = \frac{d\Phi(\lambda)}{\Phi(\lambda)} = -\beta_\alpha(\lambda) \sec \theta dz \quad (3.16)$$

where θ is the zenith angle through the layer, Φ is the incident flux entering the layer and $d\Phi$ is the flux lost to absorption in the layer. Integrating both sides and taking the antilog yields the transmission,

$$\tau_\alpha(\theta, \phi, \lambda) = e^{-\int_{z_1}^{z_2} \beta_\alpha(\lambda) \sec \theta dz} \quad (3.17)$$

where the integral is performed over the starting and ending altitudes of the path. If there is more than one constituent gas in the layer, then the absorption coefficient is the sum of the absorption coefficients of the constituent gases.

3.4.2.1.2 Scattering Transmission losses are also the result of photons being scattered out of the propagating beam. The transmission loss due to scattering can be written similar to the transmission loss due to absorption as

$$\tau_s(\theta, \phi, \lambda) = e^{-\int_{z_1}^{z_2} \beta_s(\lambda) \sec \theta dz} \quad (3.18)$$

where $\beta_s(\lambda)$ is the *scattering coefficient*. The scattering coefficient is a function of the index of refraction of the scattering particles. It can also be expressed as a function of a size parameter $a = 2\pi r/\lambda$ which is a measure of the size of particles in comparison to the wavelength of radiation [12].

A complete theory on the scattering of electromagnetic radiation involves developing solutions to the Maxwell equations. In a given volume of air, a variety of particle shapes and sizes are present [12]. For the idealized case of spherical particles, Gustav Mie developed a complete analytical solution to Maxwell's equations. The Mie solution, commonly referred to as *Mie scattering*, is valid for all possible size parameters, a . The angular distribution of the scattered radiation varies greatly depending on the particle size and wavelength of radiation. In general, however, forward scattering dominates over back scattering. Mie scattering also depends weakly on wavelength and becomes independent of it when the particle size exceeds the wavelength [11].

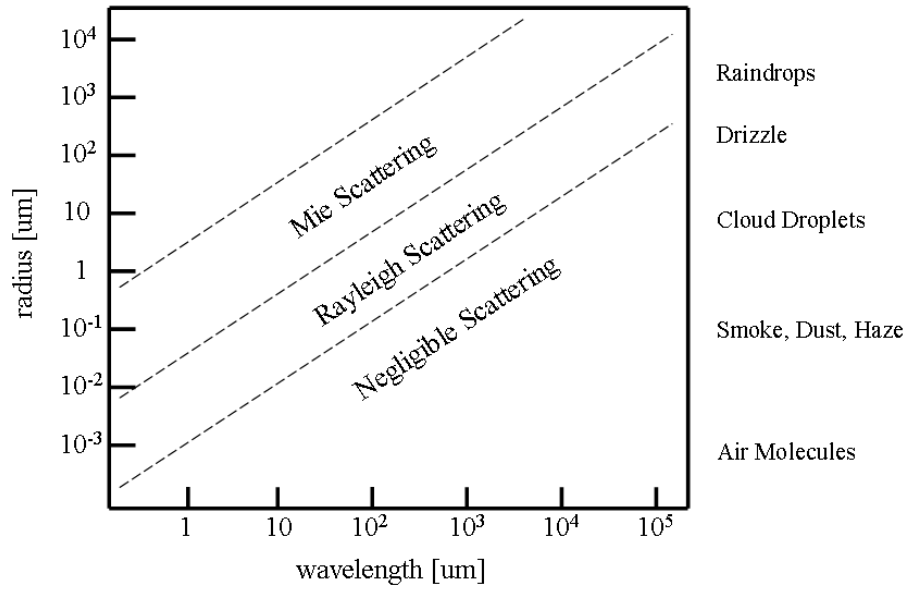


Figure 3.3: Atmospheric scattering as a function of particle radius and incident radiation wavelength. (Adopted from Wallace and Hobbs, pg. 307) [12])

For the special case where the particle size is much less than the wavelength of radiation ($a \ll 1$), Lord Rayleigh showed that for a given refractive index, the scattering coefficient is inversely proportional to the fourth power of wavelength ($\beta_s \propto \lambda^{-4}$). The predominance of short wavelengths scattered by air molecules is responsible for the blueness of the sky in the visible region. The scattered radiance is also evenly divided between the forward and back scattered hemispheres [12]. This small-size limiting case of the Mie solution is commonly known as *Rayleigh scattering*.

When the size of the particles are much larger than the wavelengths of the incoming radiation ($a > 50$), the angular distribution of the scattered radiation can be described by the principles of geometrical optics. In this so-called *nonselective scattering* regime, the scattering is independent of wavelength. For example, at visible wavelengths scattering by cloud droplets, raindrops, and ice crystals fall within this regime and are responsible for distinctive phenomena such as rainbows and halos [12].

Figure 3.3 illustrates the dependence of scattering on particle size and wavelength in the atmosphere. Ordinary gas molecules in the atmosphere do not produce significant scattering in the longwave infrared [1] [12]. Scattering will become important in the LWIR if dust particles and aerosols are present in the atmosphere [12].

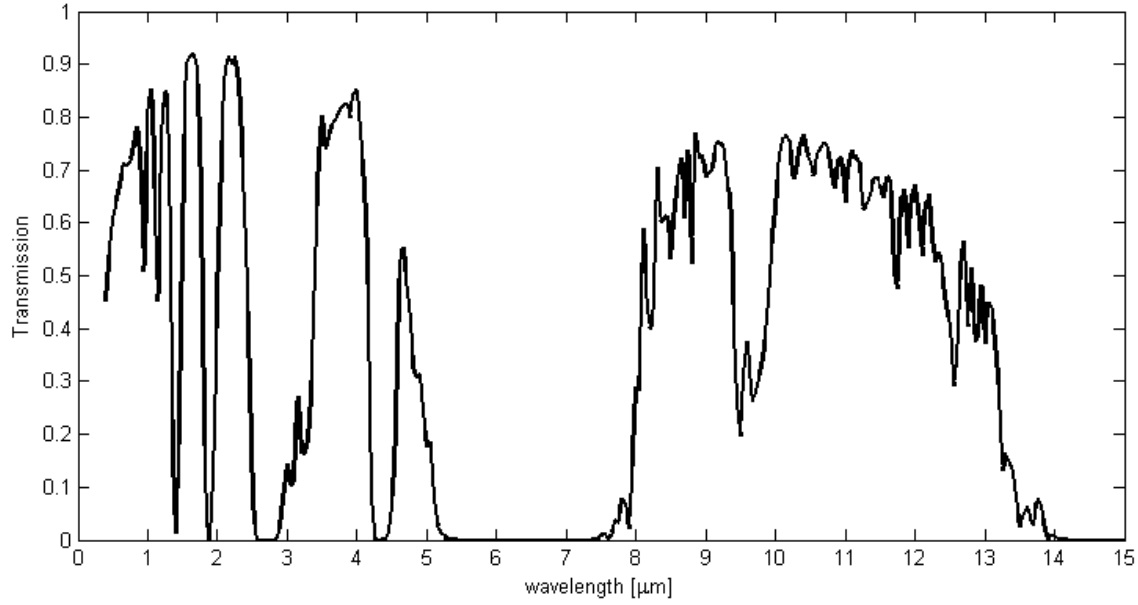


Figure 3.4: Atmospheric spectral transmission along a vertical space-to-ground path generated from a MODTRAN mid-latitude summer atmosphere[13].

3.4.2.1.3 Total Transmission The transmission due to absorption and scattering effects can be combined to describe the total transmission by

$$\tau(\theta, \phi, \lambda) = e^{-\int_{z_1}^{z_2} \beta_{ext}(\lambda) \sec \theta dz} \quad (3.19)$$

where $\beta_{ext}(\lambda)$ is known as the *extinction coefficient* and is the sum of the absorption and scattering coefficients. The total spectral atmospheric transmission is visualized in Figure 3.4.

3.4.2.2 Atmospheric Emission

The constituents of the atmosphere have a finite temperature and will therefore be a source of energy [1]. To calculate this radiance, the continuously varying atmosphere is approximated as a set of homogeneous layers as in Figure 3.5. Each layer has an effective transmission, $\Delta\tau_i$, along the line of sight of the sensor defined by the angles (θ, ϕ) . Since scattering is negligible in the LWIR, the effective emissivity of the i^{th} layer is $\Delta\varepsilon_i = 1 - \Delta\tau_i$ [1]. The self-emitted radiance of the i^{th} layer is the blackbody radiance, $L_{BB}(T_i)$, due to its temperature, modified by the effective emissivity of that layer and the product of the effective transmissions of the $(i - 1)$ layers. If the number of layers in direction (θ, ϕ) is N ,

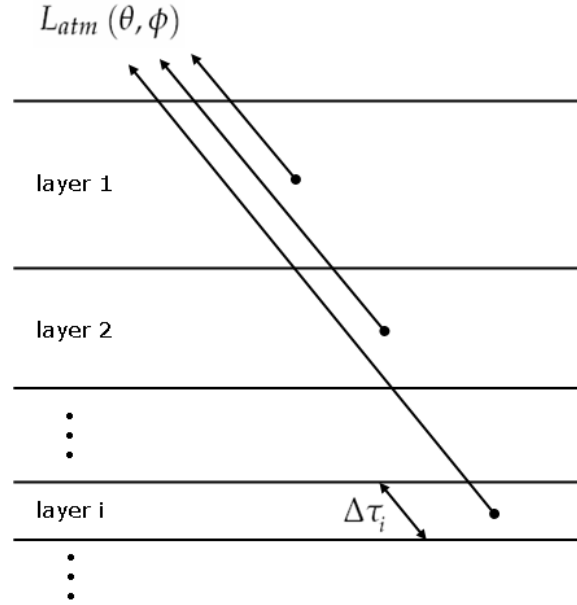


Figure 3.5: Self-emitted atmospheric radiance into the (θ, ϕ) direction is the sum of the self-emitted radiance from each homogeneous atmospheric layer (Adopted from Schott 1997, pg 109 [1]).

then the atmospheric radiance is

$$L_{atm}(\theta, \phi, \lambda) = \sum_{i=1}^N L_{BB}(\lambda, T_i) [1 - \Delta\tau_i(\theta, \phi, \lambda)] \prod_{j=1}^{i-1} \Delta\tau_j(\theta, \phi, \lambda) \left[\frac{W}{m^2 sr \mu m} \right]. \quad (3.20)$$

The atmospheric radiance that is emitted towards the target material is known as the emissive downwelled radiance, $L_d(\theta, \phi, \lambda)$. This may contribute to the background radiance that is reflected from the target material (see Section 3.4.1). The atmospheric thermal energy that is emitted towards the sensor is known as the emissive upwelled radiance, $L_u(\theta, \phi, \lambda)$. The upwelled radiance and the reflected downwelled radiance add to the target material's signal as recorded by the sensor [1].

3.4.3 Governing Equation

Combining all these radiometric effects into a single equation, the total spectral radiance reaching the sensor is then

$$L(\theta, \phi, \lambda) = \left[\varepsilon(\theta, \phi, \lambda) L_{BB}(\lambda, T) + \int_{2\pi} L_{bkgd}(\theta_i, \phi_i, \lambda) \rho'(\theta_i, \phi_i, \theta, \phi, \lambda) \cos(\theta_i) d\omega_i \right] \tau(\theta, \phi, \lambda) + L_u(\theta, \phi, \lambda), \quad (3.21)$$

in units of $[W/m^2/sr/\mu m]$ and where (θ, ϕ) indicate the direction of the sensor. This is the *governing equation* for radiance reaching the sensor. For uniform backgrounds, the reflected component in equation (3.21) reduces to the DHR multiplied by the background radiance.

From equation (3.21) it is clear that the radiance from the target itself is substantially modified on its way to the sensor. The directional emissivity, BRDF, background radiances, atmospheric transmission and upwelled radiances all work to alter the blackbody radiance from the target. This makes deriving the temperature of the target rather difficult. Each of the mentioned variables must be modeled or estimated in order to reconstruct the original blackbody radiance. Uncertainties in these parameters will lead to uncertainty in the derived temperature.

3.5 Imaging System

The combined spectral radiance from all the energy paths, $L(\theta, \phi, \lambda)$, is then incident on the sensor, or imaging system. In the general sense, an imaging system is a series of processes in which the incoming spectral radiances are represented as an image. The spectral radiances from all points visible to the sensor are collected, sampled, and measured to produce a quantifiable signal. The imaging system can be divided into several steps serving a specific task. Each step in this process unavoidably degrades the incoming signal so that the final image cannot be a perfect representation of the original signal.

3.5.1 Collection

The radiance incident on the sensor must first be collected. This operation is performed by the optical elements of the sensor. The radiance entering the aperture is focused onto the focal plane. Ideally, radiance from a point entering the aperture (*i.e.*, a point on the object plane) would be perfectly focused onto a point on the focal plane (image plane). However, for a diffraction-limited system, radiance from a point source on the object plane will be spread out over a finite area on the focal plane [11]. In other words, even a perfect point source (mathematically represented by a delta function [14]) will be blurred by the optical system. Figure 3.6 demonstrates this effect.

The image produced by a point source is called the *point-spread function* (PSF). For a shift-invariant linear system, the output signal (image) is the summation of spatially dis-

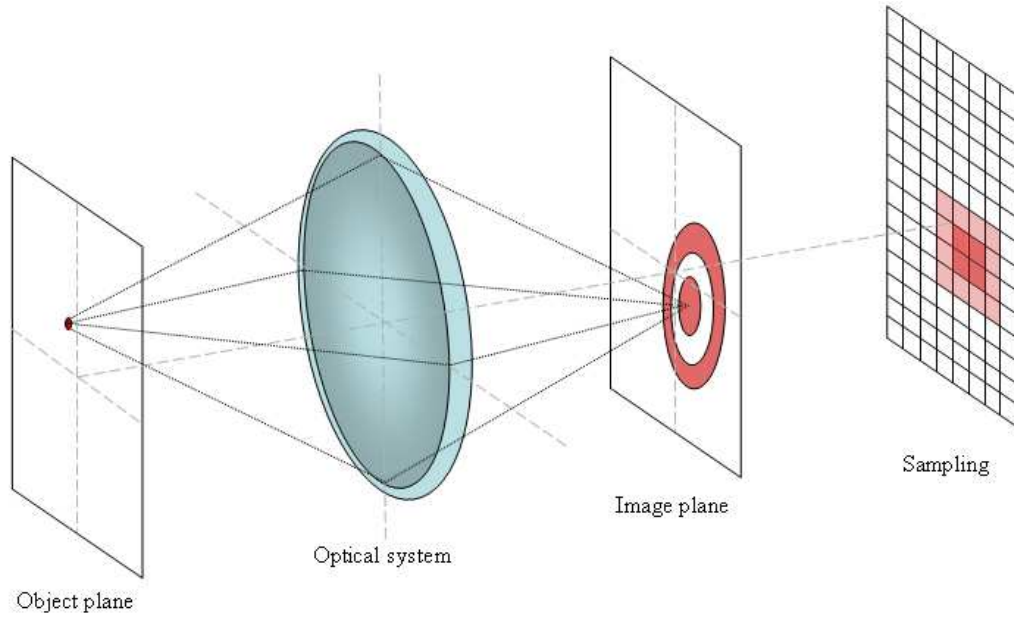


Figure 3.6: Illustration of the blurring effect and sampling as radiance from a point source passes through an imaging system (Adopted from Hecht 2002 [11]).

tributed PSF spots resulting from each point on the object plane [15]. Therefore, the output image can be described as the convolution of the input radiance signal (object) with the PSF of the optical system. This statement is written mathematically as

$$g(X, Y) = f(x, y) * h(x, y) = \int_{-\infty}^{+\infty} \int_{-\infty}^{+\infty} f(x, y) h(X - x, Y - y) dx dy, \quad (3.22)$$

where $g(X, Y)$ is the radiance pattern on the image plane, $f(x, y)$ is the radiance pattern on the object plane, and $h(x, y)$ is the point-spread function. The $h(x, y)$ term is also known as the *impulse response* function. In general, other steps in the imaging process will have an impulse response function which describes the degradation of the signal as a result of that process. The impulse responses of each process may be convolved together to arrive at the total impulse response of the entire imaging system.

In essence, the PSF accounts for the spatial loss of detail that is inherent in the optical system [15]. It is worth noting that a typical optical system will consist of a circular aperture. In this case, the diffraction-limited PSF is known as an Airy disc [11]. The formula for the Airy disc pattern is

$$h(r) = \left[\frac{2 J_1(\pi r/r_0)}{\pi r/r_0} \right]^2, \quad (3.23)$$

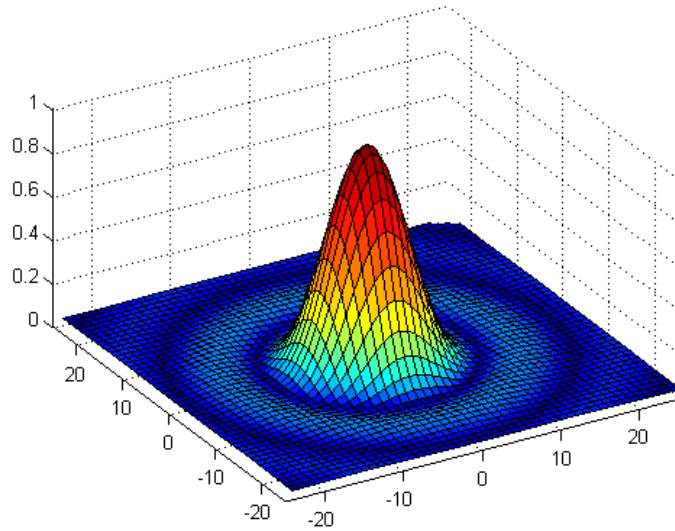


Figure 3.7: Airy disc pattern representing the PSF of a diffraction-limited circular aperture system.

where $J_1()$ is the first-order Bessel function of the first kind [15], r is the radial distance from the center of the Airy disc on the image plane, and r_0 is the radial distance from the center of the disc to the first minimum (see Figure 3.7). The Bessel function is written as

$$J_1(r) = \frac{1}{\pi} \int_0^{\pi} \cos(t - r \sin(t)) dt. \quad (3.24)$$

The constant r_0 is computed by

$$r_0 = \frac{1.22 \lambda f}{a} \quad [\mu m], \quad (3.25)$$

where a is the diameter of the circular aperture, f is the focal length, and λ is the wavelength of the radiation.

3.5.2 Detection

The optical system focuses the sensor reaching radiance onto the focal plane. Detectors located on the focal plane then convert this radiance into a quantifiable signal. For electro-optical systems, the detector converts the incident flux on it into an electronic signal. This is accomplished when a photon is absorbed by the detector material and induces a charge in the material. The accumulated charge is then read out as an electronic signal. A typical sensor might consist of a two-dimensional array of detector elements called pixels. Each pixel acts as a tiny detector that absorbs the incident photons and stores the accumulated

charge. The two-dimensional array therefore allows the spatial distribution of the incident flux to be recorded as an image. As with the collection process, the detector process further degrades the incoming radiance signal.

3.5.2.1 Spatial Sampling

The incoming flux is sampled and quantized by the detector in order to convert that flux into a digital form. Each pixel spans a finite area such that photons that are absorbed in this area contribute to the signal in that pixel. Therefore, the incident photon flux is essentially integrated over the physical dimensions of the pixel resulting in a loss of spatial information within the pixel. The physical dimensions of the pixels influence the ground sampling distance (GSD) of the sensor. The GSD corresponds to the projection of the pixel size onto the ground. The GSD can be calculated from basic geometry and knowledge of the focal length, pixel size, and distance to the target (ground).

As mentioned previously, each step in the imaging process might have an impulse response associated with it. The impulse response associated with the loss of spatial detail in the sampling process could be described by a two-dimensional RECT function, $h(x, y) = \text{RECT}\left(\frac{x}{p_x}, \frac{y}{p_y}\right)$, where p_x and p_y are the x and y pixel dimensions. In some circumstances, the GSD may be defined as the full-width at half-maximum amplitude of the total system impulse response projected onto the ground [1]. See Gaskill (1978) [14] for detailed information about impulse response functions.

3.5.2.2 Temporal Sampling

The detector material is only exposed to the incident flux for a finite time. The interval of time in which the detector is allowed to absorb photons is known as the integration time. It is typically controlled with a mechanical shutter or through electronic means. The integration time represents the temporal averaging of the incident photon flux over the finite time interval which results in a loss of temporal information.

3.5.2.3 Spectral Sampling

In addition to spatial and temporal sampling, the detector also performs spectral sampling of the incident photon flux. The detector is only sensitive to a certain range of wavelengths known as the bandpass. The sensitivity of the detector to each wavelength is represented by the spectral response function, $R(\lambda)$. It is defined as the signal output, S , per unit

incident flux, $\Phi_i(\lambda)$ at a particular wavelength. The detector material is carefully chosen such that photons of the desired wavelength are absorbed with relatively high efficiency. A detector designed for LWIR photons would consist of Mercury Cadmium Telluride (HgCdTe) semiconductor material, for example, which has a high response in the 8 - 14 μm region.

The incident flux on the detector is weighted by the response function and integrated over all wavelengths (essentially the bandpass of the sensor) to produce an output signal. Mathematically, this detector signal relative to the spectral response of the sensor is stated as

$$S = \int \Phi_i(\lambda) R(\lambda) d\lambda. \quad (3.26)$$

The signal is typically expressed in units of Amperes or Volts depending on the detector.

3.5.2.3.1 Band Effective Values

In general, the term "band effective" value is often used to describe the effective value of a spectral parameter in the sensor band of interest. For a generic spectral parameter, $\varphi(\lambda)$, its band effective value is written as

$$\hat{\varphi} = \int \varphi(\lambda) R'(\lambda) d\lambda. \quad (3.27)$$

The hat ($\hat{}$) indicates a band effective value and $R'(\lambda)$ is the spectral response function of the detector normalized by its maximum value.

The band effective value may be expressed "per wavelength" by normalizing equation (3.27) by the sensor response,

$$\hat{\varphi}_\lambda = \frac{\int \varphi(\lambda) R'(\lambda) d\lambda}{\int R'(\lambda) d\lambda}. \quad (3.28)$$

3.5.2.4 Noise

Another degradation of the signal as it passes through the imaging system will be the addition of noise. Noise corresponds to random variations in the output signal level even when the detector is exposed to a uniform flux. These random fluctuations are due to such factors as thermal variation in the detector and the random occurrence of photon events. Noise is usually characterized as the root mean square (RMS) variation about the mean signal.

For thermal imaging, it may be useful to express the concept of noise in terms of detectable temperature [1]. The noise equivalent change in temperature (NE Δ T) is a measure of the change in temperature of a blackbody at the front of the sensor that would produce a change in the sensor output equal to the sensor's noise level [1].

3.5.3 Calibration

The result of the imaging process is a temporally-averaged, and a spatially- and spectrally-integrated signal for each pixel. This signal is then read out by the sensor electronics. The amplitude of the output signal is quantitized into discrete digital values. The resulting digital image consists of a spatial distribution of recorded digital count values.

Sensors are usually calibrated so that the digital count values can be converted into a sensor-reaching radiance. This calibration may be performed in a laboratory in which radiance from a known source is recorded by the sensor. A calibration curve is constructed by altering the source radiance and recording the resulting output signal from the sensor. The digital image may now be presented as a distribution of radiance values in which each pixel contains the spatially, temporally, and spectrally degraded radiance for that pixel location. These radiance values are essentially the output sensor digital count values projected back to the front of the sensor. This *effective radiance* is denoted here as \hat{L} .

3.6 Apparent Temperature

In the previous sections, the energy paths reaching a sensor were examined. The effective radiance recorded by the sensor, \hat{L} , is usually expressed in terms of an apparent temperature (also called brightness temperature in the literature). The apparent temperature is the equivalent temperature of a spatially homogeneous and temporally constant blackbody that will produce the same sensor effective radiance when cascaded with the spectral response of the sensor [16]. This is written mathematically as

$$\hat{L} = \int_0^\infty L_{BB}(\lambda, T_{app}) R'(\lambda) d\lambda \quad \left[\frac{W}{m^2 sr} \right]. \quad (3.29)$$

It is important to note that the temperature derived from the integrated sensor radiance is an "apparent" temperature since the Planck function predicts radiances from a perfect blackbody in a perfect transmitting, non-scattering, non-absorbing media. Real-world objects with emissivities less than unity radiate less than a blackbody at the same temperature. Furthermore, the radiance reaching the sensor is not solely from the target of

interest, but rather from a variety of energy paths as described in Section 3.4.

3.6.1 Planck Formula Inversion

Given the integrated radiance as measured by the sensor for a particular band \hat{L} , the apparent temperature of the blackbody, T_{app} , can be estimated by inverting the Planck equation,

$$T_{app} = \frac{hc}{\hat{\lambda}k} \left[\ln \left(\frac{2hc^2 \Psi}{\hat{L} \hat{\lambda}^5} + 1 \right) \right]^{-1} \quad [K], \quad (3.30)$$

where $\hat{\lambda}$ is the effective wavelength in the band (see Section 3.5.2.3.1), Ψ is the integral of the sensor response function in the spectral band, and \hat{L} is the integrated radiance in the band in $[W/m^2/sr]$. Note that by equation (3.28), $\hat{L}_\lambda = \hat{L}/\Psi$.

This method is attractive due to its simplicity, however, it overlooks the spectral nature of the signal. The Planck formula produces a spectral radiance for a given temperature and wavelength. Since the sensor output is an integrated radiance and not a spectral radiance, the radiance used in equation (3.30) should be deconvolved to separate out the sensor's spectral response and the spectral blackbody radiance. This is a very difficult task and therefore the integrated radiance and the effective wavelength are used instead. As an example, the DIRSIG tool (see Section 4.1.2) was used to simulate the radiance from a blackbody plate as recorded by a LWIR sensor. The blackbody had a temperature of 300 K and the sensor had a perfect response from 8 to 14 μm with a wavelength spacing of 0.001 μm . There was no intervening atmosphere in the simulation. The integrated radiance reported by the sensor was 54.9410 $[W/m^2/sr]$. The resulting apparent temperature is 297.0071 K. This difference from the actual temperature of 300 K is due to the use of the effective wavelength in the Planck function. The spectral aspect of the Planck function was not taken into account.

3.6.2 Temperature-Radiance Look-Up Table

To incorporate the spectral nature of the blackbody radiance and the spectral response of the sensor, a look-up table (LUT) can be generated to convert the sensor's integrated radiance into an apparent temperature. Sospedra *et al.* (1998) notes that this is the most accurate way to perform the band radiance to temperature conversion [17].

The Planck equation is evaluated at the sensor wavelengths and weighted by the sensor response and finally integrated to produce an integrated effective radiance via equation

(3.29) for a range of temperatures. The temperature range should be wide enough to cover the suspected range of temperatures for the objects in the scene. The temperature resolution should also be very high (temperatures were calculated in 0.001 K increments for this project). Note that the sensor response function is taken into account so the LUT is only valid for that particular sensor. It must be regenerated for other sensors with different responses. The LUT now provides a relationship between the integrated sensor radiance and the blackbody temperature.

The integrated radiance from the sensor is then compared to the radiances in the LUT and a temperature is chosen through an interpolation scheme. For example, a nearest neighbor interpolation would select the temperature whose associated integrated radiance in the table had the smallest absolute difference with the sensor's reported integrated radiance. For the same DIRSIG simulation in Section 3.6.1, an integrated LWIR sensor radiance of $54.9410 \text{ [W/m}^2\text{/sr]}$ yields an apparent temperature of 299.9970 K using the LUT method.

Chapter 4

Background

In the last chapter, the interaction between the self-emitted signal from a target and its radiometric environment was discussed. The self-emitted radiance from the target, carrying the desired information about the target's temperature, is heavily modified before it is finally recorded by the sensor. The objective of temperature retrieval from remote thermal imagery is to account for the discrepancy between the at-sensor apparent temperature and the absolute temperature of the target as accurately as possible. There are several tools and methods used to extract the absolute temperature from the radiance recorded by the sensor. There is currently no single approach that is widely accepted and used by the thermal remote sensing community [1]. Therefore, a number of different methods exist that are useful for a particular type of problem. An overview of common methods is presented in this chapter.

4.1 Modeling Tools

It is clear from the previous chapter that the signal from a target material is significantly altered before being recorded by the sensor. The terms in the governing equation may be modeled in order to back out the original target signal. There are several tools available to model radiometric phenomena and radiation propagation. The two major tools used in this project are MODTRAN and DIRSIG.

4.1.1 MODTRAN

The MODerate spectral resolution TRANsmittance tool is an atmospheric radiative transfer code [18]. It was developed by the Air Force Research Laboratory (AFRL) and Spectral Sciences, Inc (SSI). MODTRAN models the atmosphere as a series of stacked homogeneous layers. The pressure and temperature of each layer is provided by several preset atmospheric profiles or by user-supplied radiosonde data. The concentration of permanent gases can be estimated from the radiosonde or from the generic preset profiles. MODTRAN contains six predefined atmospheres that can be supplemented with radiosonde

data if available. The user may also specify meteorological conditions such as visibility, season, air mass type, etc. to estimate the size and distribution of aerosols [1]. MODTRAN will provide the spectral absorption, transmission, emission and scattering characteristics of the atmosphere based on the given input data for a spectral range of 0 to 50,000 cm^{-1} [19]. It is based on the lower spectral resolution LOWTRAN 7 code. MODTRAN 4 incorporates all the LOWTRAN 7 options but also improves the spectral resolution to 2 cm^{-1} [18].

As previously mentioned, MODTRAN divides the atmosphere into homogeneous layers as illustrated in Figure 3.5. The transmission between the sensor and target is calculated from equations (3.15) and (3.19). The transmission is expressed as

$$\tau(\theta, \lambda) = \prod_i e^{-\sum_k m_{ik} C_{ik}(\lambda) \sec \theta z_i} \quad (4.1)$$

where again m_{ik} and $C_{ik}(\lambda)$ are the number density and extinction cross-section of the k^{th} atmospheric constituent in the i^{th} layer, respectively. The thickness of the layer is z_i and the zenith view angle is θ . The summation in the exponent is taken over all the constituent gases and the total transmission is the product of the transmissions of the individual layers. MODTRAN derives the number densities from the atmospheric profile data and derives extinction cross-sections from database values of the atmospheric constituents [1].

The emission of the atmosphere is calculated similar to equation (3.20) rewritten here as

$$L_{atm}(\theta, \lambda) = \sum_{i=1}^N L_{BB}(\lambda, T_i) [1 - \Delta\tau_i(\theta, \lambda)] \prod_{j=1}^{i-1} \Delta\tau_j(\theta, \lambda) \left[\frac{W}{m^2 \text{ sr } \mu\text{m}} \right]. \quad (4.2)$$

where T_i and $\Delta\tau_i$ are the temperature and transmission of the i^{th} layer, respectively. Note that the transmission and self-emitted atmospheric radiance are independent of the azimuth angle since the atmosphere is modeled as a series of homogeneous layers.

MODTRAN can be manipulated to estimate the atmospheric parameters in the governing equation (Section 3.4.3). The total spectral transmission and upwelling radiance are provided in the MODTRAN output. The downwelling radiance can be calculated through equation (4.2) for various look angles. MODTRAN can also provide the spectral transmissions of the individual gas species and aerosols in the path. The aerosol models in MODTRAN are defined by regions that contain typical aerosol sources. The sources are

representative of rural, urban, desert and maritime environments [20]. The predefined atmospheric profiles are characteristic of tropical, mid-latitude, and arctic atmospheres for summer and winter seasons [20].

4.1.2 DIRSIG

The Digital Imaging and Remote Sensing Image Generation (DIRSIG) tool was developed by the Digital Imaging and Remote Sensing (DIRS) Laboratory at the Rochester Institute of Technology (RIT) [21]. It is a synthetic image generation application that produces simulated visible through thermal imagery. DIRSIG utilizes ray tracing and first principle physics, chemistry, and mathematical theories to accurately reproduce the radiometry of a scene [22]. The simulated images are generated through the integration of first principle based sub-models. These sub-models include BRDF predictions, facet temperature prediction, sensor models, and atmospheric models, among others. The modeled components are combined spectrally to create a simulated integrated radiance image of the scene for the given sensor and viewing geometry. DIRSIG also has the capability to model polarimetric, RADAR, and LIDAR imaging systems.

A DIRSIG scene consists of full three-dimensional facetized object geometries usually created with a CAD software package. A material's physical and optical properties are assigned to each facet. These properties may be obtained through field and laboratory measurements or from material databases. A temperature prediction model estimates the temperature of every facet in the scene based on material thermodynamic and optical properties, illumination history, and local weather history. The atmospheric model uses the MODTRAN radiative transfer code. DIRSIG creates a MODTRAN look-up table for a series of atmospheric paths of interest. An accurate estimate of the atmospheric transmission, upwelling and downwelling radiances is therefore possible. The geometric sensor model allows the user to simulate broadband, multispectral, and hyperspectral sensors in a variety of geometries such as framing arrays, line scanners, etc. [22].

DIRSIG is a powerful tool for the remote sensing community [22]. The synthetic data produced by the model is useful for a range of applications. These application areas range from algorithm training and testing to instrument prototyping.

4.2 Temperature Retrieval Methods

The ultimate goal in thermal remote sensing is to obtain the absolute temperature of a material surface. The atmospheric and emissivity effects must be isolated and accounted for in order to arrive at the “pure” blackbody signal from the target material.

4.2.1 Atmospheric Compensation

The term *atmospheric compensation* refers to the removal of atmospheric effects in an image. Specifically, these effects are the atmospheric transmission and upwelling radiance from equation (3.21). The sensor-reaching radiance is atmospherically corrected to arrive at the surface-leaving radiance. Since the emissivity and other surface effects are not accounted for, the surface-leaving radiance will yield only the apparent surface temperature and not the absolute surface temperature.

4.2.1.1 Ground Truth

Probably the most straightforward method of atmospheric compensation is to perform surface measurements of objects in the scene coincident with the time of image acquisition [1]. These “ground truth” collects are measurements of the absolute temperatures of fully resolved targets with known emissivities in the scene. Recall that the radiance reaching a sensor from a surface after passing through the atmosphere is

$$\hat{L}_{sensor} = \left[\hat{\epsilon} \hat{L}_{BB}(T) + (1 - \hat{\epsilon}) \hat{L}_d \right] \hat{\tau} + \hat{L}_u \quad \left[\frac{W}{m^2 sr} \right]. \quad (4.3)$$

If the calibration targets are blackbodies ($\epsilon = 1$), then the downwelling term in equation (4.3) is zero. By taking temperature measurements of blackbody objects in the scene having a range of temperatures, a linear regression can be performed to yield the band effective transmission and upwelling radiances from the slope and intercept of the regression for the given scene atmosphere. Once the atmospheric terms are known, a calibration curve now exists that relates the sensor effective radiance to the surface-leaving effective radiance. This can then be converted into an apparent temperature of the surface.

This method may also work for non-blackbody targets if the emissivity is known. In this case, the downwelling sky radiance must also be known. It can be measured with a radiometer in the scene that collects and integrates the radiance over the same pass band as the sensor [1]. The downwelling radiance may also be approximated through an

atmospheric modeling tool such as MODTRAN.

4.2.1.2 Single-Channel Method

The absolute temperature of the target may be obtained from radiance measurements in a single IR channel which have been corrected for atmospheric effects [23]. A radiative transfer model is used to derive the atmospheric terms in equation (3.21). This method assumes knowledge of the bidirectional reflectance characteristics of the target material. The MODTRAN tool is commonly used to model the state of the atmosphere and numerically calculate the spectral transmission and upwelling and downwelling radiances for the given image acquisition time and location. The horizontal and vertical distribution of temperature and water vapor must be accurately known for input into the radiative transfer model. Atmospheric profiles may be obtained from satellite sounding instruments, numerical weather prediction models, and radiosondes. Since profile data is discrete in time and space, the data must be spatially and temporally interpolated for the target of interest. Once the atmospheric terms are accounted for, the kinetic temperature of the target can be determined given that its BRDF and geometry are known [23].

For the given spectral channel, the surface radiance can be computed from the sensor radiance and the MODTRAN calculated transmission and upwelling radiance as

$$\hat{L}_{surf} = \frac{\hat{L}_{sensor} - \hat{L}_u}{\hat{\tau}} \quad \left[\frac{W}{m^2 sr} \right] \quad (4.4)$$

where each of the parameters are band effective values [1]. The surface radiance can then be converted into an apparent surface temperature (see Section 3.6).

An alternative approach is to make use of a LUT to relate the apparent surface temperature to an effective sensor radiance in the channel of interest. The method is similar to the one presented in Section 3.6.2. For a given temperature, the spectral blackbody radiance is calculated from the Planck equation. This radiance is then multiplied by wavelength by the spectral transmission and then added to the spectral upwelled radiance generated from MODTRAN. Finally, this spectral radiance is multiplied with the sensor response and integrated to arrive at a band effective radiance for the given blackbody temperature. This is written mathematically as

$$\hat{L} = \int [L_{BB}(\lambda, T) \tau(\lambda) + L_u(\lambda)] R'(\lambda) d\lambda \quad \left[\frac{W}{m^2 sr} \right]. \quad (4.5)$$

A LUT is created that relates a range of blackbody temperatures to a range of effective radiances. The surface apparent temperature is therefore the temperature from the LUT whose radiance is the closest match to the actual effective radiance recorded by the sensor.

The single channel method was successfully used by Qin *et al.* (2001) to retrieve desert land surface temperatures using the Landsat TM thermal band [24]. The authors used *in situ* atmospheric profile data that was coincident with the satellite pass to compensate for the atmosphere. The resulting temperature errors were approximately 1.1 K.

4.2.1.3 Multi-Channel Method

The multi-channel method uses differential absorption in several spectral channels to eliminate atmospheric effects. The split-window technique makes use of two channels within one atmospheric window [23]. The target's temperature is usually taken as a linear or quadratic function of the apparent temperatures in the two channels [25]. The coefficients of these temperature retrieval algorithms are usually determined by a regression of the apparent temperature measured by the sensor with coincident *in situ* surface temperature measurements. The regression analysis can also be performed on synthetic data generated from a large sample of atmospheric profiles using a radiative transfer model.

There are numerous split-window algorithms depending on the specific sensor and application [23]. Schott (1997) describes a general split-window technique in which the apparent surface temperature can be derived from the apparent temperature in two spectral bands as

$$T_{surf} = \frac{T_i - b T_j}{1 - b} \quad [\text{K}], \quad (4.6)$$

where T_i and T_j are the apparent temperatures in the two bands and $b = \hat{\beta}_{ext,i} / \hat{\beta}_{ext,j}$, the ratio of the effective extinction coefficients in the two channels [1]. The extinction coefficients can be computed through the use of radiation propagation models [1].

Prata (1993) developed a dual-channel method to retrieve land surface temperatures [26]. This approach uses the brightness temperatures in the two channels along with an estimate of the atmospheric transmission, the downwelling radiance, and the surface emissivity in each channel. Prata's method yielded land surface temperatures to within ± 1.5 K for flat terrain with uniform surface composition in relatively dry atmospheres [26].

The split-window technique has been used successfully on data from the Advanced Very

High Resolution Radiometer (AVHRR) instrument on the NOAA polar-orbiting satellites [27]. The instrument uses three bands for sea surface temperature retrieval at $3.7 \mu m$ (band 3), $11 \mu m$ (band 4), and $12 \mu m$ (band 5). The non-linear algorithm uses two bands for daytime temperature retrieval and three bands for nighttime temperature retrieval. The coefficients of these algorithms are calculated by matching a set of AVHRR data with buoy observations. A global dataset is assembled of AVHRR data and coincident temperature measurements from buoys. This dataset contains a global range of sea surface temperatures and atmospheric moisture content. A regression analysis is then performed on this dataset to calculate coefficients for the split-window algorithms. A validation of these algorithms by Li *et al.* (2001) indicate a small temperature bias of $0.08^\circ C$ to $0.14^\circ C$ with a standard deviation of $0.50^\circ C$ or less [27].

4.2.1.4 Multi-Angle Method

The multi-angle approach takes advantage of the differential absorption arising from the difference in path length when a target is viewed from two different angles [23]. The same target is viewed from a small zenith angle (usually at nadir) and then near-simultaneously from a high zenith angle. The ATSR instrument aboard the ERS-1 satellite uses a nadir view and a forward-looking 55° view, for example. The atmospheric transmission and upwelling radiance are approximated from the differing radiances resulting from the different view angles. This method assumes a spatially uniform air column. It also strictly requires that one view path be significantly longer than the other [23]. The angular variation of the target's emissivity is assumed to be negligible. However, to reduce errors in the derived apparent surface temperature, angular emissivity effects should be taken into account if known.

Schott (1997) provides an overview of the procedure for this method [1]. Assuming that the targets in the scene are Lambertian, the relationship between the observed radiance at nadir, $L(\theta = 0)$, and at some other angle, $L(\theta = \theta')$, is given as

$$\hat{L}(\theta = \theta') = \left[\frac{\hat{\tau}(\theta')}{\hat{\tau}(0)} \right] \hat{L}(\theta = 0) + \left[\hat{L}_u(\theta') - \frac{\hat{\tau}(\theta')}{\hat{\tau}(0)} \hat{L}_u(0) \right] \quad (4.7)$$

If several Lambertian targets are imaged, then a linear regression may be performed in which the first bracketed term in equation (4.7) is the slope, m , and the second bracketed term is the intercept, b . For clear atmospheres, the effective transmission and upwelled

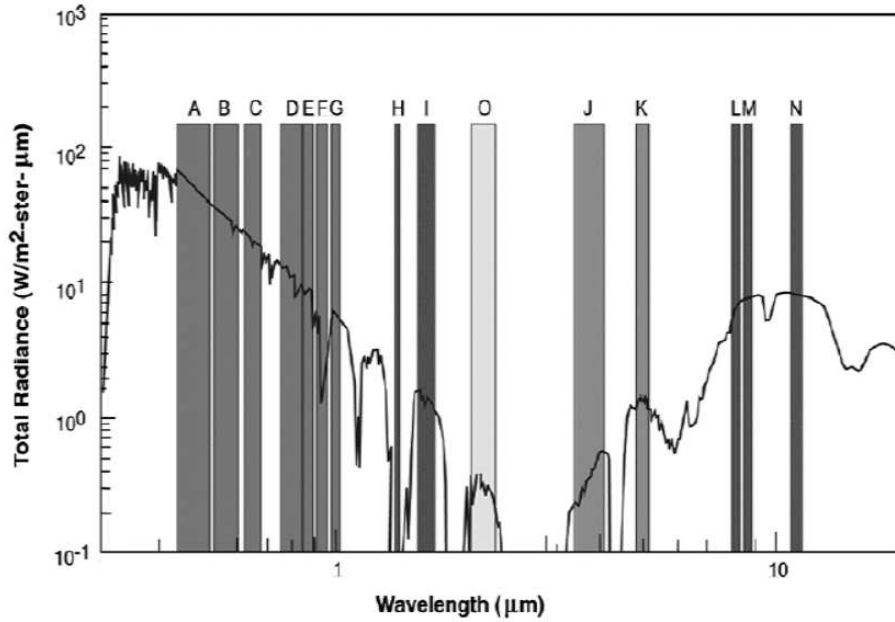


Figure 4.1: Multispectral Thermal Imager (MTI) band locations (Szymanski and Weber 2005 [28]).

radiance for nadir-viewing can be derived from the slope and intercept by

$$\begin{aligned}\hat{\tau}(0) &= m^{1/(\sec \theta')-1} \\ \hat{L}_u(0) &= \frac{b}{\sec \theta' - m}.\end{aligned}\tag{4.8}$$

4.2.1.5 MTI Sea Surface Temperature Retrieval

The Multispectral Thermal Imager (MTI) is a Department of Energy (DOE) mission to demonstrate technology and algorithms for industrial and environmental remote sensing research [28]. The MTI sensor contains 15 spectral bands between 0.4 and 11 μm which include two bands in the MWIR (bands J and K) and three bands in the LWIR (bands L, M, and N) (See Figure 4.1). The visible and infrared bands have a GSD of 5 m and 20 m, respectively. Borel *et al.* (1999) developed a method to use the thermal bands on MTI to retrieve sea surface temperatures [29]. The method is based on linear combinations of the brightness temperatures in the MTI bands J, K, L, M, and N for night time imaging. It also relies on two view angles of a body of water at nadir and at 60°. First an atmospheric database (LUT) is created using a radiative transfer code such as MODTRAN. The database contains the atmospheric transmission, upwelling, and downwelling radiances for a wide range atmospheric conditions as seen in the five MTI bands at the two view angles. Next, from the atmospheric database, the top-of-atmosphere (TOA) radiance is computed for a given water emissivity and temperature. A TOA database is created from

the atmospheric database and a range of water temperatures. Finally, a linear regression model is fit to this database. The sea surface temperature is then a linear combination of the brightness temperatures in the five bands [29]. Preliminary post-launch validation of this algorithm was performed by Clodius *et al.* (2002) using available ocean and lake buoy data [30]. The results indicated that the algorithm was able to retrieve sea surface temperatures to within approximately ± 3 K.

4.2.1.6 AAC Algorithm

The autonomous atmospheric compensation (AAC) algorithm was designed to compensate for atmospheric effects in high resolution, hyperspectral thermal infrared imagery [31]. In particular, atmospheric compensation of natural land surface image data is of interest. It was developed out of the desire to have an atmospheric correction technique using only data from the image.

This method attempts to separate atmospheric effects from temperature/emissivity effects by assuming the image data obey certain conditions. The first condition is that the atmospheric parameters vary significantly less than the land surface parameters. The variability of atmospheric parameters occur on larger spatial scales compared to land surface parameters. The local atmosphere is therefore generally homogeneous. The high variability of the land surface is ensured if the sensor has high spatial resolution. The second assumption of this method is the at-surface spectral radiances are significantly smoother than the atmospheric spectral absorption and emission. This assumption depends on the spectral resolution of the sensor and the spectral emissivity of the surface. A high emissivity surface is ideal so that the reflected downwelling sky radiance is small. Therefore, the algorithm may not be directly applied to scenes with low-emissivity man-made surfaces.

The water absorption band at $11.73 \mu m$ is used to estimate the atmospheric profile. If the two conditions previously mentioned hold, then the variability at this wavelength is predominately the result of atmospheric effects. A strong absorption channel at $11.73 \mu m$ and an adjacent, weak absorption channel are used to calculate a transmission index and an upwelled radiance index. These indices, along with a radiative transfer code, are used to derive the spectral transmission and upwelled radiance.

Gu *et al.* (2000) show that the accuracy of the AAC algorithm in retrieving surface apparent temperatures is comparable to the accuracy of algorithms based on radiosonde

measurements [31]. The algorithm also does not have the temporal and spatial limitations of radiosonde measurements. The authors note too that it is possible to automate the process since the algorithm is driven by the image data alone.

4.2.1.7 ISAC Algorithm

The in-scene atmospheric compensation (ISAC) method attempts to correct for the atmosphere to recover the apparent surface temperature for hyperspectral imagery [32]. The algorithm assumes that the atmosphere is homogeneous over the entire scene. It depends on the natural occurrences of blackbodies in the scene, such as vegetation and water. For each pixel, the sensor radiance in each channel, $L(\lambda_i)$, is converted into an apparent temperature. The channel with the highest apparent temperature for the given pixel is denoted as λ_m . The channel with the most occurrences (pixels) of λ_m is chosen as the reference channel, λ_{ref} . For each channel λ_i , the blackbody radiance from the apparent temperature in that channel is calculated for only the pixels where $\lambda_m = \lambda_i$. A scatter plot of $L(\lambda_i)$ versus $L'_{BB}(\lambda_i)$ is constructed for each channel. Pixels for which $\varepsilon(\lambda) \approx 1$ (blackbodies) are represented by points near the top edge of the scatter plot. The slope of a line fit through these points represents the effective spectral transmission, $\tau'(\lambda_i)$, while the vertical intercept is the effective spectral upwelling radiance, $L'_u(\lambda_i)$ in the channel. These effective values may not be physical. For example, the slope may be greater than one. Estimated quantitative values can be obtained by scaling these effective values to true atmospheric conditions. This can be done by creating an independent estimate of the spectral transmission and upwelled radiance at the reference channel using an atmospheric model such as MODTRAN. The effective values are then scaled to the modeled values at the reference channel. The effective transmission and upwelled radiance values may also be scaled by taking advantage of the water vapor absorption band at $11.7\mu m$. A detailed procedure for this method is presented in Young *et al.* (2002) [32].

4.2.1.8 Physics-Based Modeling

The atmospheric compensation methods discussed thus far remove atmospheric effects by converting the sensor-reaching radiance into a surface-leaving radiance. This is accomplished using in-scene or auxiliary information about the state of the atmosphere. Another approach is to take advantage of physics-based models to anticipate the radiance reaching the sensor from a target for a variety of atmospheric conditions. These anticipated sensor radiances form a *target space* of possible sensor radiances from a fixed surface leaving target radiance.

The invariant method proposed by Healey and Slater (1999) uses a physical model for the sensor-reaching radiance along with MODTRAN to generate a target space of spectral radiance vectors [33]. Healey and Slater used their method to perform target detection at visible and near-infrared (VNIR) wavelengths. The sensor reaching radiance is calculated by a physics-based governing equation similar to equation (3.21) except with the emissivity replaced with the VNIR spectral reflectance. Only the spectral reflectance contains any information about the target. The other parameters in the radiative transfer equation describe the atmospheric effects. For a known target spectrum, the atmospheric parameters are varied in MODTRAN to generate a multitude of spectral sensor-reaching radiances. Healey and Slater produced 17,920 physical estimates of how a given target signature might appear to a sensor [33]. An image pixel containing the target of interest is then compared to the spectra in the target space. The target space is essentially a look-up table relating the atmospheric parameters to the sensor radiance from the target. The closest estimate of the atmospheric parameters in the scene correspond to the closest match of the given pixel spectrum to the spectra in the target space.

Borel developed a physics-based algorithm for temperature retrieval using the MTI instrument [29]. This approach uses a radiative transfer model such as MODTRAN to model the atmospheric column. The water vapor column density and the effective water vapor temperature is varied in the model and for each combination of these two parameter values, an estimate of the water surface temperature in the MTI bands is produced. The water vapor density and temperature combination that produced the most consistent water surface temperature over the region of interest is selected as the best atmosphere. It is then used to retrieve the water surface temperature for the whole image. Clodius *et al.* notes that the combination of bands L, M, and N produced consistently good results [30].

4.2.2 Temperature/Emissivity Separation

Atmospheric compensation allows for the recovery of the surface-leaving radiance. This radiance must now be deconvolved in order to extract the absolute temperature of the surface. If there is *a priori* knowledge of the surface emissivity and BRDF, then the absolute temperature can be calculated from equation (3.21). However, if the emissivity is unknown, then it is not possible to obtain the surface temperature from a passive radiometer alone [23]. Given a sensor with N channels, there are always $N + 1$ unknowns: an emissivity value for each of the N channels plus the absolute temperature of the surface. This yields an infinite number of solutions to the corresponding system of equations. There-

fore, an assumption is usually made to constrain the extra degree of freedom. There are several temperature/emissivity separation techniques that rely on different assumptions. All of the following techniques assume that the image has already been atmospherically compensated.

4.2.2.1 Reference Channel Method

The reference channel method is based on the assumption that a pixel will have a constant emissivity at some spectral channel [34]. If the emissivity in this reference channel is known then the temperature in the channel can be calculated using the methods in Section 3.6. This temperature is then used along with equations (3.1) and (3.3) to calculate the emissivity in the other channels. The drawback of this method is the requirement for *a priori* knowledge of the material's emissivity at some wavelength. However, this is possible if laboratory measurements of the material exist. Kealy and Hook (1993) demonstrated the use of the reference channel method on data from the Thermal Infrared Multispectral Scanner (TIMS) instrument for land surface studies [34]. The authors used channel 6 with an emissivity of 0.95 since it represents an average emissivity value for silicate rocks in channel 6 (11.655 μm).

4.2.2.2 Normalized Emissivity Method

The normalized emissivity method (NEM) is similar to the reference channel method except that it assumes a constant emissivity in every channel [34]. The apparent temperature is calculated for each channel using the assumed emissivity value. The highest channel temperature is designated as the temperature of the pixel. Now that the temperature of the material is defined, the emissivity of every channel can be calculated. Kealy and Hook (1993) note that an emissivity of 0.96 is often used for land surface studies since it represents an average of likely values for geologic surfaces [34].

4.2.2.3 Temperature/Emissivity Separation Algorithm

The Temperature/Emissivity Separation (TES) algorithm was developed for the Advanced Spaceborne Thermal Emission and Reflection Radiometer (ASTER) sensor [35]. ASTER has five bands in the LWIR to estimate land surface temperatures and emissivity spectra with a noise equivalent temperature (NE ΔT) of <0.3 K. The sensor data must first be atmospherically compensated to arrive at the surface-leaving radiance for each pixel. The algorithm also requires the downwelling radiance in the scene. The ASTER standard product AST09 provides the necessary surface-leaving and downwelling radiances [36].

The TES algorithm uses several modules to arrive at the temperature and emissivity spectra of the surface. The first module is the NEM module which assumes a maximum emissivity. Using this emissivity and the provided downwelling radiance, the surface-emitted radiance is estimated from the surface-leaving radiance as

$$L_{self}(\lambda) = L_{surf}(\lambda) - [1 - \varepsilon(\lambda)] L_d(\lambda) \left[\frac{W}{m^2 sr \mu m} \right], \quad (4.9)$$

where L_{surf} is the atmospherically-corrected surface-leaving radiance in the channel, and L_{self} is the estimated self-emitted radiance. The assumed maximum emissivity is used for the value of ε . As with the normalized emissivity method, the apparent temperature is calculated in each band and the estimated surface temperature is taken as the maximum apparent temperature over all bands. This NEM temperature is then used to calculate the emissivity in each channel. The self-emitted term from equation (4.9) is then re-calculated using the NEM channel emissivities. This process is repeated until the change in the estimated self-emitted radiance is less than a defined threshold [36].

Next, the NEM emissivities are scaled by the Ratio module. The relative emissivity, $\beta(\lambda)$, is found by dividing each NEM emissivity by its average for the channel. Finally, the relative emissivities are scaled to absolute emissivities by the maximum-minimum relative emissivity difference (MMD) module. An empirical relationship predicts the minimum emissivity from the maximum-minimum relative emissivity difference, $MMD = \beta(\lambda)|_{max} - \beta(\lambda)|_{min}$. The minimum emissivity/MMD relationship was established using laboratory and field spectra of naturally occurring materials. This process is described in Gillespie *et al.* (1998) and the result is written here as

$$\varepsilon_{min} = 0.994 - 0.687 \times MMD^{0.737}. \quad (4.10)$$

The absolute emissivities are then calculated by

$$\varepsilon(\lambda) = \beta(\lambda) \left[\frac{\varepsilon_{min}}{\beta(\lambda)|_{min}} \right]. \quad (4.11)$$

The surface temperature must be recalculated from these new emissivities and from the atmospherically corrected radiances. These TES temperature and emissivity values comprise the ASTER Standard Products [35]. Gillespie *et al.* (1998) demonstrate that the TES algorithm was able to recover the surface temperature and emissivity to within 1.5 K and 0.015, respectively, for an ASTER test data set [35].

4.2.2.4 ARTEMIS Algorithm

The Automatic Retrieval of Temperature and Emissivity using Spectral Smoothness (ARTEMIS) is a temperature/emissivity method developed by Borel (2003) [37]. It is based on the observation that in the thermal infrared region, the spectra of solids are smoother than the spectra of gases. First, an atmospheric LUT of transmission, upwelling, and downwelling radiance is created for a range of atmospheric conditions. The ISAC algorithm is used to narrow down the number of atmospheres in the LUT to a handful of candidate atmospheres. Next, the spectral emissivity is estimated. Given knowledge of the atmosphere, the surface temperature can be estimated by

$$T_{est} = L_{BB}^{-1} \left[\lambda_0, \frac{L_i - L_u - (1 - \epsilon_0) L_d \tau}{\epsilon_0 \tau} \right], \quad (4.12)$$

where ϵ_0 is an assumed emissivity of 0.95, λ_0 is a channel where the atmosphere is highly transmissive, and L_i is the measured radiance in the channel. The estimated surface temperature is used to calculate an estimated spectral emissivity by

$$\epsilon = \frac{L_i - L_u - L_d \tau}{[L_{BB}(\lambda, T_{est} - L_d) \tau]}. \quad (4.13)$$

This emissivity spectrum will show some atmospheric line features. The smoothness of the spectrum is measured by the standard deviation of the spectral emissivity and the local 3-point average emissivity. Low standard deviation values indicate smoother spectra.

The transmission, upwelling, and downwelling radiance from each candidate atmosphere from the ISAC algorithm are used in equations 4.12 and 4.13. The atmospheric case with the smallest smoothness is found for every pixel. The atmosphere that occurs the most often is selected as the best atmosphere. Now that an atmosphere has been chosen, the estimated emissivity can be smoothed by adding an offset to the estimated surface temperature T_{est} . A range of temperature offsets is applied until a minimum standard deviation is found. The result is an accurate estimate of the surface emissivity and temperature.

4.2.3 Temperature Retrieval Summary

Each of the temperature retrieval techniques just presented is useful for a particular set of scene and sensor characteristics. The modeling tools presented in Section 4.1 are intended to aid the temperature retrieval process. The methods and modeling tools will now be adapted to derive the temperature of a mechanical draft cooling tower.

Chapter 5

Methodology

Derivation of the exit air temperature of a mechanical draft cooling tower (MDCT) is a complex radiometric problem. The ultimate goal is to reconstruct the blackbody radiance of the tower from a thermal image in order to solve for the absolute temperature. The problem is unique due to the cavity properties of the tower and due to the presence of an exhausted water vapor plume. This chapter explores the role that these factors have on the apparent temperature of the MDCT. A detailed methodology is developed that will provide a correction factor to convert the image-derived apparent temperature into the exit air temperature of the MDCT.

5.1 Tower Leaving Radiance

Recall from equation (3.13) that the radiance leaving the surface of an object consists of a self-emitted term and a reflected background term. Equation (3.13), representing the tower-leaving radiance, is rewritten here as

$$L_{tower}(\theta, \phi, \lambda) = \varepsilon(\theta, \phi, \lambda)L_{BB}(\lambda, T) + \int_{2\pi} L_{bkgd}(\theta_i, \phi_i, \lambda) \rho'(\theta_i, \phi_i, \theta, \phi, \lambda) \cos(\theta_i) d\omega_i, \quad (5.1)$$

where again the units are $[W/m^2/sr/\mu m]$ and (θ, ϕ) indicate the direction of the sensor. From this equation, it is apparent that the tower-leaving radiance will be affected by the background radiance and by the optical properties of the tower. The background radiance will depend on the geometry of the tower and on the reflected downwelling radiance from the interior elements of the tower. The optical properties consist of the BRDF and directional emissivity of the tower materials.

The geometry of an MDCT introduces an added complexity when determining the tower-leaving radiance. For an exposed, level surface the reflected background $L_{bkgd}(\theta_i, \phi_i, \lambda)$ is the reflected downwelled radiance from the (θ_i, ϕ_i) direction. The downwelling radiance is the self-emitted radiance from the skydome. However, for a cavernous object such as an MDCT, the background radiance is a collection of the self-emitted and reflected energies

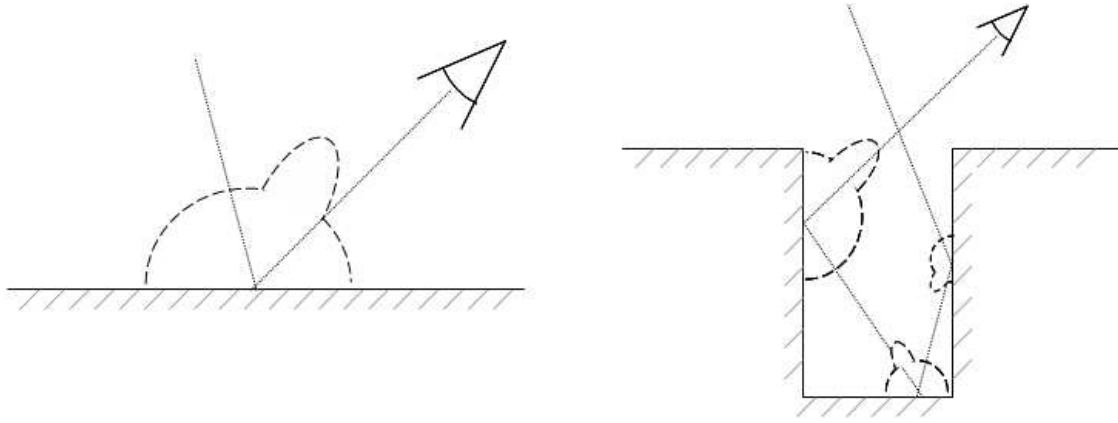


Figure 5.1: Diagram of a single photon path for an exposed object (left) and a cavity object (right). The photon is emitted from the sky and reflects off the target surface into the sensor. The dotted outline indicates the BRDF of the surface and the thickness of the BRDF in a particular direction represents the magnitude of the reflected component in that direction. The self-emitted photons from the object are not shown here.

from the interior surfaces of the cavity as well as the downwelling sky radiance. The background radiance $L_{bkgd}(\theta_i, \phi_i, \lambda)$ from a particular direction may be the downwelling sky radiance or radiance from one of the other interior surfaces of the cavity. In the latter case, the radiance leaving another interior surface would be the sum of *its* self-emitted component and *its* reflected background. The reflected background therefore does not “stop” with the sky as in the exposed surface case. For a cavity object, the reflected background must be calculated for each generation and for every angle, hence the added complexity of cavernous objects. Figure 5.1 illustrates the importance of the object geometry on the target-leaving radiance.

The reflective/emissivity properties are summarized by the BRDF of the material. The magnitude and directional characteristics of the BRDF greatly influence the target-leaving radiance since the BRDF will determine the proportion of sky radiance and interior surface radiance that contributes to the background radiance. Recall from Section 3.2 that the integral of the BRDF over the hemisphere above a surface is the DHR and that the DHR and directional emissivity are related through Kirchhoff’s law. The magnitude of the DHR controls the magnitude of the self-emitted term in equation (5.1) while the angular characteristics of the BRDF influence the reflected term. The BRDF affects what direction in the hemisphere has the largest contribution to the reflected background radiance. For example, for a diffuse BRDF every direction is equally weighted so the background radiance from the entire hemisphere has equal importance. For a specular BRDF, radiances in the specular direction will contribute more to the target-leaving radiance than radiances in non-specular directions.

Since an MDCT is a large cavity, the tower-leaving radiance might reduce to the blackbody radiance of the interior tower surfaces under certain conditions.

Emissivity: Relatively low DHR values of the tower materials in the thermal infrared would translate to high emissivities. This would cause the self-emissive term in equation (5.1) to dominate the tower-leaving radiance. The tower-leaving radiance would therefore approach the blackbody radiance if the actual emissivities were sufficiently high.

BRDF: The shape of the BRDF of the tower materials would greatly influence the reflected radiance within the tower. For a sensor placed above the tower and targeted at an interior surface through the fan stack opening, a specular BRDF would allow more radiance from within the tower to be reflected back to the sensor.

Bounces: As with a perfect blackbody cavity, the radiance exiting the cavity approaches the blackbody radiance as the number of internal reflections within the cavity increase.

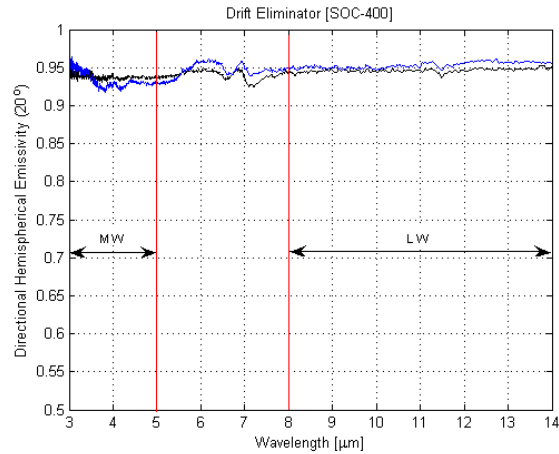
The magnitude and shape of the BRDF and also the number of reflections within the tower are therefore free parameters that affect the radiance leaving the tower. In the following sections, constraints are placed on these parameters through measurements and modeling of the physical phenomena.

5.1.1 Spectral Measurements of MDCT Materials

Spectral reflectance measurements were taken of several MDCT construction materials obtained from the Johnston Equipment Company in Rochester, New York. The reflectance spectrum from approximately 2 to 25 μm was measured with a SOC-400 instrument. The device illuminates the sample with an infrared beam at a 20° angle to the surface normal of the sample and measures the total directional reflectance of the sample [38]. The reflectance measurements have been converted to an emissivity spectrum through Kirchhoff's law. In each figure, a photograph of the material is shown at left and the emissivity spectrum is shown at right. There are two emissivity curves for each material which were measured from two different points on the material. This was meant to show any variation in emissivity for the material.



(a) Photograph of Sample

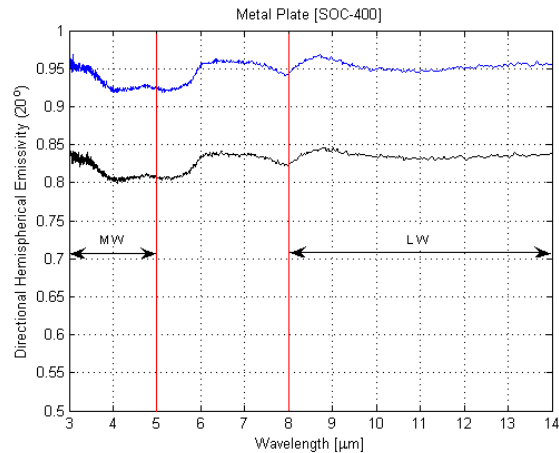


(b) Emissivity Spectrum

Figure 5.2: Drift eliminator emissivity spectra of two separate physical locations on the material.

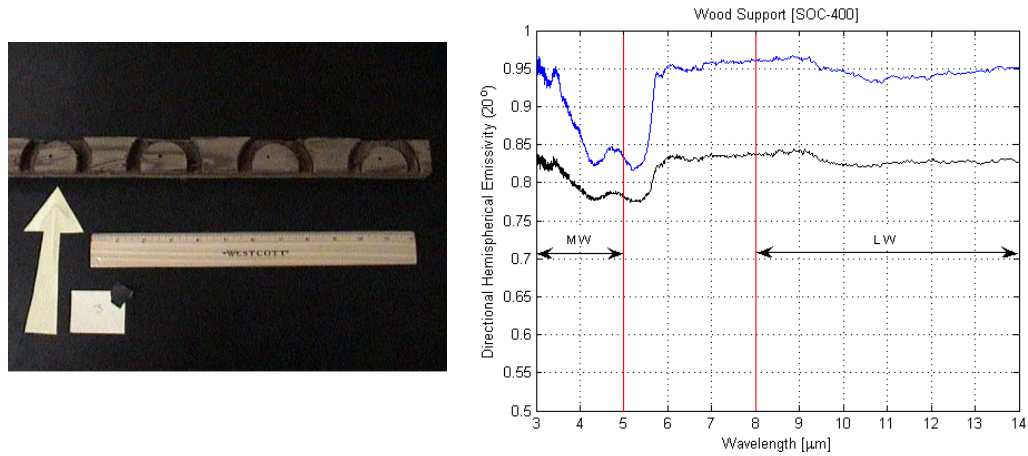


(a) Photograph of Sample



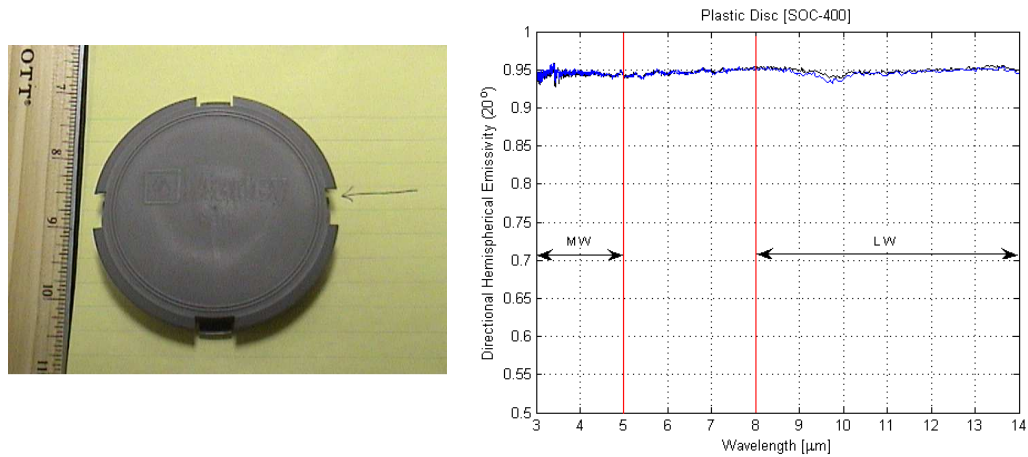
(b) Emissivity Spectrum

Figure 5.3: Metal plate emissivity spectra of two separate physical locations on the material.



(a) Photograph of Sample

(b) Emissivity Spectrum

Figure 5.4: Wood support emissivity spectra of two separate physical locations on the material.

(a) Photograph of Sample

(b) Emissivity Spectrum

Figure 5.5: Plastic disc emissivity spectra of two separate physical locations on the material.

The spectra shown here cover a wide range of construction materials encompassing metal, plastic, wood, and vinyl. The MWIR and LWIR spectra of the materials exhibit emissivity values above 0.75 for all the sample points of measure in the 3-5 μm and 8-14 μm bands. These results demonstrate that, in general, typical cooling tower materials will have relatively high emissivities (low DHR) in the midwave and longwave infrared regions.

5.1.2 BRDF of NEFDS Materials

Materials similar to those in Section 5.1.1 were found in the NEF database. Recall from Section 3.2.1.1.4 that the NEFDS is a collection of BRDF model parameters for several hundred different materials. The materials selected represent metal, wood, plastic, and insulation and all have a DHE of at least 0.93. The BRDF of each material at $3.5\ \mu\text{m}$ and at $10.0\ \mu\text{m}$ at an incident illumination angle of 20° are plotted in Figures 5.6 - 5.9.

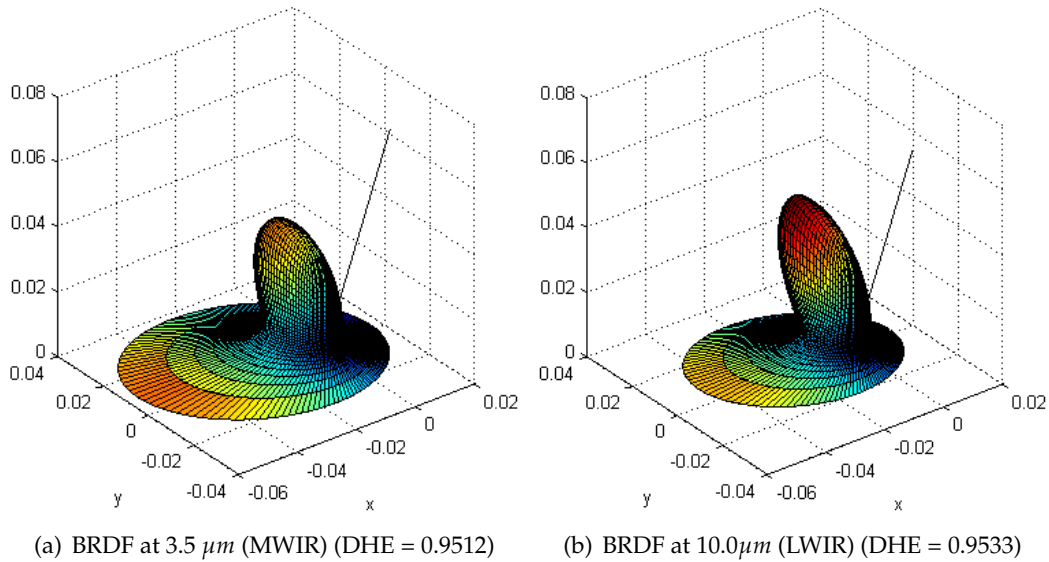


Figure 5.6: NEFDS BRDF of weathered galvanized bare steel (NEF #0525UUUSTLa) measured at an illumination angle of 20° .

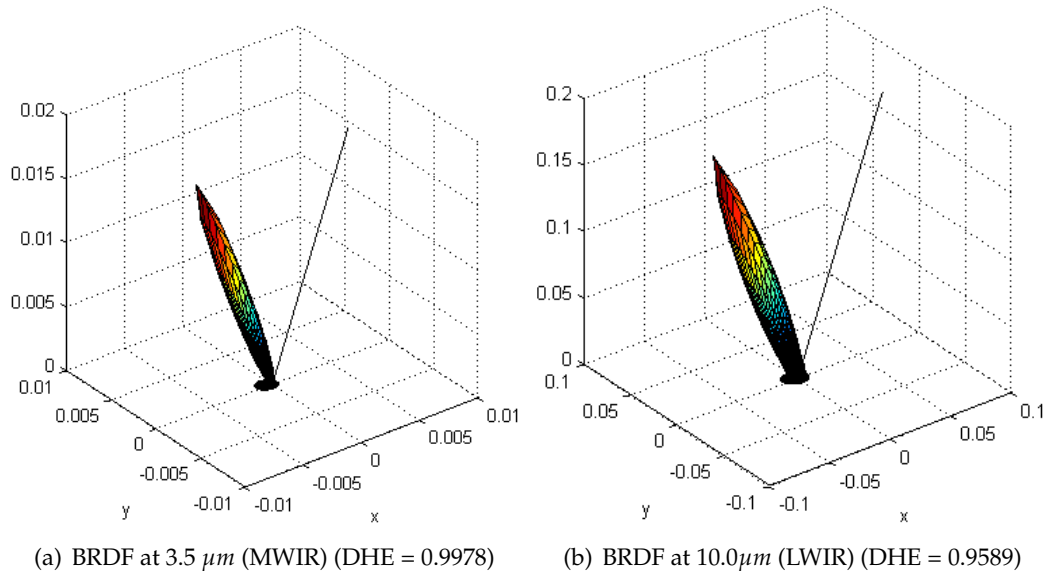


Figure 5.7: NEFDS BRDF of mildly weathered plastic tarp (NEF #1019UUUFABa) measured at an illumination angle of 20° .

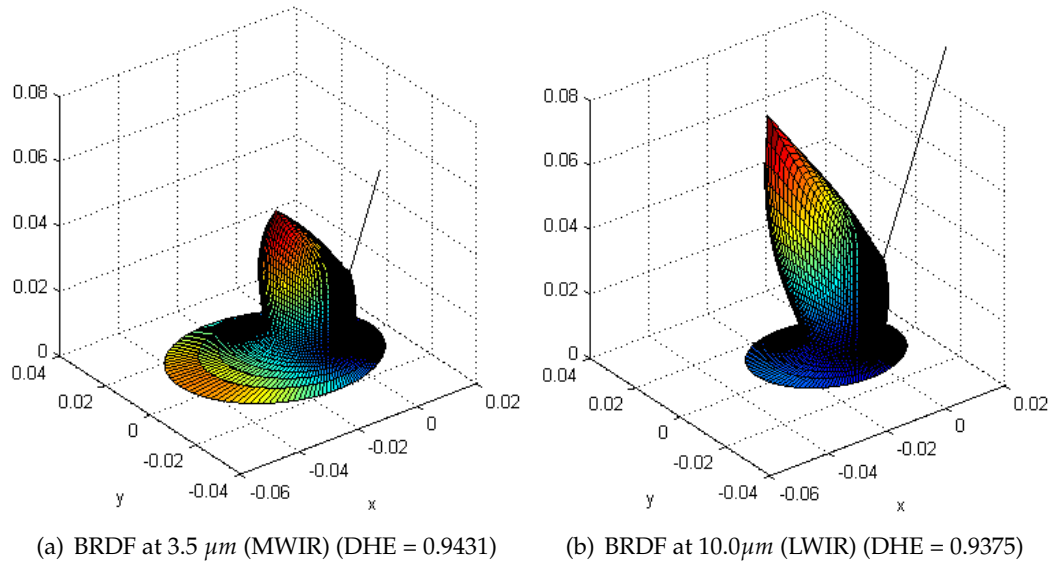


Figure 5.8: NEFDS BRDF of weathered bare construction lumber (NEF #0404UUUWOD) measured at an illumination angle of 20° .

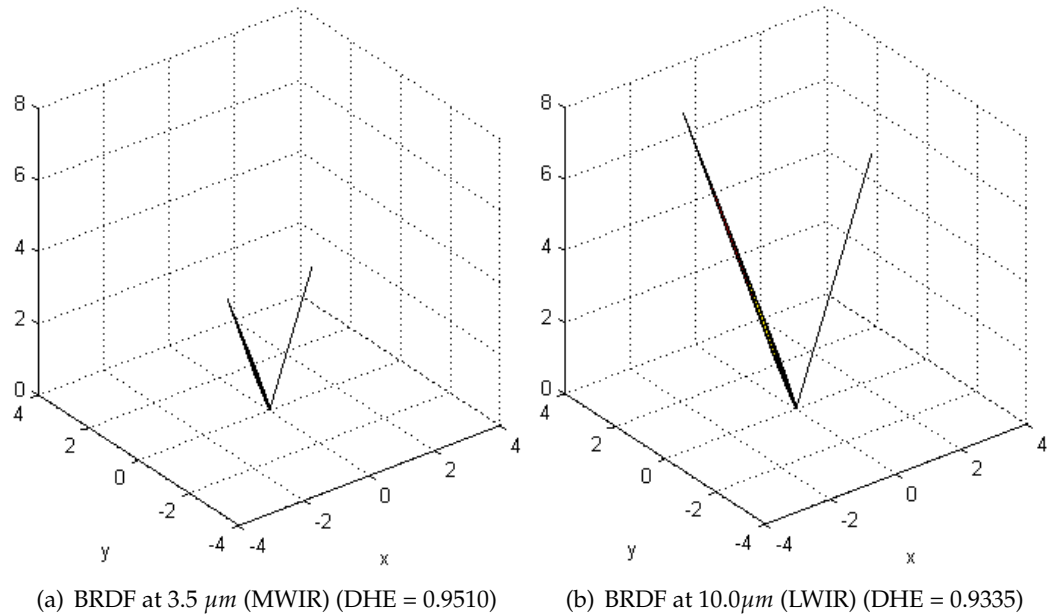


Figure 5.9: NEFDS BRDF of weathered paint on insulation panel (NEF #0887UUUPNT) measured at an illumination angle of 20° .

The BRDF plots indicate that typical MDCT construction materials are relatively specular in the MWIR and LWIR. In addition, these selected materials also have high emissivity (at least 0.93) at these wavelengths as consistent with Section 5.1.1.

5.1.3 DIRSIG Model of Closed and Open Cavities

The geometry of an object will have an important influence on its apparent temperature. A three-dimensional cavity was modeled in DIRSIG to study the relationship between the number of internal reflections resulting from the cavity geometry and the reflectance characteristics of the internal surfaces on the apparent temperature of the cavity. Both a closed cavity and an open cavity were studied.

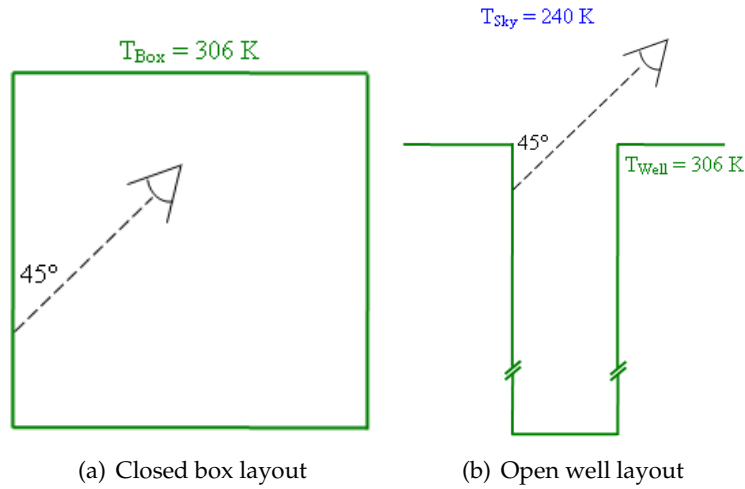


Figure 5.10: DIRSIG cavity simulation layouts (not to scale)

The first simulation consisted of a sealed six-facet box. A broadband 8 - 14 μm sensor with a unit spectral response was placed inside the box and targeted at one of the interior faces at a 45° angle (Figure 5.10(a)). The total number of reflections that a photon is allowed to make before being recorded by the sensor can be set manually in DIRSIG. Several runs were performed with a diffuse (no specular component) Ward BRDF and then with a specular (no diffuse component) Ward BRDF in which the number of internal reflections were increased incrementally. The BRDF shapes used in the simulations were shown in Figure 3.2. The model parameters were carefully chosen so that that DHR values were 0.05, 0.15, and 0.25 for the diffuse and specular models. These DHR values correspond to emissivity values of 0.95, 0.85, and 0.75, respectively, through equation (3.12). The box facets were also assigned a temperature of 306 K. The radiance recorded by the sensor is an integrated radiance between 8 and 14 μm . This radiance is then converted into an apparent temperature. For both the diffuse and specular BRDF models and for each DHR value, trends in the apparent temperature as a function of the number of internal bounces were investigated.

The second scenario consisted of an open, deep well. A broadband 8 - 14 μm sensor with a

unit spectral response was placed outside the well and targeted at one of the interior faces at a 45° angle (Figure 5.10(b)). Several runs were performed with a diffuse (no specular component) Ward BRDF and then with a specular (no diffuse component) Ward BRDF in which the number of internal reflections were increased incrementally. As before, DHR values of 0.05, 0.15, and 0.25 were chosen for the diffuse and specular models. The well facets were assigned a temperature of 306 K while the atmosphere was a spectrally flat 240 K source with a transmission of unity. Again, the integrated radiance recorded by the sensor was converted into an apparent temperature. For both the diffuse and specular BRDF models and for each DHR value, trends in the apparent temperature as a function of the number of internal bounces were investigated.

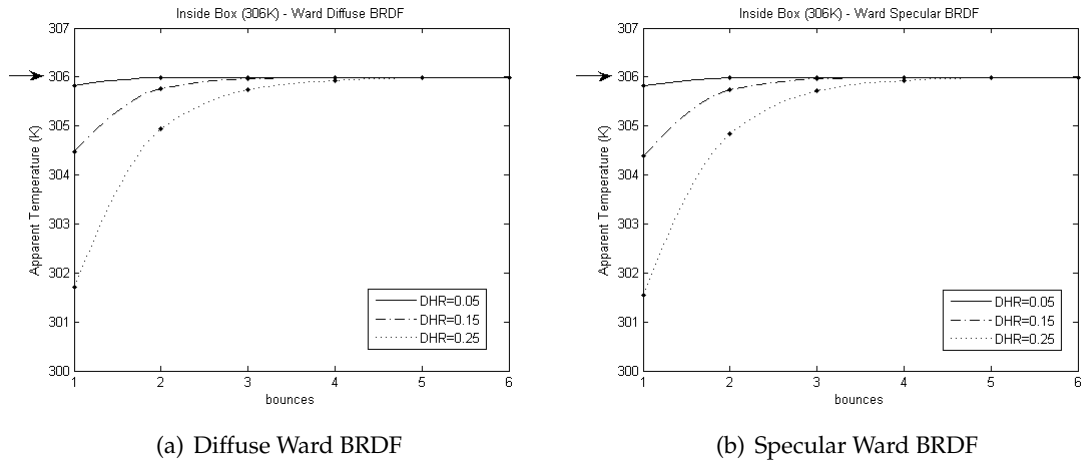


Figure 5.11: Results of the closed box simulation. Actual temperature is 306 K (indicated by arrow)

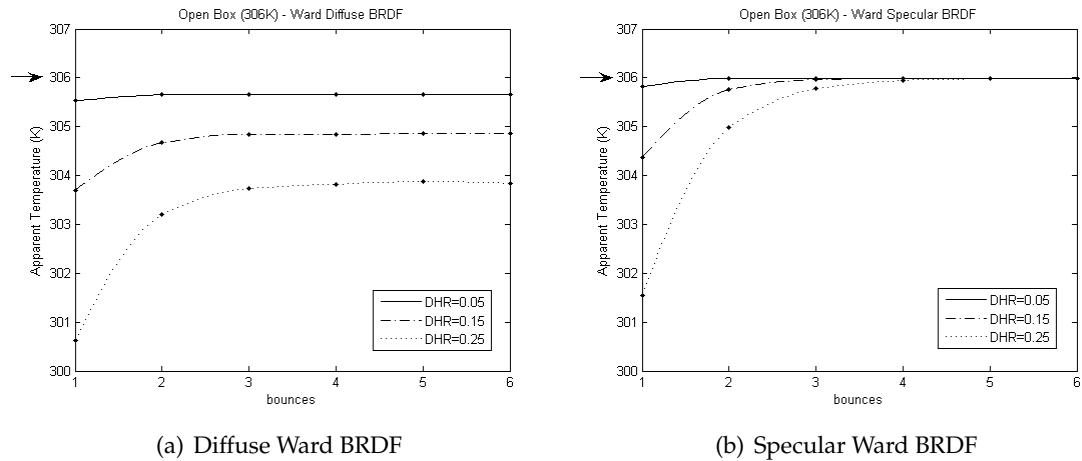


Figure 5.12: Results of the open well simulation. Actual temperature is 306 K (indicated by arrow)

The results of the sealed box and open well simulations are shown in Figures 5.11 and 5.12, respectively. The DIRSIG output is an integrated 8 - 14 μm radiance image. The average radiance of 100 pixels was converted to an apparent temperature using a radiance-to-temperature look-up table. The apparent temperature for up to six internal reflections are shown for each DHR value on the same plot.

Theoretically, the apparent temperature should increase and approach a final apparent temperature as the number of bounces increases. The radiance reaching a sensor is the self-emitted radiance of the target facet, modified by its emissivity, plus the reflected background radiances written as

$$L_{\text{sensor}} = \varepsilon L_{\text{target}} + \rho L_{\text{background}}. \quad (5.2)$$

The BRDF of the target facet will affect which direction in the hemisphere has the largest contribution to the reflected background radiance. For example, for a diffuse BRDF, every direction is equally weighted so the background radiance from the entire hemisphere has equal importance. For a specular BRDF, radiances in the specular direction will contribute more to the sensor-reaching radiance than radiances in non-specular directions. For the sealed box, since the background radiances are always just the other facets of the box (at the same temperature) the shape of the BRDF should not matter so the apparent temperature should approach the actual assigned blackbody temperature of 306 K. This can be seen in Figure 5.11. However, in the open well case, the background consists both of the other well facets and also the much colder sky. A specular BRDF would cause the sensor to see more of the warmer well than the colder sky, so the apparent temperature should still approach the actual blackbody temperature of 306 K as it does in Figure 5.12(b). On the other hand, a diffuse BRDF would cause the sensor to see both the other well facets and the sky. The apparent temperature in this last case will therefore be a weighted average of the cold sky and the warm well temperature as seen in Figure 5.12(a).

In addition, the DHR of the BRDF will affect how quickly the apparent temperature approaches its asymptote. A lower DHR value will result in a higher emissivity by equation (3.12). A higher emissivity will cause the apparent temperature to approach its asymptote more quickly since a higher emissivity indicates an object has a higher efficiency as a radiator. In other words, a high-emissivity object behaves more like a blackbody and the dependence on the number of internal reflections is diminished. This trend is evident in all of the plots shown in Figures 5.11 and 5.12.

The results of this study confirm that a cavity will behave as a blackbody radiator if there have been a sufficient number of internal reflections. The sealed box scenario demonstrated that the apparent temperature approaches the actual blackbody temperature after approximately one, two, and three reflections for DHR values of 0.05, 0.15, and 0.25, respectively. This scenario also confirmed that the shape of the facet BRDF does not matter since the sensor will always see one of the box facets. The open well scenario demonstrated that the shape of the facet BRDF is important when there are multiple background sources at disparate temperatures. A diffuse BRDF will cause more radiometric mixing between the warm well radiance and the cold sky radiance, resulting in a lower apparent temperature than the blackbody temperature of the well. A specular BRDF on the other hand will cause more of the warm well radiance to reach the sensor, producing a result similar to the sealed box simulation. Again, the DHR will determine how quickly the apparent temperature approaches its asymptotic temperature.

For an MDCT, the open well, diffuse case represents the worst-case scenario in terms of the internal geometry and material properties. If the internal tower materials are perfectly diffuse and have sufficiently high emissivities in the longwave infrared, then the apparent temperature will be within one or two Kelvin of the actual blackbody temperature if there has been approximately three internal reflections.

5.1.4 Effective Emissivity of Drift Eliminators

The primary interior component of a counter-flow MDCT that is visible to an overhead sensor is the drift eliminators. This material has a complex geometry that must be carefully modeled in order to determine its contribution to the radiance leaving the tower. An investigation was performed to determine if the geometry and optical properties of the drift eliminators would cause them to behave as a blackbody. If the effective emissivity is indeed unity, then the complex drift eliminators could be replaced with a simple blackbody plate in the radiometry models, allowing for much more rapid simulations to be used in the development of the parametric model for temperature error prediction.

As suggested by Figure 2.2, an overhead sensor targeted at the fan stack opening will probably not be able to see past the drift eliminator layer. Therefore, the drift eliminators are the last surface seen by the sensor which makes them very important since they are the closest surface to the hot cooling water.

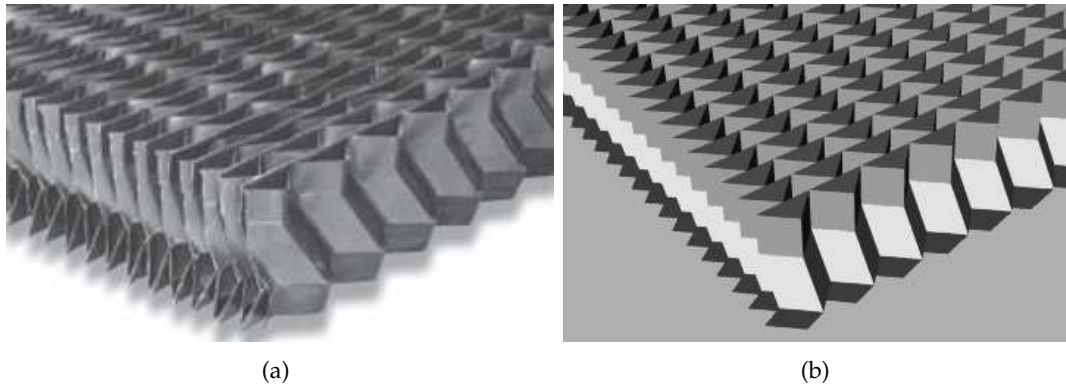


Figure 5.13: Photograph of the drift eliminators (a) and the CAD drawing reproduction (b).

The drift eliminators have a complex cavity geometry. As mentioned in Section 2.1, they are designed to change the direction of the air stream multiple times. In order to model their radiometry, a detailed representation of the drift eliminators must be produced. A high fidelity geometric model contains a very large number of facets and may greatly affect the execution speed of the simulations. A close-up photograph and a carefully drawn CAD model of the drift eliminator are shown in Figure 5.13.

Spectral reflectance measurements were taken of a drift eliminator sample as shown in Figure 5.2. The spectral emissivity plots demonstrate that the drift eliminators have a relatively high emissivity in the longwave infrared. The average emissivity of all the measured spectra from the sample in the 8 to 14 μm range is 0.941.

The BRDF of the drift eliminator material also demands careful attention. The sample material appears to be plastic or vinyl. Although a direct BRDF measurement of this sample is not available, the BRDF of a similar material can be found in the Nonconventional Exploitation Factors Data System (NEFDS). Two such materials were found: mildly weathered plastic tarp (NEF 1019UUUFABa) and weathered paint on insulation panel (NEF 0887UUUPNT). The BRDF of each material at a wavelength of 10 μm was shown in Figures 5.7 and 5.9. The BRDF for both of these materials is very specular in the longwave infrared. Since the drift eliminator material is similar to these materials, the drift eliminators could be considered fairly specular in the LWIR.

The study in Section 5.1.3 investigated the apparent temperature and effective emissivity of an open cavity for multiple internal reflections. That study concluded that an open cavity with high emissivity and a specular BRDF would have an effective emissivity of unity if photons underwent at least three internal reflections before exiting the cavity.

The DIRSIG simulations conducted in that study are now adapted to the drift eliminators specifically. A detailed CAD drawing of the drift eliminators as shown in Figure 5.13(b) was created. The Ward BRDF model was used to represent the BRDF of the drift eliminator material. The spectral measurements of the sample indicated an average emissivity of 0.941 in the longwave infrared. The Ward model was adjusted to provide several BRDFs having a directional emissivity of 0.941 measured at 20° to the surface normal. Since drift eliminators are designed to allow air to change direction three times, photons were allowed to make a maximum of three bounces in the simulation. A broadband 8 - 14 μm sensor was placed approximately 150 meters above the drift eliminators. The entire drift eliminator was assigned a temperature of 306 K. A flat blackbody plate having a temperature of 276 K was placed under the drift eliminator to provide a low temperature background source. The atmosphere was a spectrally flat 240 K source with a transmission of unity. The apparent temperature of the drift eliminator was determined from the at-sensor radiance.

The shape of the BRDF and the sensor zenith view angle were varied in these simulations. Ward BRDF models included one diffuse-only BRDF and four specular-only BRDFs. The specular BRDFs had lobes exhibiting various widths as shown in Figure 5.14(b) - 5.14(e). The drift eliminators were viewed from zenith angles of 0, 10, and 20 degrees.

The results of these various simulations are listed in Table 5.1. The drift eliminators were assigned a temperature of 306 K. The table shows the apparent temperature recorded by the sensor as a function of the sensor view angle and the shape of the BRDF. Recall that for all the BRDF shapes, the directional emissivity was fixed at 0.941.

The data indicates that the apparent temperature increases and approaches the absolute

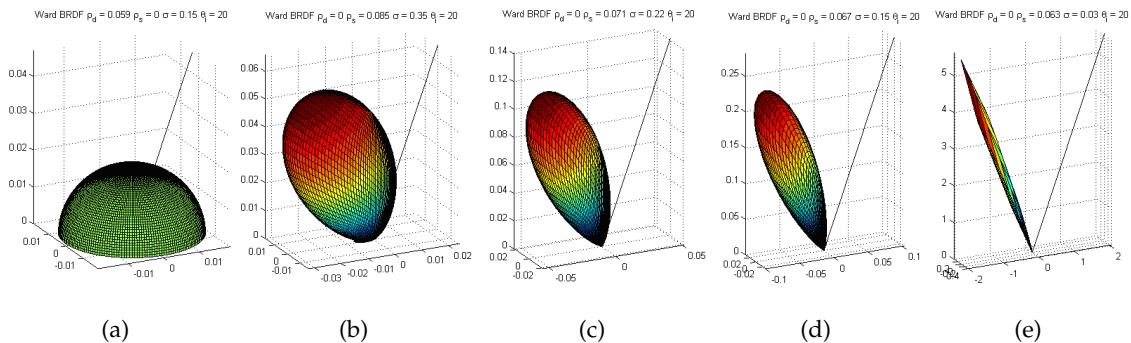


Figure 5.14: Ward BRDF shapes used in the DIRSIG simulations. Diffuse (a), specular, $\sigma = 0.35$ (b), specular, $\sigma = 0.22$ (c), specular, $\sigma = 0.15$ (d), and specular, $\sigma = 0.03$ (e).

Sensor Angle	Perfectly Diffuse	Specular $\sigma = 0.35$	Specular $\sigma = 0.22$	Specular $\sigma = 0.15$	Specular $\sigma = 0.03$
0°	305.638 K	305.955 K	305.975 K	305.985 K	305.997 K
10°	305.363 K	305.938 K	305.971 K	305.982 K	305.995 K
20°	305.282 K	305.931 K	305.970 K	305.982 K	305.995 K

Table 5.1: Results of the DIRSIG drift eliminator simulations. The apparent temperature of the drift eliminators is shown as a function of the BRDF shape of the material and the sensor view angle. The absolute temperature is 306 K.

temperature of 306 K as the BRDF becomes more specular. For the specular BRDF shapes, all apparent temperatures are within 0.1 K of the absolute temperature. Since typical longwave infrared sensors have a sensitivity of about 0.1 K, the results show that a specular BRDF will reveal the absolute temperature of the drift eliminators. This is true even for a broad-lobed BRDF. A diffuse BRDF, however, can be several tenths of a Kelvin less than the absolute temperature. The results also indicate that the apparent temperature decreases slightly as the sensor angle increases. This decrease is significant for the diffuse BRDF. However, for the specular BRDFs, the decrease in apparent temperature with sensor angle is negligible since the difference is still within typical sensor noise.

These simulations revealed that the apparent temperature of the drift eliminators as recorded by a LWIR sensor will equal the absolute temperature of the drift eliminators under certain conditions. Previous studies and measurements have shown that the drift eliminator material has a high emissivity and is specular in the LWIR. Furthermore, due to the complex geometry of the drift eliminators, photons will undergo at least three internal reflections. These conditions imply that the effective emissivity of the drift eliminators will be unity over the range of sensor zenith angles typical for remote sensing of MDCTs. Therefore, the complex geometry and optical properties of the drift eliminators can be represented as a simple blackbody plate for subsequent DIRSIG simulations.

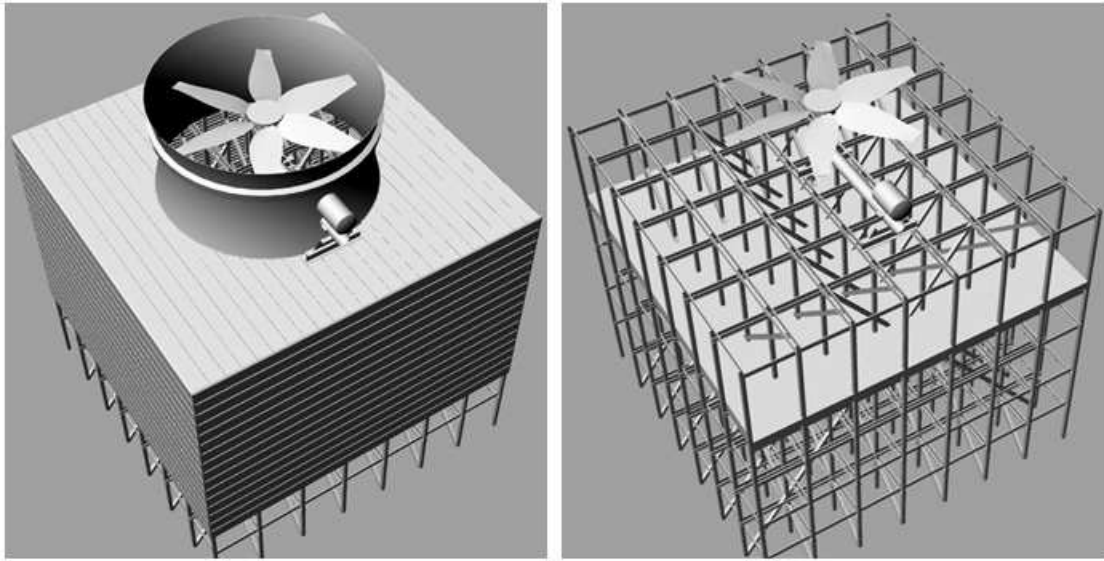


Figure 5.15: CAD drawing of a counter-flow MDCT exterior view (left) and interior view (right).

5.1.5 MDCT DIRSIG Rendering with BRDF Materials

The DIRSIG modeling tool was used to investigate the apparent temperature of an MDCT model. The DIRSIG rendering was generated by assigning basic thermal properties to a geometric model of a tower. The geometrically detailed three-dimensional CAD drawing was intended to mimic a counter-flow tower similar to the F-area and H-area units at the Savannah River Site (SRS). The geometry of the drawing was based on measurements taken at SRS and on schematics obtained from SPX Cooling Technologies [39]. A high fidelity geometric model is necessary to reproduce the geometry for multiple reflections within the cooling tower.

Recall that a sensor targeted at the fan stack opening will not be able to see past the drift eliminator layer. Therefore, the geometry above the drift eliminators was carefully reproduced, as it would have the greatest influence on the observed radiance. Structures located below the drift eliminators were only approximated or deleted altogether. Detailed views of the CAD drawing are shown in Figure 5.15.

For the DIRSIG model, each facet of the CAD drawing was assigned a temperature of 306 K. In the first scenario, a diffuse Ward BRDF (no specular component) was assigned to every facet. The model parameters were adjusted to produce a DHR of 0.15. In the second scenario, a specular Ward BRDF (no diffuse component) was assigned to every facet. The approximate shapes of the Ward models used were shown in Figure 3.2.

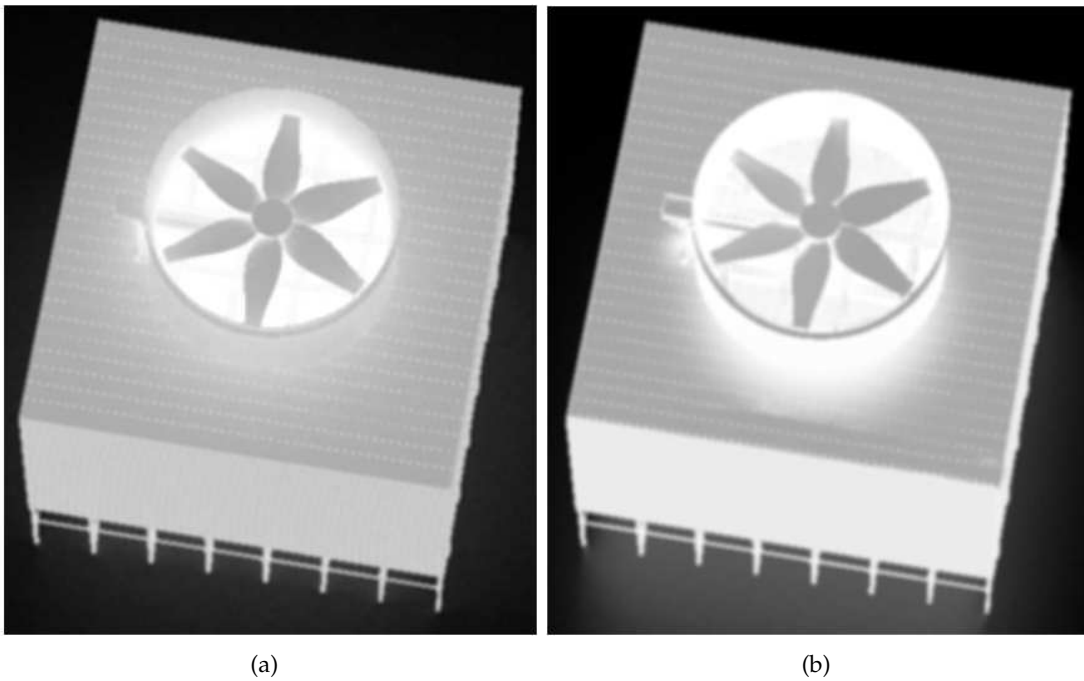


Figure 5.16: DIRSIG radiance image with diffuse Ward BRDF (a) and specular Ward BRDF (b).

The total number of reflections that a photon is allowed to make before being recorded by the sensor can be set manually in DIRSIG. This parameter was held fixed at three bounces since it has been shown that for a relatively low DHR value, the apparent temperature would reach the blackbody temperature after approximately three internal reflections (see Section 5.1.3). In the DIRSIG environment, the time was set to 23:00 local time in mid-June in the south-eastern United States. A broadband 8 - 14 μm sensor was positioned 25° from zenith at a distance of 120 m from the fan stack opening. A standard mid-latitude summer atmosphere was generated. These parameters were chosen to approximate the conditions at the Savannah River Site where actual infrared images of such towers were obtained. DIRSIG outputs a radiance image of the scene visible by the sensor. Bright pixels indicate higher radiances while dark pixels indicate lower radiance values. The DIRSIG renderings for both scenarios are shown in Figure 5.16.

A quick look at the DIRSIG image indicates that the general output is as expected. The brightest pixels, representing the highest temperatures, are deep within the tower. The exterior of the tower is cooler than the interior because it partially reflects the colder sky. The ground plane was assigned a temperature of 288 K and makes up the darkest pixels in the image, as expected. The differences in the two Ward models are apparent in the images. In the right hand image, the warm pixels on the deck and on the ground plane

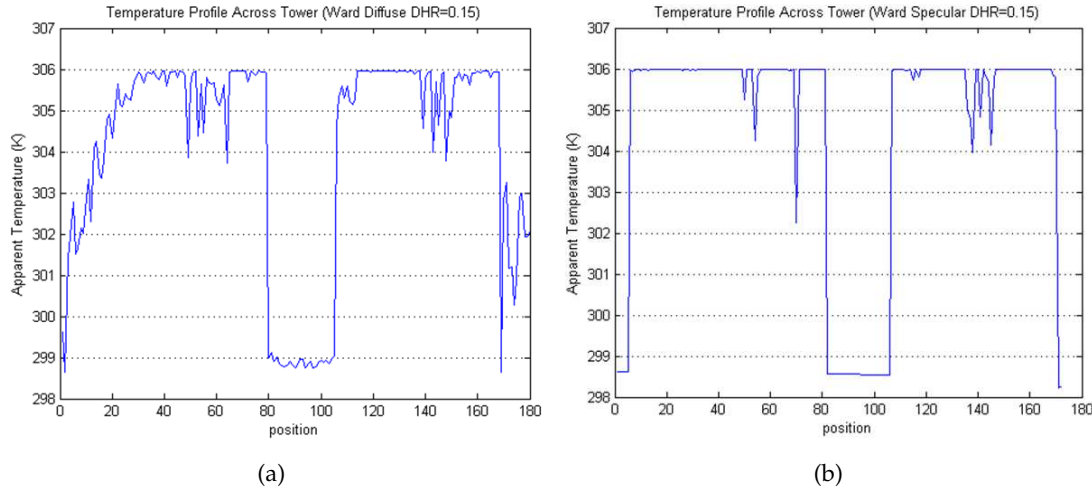


Figure 5.17: Apparent temperature profiles across the fan stack opening of the MDCT for the diffuse Ward BRDF image (a) and the specular Ward BRDF image (b).

are the result of specular reflections from the hot tower surfaces due to the specular Ward BRDF. An analysis of the DIRSIG images was performed by taking profiles across the fan stack openings. The radiances were converted into apparent temperatures. These profiles are shown in Figure 5.17.

The profiles indicate that for both BRDF models, the maximum apparent temperature detected is the blackbody temperature of the tower, 306 K. The highest values in the plots are pixels located deep within the tower. The central depression indicates the fan hub while the low values at the left and right extremes of the plots indicate the tower decking. The apparent temperatures at these points are lower than the interior of the tower due to the reflected sky radiance. The specular material contains more pixels at 306 K because it reflects the warm interior directly into the sensor. The diffuse material, on the other hand, reflects the warm interior and the cooler sky into the sensor, resulting in a lower apparent temperature.

The results of the DIRSIG simulation show that a detailed geometric model along with basic thermal properties can produce a good approximation of the apparent temperatures of a mechanical draft cooling tower. For both a diffuse and specular material with a low DHR of 0.15, the apparent temperature of the MDCT approaches the blackbody temperature of the tower if there are at least three internal reflections.

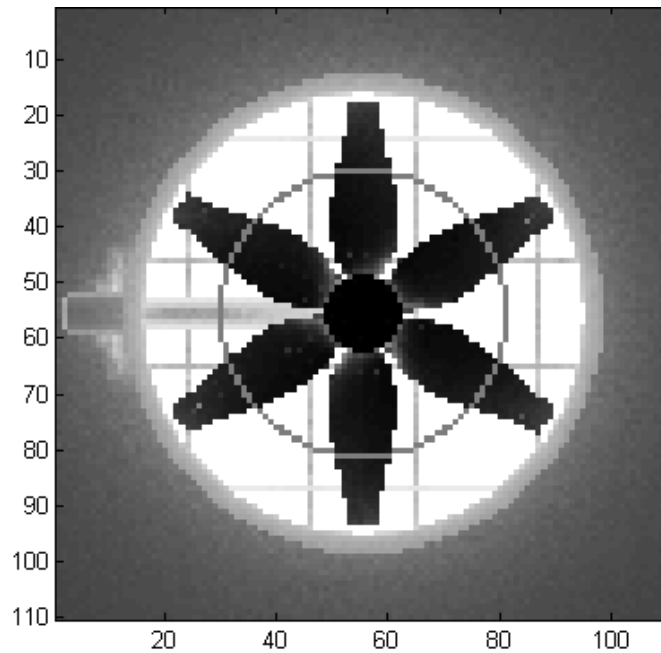


Figure 5.18: DIRSIG rendering of an MDCT with a one-pixel-wide ring drawn.

5.1.6 MDCT Fan Blade Motion

A methodology is needed to model the spinning fan blades of an MDCT. Recall from Section 2.2 that an MDCT may operate in two states. In the *fans off* case, hot water is flowing through the tower and the warm, moist air exits the tower stack through natural convection. The fan blades are motionless so the fan blades and tower cavity can be distinguished in an image from an overhead sensor of fine enough spatial resolution. In the *fans on* case, the fan in the stack rotates to force the warm, moist air out of the fan stack opening. The spinning fan blades will appear blurred in an image from an overhead sensor assuming a significant temporal integration time. The effect of the spinning fan blades on the tower-leaving radiance was investigated.

The first study conducted was to determine if the radiance from the tower opening depends on the fan speed and/or on the integration time of the sensor. Consider the image of the tower opening in Figure 5.18. At any radius r , a ring may be drawn that is one pixel in thickness. In the *fans off* case, the pixels in this ring can be distinguished as “fan” pixels or “cavity” pixels. In the *fans on* case, however, the fan and cavity pixels in this ring cannot be distinguished due to the blurring effect caused by the rotating fans and due to the integration time of the sensor. To model the *fans on* case, a square-wave signal was generated in Matlab. The signal has a value of one to represent cavity pixels

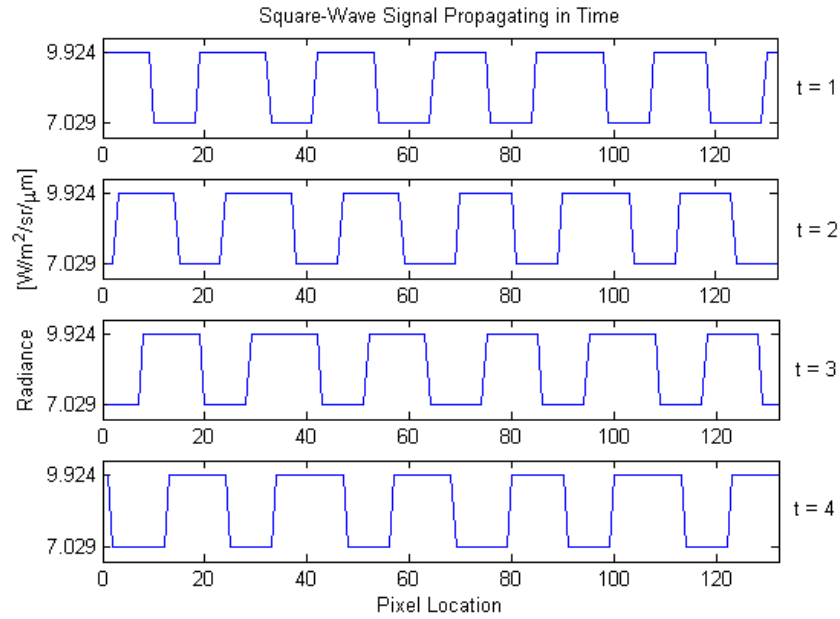


Figure 5.19: Square-wave signal representing the fan blade and cavity radiances at each pixel location in the ring at different times.

and a value of zero to represent fan pixels. To give the simulation some physical meaning, the fan pixels were given a blackbody radiance at $10\ \mu\text{m}$ for a temperature of 280 K ($L = 7.0286\ [\text{W}/\text{m}^2/\text{sr}/\mu\text{m}]$) while the cavity pixels were given a blackbody radiance at $10\ \mu\text{m}$ for a temperature of 300 K ($L = 9.9240\ [\text{W}/\text{m}^2/\text{sr}/\mu\text{m}]$).

The signal was modified so that for each iteration, the signal would shift by v pixels. The variable v represents the speed of the signal (*i.e.*, the linear speed of the fan blades at the given radius). One iteration represents one unit of time (*e.g.*, one second). The radiance value is observed at each pixel location on the signal and for every iteration. The number of iterations (the number of seconds) represents the integration time of the sensor. For each pixel location, the radiance was summed for the time interval and then normalized by the total integration time. In other words, for a particular pixel, the “shutter” was opened for the specified integration time so that the time-averaged signal could be collected. This simulation is illustrated in Figure 5.19.

The result is a vector of radiance values that represent the time-averaged radiances of a square-wave passing through each pixel location. These integrated radiance values differ for each pixel location and will depend on the speed of the signal and on the integration time. The **mean value** of the radiances is always constant regardless of the signal speed or the integration time. The reason for this observation is that, for the entire sampling

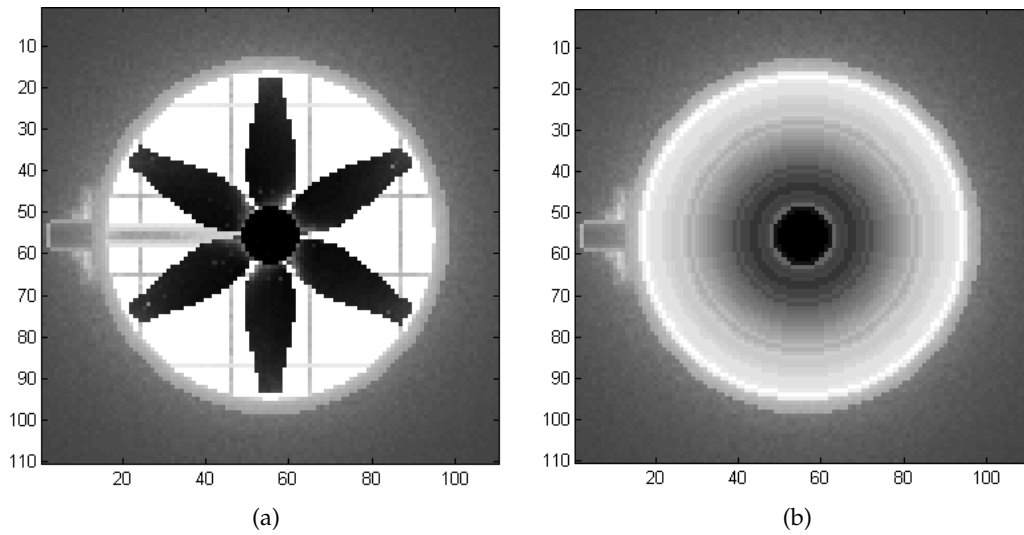


Figure 5.20: DIRSIG rendering of an MDCT with a stationary fan (a) and a blurred rendering representing a rotating fan (b).

ring (vector) in Figure 5.18, there are always the same number of fan pixels and the same number of cavity pixels. Therefore, the average value of the vector remains constant.

The conclusion of this investigation was that the average radiance in a ring at radius r was the same for a stationary fan blade as it was for a spinning fan blade. Based on this information, the next study seeks to determine if the spinning fan blade can be modeled using the stationary fan model. In other words, is it possible to represent the *fans on* case from the *fans off* model?

As mentioned previously, the rotating fan blade will blur the radiances in each ring drawn in the fan stack opening. The average value in each ring is constant. For every ring, the pixel values in the ring were replaced with the average pixel value of the ring. This ring averaging represents the blur caused by the rotating fan. Figure 5.20 illustrates a stationary fan image and a motion-blurred spinning fan image.

The images in Figure 5.20 show the apparent temperature of each pixel (bright pixels are hot). In a *fans on* case, the user would have to take an average value over the entire opening since the fan and cavity pixels cannot be distinguished. Therefore, a region of interest (ROI) was drawn over the entire opening for the *fans off* and the *fans on* image and the average value was computed. The average value for both the *fans off* and the *fans on* image is 294.57 K.

This result is expected since in the *fans on* image the average was taken over the fan stack opening which was a collection of rings whose values were the average values in each ring. This is essentially an "average of averages" problem. The mean of the means of subsets of a population is the same as the mean of the entire population. The mean value in a subset is

$$\bar{x}_j = \sum_{i=1}^{n_j} p(x_i) x_i, \quad (5.3)$$

where n_j is the number of samples in the j^{th} subset and $p(x_i)$ is the probability that observation x_i occurs. The mean value of the means of the subsets is then

$$\bar{x} = \sum_{j=1}^m p(\bar{x}_j) \bar{x}_j, \quad (5.4)$$

where m is the number of subsets and $p(\bar{x}_j)$ is the probability that the \bar{x}_j subset mean occurs. Combining equations (5.3) and (5.4) yields

$$\bar{x} = \sum_{j=1}^m p(\bar{x}_j) \bar{x}_j = \sum_{j=1}^m p(\bar{x}_j) \sum_{i=1}^{n_j} p(x_i) x_i = \sum_{j=1}^m \frac{n_j}{N} \sum_{i=1}^{n_j} \frac{1}{n_j} x_i = \frac{1}{N} \sum_{j=1}^m \sum_{i=1}^{n_j} x_i = \frac{1}{N} \sum_{i=1}^N x_i, \quad (5.5)$$

where N is the total number of observations (pixels) in the population. This confirms that the average value over the fan stack opening is equal to the average of the rings, where the value in each ring is the average value in that ring.

The result of these studies indicates that the *fans on* case can be modeled by taking the average pixel value over the entire fan stack opening of the MDCT from the *fans off* case. Since cavity pixels and fan pixels cannot be distinguished in the *fans on* case, an ROI can be drawn over the entire fan stack opening and the average radiance in this ROI can be taken as the tower-leaving radiance. For modeling purposes, the DIRSIG model with the stationary fan blades will be sufficient in representing the spinning fan blades due to this equivalency. As with a real image, an ROI can be drawn over the entire fan stack opening in the DIRSIG model and the average radiance can be used as the tower-leaving radiance. This result is important since it eliminates the need to run DIRSIG temporally (to model fan blades in motion) which would drastically increase run time.

5.1.7 Atmospheric Downwelled Radiance

The previous sections investigated the behavior of the self-emitted radiance of the MDCT. The reflected component of the tower-leaving radiance must also be considered. An analysis was performed to determine how sensitive the derived apparent temperature is to changes in the atmospheric downwelling radiance. The MODTRAN atmospheric modeling tool was used to aid this analysis. The total sky downwelling radiances in the long-wave infrared spectral region for the six MODTRAN standard atmospheres were computed. These spectral radiances were used in the reflected term of the governing radiometry equation. The influence of each atmosphere on the radiance reaching the sensor was investigated.

The reflected radiance component consists of the sky downwelling radiance modified by the reflectance of the object. By Kirchhoff's law, the sum of the reflectivity and the emissivity of an opaque object is unity. For a diffuse object, the reflectance is the same for every view angle. The surface-leaving radiance from equation (3.14) is then

$$L_{surf}(\lambda) = \varepsilon(\lambda) L_{BB}(\lambda, T) + [1 - \varepsilon(\lambda)] L_d(\lambda), \quad (5.6)$$

where $L_d(\lambda)$ is the downwelling sky spectral radiance and is assumed to be uniform. The spectral response of the sensor is then applied to the surface-leaving spectral radiance to arrive at an integrated radiance value for the passband of the sensor. This band radiance is converted into an apparent temperature. A temperature error metric is defined as the difference between the apparent temperature at the sensor and the actual temperature of the object.

The six MODTRAN standard atmospheres used in this study were tropical, mid-latitude summer, mid-latitude winter, sub-arctic summer, sub-arctic winter, and 1976 U.S. standard [13]. These atmospheric profiles were processed in the DIRSIG utility called `make.adb` [22]. The utility samples the hemispheric sky dome at discrete angles and for each sample direction, the path radiance is computed from MODTRAN. A table is built of the zenith and azimuth angle of the sample and the spectral downwelling radiance from the sample. The sky is sampled from 7.5 to 82.5 degrees on 15 degree intervals in the zenith direction and from 0 to 330 degrees on 30 degree intervals in the azimuth direction. This results in six zenith samples and twelve azimuth samples which yield 72 total sky samples. The samples are then integrated over the hemisphere to arrive at the diffuse spectral downwelling radiance [22].

The downwelling radiance can be converted into an apparent temperature. This temperature is the effective blackbody temperature of the sky. Table 5.2 lists these temperatures for each atmospheric profile. The sky temperatures shown in this table cover a wide range from 203 K to 276 K. The range in effective sky temperatures is due to the differences in the air and dew point temperature profiles for each standard atmosphere.

MLS	MLW	SAS	SAW	Trop	US Std.
262.40 K	218.62 K	245.97 K	203.09 K	276.15 K	235.87 K

Table 5.2: Effective sky apparent temperatures for the standard MODTRAN atmospheres.

Next the sensitivity of the downwelling radiance on the apparent temperature error was investigated. A broadband sensor with a spectral response of unity between 8 and 14 μm was used. The absolute temperature of the object was assigned a value of 300 K. For each atmospheric profile, the diffuse spectral downwelling sky radiance that was computed from the make_adb utility was used in the reflected term in equation (5.6). The apparent temperature at the sensor was calculated for each profile and for a range of emissivity values from 1.0 to 0.7. The temperature error was defined as the difference between the apparent temperature and the assigned absolute temperature of the object (300 K). Figure 5.21 illustrates the results.

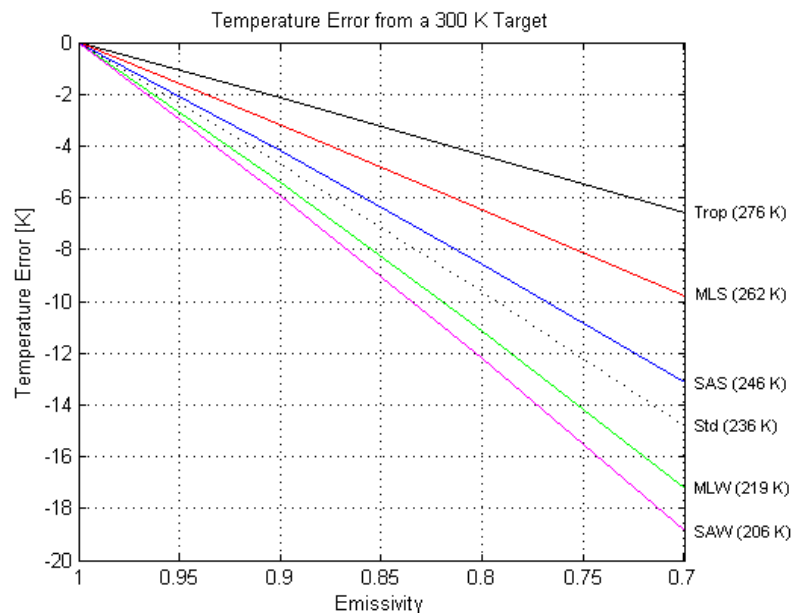


Figure 5.21: Temperature error from a 300 K object as a function of emissivity and MODTRAN standard atmospheric profile.

The magnitude of the temperature errors increase as the emissivity decreases. This is due to a decrease of the self-emitted radiance component as the emissivity decreases resulting in more of the colder sky radiance being included in the sensor-reaching radiance. The temperature errors also increase as the apparent sky temperature decreases. The sky temperatures are less than the object temperature of 300 K for all the atmospheric profiles. Therefore, if a “colder” radiance is reflected to the sensor, the apparent temperature at the sensor will be colder as well, resulting in a higher temperature error.

This study demonstrated that the atmospheric downwelling radiance may have a significant effect on the derived temperature error. Knowledge of the atmospheric profile is important to accurately determine the temperature of a remotely-sensed object.

5.1.8 Tower Leaving Radiance Summary

The radiance leaving the tower consists of both self-emitted radiance and also reflected downwelled radiance. Typical MDCT construction materials have relatively high emissivities at longwave infrared wavelengths (Section 5.1.1). Therefore, the self-emissive term in equation (5.1) will be dominant. Emissivities of 0.80 and 0.90 translate into DHR values of 0.20 and 0.10, respectively. These DHR values are still significant so the reflected terms cannot be ignored. an MDCT can be represented as an open well. If the tower materials are relatively specular for longwave infrared wavelengths, as indicated by Section 5.1.2, then background radiance reflected to an airborne sensor will be dominated by the self-emitted radiances from the other interior surfaces of the tower. Finally, given the above constraints, the radiance leaving the tower will be the blackbody radiance of the tower materials if there has been at least three internal reflections. Given the complex internal geometry of an MDCT, there is a high probability a photon will undergo at least three reflections before exiting the tower. Therefore, pixels from deep within the tower cavity will have an effective emissivity of unity. On the other hand, pixels from “shallow” regions of the tower will have an effective emissivity less than unity.

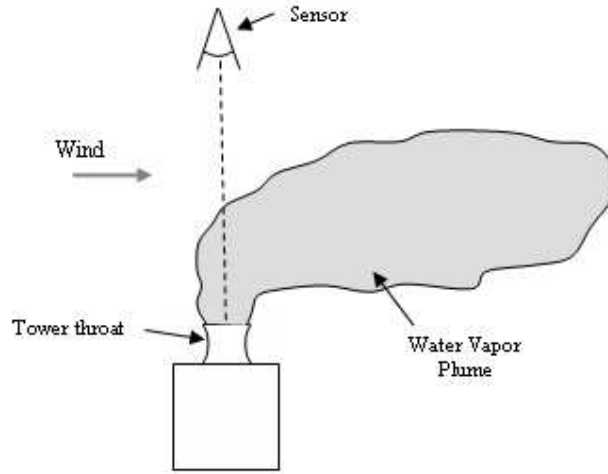


Figure 5.22: Radiance from the tower passes through the exhaust plume to reach the sensor.

5.2 sensor-reaching Radiance

Radiance leaving the tower cavity must now propagate through the intervening column of air between the tower and the sensor. Recall from Section 3.4.2 that the atmosphere will both attenuate and exaggerate the signal through transmission losses and additive upwelling radiance. The radiance reaching the front of the sensor after passing through the air column is

$$L_{sensor}(\theta, \phi, \lambda) = \tau(\theta, \phi, \lambda) L_{tower}(\theta, \phi, \lambda) + L_u(\theta, \phi, \lambda) \left[\frac{W}{m^2 sr \mu m} \right]. \quad (5.7)$$

For a mechanical draft cooling tower, the target-to-sensor air column not only consists of the ambient atmosphere, but will also include a localized water vapor plume directly above the tower. The additional water vapor introduced by this plume will contribute an additional error in the derived apparent temperature. Figure 5.22 demonstrates radiance from the tower passing through the exhaust plume to reach the sensor. The air column can be divided into two segments. The first segment falls within the exhaust plume of the tower. The second segment is the free atmosphere not influenced by the plume.

The exhaust plume from an MDCT would introduce water vapor at an elevated temperature into the volume immediately above the tower. Radiance emitted within the tower must pass through this plume to reach an airborne sensor. Transmission values of less than unity will decrease the radiance at the sensor resulting in an apparent temperature that is lower than the actual material temperature. Conversely, the upwelled radiance will increase the radiance at the sensor resulting in an apparent temperature that is higher

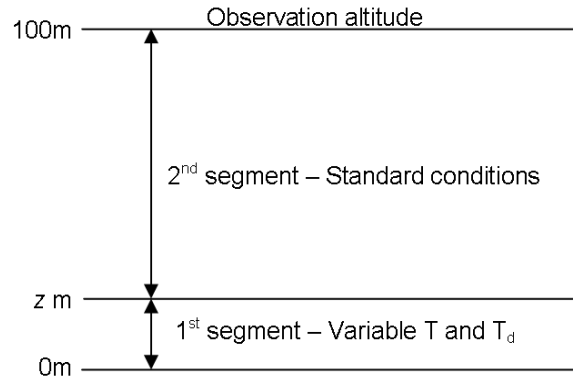


Figure 5.23: Atmospheric column representing the plume layer and the ambient atmosphere modeled in MODTRAN.

than the actual material temperature. These two effects compete with each other so that the apparent temperature at the sensor may be higher or lower than the actual temperature depending on the atmospheric conditions. The atmospheric conditions must be carefully modeled in order to correct for errors in the derived temperature.

The first segment of the air column would contain a higher water vapor concentration than the second segment (in most cases). The free parameters of the plume are the air temperature, the water vapor concentration, and the height. The ambient atmospheric conditions (second segment) will also affect the transmission and upwelled radiance separately.

5.2.1 MODTRAN Simulation of Air Column

The MODTRAN radiative transfer model was used to simulate how the water vapor concentration affects the target-to-sensor transmission and upwelled radiance in the atmosphere at longwave infrared wavelengths. The dew point depression and air temperature were chosen as measures of the water vapor concentration in the column due to their feasibility of measurement in situ. The air column was divided into two layers in MODTRAN. The first layer extends from the ground to a height of z meters to represent the exhausted plume. The second layer extends from the terminating point of the first layer up to an observation altitude of 100 meters. The second layer was assigned standard atmospheric conditions. The first layer was also assigned standard conditions for all parameters except the air temperature and the dew point depression which were varied to simulate various temperatures and water vapor concentrations. Figure 5.23 illustrates this layout.

Several MODTRAN runs were conducted under a variety of conditions. The air temper-

ature in the first layer was varied in increments of 5 K from 280 K to 310 K. For each temperature, dew point depressions of 0, 2, 5, 10, and 20 K were used. The dew point depression is the difference between the air temperature and the dew point temperature. A dew point depression close to zero indicates near saturated air while a large depression indicates dry air. The observation altitude was held fixed at 100 m. The thickness of the first layer, z , was set to values of 1, 5, 10, and 20 m representing various plume thicknesses under a variety of ambient wind conditions (*i.e.*, lower wind speed indicates a more vertical plume and a thicker layer). The above parameters were run for standard mid-latitude summer conditions and then repeated for sub-arctic winter conditions representing relatively wet and dry ambient atmospheres, respectively. The target material was a perfect blackbody. Several runs were performed with blackbody targets of 302 K, 306 K, and 310 K. MODTRAN4v3r1 was run in solar/thermal radiance mode between 8 and 14 μm at a resolution of 0.3 μm with an 8-stream discrete ordinate multiple scattering algorithm [40].

The intent of the MODTRAN simulation was to model an air column containing a high water vapor concentration layer within a column of standard water vapor conditions. The transition between this lower layer and the standard atmosphere is marked by a dramatic gradient in the water vapor profile. In a user-defined atmosphere, MODTRAN allows the user to specify the height, pressure, temperature and dew point of the atmospheric layer at each altitude. These supplied values are used at the exact heights specified. However, MODTRAN's interpolation scheme is inadequate for such large gradients across large, relatively broad altitude ranges [41]. Therefore, in order to realize the strength of this gradient, several thinner (one meter thick) layers were inserted between the standard layers of the upper atmosphere and the user-defined, high humidity conditions of the lowest layer. These extra layers provided the necessary buffer to allow a sharp fall off in temperature and dew point depression between the first and second layers. Figure 5.24 demonstrates the layers set in MODTRAN.

The variables for the MODTRAN simulations were the height of the plume segment, the air temperature and dew point depression in the plume, and the ambient atmospheric conditions. Table 5.3 summarizes the values used in the simulation. A MODTRAN run was performed for every combination of the variables. The model output contains spectral values of the transmission (TRANS) and upwelled radiance (PATH_THERMAL) between wavelengths of 8 and 14 μm . These spectral values were used to calculate the radiance reaching a sensor from several blackbody targets through equation (5.7). The

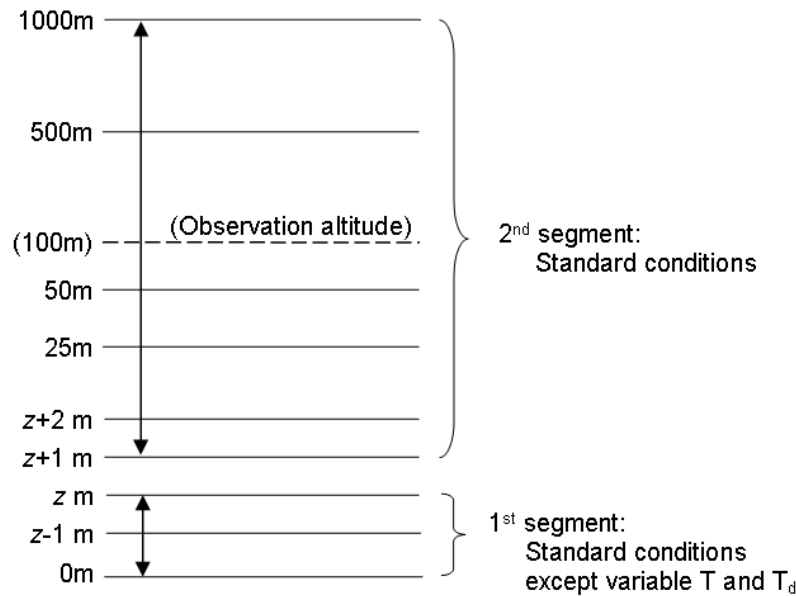


Figure 5.24: Schematic of the atmospheric layers assigned in MODTRAN. The first segment represents the exhaust plume while the second segment represents the rest of the air column. Standard atmospheric conditions are assigned to every layer except for those in the first segment where the air temperature and dew point temperature are varied (not to scale).

material radiance was taken as the spectral blackbody radiance from the Planck equation. Temperatures of 302 K, 306 K, and 310 K were used for the targets. The spectral radiance at the sensor from equation (5.7) was integrated between 8 and 14 μm to arrive at an integrated radiance at the sensor. The sensor had a flat, unit spectral response function between 8 and 14 μm and a zero response outside that region. The integrated sensor radiance was converted to an apparent temperature. Finally, the temperature error was defined as the difference between the blackbody temperature used in the Planck equation and the apparent temperature derived from the integrated sensor radiance. The results are shown in Figures 5.25 and 5.26.

Blackbody Temp. [K]	Plume Height [m]	Plume Air Temp. [K]	Plume Dew Pt. Depression [K]	Ambient Conditions
302	1	280	0	mid-latitude summer sub-arctic winter
306	5	285	2	
310	10	290	5	
	20	295	10	
		300	20	
		305		
		310		

Table 5.3: Parameter values for the MODTRAN plume simulations.

Mid-Latitude Summer Conditions

Atmospheric Conditions at $z = 25m$: $P = 1010.065mb$, $T = 294.09K$, $Dew Pt. Depress. = 4.41K$

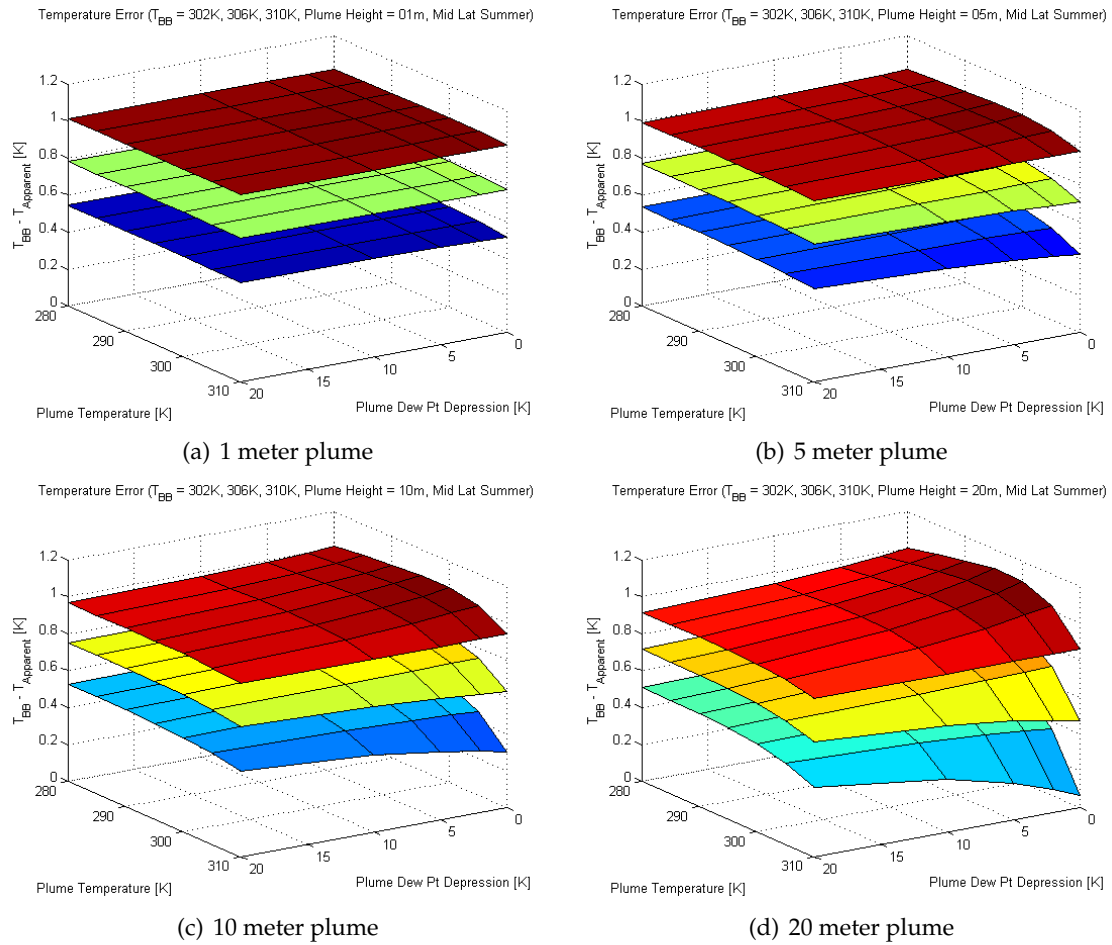


Figure 5.25: Errors between material blackbody temperature and the sensor derived apparent temperature. The surfaces are for material blackbody temperatures of 310 K, 306 K, and 302 K from top to bottom in each plot.

Sub-Arctic Winter Conditions

Atmospheric Conditions at $z = 25m$: $P = 1009.664mb$, $T = 257.25K$, $Dew Pt. Depress. = 2.36K$

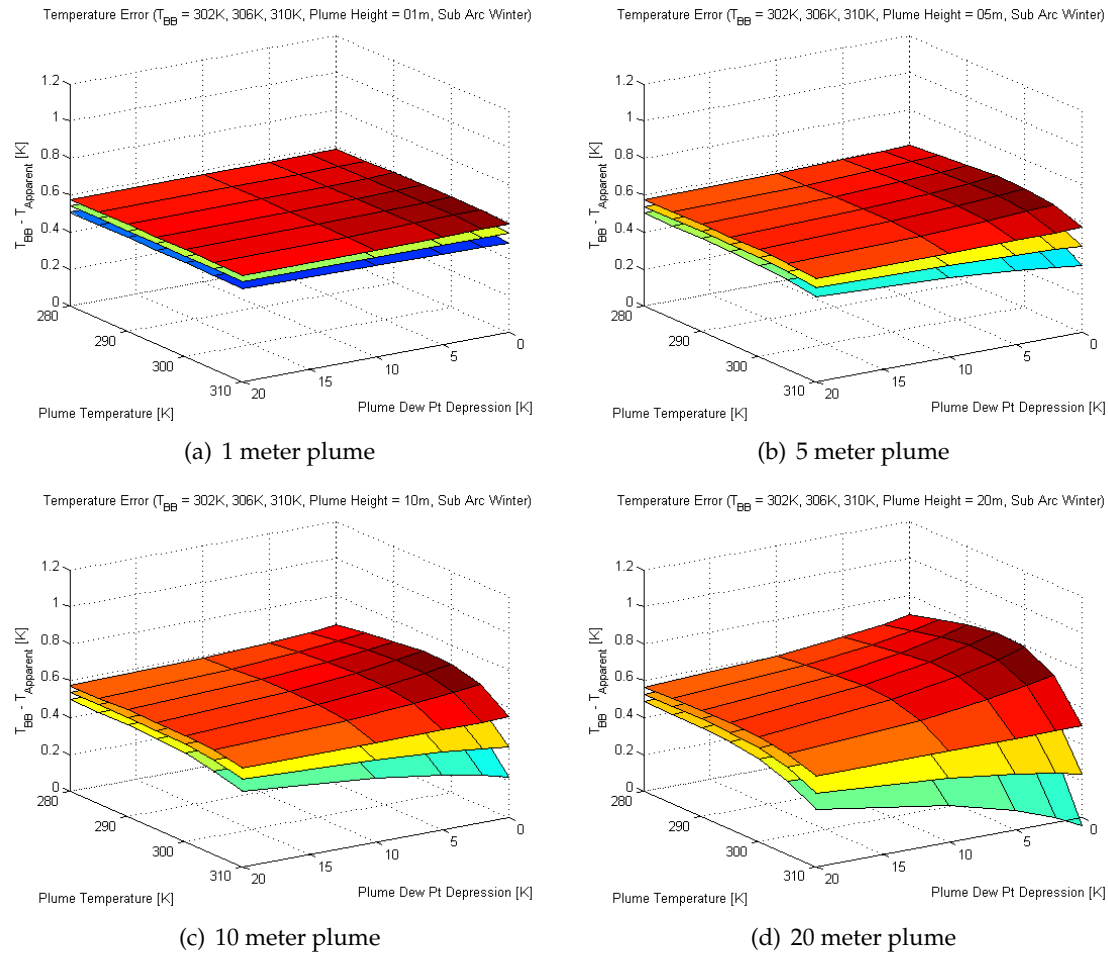


Figure 5.26: Errors between material blackbody temperature and the sensor derived apparent temperature. The surfaces are for material blackbody temperatures of 310 K, 306 K, and 302 K from top to bottom in each plot.

Several trends are apparent in the plots. By visual inspection, the material blackbody temperature has the greatest influence on the temperature error, followed by the ambient atmospheric conditions, and then the plume. In general, the target blackbody temperature and the ambient atmospheric conditions affect the overall magnitude of the temperature errors (magnitude of the surfaces in Figures 5.25 and 5.26) and the plume influences the shape of the surface.

The material kinetic temperature influences the temperature errors. A greater kinetic temperature for the material results in a higher temperature error. The reason for this trend is apparent from equation (5.7). The temperature error is proportional to the difference between the material blackbody radiance and the sensor-reaching radiance such that,

$$\begin{aligned} T_{error} &\propto L_{BB} - L_{sensor} \\ &\propto L_{BB} - (\tau L_{BB} + L_u) \\ &\propto (1 - \tau) L_{BB} - L_u. \end{aligned} \tag{5.8}$$

A higher blackbody temperature, L_{BB} , would result in a higher radiance. Although the transmission does not change as the blackbody temperature changes, the result of the blackbody radiance multiplied by the transmission is greater for high target temperatures than for low temperatures. The first term is larger for a higher blackbody radiance than for a lower blackbody radiance. The sensor radiance will therefore also be higher as will the resulting temperature errors.

The effect of the plume becomes apparent as the plume thickness increases, thus increasing the integrated water vapor along the path. There is a competing effect of transmission losses and additive upwelled radiance. The temperature error seems to peak for a plume temperature of 295 K to 300 K at a dew point depression of 0 K (saturated). The minimum temperature error occurs for the highest set plume temperature of 310 K and a dew point depression of 0 K. The range of temperature errors increase as the plume thickness increases.

Finally the overall temperature errors are greater under mid-latitude summer conditions than for sub-arctic winter conditions. A mid-latitude summer atmosphere is warmer and contains a greater amount of water vapor which leads to a decreased transmission and increased upwelled radiance. However, the transmission loss has a greater effect than the upwelled radiance in this case which results in increased temperature errors. Conversely,

a sub-arctic winter atmosphere is much drier and colder. The transmission values are higher and the upwelled radiance is less for this atmosphere. The combined effect is a lower temperature error.

The result of this analysis reveals that knowledge of the water vapor content in the target-to-sensor path is very important to accurately derive the temperature of the MDCT. There is a competing effect of transmission loss and additive upwelled radiance. In general, the temperature errors are higher for a thicker plume and when the ambient conditions are warmer and wetter. The target's blackbody temperature also affects the temperature errors such that a higher blackbody temperature results in a higher temperature error.

5.2.2 MODTRAN Simulation of MDCT Exhaust Plume

The effect of the plume is not immediately apparent from the plots in Section 5.2.1. This indicates that the influence of the plume becomes less significant with increasing sensor altitude compared to the effects of the ambient atmosphere. In order to isolate the effects of the plume, the MODTRAN simulations were modified so that the sensor altitude equals the plume height. In this scenario, the target-to-sensor air column consists of only the water vapor plume. As with the previous simulations, a standard atmosphere is first assigned to the air column. The air temperature and the dew point depression in the air column were varied in the same fashion as the original MODTRAN simulations. The plume/sensor height was set to values of 1, 5, 10, 20, 50, and 100 meters in order to span the range of physically realistic plume heights. Blackbody target temperatures of 302, 306, and 310 Kelvin were also used. Table 5.4 lists the parameter values for these simulations. The difference between the target blackbody temperature and the apparent temperature from a 8 - 14 μm broadband sensor for each combination of parameter values were observed. The results are shown in Figures 5.27 and 5.28.

Blackbody Temp. [K]	Plume Height [m]	Plume Air Temp. [K]	Plume Dew Pt. Depression [K]	Ambient Conditions
302	1	280	0	mid-latitude summer sub-arctic winter
306	5	285	2	
310	10	290	5	
	20	295	10	
	50	300	20	
	100	305		
		310		

Table 5.4: Parameter values for the plume-only MODTRAN simulations.

Mid-Latitude Summer Conditions

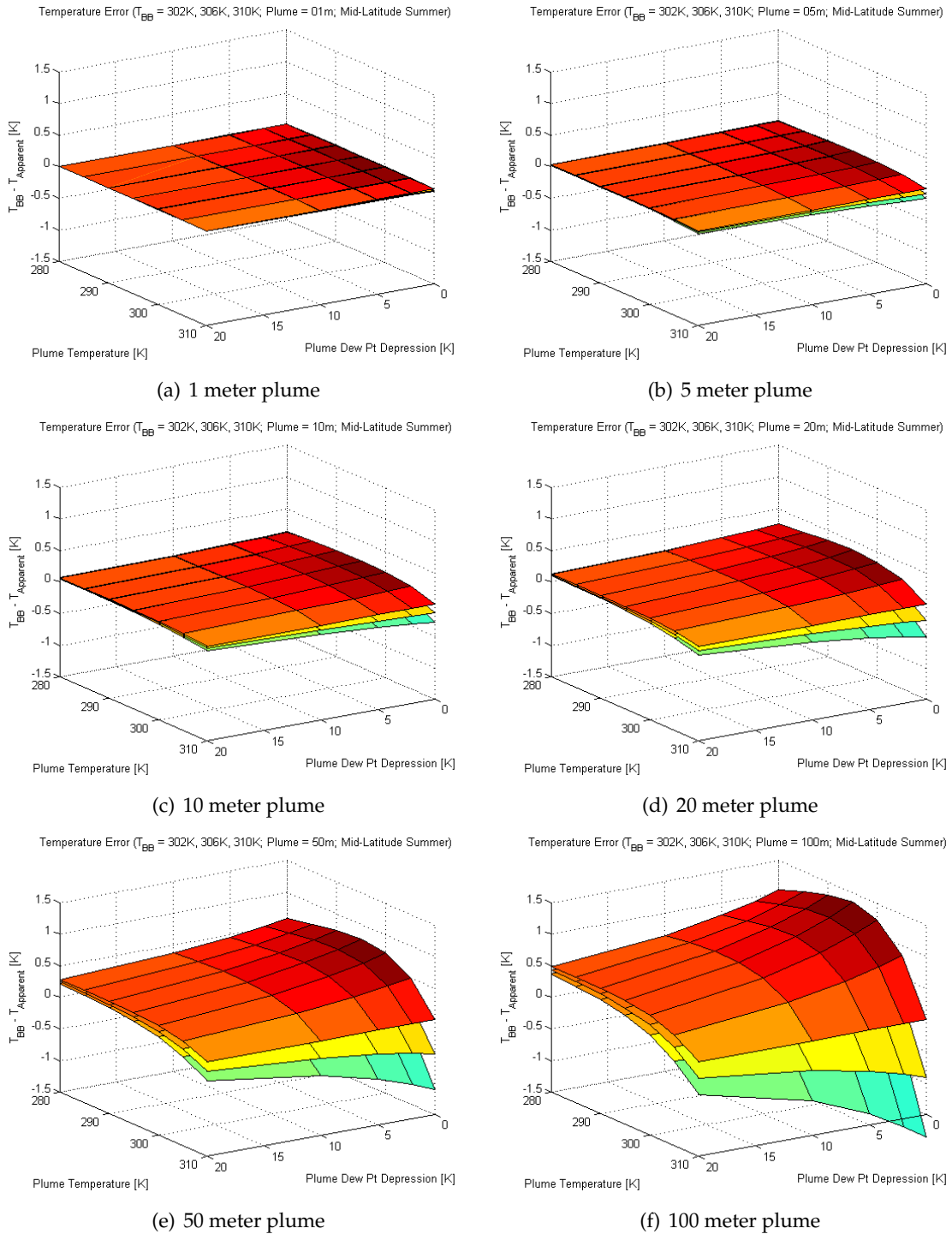


Figure 5.27: Errors between material blackbody temperature and the sensor derived apparent temperature. The surfaces are for material blackbody temperatures of 310 K, 306 K, and 302 K from top to bottom in each plot.

Sub-Arctic Winter Conditions

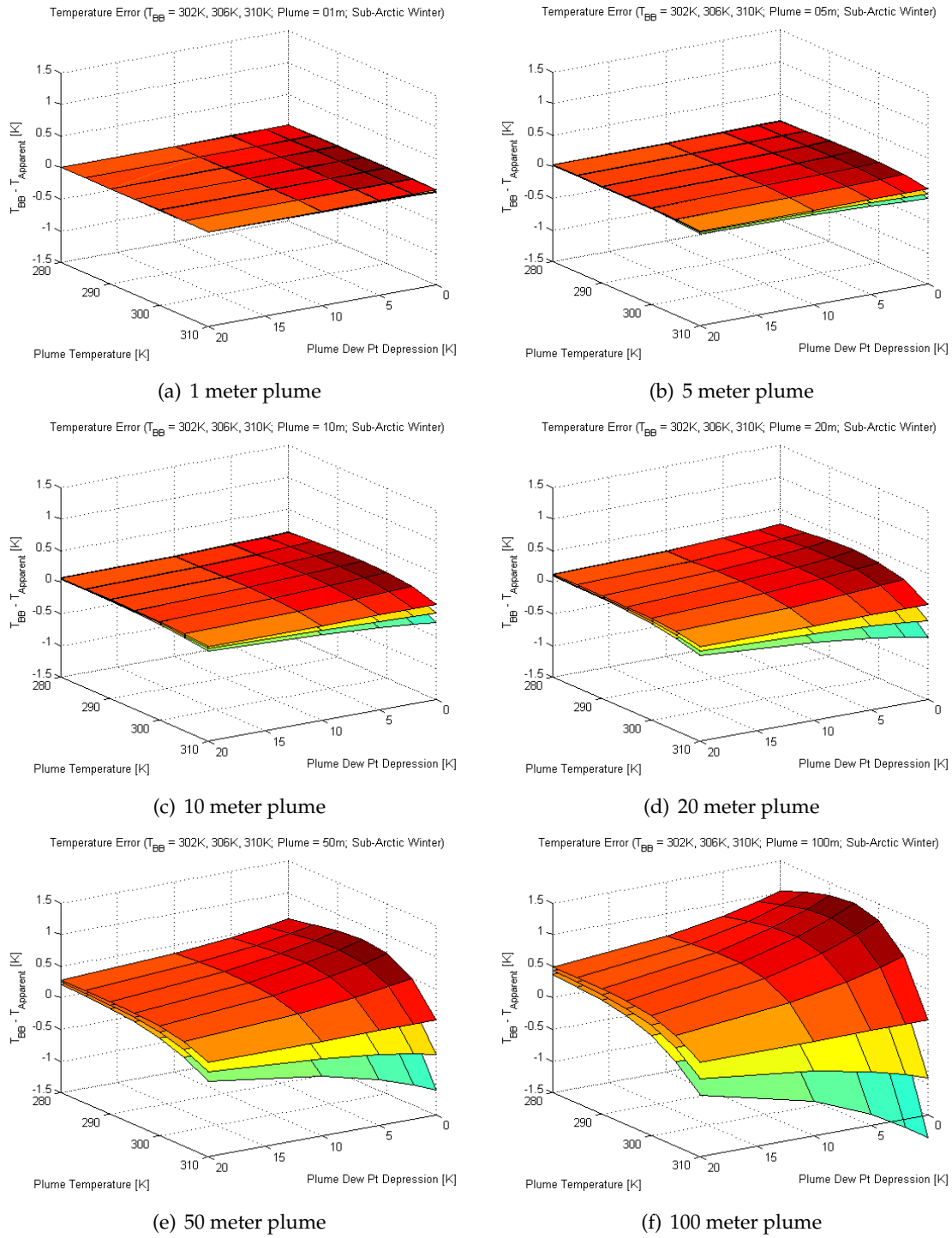


Figure 5.28: Errors between material blackbody temperature and the sensor derived apparent temperature. The surfaces are for material blackbody temperatures of 310 K, 306 K, and 302 K from top to bottom in each plot.

The effect of the plume is apparent in that it affects the shape of the plot. There is a competing effect of transmission losses and additive upwelled radiance. The largest temperature errors occur for a plume temperature of 290 K to 295 K and for a temperature of 310 K with a dew point depression of 0 K (saturated). The absolute magnitude of the errors increase as the plume height increases. The maximum temperature errors introduced by plumes with heights of 1, 5, 10, 20, 50, and 100 meters are approximately ± 0.03 , ± 0.1 , ± 0.2 , ± 0.4 , ± 0.8 , and ± 1.4 Kelvin, respectively. The blackbody target temperature along with the plume air temperature and dew point depression determine whether the additional temperature error introduced by the plume is less than or greater than zero. Finally, the ambient atmospheric conditions appear to have an insignificant effect on the temperature errors.

To provide a context for the error introduced by the plume, it is compared to a typical residual error after a standard atmospheric compensation method. For example, Qin *et al.* (2001) used the Landsat TM thermal band to retrieve desert land surface temperatures [24]. The authors used in situ atmospheric profile data that was coincident with the satellite pass to compensate for the atmosphere. The resulting temperature errors were approximately 1.1 K. When in situ atmospheric data is not available, a multi-channel approach can be used. Using such a dual-channel method, the algorithm presented by Prata (1993) yielded land surface temperatures to within ± 1.5 K for flat terrain with uniform surface composition in relatively dry atmospheres [26]. These temperature errors are several times the temperature errors introduced from plumes with heights of zero to 20 meters. However, 50 and 100 meter high plumes will introduce errors roughly the same as the residual errors of the atmospheric compensation methods mentioned. The temperature error caused by the plume can also be compared to the temperature error due to uncertainties in the surface emissivity. Dash *et al.* (2002) points out that for mid-latitude vegetated areas, for example, an emissivity error of ± 0.025 results in a land surface temperature error of ± 2 K when a single channel is used [23].

From these studies, it appears that the temperature error introduced by plumes with heights less than about 20 meters is roughly an order of magnitude less than the magnitude of the residual errors from the aforementioned atmospheric compensation techniques and sensitivity of surface emissivity. The additional temperature errors caused by the plume will become significant as the plume height reaches approximately 50 meters and greater.

5.2.3 Sensitivity of Plume Gradient

In an MDCT, the air mass inside the tower between the drift eliminators and the fan stack opening is assumed to be at a homogeneous temperature. The initial air temperature of the plume in the tower throat is therefore assumed to be at the same temperature as the internal air. Since the tower operates through evaporative processes, the initial dew point depression of the plume is assumed to be very close to zero. As the plume rises and travels downwind, it will diffuse within the ambient air. The plume air temperature will gradually cool and the moisture content will decrease. Therefore, there will be a temperature and moisture gradient along the line-of-sight of the sensor through the plume. The gradient in the plume is of interest since it may affect the derived apparent temperature of the cooling tower. A perfect atmospheric compensation is assumed to have been performed on the image. This compensation essentially removes the atmospheric effect along the line-of-sight path from the sensor down to the edge of the plume. This "edge" of the plume is not well defined since the diffusion of the plume is a gradual process. The edge will be dependant on the functional form of the gradient in the plume.

To investigate this "edge" problem further, several gradients were modeled using the MODTRAN software. The purpose of this study was to determine the effect of various plume air temperature and dew point temperature gradients. A user-defined atmospheric profile was created in MODTRAN. The air temperature and dew point temperature at the first level (ground) was set to 295.0 K. A sensor covering the 8 to 14 μm spectral range was placed at an altitude of 20 meters. This altitude represents the "top" of the plume. In other words, in a real scene, it is assumed that an atmospheric compensation has been performed that removes the atmospheric effect from the sensor to the "top" of the plume (the "top" being 20 meters in this case). The temperature gradient in the intervening levels determines how the air temperature and dew point temperature changes from the initial temperature at the surface to the ambient temperature and dew point at the "top" of the plume. For this study, the ambient air temperature was 290 K and the ambient dew point temperature was 285 K. Three different gradients were investigated. The first profile followed a Gaussian function in which the maximum value of the Gaussian is the initial temperature. The temperature gradually decreases to the ambient temperature as the height increases. The standard deviation of the Gaussian was 10 meters. The top of the plume (20 meters) is defined as two standard deviations. The second profile was a Step function in which the temperature remained constant at the initial temperature up to a height of 10 meters, and then dropped suddenly to the ambient temperature for heights

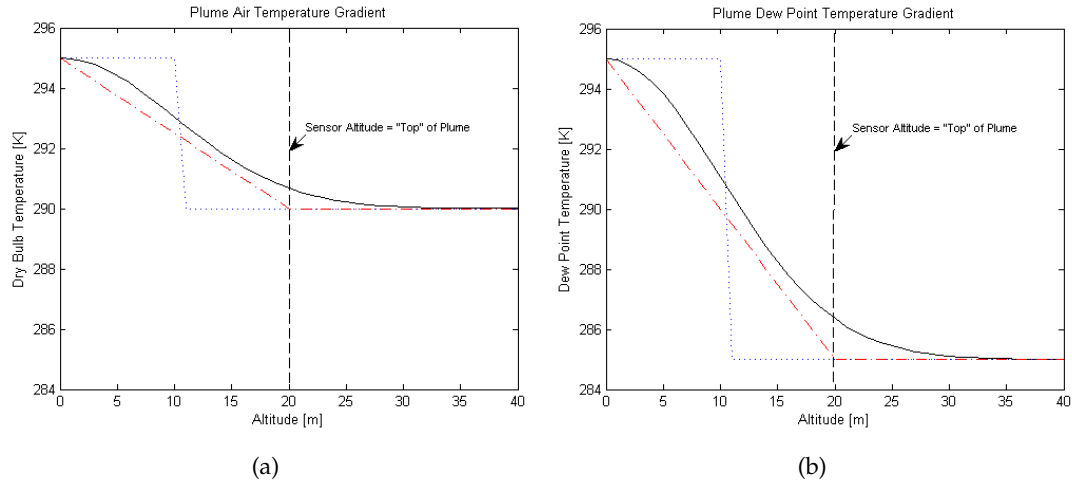


Figure 5.29: Linear, Step, and Gaussian temperature gradients modeled in MODTRAN. Air temperature (a) and dew point temperature (b). The sensor altitude is marked at 20 meters..

greater than 10 meters. The last profile was a linear gradient in which the temperature decreased linearly from the initial temperature at zero meters to the ambient temperature at 20 meters. Figure 5.29 illustrates the three gradients used in the simulation.

For each profile, the spectral transmission and spectral upwelled radiance was computed in MODTRAN. Recall that the initial temperature of the plume equals the internal temperature of the MDCT. The tower cavity is modeled as a blackbody with a temperature of 295 K. The sensor-reaching radiance is computed through equation (5.7). The spectral radiance was then multiplied with the spectral response of the sensor to arrive at an integrated radiance value. For this analysis, a broadband sensor with a spectral response of unity between 8 and 14 μm was used. This band radiance is converted into an apparent temperature. A temperature error metric is defined as the difference between the apparent temperature at the sensor and the internal temperature (also the initial plume temperature) of 295 K.

The resulting temperature errors for the Gaussian, step, and linear gradients are shown in Table 5.5. Plume lengths of 20, 50, and 100 meters were simulated. These results indicate

Plume Length	Gaussian	Step	Linear
20 m	-0.0269 K	-0.0245 K	-0.0317 K
50 m	-0.0637 K	-0.0607 K	-0.0744 K
100 m	-0.1162 K	-0.1121 K	-0.1350 K

Table 5.5: Apparent temperature errors for three plume gradient functions and for three plume lengths.

that the error which occurs is independent of gradient type. The Gaussian gradient, however, is believed to be more representative of actual plume scenarios.

The conclusion of this study is that the effect of the MDCT exhaust plume will be modeled using the MODTRAN software. The initial air temperature of the plume will be equal to the selected internal temperature of the tower. The initial dew point depression of the plume will be zero to indicate a saturated water vapor plume. The air temperature and dew point temperature gradient will follow a Gaussian function in which the plume length is defined as two standard deviations from the tower opening. The air temperature of the plume will approach the ambient air temperature as the distance from the tower throat increases. Similarly, the dew point temperature will approach the ambient dew point temperature as the distance from the opening increases. The plume parameters that will be varied in the MDCT target space are the initial plume temperature (the internal MDCT temperature), the plume length, the ambient air temperature, and the ambient dew point temperature.

5.2.4 sensor-reaching Radiance Summary

The atmosphere greatly affects the derived temperature at the sensor. For an MDCT, the target-to-sensor air column consists of an additional water vapor plume. The air temperature, moisture content, and path length through the plume are all parameters that influence the transmission and upwelling radiance of the plume. The ambient atmosphere also influences the signal at the sensor for the reasons discussed in Section 3.4.2. The atmospheric effects become more apparent as the observation altitude increases. Accurate atmospheric compensation of the recorded signal is key to determine the temperature of an MDCT. In general, for a moderately sized plume of approximately 10 to 20 meters in height, the temperature error introduced by the plume is smaller than the residual error from standard atmospheric compensation techniques (see Section 4.2.1).

5.3 Approach

The studies discussed to this point in this chapter allow constraints to be placed on the parameters listed in Figure 2.8. The construction materials of an MDCT were found to be relatively specular and to have relatively high emissivities in the LWIR. Due to the geometry of the tower, a photon is likely to undergo approximately three internal reflections before escaping the tower. These properties indicate that the radiance originating from deep in the tower cavity will be the blackbody radiance of the internal tower surfaces. This means that the tower cavity has an effective emissivity of unity. Radiances from shallow portions of the tower, such as the fan blades and throat, will not be the blackbody radiance. This means that the effective emissivity of these surfaces is less than unity since their actual emissivity is less than unity, there is a greater amount of reflected downwelling sky radiance, and there is not more than one reflection off these surfaces. These conclusions imply that the ground sampling distance (GSD) of the sensor is important since it will determine whether the “shallow” and “deep” surfaces can be resolved and separated. This was seen in the imagery from Section 2.3 which indicated that the temperature error increased as the GSD increased.

The atmosphere will have a profound effect on the temperature error. The error increases as the observation altitude increases due to the increase in atmospheric path. A warmer and more moist atmosphere will produce a greater temperature error than a cooler and drier atmosphere. This difference is magnified as the observation altitude increases. The atmosphere will introduce the largest error if not accurately accounted for. The exhaust plume of the MDCT also introduces an error in the derived temperature. Depending on the characteristics of the plume, an additional temperature error as much as ± 1.4 K is introduced by the plume in the extreme case.

Several assumptions are made before beginning the approach. First, only night time imaging will be used. The radiometric effects that occur during the day will not be considered. Second, the internal surfaces of the MDCT and the exit air are assumed to be at the same

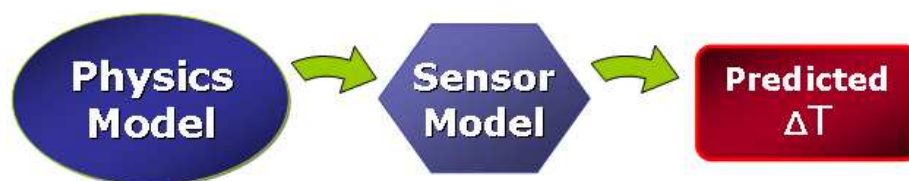


Figure 5.30: Illustration of the procedure to predict the MDCT temperature error.

temperature. The exit air is also assumed to be nearly saturated. Lastly, an atmospheric compensation is assumed to have been performed on the images. Therefore, the effects of the atmospheric column (other than the exhausted vapor plume) are not considered.

5.3.1 Overview

A camera sensitive to the LWIR spectral region (approximately 8 - 14 μm) is used to observe the cooling tower. Each pixel in the resulting thermal image is converted into an apparent temperature, or image-derived temperature. The apparent temperature of pixels inside the fan stack opening of the tower is to be correlated to the exit air temperature. To do so, a 3-D physics model of the radiation transfer is necessary to accurately derive the exhaust air temperature from the thermal image. A sensor model is necessary to derive the apparent temperature of the MDCT from the simulated image for a particular sensor. Finally, a target space is constructed to predict the apparent temperature of the MDCT for a range of model parameters. This target space information will allow a temperature correction factor to be assembled that will be applied to the thermal image to produce an accurate MDCT temperature.

5.3.2 Physics Model

Based on the studies performed in Sections 5.1 and 5.2, a methodology is developed to accurately model the radiance field from the MDCT, through the exhausted plume, and into the sensor. The DIRSIG software developed at RIT and the MODTRAN software developed by the AFRL are used to model the internal and propagated radiometry of the MDCT. The parameters used in these simulations are listed here along with a detailed description of how they will be modeled. Eventually, every combination of parameter values will be used to create a target space (look-up table) that will predict the at-sensor radiance and therefore the necessary temperature correction factor.

5.3.2.1 Tower Leaving Radiance with DIRSIG

The tower-leaving radiance is modeled using DIRSIG. This radiance includes the self-emitted radiance and any reflected radiance from the tower surfaces. The simulation is based on a CAD drawing of an MDCT. Given the results from Section 5.1, a highly detailed CAD model does not appear to be necessary to reproduce the exact radiometry inside the tower. Instead, a simplified drawing derived from that shown in Figure 5.15 will be used. The diagonal internal support structure, water distribution system, and fill was deleted. The exterior surfaces (*i.e.*, the siding and decking) were drawn as plain facets

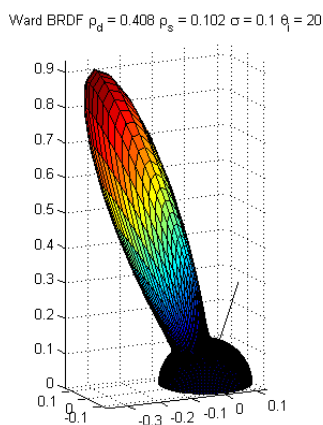


Figure 5.31: Ward BRDF model assigned to the facets in the DIRSIG CAD model.

instead of grooved facets. The siding, decking, and shroud of the drawing were redrawn as double-sided facets so that different temperatures may be assigned to the interior and exterior facets. The drift eliminators are represented by a single blackbody plate as per the results of Section 5.1.4. The geometry of the fan blades and mechanical system will remain unchanged.

The facets of the CAD drawing are assigned a Ward BRDF model. A description of the Ward BRDF was presented in Section 3.2.1.1.2. The diffuse and specular weights of the Ward BRDF model are adjusted to provide a mostly specular reflectance with a small diffuse component. The Ward parameters for this BRDF model are $\rho_d = 0.12$, $\rho_s = 0.03$, and $\sigma = 0.10$. This BRDF shape is consistent with typical MDCT construction materials found in the NEFDS (See Section 5.1.2). Figure 5.31 illustrates the BRDF shape used for the DIRSIG model. The reflectance (DHR) of this BRDF when measured from an angle of 20° is 0.15. Therefore, the emissivity (DHE) is 0.85 through Kirchhoff's law. The measurement angle of 20° was selected to keep the model consistent with the measurements in Sections 5.1.1 and 5.1.2. Every facet in the CAD model except for the drift eliminator blackbody plate was assigned this BRDF.

The DIRSIG simulation provides a spatially and spectrally high resolution tower-leaving radiance. The output image is 110 by 110 pixels that cover the entire fan stack opening and part of the tower deck. The ground sampling distance (GSD) of this high resolution image is 0.05 meters. The spectral extent of the image covers the LWIR wavelength regions at a spectral resolution of one wavenumber.

5.3.2.1.1 DIRSIG Parameters

The list of DIRSIG parameters that will be varied are presented here along with a description of each.

MDCT Internal Temperature is the temperature assigned to the internal facets of the MDCT DIRSIG model. These internal facets include the interior faces of the decking and siding, the drift eliminator plate, the internal tower support structures, the fan support structure, and the fan mechanical structures. This internal temperature is important since it is the desired temperature to be retrieved from the remotely-sensed image.

MDCT External Temperature is the temperature assigned to the exterior facets of the MDCT DIRSIG model. These external facets include the exterior faces of the decking and siding, the fan stack shroud (cowling), and the fan blades. The important external facets for the physics model are the fan blades and the shroud since these objects are in the line-of-sight between the sensor and the tower cavity. The *MDCT external temperature* is set to be less than or equal to the assigned *MDCT internal temperature* (assuming night time imaging only). From the MDCT experimental collection performed at SRS in the spring of 2004 and 2005, the external apparent temperatures appear to be between 0 and 4 Kelvin less than the internal temperature for the nighttime scenes (see Section 2.3).

Fan Blade Emissivity can be adjusted by altering the Ward BRDF model parameters for the fan blade facets. The *fan blade emissivity* parameter is used to scale the magnitude of the BRDF assigned to the fan blades. To do so, a reference Ward BRDF is set in which the diffuse and specular weights were chosen to produce the desired BRDF shape of a mostly specular lobe with a small diffuse component ($\rho_d = 0.0408$ and $\rho_s = 0.0102$). The integral of this BRDF shape yields a DHR of 0.05 for a measurement angle of 20° . To scale the magnitude of this BRDF while maintaining its shape, the diffuse and specular weights are adjusted by

$$[\rho_d, \rho_s] = \frac{1 - \varepsilon_{fan}}{0.05} [0.0408, 0.0102]. \quad (5.9)$$

Effective Sky Temperature is the apparent temperature of the sky computed from the integrated downwelling sky radiance. This is the equivalent blackbody temperature of the sky. It can be computed from a known atmospheric temperature and moisture profile (sounding). The profile is used as input into MODTRAN and the

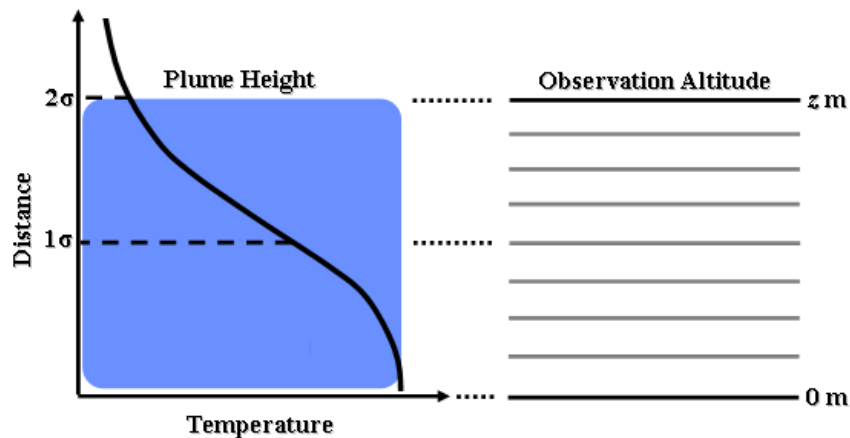


Figure 5.32: Illustration of atmospheric layers in MODTRAN used to model the moisture gradient in the plume.

path radiance from sample points covering the entire sky hemisphere is computed. The downwelling radiance from the computed samples is integrated over the entire sky hemisphere and converted into an apparent temperature. The *effective sky temperature* is used by DIRSIG to compute the thermal downwelling radiance from the sky. This downwelling radiance is necessary since it reflects off the tower facets and therefore becomes a component of the tower-leaving radiance. A utility is provided that calculates the effective sky temperature given an atmospheric sonde profile (See Appendix D).

Sensor Zenith Angle is the view angle of the sensor measured relative to a nadir (down-looking) viewing position of the MDCT. The radiance leaving the tower has an angular distribution. The view angle is important since it determines what features of the tower, such as the tower cavity and shroud side, are visible by the sensor and may therefore be included in the interior radiance field due to optical, mechanical, and atmospheric blurring.

5.3.2.2 Plume Leaving Radiance with MODTRAN

The tower-leaving radiance produced by DIRSIG must now propagate through the exhausted water vapor plume to reach the sensor. The MODTRAN software is used to model the plume. A standard atmosphere is used as the base atmosphere to be modified. A plume layer is then defined that extends from the ground to a height, z . The surface temperature in this profile is assigned the same value that was used for the *MDCT internal temperature* in the DIRSIG model since the assumption is made that the interior MDCT surfaces and the exit air are at the same temperature. Similarly, the surface dew point

depression is set to zero since the assumption is made that the exit air is nearly saturated. The sensor is placed at the height of the plume layer (z) so that the atmospheric effect of the plume is isolated. Figure 5.32 illustrates this layout.

A temperature and moisture gradient established in the atmospheric profile follows a Gaussian function decay. The temperature approaches the ambient air temperature as the height increases. Similarly, the dew point temperature approaches the ambient dew point temperature as the height increases. The height of the plume is defined as the two standard deviations distance of the Gaussian (2σ) as per the results of Section 5.2.3. The MODTRAN simulation provides spectral atmospheric transmission and spectral atmospheric path radiance curves for the same spectral range as the DIRSIG simulation.

5.3.2.2.1 MODTRAN Parameters

The list of MODTRAN parameters that will be varied are presented here along with a description of each.

Ambient Air Temperature is the temperature of the ambient air measured at the surface. This value will be the final temperature the plume approaches.

Ambient Dew Point Temperature is the dew point temperature of the ambient air measured at the surface. This value will be the final dew point temperature of the plume.

Water Vapor Plume Path Length is the effective length of the line-of-site path through the plume. This parameter is estimated by the user based on knowledge of the sensor view angle, air flow through the tower, and wind speed and direction. The plume path length is modeled as the height of the plume layer (z) in the MODTRAN user-defined atmosphere. A utility has been produced to estimate the plume path length if a more sophisticated plume model is not available (See Appendix E).

5.3.2.3 Physics Model Summary

Each spectral pixel in the DIRSIG tower-leaving radiance image is multiplied by wavelength with the spectral transmission data and then added by wavelength to the spectral path radiance from MODTRAN. The result of the DIRSIG and MODTRAN simulations is a sensor-reaching radiance that is spatially and spectrally high resolution. Note that it is assumed that an atmospheric compensation has been performed on the image that removed the effect of the air column from the sensor to the ground. The remaining sources of error to account for are due to the effects of the tower geometry and of the exhausted

plume. Therefore, the result of the DIRSIG and MODTRAN run is essentially a "top of plume" radiance.

5.3.3 Sensor Model

The high spatial and spectral resolution image generated by the physics model represents the radiance reaching the sensor. The sensor will degrade and record the incident radiance as described in Section 3.5. The sensor model accepts sensor specifications from the user and applies those specifications to the high resolution physics model radiance image. An algorithm was written in the Matlab programming environment that processes the high resolution image according to the sensor information provided by the user. Specifically, the spectral response, the GSD, and the radius of the system point spread function are necessary.

The sensor spectral response consists of a vector of wavelengths and a corresponding vector of response weights for a particular spectral band. The algorithm first spectrally samples the radiance images with the supplied spectral response. The spectral response function is resampled to the wavelengths used in the radiance image. The response function and the high resolution image radiance are then multiplied together by wavelength for every pixel and integrated over all wavelengths to arrive at a band integrated image. This new image now consists of a single band but is still spatially high resolution (110 by 110 pixels).

Next, a system point spread function (PSF) (modeled as an Airy disc) whose radius was provided by the user is applied to the image thereby blurring it. The user-supplied radius is in units of microns. If the user does not wish to apply a PSF, the radius should be set to zero. An image of an Airy disc with the proper radius is created that has the same dimensions as the radiance image. To make the computations easier, the Fourier transform of the Airy image and of the radiance image were taken. The transformed images were multiplied together and then the inverse Fourier transform was taken. The result of the PSF application is a blurred image that still consists of 110 by 110 pixels.

Finally, the image must be down-sampled such that the final image has the user required GSD. The GSD of the high resolution radiance image is 0.05 meters. The user-supplied GSD is rounded to the nearest 0.05 meters so that the final GSD is an integer multiple of the original GSD to make the computations easier. The image is then divided into blocks

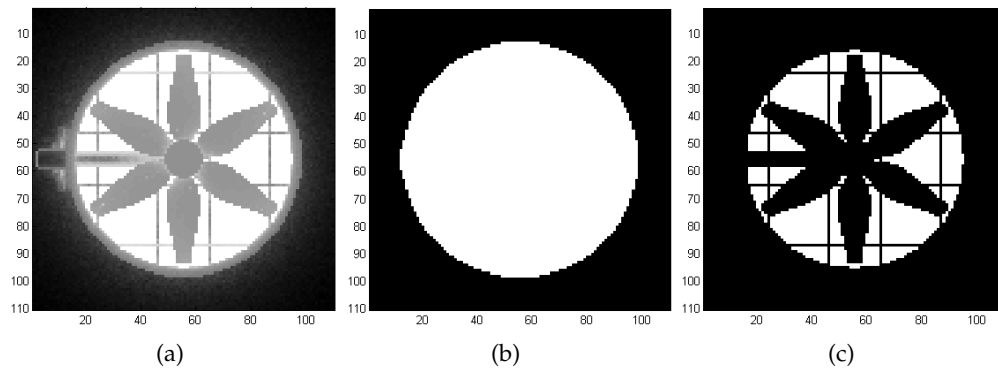


Figure 5.33: High resolution DIRSIG image (a) along with the mixed ROI (b) and cavity-only ROI (c) drawn for sensor angle of 0 degrees. White pixels in the masks indicate pixels that were included in the apparent temperature mean.

whose dimensions are equal to the ratio of the original GSD to the new GSD. The mean value in each block is taken as the value of the corresponding pixel location in the final down-sampled image. For example, if the user required a GSD of 0.1 meters, the original-to-new GSD ratio would be two. Therefore, the image would be divided into 2 by 2 blocks and the mean radiance value in each 2 by 2 block is calculated. The final down-sampled image would be 55 by 55 pixels.

The result of the sensor application is a final down-sampled and band integrated image whose pixel GSD, system blur, and spectral band was specified by the user.

5.3.3.1 Region of Interest - Mixed vs. Cavity

The MDCT apparent temperature may now be derived from the processed images. Two region of interest (ROI) masks were created. The first mask covered the entire fan stack opening. The second mask was carefully constructed to avoid the fan blades and visible support structures so that only the cavity pixels were taken. Figure 5.33 illustrates the high resolution images for a sensor zenith angle of 0 degrees and the mixed and cavity ROIs for the radiance images. The same sensor model used on the high resolution image is also applied to the ROI masks so that the masks fit the processed image.

Recall from Section 5.1.6 that the *fans on* operating state of an MDCT may be modeled from the *fans off* case. Each simulated image contains stationary fan blades. If the *fans on* case is desired, then a mixed ROI should be used.

The mean radiance for the pixels in each ROI is then calculated and then converted into

an apparent temperature. The *predicted temperature error* was defined as the difference between the predicted apparent temperature (*i.e.*, mean ROI apparent temperature) and the assigned *MDCT internal temperature*. The temperature errors were calculated for both the mixed ROI and the cavity-only ROI.

5.3.4 Target Space Look-Up Table

The physics model and the sensor model generate a single simulated thermal image for a given set of parameter values and for a given sensor. The result is a predicted temperature error (temperature correction) for the set of parameter values. To be useful for an image analyst, a temperature correction must be known for any scene. Since the values of each of the eight parameters will probably not be known exactly, the physics model may be run many times with various parameter values. The resulting list of temperature correction factors for each combination of parameter values is known as a target space. This concept is similar to the target space used by Healey and Slater [33] and Ientilucci and Schott [42] for target detection (See Section 4.2.1.8). The target space is essentially a look-up table (LUT) that lists the predicted image-derived apparent temperature for a specific sensor for each combination of parameter values.

5.3.5 Parameterized Model

Multiple regression analysis may be performed on the LUT of temperature corrections (Appendix B). A multiple linear regression equation may be fit to the dataset to arrive at a single multi-parameter equation that predicts the temperature error given a set of parameter values. A multiple linear regression model has the form [43],

$$y_i = \beta_0 + \beta_{i,1} x_{i,1} + \beta_{i,2} x_{i,2} + \dots + \beta_{i,p-1} x_{i,p-1} + \varepsilon_i \quad (5.10)$$

where the β variables are the model-fit coefficients. A relationship between the response variable (the temperature error) and the predictor variables (the target-space parameters) is desired. Since the first target-space parameter, *MDCT internal temperature*, is the ultimate variable that is to be determined, it is not included in the regression model. The model predictors are therefore the other seven parameters.

The least-squares regression equation may be expressed in matrix form as

$$Y = X\beta + \varepsilon. \quad (5.11)$$

The estimated fit coefficients, b , are found by

$$b = (X' X)^{-1} X' Y. \quad (5.12)$$

Therefore, the predicted temperature error, \hat{Y} , is

$$\hat{Y} = X b. \quad (5.13)$$

5.4 Methodology Summary

The problem of determining the exit air temperature of an MDCT is unique due to the geometry of the tower and due to the exhausted water vapor plume. These two factors represent the remaining sources of error in the extracted tower temperature that must be accounted for given that the image has been atmospherically compensated. The studies presented in this chapter investigated the sensitivity of these factors and placed constraints on the variables affecting the derived temperature estimation. The results of those investigations allowed a methodology to be developed to estimate the temperature correction factor that must be applied to a thermal image to remove the effects of the tower geometry and the exhausted plume. The result should be a more accurate estimate of the MDCT exit air temperature.

Chapter 6

Results

The methodology developed in the previous chapter may now be implemented in order to achieve the ultimate goal of deriving a temperature correction factor for an MDCT thermal image. The process yields a LUT of predicted correction factors for each set of model parameters. A parameterized model is then fit to this data set. The parameterized model is tested with simulated data and then applied to the SRNL data set to test its utility with actual image data.

6.1 Physics Model Generation

All eight target space parameters described in Sections 5.3.2.1.1 and 5.3.2.2.1 were varied in this study. The physics model consists of the DIRSIG and MODTRAN simulation tools. The model parameters are listed in Table 6.1 for reference.

Parameter	Modeling Tool
MDCT Internal Temperature	DIRSIG
MDCT External Temperature	DIRSIG
Fan Blade Emissivity	DIRSIG
Effective Sky Temperature	DIRSIG
Sensor Zenith Angle	DIRSIG
Ambient Air Temperature	MODTRAN
Ambient Dew Point Temperature	MODTRAN
Plume Path Length	MODTRAN

Table 6.1: MDCT physics model parameters and associated modeling tools.

UNIX scripts were written to easily change these parameter values in the DIRSIG and MODTRAN models. The values for each parameter were chosen to cover the possible range of values for the datasets presented in Section 2.3. These values are summarized in Table 6.2.

The DIRSIG simulation was set at midnight local time. There was no atmospheric transmission loss or path radiance. Therefore, the DIRSIG simulation represents the tower-

Internal Temp. [K]	External Temp. [K]	Fan ϵ	Sky Temp. [K]	Angle [°]	Ambient Temp. [K]	Ambient Dew Pt. [K]	Plume Length [m]
290	Int. Temp. - 0	0.95	276.15	0	290	Amb. Temp. - 1	5
295	Int. Temp. - 2	0.80	262.40	10	294	Amb. Temp. - 5	10
300	Int. Temp. - 4	0.65	245.97	20	298	Amb. Temp. - 10	20
305			218.62	30			50
			203.09				100

Table 6.2: MDCT parameter values used for the target-space LUT.

leaving radiance. Each run produced a spatially and spectrally high resolution radiance image. The images were 110 by 110 pixels with a GSD of 0.05 meters. There were 746 spectral channels spanning approximately 1425 to 680 wavenumbers at a resolution of one wavenumber. This corresponds to roughly 7.0 to 14.7 μm in wavelength. The MODTRAN simulation produced spectral transmission and path radiance curves for the same spectral range and resolution as the DIRSIG simulations. Midwave infrared wavelengths may be included in the target space if desired by running the DIRSIG and MODTRAN models for the appropriate wavelengths values of interest.

The DIRSIG and MODTRAN simulations were run on the research computing cluster at RIT. The cluster consists of ninety-six 64-bit x86 processor cores running at approximately 3 Ghz. A single DIRSIG simulation runs in roughly 2.5 days on a single core. A single MODTRAN simulation runs in approximately one second on a single core.

6.2 Sensor Model and LUT Generation

There are 32,400 parameter value combinations from those listed in Table 6.2. Therefore there are 32,400 high resolution sensor-reaching radiance images from the physics model. The next step in the method involves processing these high resolution radiance images with the sensor model. The resulting temperature errors can be organized into a LUT of 32,400 entries that lists the temperature error for the mixed and cavity ROI for every combination of target space parameter values.

Statistical analysis was performed on this 32,400 element dataset. The model predictors are the *MDCT external temperature*, the *fan blade emissivity*, the *effective sky temperature*, the *sensor zenith angle*, the *ambient air temperature*, the *ambient dew point temperature*, and the *plume path length* are labeled x_1 through x_7 , respectively. As mentioned previously, the first target-space parameter, *MDCT internal temperature*, is not included in the regression model since it is the ultimate variable that is to be determined. The temperature error for

Label	Physical Term
x_1	MDCT External Temperature
x_2	Fan Blade Emissivity
x_3	Effective Sky Temperature
x_4	Sensor Zenith Angle
x_5	Ambient Air Temperature
x_6	Ambient Dew Point Temperature
x_7	Plume Path Length
y_1	Temperature Error (Mixed ROI)
y_2	Temperature Error (Cavity ROI)

Table 6.3: Regression model parameter labels.

the mixed ROI is labeled y_1 while the cavity ROI is labeled y_2 . The parameter labels are included in Table 6.3 for reference.

To gain confidence in the method, first an ideal sensor is used to produce the temperature error LUT. Then, sensor specifications from an actual sensor is used to generate a LUT.

6.2.1 Ideal Sensor

An ideal sensor was selected for the initial attempt to create the LUT. This sensor causes no spatial degradation of the image. Only a spectral sampling is performed on the high resolution radiance images. The sensor had an ideal spectral response of unity between 8.0 and 14.0 μm with a resolution of 0.3 μm .

The regression analysis was performed on the ideal sensor data in Matlab and the results were confirmed and analyzed for quality using the Minitab statistical software. Following the procedure in Section 5.3.5, the resulting multiple linear regression equation for the mixed ROI temperature error is

$$\begin{aligned} \hat{y}_1 = & -17.2534 - 0.0340224 x_1 + 11.2511 x_2 + 0.0357615 x_3 \\ & - 0.0068026 x_4 + 0.019290 x_5 + 0.001709 x_6 + 0.0023038 x_7. \end{aligned} \quad (6.1)$$

This regression equation predicts the mixed ROI temperature error, \hat{y}_1 , given the seven predictors, x_1 through x_7 .

To investigate the sensitivity of the regression equation, a regression analysis may be performed on standardized variables. Standardization involves transforming a variable so that it has a zero mean and a unit standard deviation [44]. This is accomplished by sub-

tracting the mean from every observation of a variable and then dividing by the standard deviation of the observations. The standardization makes it easier to compare the relative magnitudes of the different regression coefficients since the variables all have a variance of one.

The standardized regression equation for the mixed ROI case is

$$\begin{aligned}\hat{y}_{1s} = & 0.000000 - 0.106243 x_{1s} + 0.738871 x_{2s} + 0.518510 x_{3s} \\ & - 0.040781 x_{4s} + 0.033781 x_{5s} + 0.004510 x_{6s} + 0.043430 x_{7s}.\end{aligned}\quad (6.2)$$

The unstandardized regression coefficients measure the expected change in the response variable, \hat{y}_1 , associated with a one unit change in the predictor variables. Therefore, the standardized regression coefficients measure the expected standard deviation change in the dependent variable associated with a one standard deviation change in the independent variable.

For the mixed ROI standardized regression equation, the *fan blade emissivity* parameter, x_2 , has the highest standardized coefficient which signifies that the temperature error is most sensitive to the fan emissivity. This makes physical sense since for the mixed ROI, the fan emissivity variable affects both the self-emitted radiance of the pixel and also affects the reflected background radiance of the pixel. The *MDCT external temperature* and the *effective sky temperature* parameters, x_1 and x_3 , also have a high standardized coefficient which also makes physical sense since the two parameters represent the self-emitted and the reflected radiance terms of the pixels.

The multiple linear regression equation for the cavity-only ROI temperature error is

$$\begin{aligned}\hat{y}_2 = & 0.67484 - 0.0193120 x_1 - 0.000000 x_2 + 0.00000000 x_3 \\ & - 0.00000000 x_4 + 0.0189788 x_5 - 0.0019372 x_6 - 0.00196813 x_7.\end{aligned}\quad (6.3)$$

This regression equation predicts the cavity ROI temperature error, \hat{y}_2 , given the seven predictors, x_1 through x_7 . The corresponding standardized regression equation for the cavity ROI case calculated in Minitab is

$$\begin{aligned}\hat{y}_{2s} = & 0.000000 - 0.611796 x_{1s} + 0.000000 x_{2s} + 0.000000 x_{3s} \\ & + 0.000000 x_{4s} + 0.337175 x_{5s} - 0.051861 x_{6s} - 0.376387 x_{7s}.\end{aligned}\quad (6.4)$$

For this case, the highest coefficient occurs for the *MDCT external temperature* parameter. Caution must be taken in interpreting this result. Recall that only a spectral integration was performed on the high resolution images. There was no spatial blurring of the images for this study. Unlike for the mixed ROI case, the cavity ROI does not include any pixels from the fan. Therefore, the only influence on the temperature error for the cavity pixel should be due to the plume. The DIRSIG parameters should have coefficients of zero, as the *fan blade emissivity*, the *effective sky temperature*, and the *sensor zenith angle* do. The non-zero coefficient occurs due to the relationship between the *MDCT internal temperature* and the *MDCT external temperature*. Recall from Table 6.2 that the *MDCT external temperature* is always less than or equal to the *MDCT internal temperature*. The non-zero coefficients on the MODTRAN parameters, however, agree with the physical understanding that the plume should be the only influential parameter over the temperature errors in the cavity ROI case.

Finally, the 32,400 observations for each parameter were used as input into the unstandardized regression equations. The root-mean-square (RMS) of the residuals was computed. For the mixed ROI regression equation, the RMS error was 0.767 K. The RMS error for the cavity ROI regression equation was 0.115 K. These RMS values represent an initial estimate of the error in the temperature correction factor.

6.2.2 SC 2000 Inframetrics Sensor

Now that the methodology has been established, the LUT may be generated for an actual sensor, the SC 2000 Inframetrics thermal camera. Recall from Section 2.3 that the SC 2000 was used to obtain LWIR imagery of several MDCT units at SRS. The camera is an un-cooled microbolometer having a 7.6 - 13.5 μm spectral range, an instantaneous field of view (IFOV) of 1.4 milliradians, an accuracy of ± 2 K, and a sensitivity of 0.1 K. The sensor altitude was between 350 and 2000 feet (106.7 and 610 meters) above the ground for the imagery presented in Section 2.3. For this study, the GSD was set to 0.22 m which corresponds to a sensor altitude of 500 feet (Figure 2.4)

The regression equation for the mixed ROI case is

$$\begin{aligned} \hat{y}_1 = & -17.5651 - 0.0340 x_1 + 10.7236 x_2 + 0.0350 x_3 \\ & - 0.0083 x_4 + 0.0223 x_5 + 0.0016 x_6 + 0.0021 x_7. \end{aligned} \quad (6.5)$$

This regression has a calculated RMS error of 0.785 K. Notice that the RMS error is slightly higher in this case than in the ideal sensor case due to the spatial blurring that occurred with this sensor. The standardized regression for the mixed ROI case is calculated as

$$\begin{aligned}\hat{y}_{1s} = & 0.0000 - 0.1090 x_{1s} + 0.7236 x_{2s} + 0.5208 x_{3s} \\ & - 0.0509 x_{4s} + 0.0402 x_{5s} + 0.0044 x_{6s} + 0.0407 x_7.\end{aligned}\quad (6.6)$$

As in the ideal sensor case, the *fan blade emissivity* appears to have the most impact on the predicted temperature error since its standardized coefficient has the highest value.

The regression equation for the cavity ROI case for the SC 2000 is

$$\begin{aligned}\hat{y}_2 = & -6.3753 - 0.0268 x_1 + 4.0693 x_2 + 0.0136 x_3 \\ & - 0.0054 x_4 + 0.0220 x_5 - 0.0006 x_6 - 0.0004 x_7.\end{aligned}\quad (6.7)$$

The RMS error for this regression is 0.355 K. This RMS is similarly higher than in the ideal sensor case since spatial blurring occurs. The corresponding standardized form of this equation is

$$\begin{aligned}\hat{y}_{2s} = & 0.0000 - 0.2117 x_{1s} + 0.6769 x_{2s} + 0.4983 x_{3s} \\ & - 0.0826 x_{4s} + 0.0976 x_{5s} - 0.0040 x_{6s} - 0.0171 x_7.\end{aligned}\quad (6.8)$$

Unlike the ideal sensor case, the DIRSIG coefficients for the SC 2000 LUT are non-zero. This is due to the spatial blurring that occurs with the SC 2000 sensor and blurring due to the atmosphere. The spatial blurring causes radiance from non-cavity pixels to be included in the cavity-only pixels and therefore alters the temperature estimate for these pixels.

6.2.2.1 SC 2000 Random Dataset

A set of 1944 random physics model runs were generated and processed using the SC 2000 sensor parameters. Each parameter value was randomly chosen from the range of the values of that parameter in the LUT (Table 6.2). The 1944 point random dataset was used with the regression equations for the SC 2000 sensor and the RMS errors between the actual temperature error for each random run and the predicted error from the regression were calculated. The parameter values used in the random dataset are listed in Table 6.4.

Internal Temp. [K]	External Temp. [K]	Fan ε	Sky Temp. [K]	Angle [°]	Ambient Temp. [K]	Ambient Dew Pt. [K]	Plume Length [m]
304.3	Int. Temp. - 2.1	0.79	235.60	27.7	293.2	Amb. Temp. - 1.7	89.9
293.5	Int. Temp. - 0.4	0.66	248.10	22.1	297.5	Amb. Temp. - 6.3	10.5
299.1	Int. Temp. - 1.0	0.90	260.90	5.3			

Table 6.4: MDCT random parameter values

The corresponding LUT for these random runs were used as input for the SC 2000 regression equations (6.5) and (6.7). The RMS error for the mixed ROI data is 0.381 K while the RMS error for the cavity ROI data is 0.224 K which both indicate that the method performs quite well for simulated data.

6.3 SRNL Data Set

The parameterized model can now be used to derive temperature corrections for the SRNL imagery from Section 2.3. There are several issues with the data that must be addressed before proceeding. Once these issues are understood, the images may be corrected using the parameterized model to obtain the desired exit air temperature of the MDCTs. The images in the data set are shown in Figure 6.1 for reference.

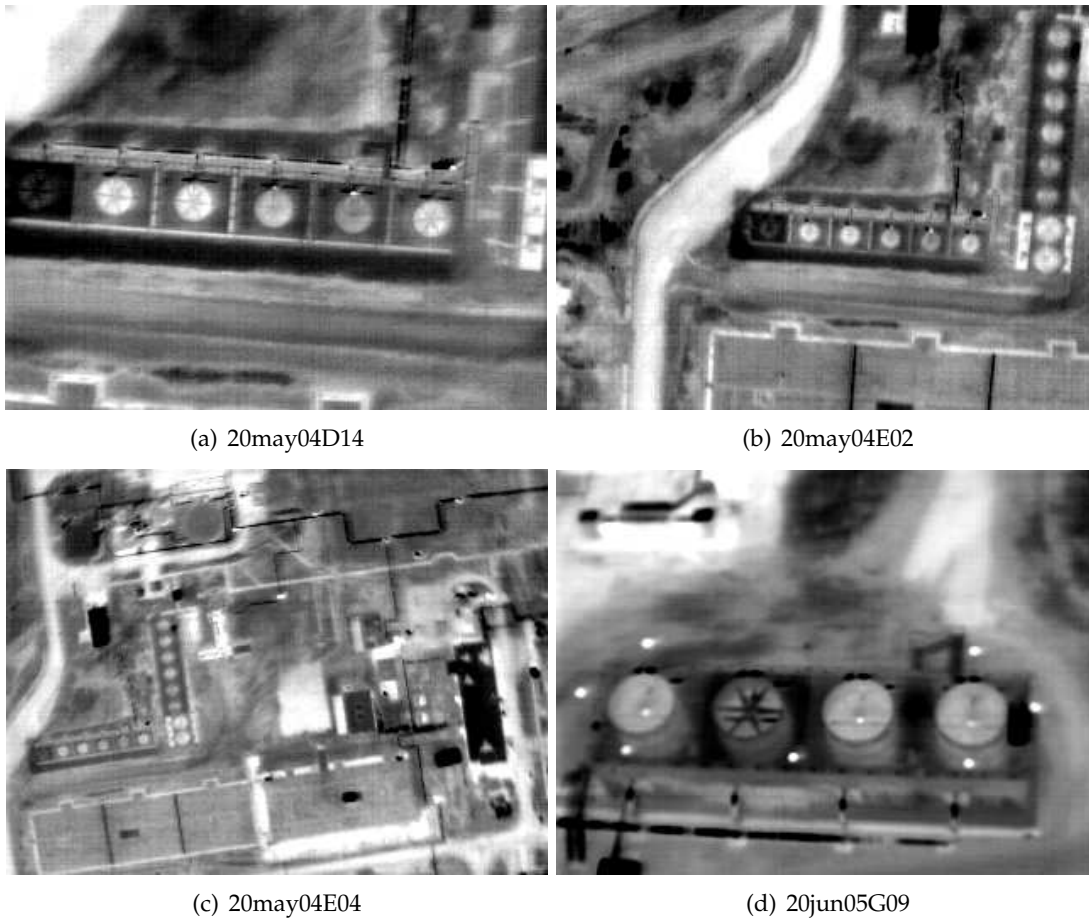


Figure 6.1: SRNL data set LWIR images.

6.3.1 Understanding the SRNL Data Set

The images and associated ground measurements in Section 2.3 have many unknown variables that must be examined. These variables include aspects of the ground measurements, the atmosphere, and the sensor.

First, the collection of simultaneous ground truth measurements is a very difficult task in general. Recall from Section 2.3 that a temperature measurement was obtained of the air exiting the fan stack. The measurement was made about two feet inside the edge of the fan stack shroud for each tower. The exit air temperature is the desired temperature that is to be determined from the thermal image. This measurement represents the only ground truth of the desired target. Ideally, several measurements of the exit air temperature would have been obtained at several places in the fan stack opening to determine any spatial variation to the exit air temperature. The uncertainty in the ground temperature measurement can be estimated as ± 0.4 K. This is based on measured accuracies for similar temperature measurement technologies. In addition, one of the predictor variables of the parameterized model is the *MDCT external temperature*. This is the temperature of the surrounding deck material. No ground-truth temperature measurements are available for the decking.

Another non-characterized aspect of the ground measurements is the atmospheric state. A meteorological station recorded ambient air temperature, dew point temperature, and wind velocity data approximately five meters away from the tower units. These environmental conditions recorded at this location are not exactly the same as those directly next to the towers. Ideally, several measurements would be obtained around the direct perimeter of the towers. Wind measurements would be taken directly at the fan stack opening to infer the exact direction of the exhausted plume. A more significant problem is the lack of atmospheric profile information. Such information is necessary to correct the images for the atmospheric effects of path transmission and path radiance.

In addition to environmental variables, there are uncertainties in the sensor used to collect the images. As mentioned previously, the SRNL images were obtained with a SC 2000 Inframetrics camera. The detector size and field of view are known fairly well so that the GSD can be calculated accurately. However, the exact spectral response of the camera is unknown. Information from the manufacturer lists the spectral response as between 7.6 and 13.5 μm . Since the exact response in this wavelength region is not available, an as-

sumption is made that the response is unity between 7.6 and 13.5 μm and is zero outside this region. Furthermore, the images are in terms of apparent temperature at the sensor. Ideally, the image would have been kept in terms of radiance at the sensor to eliminate any errors associated with converting radiance to temperature. The manufacturer reports a temperature accuracy of ± 2 K and a thermal sensitivity of 0.1 K. The thermal sensitivity is the precision level of the camera (*i.e.*, image temperatures are reported to one decimal place). The accuracy value is a measure of the sensor noise. The value of ± 2 K can be interpreted as the three standard deviation value (3σ) for a random normal distribution of noise. Therefore, the uncertainty in the camera measurement is ± 0.66 K.

6.3.2 Atmospheric Compensation

Most of the factors discussed in the previous section are already set and cannot be changed. The atmospheric compensation issue, however, is manageable to a certain extent. Although a true atmospheric sounding at the time of image acquisition is not available, the atmospheric profile can be interpolated from nearby radiosonde stations. These radiosonde profiles must be spatially and temporally interpolated to estimate the profile at SRS at the time of image acquisition. The five surrounding radiosonde locations are listed in Table 6.5.

Each radiosonde profile contains measurements of the atmospheric pressure, air temperature, and dew point temperature at various pressure levels. The measurement altitude is calculated from the atmospheric pressure through the hydrostatic equation and the ideal gas equation [12]. The radiosonde measurements are not taken at regular altitude intervals. Therefore, each radiosonde profile is first interpolated to regular altitude intervals. Next, a temporal interpolation is performed. Each radiosonde location contains a profile before and after the time of image acquisition. A linear interpolation is performed to calculate the atmospheric profile for each of the five locations for the time of image acquisition. The next step is a spatial interpolation. A weighted average of the five radiosonde station profile is taken to calculate the atmospheric profile at SRS. The weights are based

Station ID	Location	Latitude/Longitude/Altitude	Distance to SRS
72206	Jacksonville, FL	30.50° / -81.70° / 9.0 m	308.74 km
72208	Charleston, SC	32.92° / -80.02° / 15.0 m	157.82 km
72214	Tallahassee, FL	30.45° / -84.30° / 53.0 m	401.52 km
72215	Peach Tree City, GA	33.35° / -84.57° / 244.0 m	271.15 km
72317	Greensboro, NC	36.07° / -79.95° / 270.0 m	345.52 km

Table 6.5: Radiosonde station information for the radiosonde profiles used to atmospherically compensate the SRNL images.

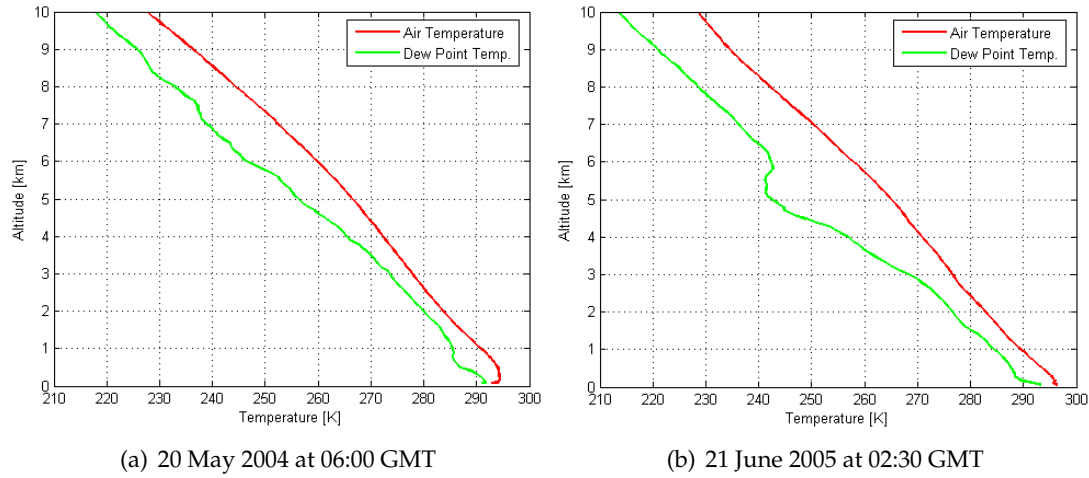


Figure 6.2: Interpolated atmospheric profiles used in MODTRAN to correct the SRNL images. These profiles are linearly interpolated both spatially and temporally from five radiosonde stations near SRS.

on the distance of each station to SRS as listed in Table 6.5. Finally, a surface correction is performed on the temporally and spatially interpolated profile for SRS. A meteorological station recorded the ambient air temperature and ambient dew point for the scenes in Section 2.3. The atmospheric pressure, air temperature, and dew point temperature of the surface level for the interpolated profile is replaced with the actual measurements obtained from the SRS meteorological station. The interpolated profiles for the SRS scenes are shown in Figure 6.2.

The spectral transmission and path radiance of this interpolated profile is then calculated in MODTRAN. Following the method in Section 4.2.1.2, the blackbody radiance is calculated for a given temperature and multiplied by wavelength by the spectral transmission and then added to the spectral path radiance. This sensor-reaching radiance is then multiplied and integrated with the spectral response function of the sensor to arrive at an integrated band radiance which is expressed as an apparent temperature. A LUT is generated that relates a range of possible surface blackbody temperatures to at-sensor apparent temperatures. The apparent temperature at the sensor can then be converted to an apparent temperature at the surface through the LUT. Note that the surface apparent temperature does not take into account any emissivity effects.

This procedure was applied to the SRNL images from Section 2.3. The mean temperature for both the mixed ROI and the cavity-only ROI was corrected for atmospheric effects. An ROI drawn on the decking of each tower was also corrected to remove these atmospheric effects. This deck ROI temperature will be used in the regression model since an

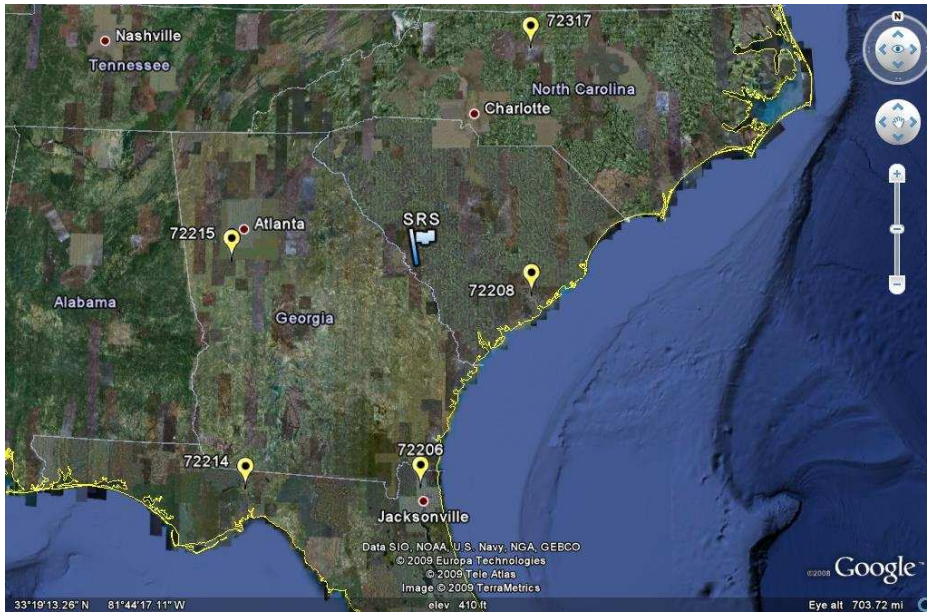


Figure 6.3: Radiosonde station locations shown relative to SRS. Graphic taken from Google™ Earth.

actual ground measurement of the deck is not available. It is important to note that the uncertainty in the atmospheric correction may range from ± 0.6 K to as high as ± 1.1 K, depending on the atmospheric conditions [45].

The raw image temperatures for the mixed, cavity, and decking ROI and their associated atmospherically-corrected values for each tower are listed in Tables 6.6 through 6.9. The ROI temperature is written as the mean value in the ROI \pm the standard deviation of the values in the ROI. The standard deviation of the ROI values will be used as a measure of the uncertainty in the ROI temperature.

ID	Image ROI Temperature [K]			Atm-Corrected ROI Temperature [K]		
	Mixed	Cavity	Decking	Mixed	Cavity	Decking
F1	294.96 \pm 0.30	295.26 \pm 0.25	293.23 \pm 0.29	295.04 \pm 0.33	295.38 \pm 0.28	293.11 \pm 0.32
F2	293.89 \pm 0.25	294.01 \pm 0.22	292.62 \pm 0.21	293.84 \pm 0.28	293.98 \pm 0.25	292.42 \pm 0.23
F3	294.55 \pm 0.31	294.65 \pm 0.27	292.66 \pm 0.31	294.58 \pm 0.35	294.69 \pm 0.30	292.46 \pm 0.34
F4	295.33 \pm 0.32	295.50 \pm 0.29	292.99 \pm 0.28	295.46 \pm 0.36	295.65 \pm 0.33	292.83 \pm 0.32
F5	295.14 \pm 0.38	295.51 \pm 0.25	293.12 \pm 0.33	295.24 \pm 0.42	295.66 \pm 0.28	292.98 \pm 0.36
F6	292.03 \pm 0.28	292.27 \pm 0.18	291.46 \pm 0.23	291.75 \pm 0.31	292.02 \pm 0.20	291.12 \pm 0.26

Table 6.6: Original and the atmospherically-corrected image ROI temperatures for the SRNL 20may04D14 image.

ID	Image ROI Temperature [K]			Atm-Corrected ROI Temperature [K]		
	Mixed	Cavity	Decking	Mixed	Cavity	Decking
F1	294.88 \pm 0.22	294.99 \pm 0.21	293.32 \pm 0.34	294.99 \pm 0.27	295.12 \pm 0.26	293.11 \pm 0.41
F2	293.91 \pm 0.22	294.03 \pm 0.16	292.79 \pm 0.22	293.82 \pm 0.27	293.97 \pm 0.20	292.34 \pm 0.27
F3	294.53 \pm 0.24	294.59 \pm 0.20	292.68 \pm 0.26	294.58 \pm 0.29	294.65 \pm 0.24	292.34 \pm 0.32
F4	295.13 \pm 0.21	295.22 \pm 0.21	293.03 \pm 0.24	295.30 \pm 0.26	295.41 \pm 0.25	292.76 \pm 0.33
F5	295.13 \pm 0.26	295.28 \pm 0.18	293.18 \pm 0.25	295.29 \pm 0.31	295.48 \pm 0.22	292.95 \pm 0.31
F6	292.34 \pm 0.26	292.53 \pm 0.16	291.86 \pm 0.13	291.93 \pm 0.32	292.16 \pm 0.19	291.35 \pm 0.16

Table 6.7: Original and the atmospherically-corrected image ROI temperatures for the SRNL 20may04E02 image.

ID	Image ROI Temperature [K]			Atm-Corrected ROI Temperature [K]		
	Mixed	Cavity	Decking	Mixed	Cavity	Decking
F1	294.82 \pm 0.14	294.83 \pm 0.14	293.38 \pm 0.23	295.07 \pm 0.19	295.09 \pm 0.18	293.18 \pm 0.31
F2	293.88 \pm 0.12	293.81 \pm 0.22	293.05 \pm 0.13	293.84 \pm 0.16	293.75 \pm 0.28	292.74 \pm 0.17
F3	294.22 \pm 0.17	294.24 \pm 0.29	293.13 \pm 0.20	294.28 \pm 0.22	294.32 \pm 0.38	292.84 \pm 0.27
F4	294.84 \pm 0.14	294.63 \pm 0.40	293.39 \pm 0.27	295.11 \pm 0.18	294.83 \pm 0.53	293.19 \pm 0.36
F5	294.68 \pm 0.14	294.70 \pm 0.11	293.34 \pm 0.26	294.89 \pm 0.18	294.92 \pm 0.14	293.13 \pm 0.35
F6	292.58 \pm 0.19	292.65 \pm 0.11	292.28 \pm 0.13	292.13 \pm 0.25	292.21 \pm 0.15	291.72 \pm 0.18

Table 6.8: Original and the atmospherically-corrected image ROI temperatures for the SRNL 20may04E04 image.

ID	Image ROI Temperature [K]			Atm-Corrected ROI Temperature [K]		
	Mixed	Cavity	Decking	Mixed	Cavity	Decking
H1	297.56 \pm 0.48	297.81 \pm 0.27	293.88 \pm 0.41	297.32 \pm 0.53	298.00 \pm 0.29	293.68 \pm 0.46
H2	297.70 \pm 0.46	297.86 \pm 0.21	293.86 \pm 0.69	297.88 \pm 0.50	298.06 \pm 0.23	293.65 \pm 0.76
H3	294.59 \pm 1.06	295.80 \pm 0.49	292.37 \pm 0.20	294.45 \pm 1.17	295.79 \pm 0.54	292.01 \pm 0.22
H4	297.45 \pm 0.54	297.64 \pm 0.29	293.70 \pm 0.44	297.60 \pm 0.60	297.81 \pm 0.31	293.48 \pm 0.49

Table 6.9: Original and the atmospherically-corrected image ROI temperatures for the SRNL 20jun05G09 image.

6.3.3 Actual Temperature Errors

The actual temperature error between the image-derived temperature and the measured ground-truth can now be re-calculated for the atmospherically compensated images. The exit air temperature, T_{ex} , of the towers is the desired temperature to be retrieved. The temperature error is defined as the difference between the image mean ROI temperature and the recorded exit air temperature. The uncertainty in the temperature error can be calculated from uncertainties in the ROI temperature, the sensor measurement, the atmospheric compensation, and the measured exit air temperature. The uncertainties in all these factors are listed in Table 6.10.

Variable	Uncertainty
Ground measurement	± 0.4 K
ROI temperature	\pm (ROI St. Dev.) K
Sensor measurement	± 0.66 K
Atmospheric compensation	± 0.6 K - ± 1.1 K

Table 6.10: Temperature uncertainties in the measured ground, ROI, sensor, and atmospheric variables

The square of the uncertainty in the temperature error can be found by summing the squares of the uncertainties in the exit air measurements, the ROI temperatures, the atmospheric compensation, and the sensor measurement assuming that each term is independent. This can be written as

$$\delta T_{error}^2 = \delta T_{ROI}^2 + \delta T_{atm}^2 + \delta T_{sensor}^2 + \delta T_{ex}^2. \quad (6.9)$$

This method of calculating the uncertainty in the temperature error is described in Appendix C.

The actual temperature errors and their associated uncertainties for each operating tower in each image are listed in Tables 6.11 through 6.14. All of the uncertainties from Table 6.10 where taken into account. The operating towers are those in which water is flowing (*i.e.*, *water on, fans on* or *water on, fans off*).

ID	T_{ex} [K]	Mixed ROI [K]	Cavity ROI [K]	Mixed ΔT [K]	Cavity ΔT [K]
F1	295.55 ± 0.40	295.04 ± 0.33	295.38 ± 0.28	-0.51 ± 1.03	-0.17 ± 1.02
F2	294.25 ± 0.40	293.84 ± 0.28	293.98 ± 0.25	-0.41 ± 1.02	-0.27 ± 1.01
F3	294.75 ± 0.40	294.58 ± 0.35	294.69 ± 0.30	-0.17 ± 1.04	-0.06 ± 1.02
F4	295.65 ± 0.40	295.46 ± 0.36	295.65 ± 0.33	-0.19 ± 1.04	0.00 ± 1.03
F5	296.75 ± 0.40	295.24 ± 0.42	295.66 ± 0.28	-1.51 ± 1.06	-1.09 ± 1.02

Table 6.11: Temperature errors between the atmospherically-corrected mean ROI temperature and the measured ground-truth exit air temperature for the SRNL 20may04D14 image.

ID	T_{ex} [K]	Mixed ROI [K]	Cavity ROI [K]	Mixed ΔT [K]	Cavity ΔT [K]
F1	295.55 ± 0.40	294.99 ± 0.27	295.12 ± 0.26	-0.56 ± 1.01	-0.43 ± 1.01
F2	294.25 ± 0.40	293.82 ± 0.27	293.97 ± 0.20	-0.43 ± 1.01	-0.28 ± 1.00
F3	294.75 ± 0.40	294.58 ± 0.29	294.65 ± 0.24	-0.17 ± 1.02	-0.10 ± 1.01
F4	295.65 ± 0.40	295.30 ± 0.26	295.41 ± 0.25	-0.35 ± 1.01	-0.24 ± 1.01
F5	296.75 ± 0.40	295.29 ± 0.31	295.48 ± 0.22	-1.46 ± 1.03	-1.27 ± 1.00

Table 6.12: Temperature errors between the atmospherically-corrected mean ROI temperature and the measured ground-truth exit air temperature for the SRNL 20may04E02 image.

ID	T_{ex} [K]	Mixed ROI [K]	Cavity ROI [K]	Mixed ΔT [K]	Cavity ΔT [K]
F1	295.55 ± 0.40	295.07 ± 0.19	295.09 ± 0.18	-0.48 ± 1.00	-0.46 ± 0.99
F2	294.25 ± 0.40	293.84 ± 0.16	293.75 ± 0.28	-0.41 ± 0.99	-0.50 ± 1.02
F3	294.75 ± 0.40	294.28 ± 0.22	294.32 ± 0.38	-0.47 ± 1.00	-0.43 ± 1.05
F4	295.65 ± 0.40	295.11 ± 0.18	294.83 ± 0.53	-0.54 ± 0.99	-0.82 ± 1.11
F5	296.75 ± 0.40	294.87 ± 0.18	294.92 ± 0.14	-1.88 ± 0.99	-1.83 ± 0.99

Table 6.13: Temperature errors between the atmospherically-corrected mean ROI temperature and the measured ground-truth exit air temperature for the SRNL 20may04E04 image.

ID	T_{ex} [K]	Mixed ROI [K]	Cavity ROI [K]	Mixed ΔT [K]	Cavity ΔT [K]
H1	297.16 ± 0.40	297.32 ± 0.53	298.00 ± 0.29	0.16 ± 1.11	0.84 ± 1.02
H2	296.78 ± 0.40	297.88 ± 0.50	298.06 ± 0.23	1.10 ± 1.10	1.28 ± 1.00
H3	296.01 ± 0.40	294.45 ± 1.17	295.79 ± 0.54	-1.56 ± 1.52	-0.22 ± 1.12
H4	296.39 ± 0.40	297.60 ± 0.60	297.81 ± 0.31	1.21 ± 1.15	1.42 ± 1.03

Table 6.14: Temperature errors between the atmospherically-corrected mean ROI temperature and the measured ground-truth exit air temperature for the SRNL 20jun05G09 image.

6.3.4 Predicted Temperature Errors

The SRNL data will serve as a test of the methodology developed in Chapter 5. The physics model data presented in Section 6.1 must be processed using the SC 2000 sensor model with the appropriate GSD. A LUT is generated for GSD values of 0.22 m, 0.43 m, 0.85 m, and 0.15 m which correspond to the 20may04D14, 20may04E02, 20may04E04, and 20jun05G09 images, respectively. Next, a multiple linear regression model for the mixed ROI case and one for the cavity-only ROI case were fit to each LUT. The associated RMS error was calculated for each regression model.

Now that a parameterized regression equation has been found, the values of the predictor variables must be estimated. Recall from Section 6.2 that the seven predictor parameters are the *MDCT external temperature* (x_1), the *fan blade emissivity* (x_2), the *effective sky temperature* (x_3), the *sensor zenith angle* (x_4), the *ambient air temperature* (x_5), the *ambient dew point temperature* (x_6), and the *plume path length* (x_7). The response variable \hat{y}_1 is the predicted temperature error for the mixed ROI case. The response variable \hat{y}_2 is the predicted temperature error for the cavity-only ROI case.

Each predictor parameter value and uncertainty must be estimated:

MDCT external temperature (x_1) is the temperature of the decking. The deck ROI temperature from Tables 6.6 through 6.9 will be used as the estimate of this predictor. The deck ROI temperature does not take into account emissivity effects. If an emissivity of 0.95 is assumed for the decking material then the actual temperature of the deck would be roughly 3 K higher than the deck ROI temperature. Therefore, the uncertainty in this predictor estimate will be set to ± 3 K. (If the emissivity was underestimated as 0.90, then the uncertainty would increase to ± 7 K.)

Fan blade emissivity (x_2) is estimated to be 0.90. This value is based on the observation that most materials in the LWIR have relatively high emissivities. The uncertainty is set as ± 0.04 which is intended to cover the expected conditions of the fan blade material.

Effective sky temperature (x_3) can be computed from the interpolated atmospheric profile from Section 6.3.2. The DIRSIG `make_adb` utility calculates the total hemispherical spectral downwelling radiance from the profile data (Appendix D). This radiance is then integrated with the SC 2000 spectral response and converted into an apparent temperature.

The uncertainty in the sky temperature is taken as the approximate difference between the interpolated profile sky temperature and the MODTRAN standard tropical profile sky temperature (276 K). The uncertainty is ± 9 K for the nadir images and ± 12 K for the oblique image.

Sensor zenith angle (x_4) is estimated from the image. The apparent diameter of the fan stack opening in the horizontal and vertical image directions are compared and an approximate view angle is computed by

$$\theta_{zenith} = \cos^{-1} \left(\frac{D_v}{D_h} \right), \quad (6.10)$$

where D_v and D_h are the diameter of the fan stack opening in the vertical and horizontal image directions, respectively, in terms of the number of pixels. The uncertainty in this measurement is found by adding and subtracting one pixel from the vertical and horizontal diameters and recalculating the angle. Half of the range bounded by these two angles is taken as the uncertainty. For example, for the D14 image, the vertical and horizontal diameters were found to be 22 and 22 pixels, respectively. One pixel is subtracted from the vertical diameter and one pixel is added to the horizontal diameter to yield 21 and 23, respectively. This yields an angle of 24° . The estimated view angle is then taken as $0^\circ \pm 12^\circ$. The estimated angles and the uncertainties for each image are listed in Table 6.15.

Image	20may04D14	20may04E02	20may04E04	20jun05G09
Angle	$0^\circ \pm 12^\circ$	$0^\circ \pm 17^\circ$	$0^\circ \pm 22^\circ$	$29^\circ \pm 6^\circ$

Table 6.15: Estimates of the sensor view zenith angle along with uncertainties. The angles were estimated by measuring the vertical and horizontal pixel diameters of the fan stack opening of each image.

Ambient air temperature (x_5) is an actual measured ground value. The uncertainty is ± 0.4 K for the HOBO temperature sensor measurement error.

Ambient dew point temperature (x_6) is an actual measured ground value. The uncertainty is approximately ± 2 K for the HOBO temperature sensor measurement error.

Plume path length (x_7) is estimated via the utility in Appendix E. The utility takes into account the environmental information from the scene and the sensor geometry to calculate an approximate path length through the plume. The calculations are based on a

Gaussian plume model. The uncertainty in the plume path length is between 1 m and 5 m for the conditions found in the SRNL data set.

Once estimates of the predictor parameters are set, the predicted temperature error for the mixed and cavity ROIs can be calculated from the regression equations. The uncertainty in the predicted temperature is found from the uncertainties of each predictor parameter using the methods in Appendix C. The uncertainty was calculated by equation (C.5) and the result was verified empirically using a set of 100,000 trials to numerically determine the uncertainty (see Section C.2). Note that the RMS error of the regression equation is included in the uncertainty in the predicted temperature. The regression RMS error is a measure of the fit of the regression model to the LUT data.

The data tables in the following pages present the regression equations for the mixed and cavity ROI and the estimates and uncertainties for each parameter value used in the regression. The resulting predicted temperature errors are compared to the actual temperature errors presented in the previous section. Finally, a plot is shown of the actual and predicted temperature errors along with the associated uncertainties for each tower.

SRNL 20may04D14 image

02:02 EDT 20 May 2004 at 500 ft (152.5 m) with a GSD of 0.22 m.
(Parameterized Model Prediction)

Mixed ROI: (RMS error = 0.79 K)

$$\hat{y}_1 = -17.5651 - 0.0340 x_1 + 10.7236 x_2 + 0.0350 x_3 - 0.0083 x_4 + 0.0223 x_5 + 0.0016 x_6 + 0.0021 x_7$$

Cavity ROI: (RMS error = 0.36 K)

$$\hat{y}_2 = -6.3753 - 0.0268 x_1 + 4.0693 x_2 + 0.0136 x_3 - 0.0054 x_4 + 0.0220 x_5 - 0.0006 x_6 - 0.0004 x_7$$

ID	x_1 [K]	x_2 []	x_3 [K]	x_4 [°]	x_5 [K]	x_6 [K]	x_7 [m]
F1	293.11 ± 3.00	0.90 ± 0.04	267 ± 9	0 ± 12	292.87 ± 0.40	291.06 ± 2.00	3 ± 1
F2	292.42 ± 3.00	0.90 ± 0.04	267 ± 9	0 ± 12	292.87 ± 0.40	291.06 ± 2.00	15 ± 5
F3	292.46 ± 3.00	0.90 ± 0.04	267 ± 9	0 ± 12	292.87 ± 0.40	291.06 ± 2.00	20 ± 5
F4	292.83 ± 3.00	0.90 ± 0.04	267 ± 9	0 ± 12	292.87 ± 0.40	291.06 ± 2.00	3 ± 1
F5	292.98 ± 3.00	0.90 ± 0.04	267 ± 9	0 ± 12	292.87 ± 0.40	291.06 ± 2.00	3 ± 1

Table 6.16: Predictor estimates used in the 20may04D14 parameterized regression model.

ID	Mixed ROI		Cavity ROI	
	Image ΔT [K]	Predicted ΔT [K]	Image ΔT [K]	Predicted ΔT [K]
F1	-0.51 ± 1.03	-1.52 ± 0.96	-0.17 ± 1.02	-0.66 ± 0.42
F2	-0.41 ± 1.02	-1.47 ± 0.96	-0.27 ± 1.01	-0.65 ± 0.42
F3	-0.17 ± 1.04	-1.46 ± 0.96	-0.06 ± 1.02	-0.65 ± 0.42
F4	-0.19 ± 1.04	-1.51 ± 0.96	0.00 ± 1.03	-0.66 ± 0.42
F5	-1.51 ± 1.06	-1.51 ± 0.96	-1.09 ± 1.02	-0.66 ± 0.42

Table 6.17: Comparison of the actual and predicted temperature errors for the 20may04D14 image. ROI, atmosphere, and sensor uncertainty is included.

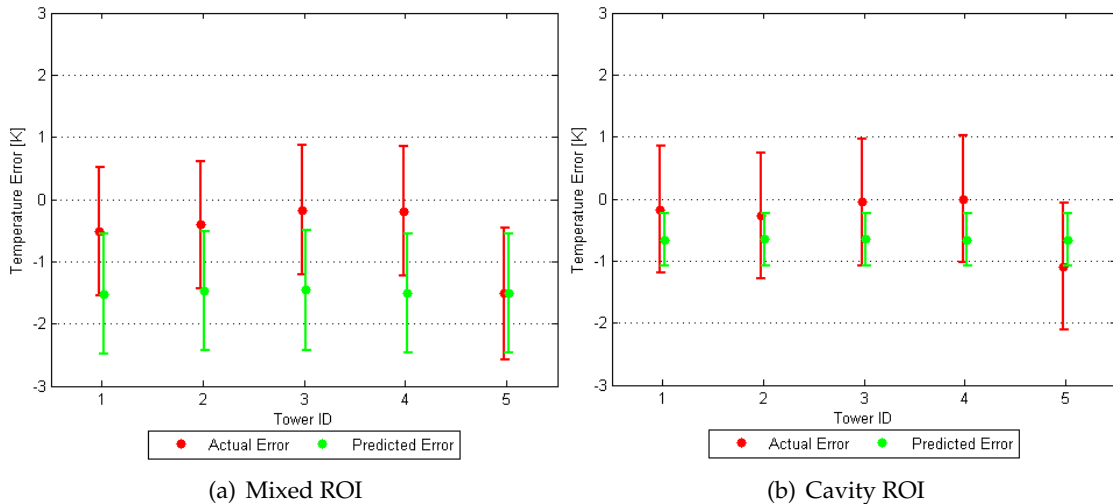


Figure 6.4: The actual and the predicted temperature error with uncertainty ranges for the 20may04D14 image. ROI, atmosphere, and sensor uncertainty is included in the error bars.

SRNL 20may04E02 image

02:04 EDT 20 May 2004 at 1000 ft (305.0 m) with a GSD of 0.43 m.
(Parameterized Model Prediction)

Mixed ROI: (RMS error = 0.80 K)

$$\hat{y}_1 = -17.8511 - 0.0335 x_1 + 10.8209 x_2 + 0.0350 x_3 - 0.0070 x_4 + 0.0223 x_5 + 0.0016 x_6 + 0.0021 x_7$$

Cavity ROI: (RMS error = 0.46 K)

$$\hat{y}_2 = -7.6545 - 0.0277 x_1 + 4.7703 x_2 + 0.0165 x_3 - 0.0124 x_4 + 0.0220 x_5 - 0.0003 x_6 - 0.0000 x_7$$

ID	x_1 [K]	x_2 []	x_3 [K]	x_4 [°]	x_5 [K]	x_6 [K]	x_7 [m]
F1	293.11 ± 3.00	0.90 ± 0.04	267 ± 9	0 ± 17	292.87 ± 0.40	291.06 ± 2.00	3 ± 1
F2	292.48 ± 3.00	0.90 ± 0.04	267 ± 9	0 ± 17	292.87 ± 0.40	291.06 ± 2.00	15 ± 5
F3	292.34 ± 3.00	0.90 ± 0.04	267 ± 9	0 ± 17	292.87 ± 0.40	291.06 ± 2.00	20 ± 5
F4	292.76 ± 3.00	0.90 ± 0.04	267 ± 9	0 ± 17	292.87 ± 0.40	291.06 ± 2.00	3 ± 1
F5	292.95 ± 3.00	0.90 ± 0.04	267 ± 9	0 ± 17	292.87 ± 0.40	291.06 ± 2.00	3 ± 1

Table 6.18: Predictor estimates used in the 20may04E02 parameterized regression model.

ID	Mixed ROI		Cavity ROI	
	Image ΔT [K]	Predicted ΔT [K]	Image ΔT [K]	Predicted ΔT [K]
F1	-0.56 ± 1.01	-1.56 ± 0.97	-0.43 ± 1.01	-0.71 ± 0.57
F2	-0.43 ± 1.01	-1.51 ± 0.97	-0.28 ± 1.00	-0.70 ± 0.57
F3	-0.17 ± 1.02	-1.50 ± 0.97	-0.10 ± 1.01	-0.69 ± 0.57
F4	-0.35 ± 1.01	-1.55 ± 0.97	-0.24 ± 1.01	-0.70 ± 0.57
F5	-1.46 ± 1.03	-1.55 ± 0.97	-1.27 ± 1.00	-0.71 ± 0.57

Table 6.19: Comparison of the actual and predicted temperature errors for the 20may04E02 image. ROI, atmosphere, and sensor uncertainty is included.

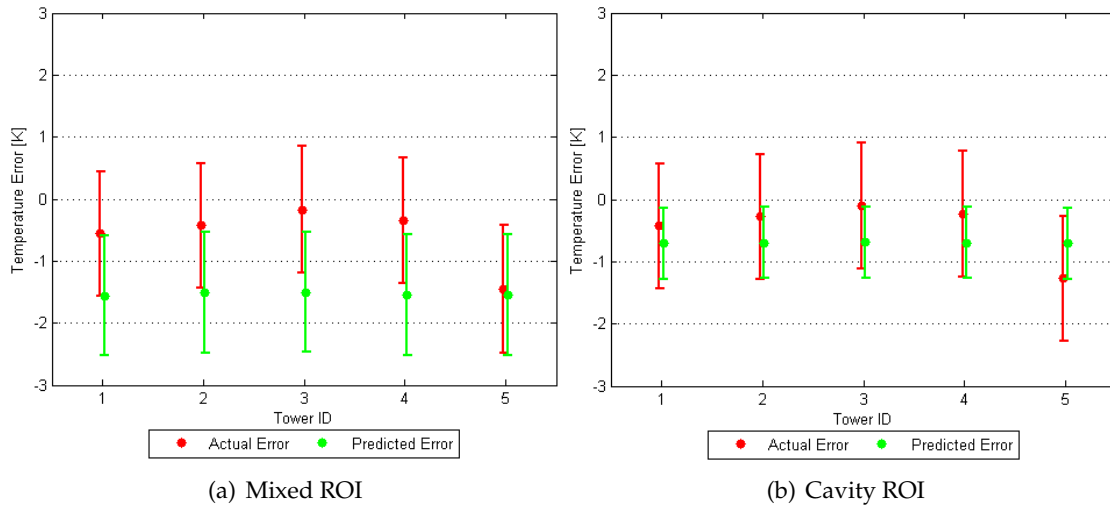


Figure 6.5: The actual and the predicted temperature error with uncertainty ranges for the 20may04E02 image. ROI, atmosphere, and sensor uncertainty is included in the error bars.

SRNL 20may04E04 image

02:07 EDT 20 May 2004 at 2000 ft (610.0 m) with a GSD of 0.85 m.
(Parameterized Model Prediction)

Mixed ROI: (RMS error = 0.82 K)

$$\hat{y}_1 = -18.1448 - 0.0325 x_1 + 10.4140 x_2 + 0.0356 x_3 - 0.0050 x_4 + 0.0224 x_5 + 0.0017 x_6 + 0.0022 x_7$$

Cavity ROI: (RMS error = 0.60 K)

$$\hat{y}_2 = -12.3001 - 0.0296 x_1 + 7.2994 x_2 + 0.0247 x_3 - 0.0117 x_4 + 0.0222 x_5 + 0.0006 x_6 + 0.0009 x_7$$

ID	x_1 [K]	x_2 []	x_3 [K]	x_4 [°]	x_5 [K]	x_6 [K]	x_7 [m]
F1	293.18 ± 3.00	0.90 ± 0.04	267 ± 9	0 ± 22	292.87 ± 0.40	291.06 ± 2.00	3 ± 1
F2	292.74 ± 3.00	0.90 ± 0.04	267 ± 9	0 ± 22	292.87 ± 0.40	291.06 ± 2.00	15 ± 5
F3	292.84 ± 3.00	0.90 ± 0.04	267 ± 9	0 ± 22	292.87 ± 0.40	291.06 ± 2.00	20 ± 5
F4	293.19 ± 3.00	0.90 ± 0.04	267 ± 9	0 ± 22	292.87 ± 0.40	291.06 ± 2.00	3 ± 1
F5	293.13 ± 3.00	0.90 ± 0.04	267 ± 9	0 ± 22	292.87 ± 0.40	291.06 ± 2.00	3 ± 1

Table 6.20: Predictor estimates used in the 20may04E04 parameterized regression model.

ID	Mixed ROI		Cavity ROI	
	Image ΔT [K]	Predicted ΔT [K]	Image ΔT [K]	Predicted ΔT [K]
F1	-0.48 ± 1.00	-1.73 ± 0.98	-0.46 ± 0.99	-1.16 ± 0.75
F2	-0.41 ± 0.99	-1.69 ± 0.98	-0.50 ± 1.02	-1.13 ± 0.75
F3	-0.47 ± 1.00	-1.68 ± 0.98	-0.43 ± 1.05	-1.13 ± 0.75
F4	-0.54 ± 0.99	-1.73 ± 0.98	-0.82 ± 1.11	-1.16 ± 0.75
F5	-1.88 ± 0.99	-1.73 ± 0.98	-1.83 ± 0.99	-1.16 ± 0.75

Table 6.21: Comparison of the actual and predicted temperature errors for the 20may04E04 image. ROI, atmosphere, and sensor uncertainty is included.

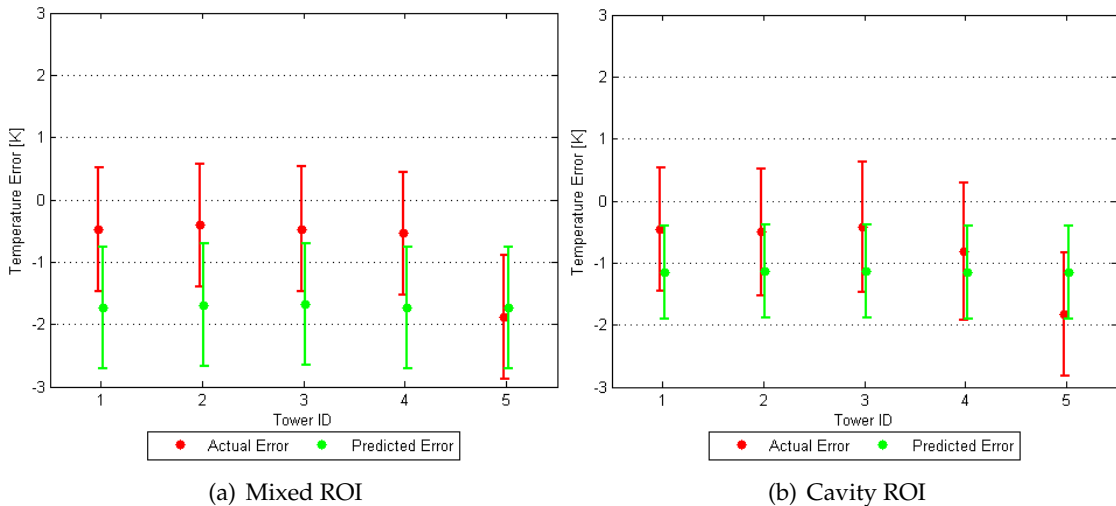


Figure 6.6: The actual and the predicted temperature error with uncertainty ranges for the 20may04E04 image. ROI, atmosphere, and sensor uncertainty is included in the error bars.

SRNL 20jun05G09 image

22:17 EDT, 20 June 2005 at 350 ft (106.7 m) with a GSD of 0.15 m.
(Parameterized Model Prediction)

Mixed ROI: (RMS error = 0.78 K)

$$\hat{y}_1 = -17.5961 - 0.0340 x_1 + 10.7930 x_2 + 0.0349 x_3 - 0.0075 x_4 + 0.0223 x_5 + 0.0016 x_6 + 0.0021 x_7$$

Cavity ROI: (RMS error = 0.35 K)

$$\hat{y}_2 = -6.3769 - 0.0273 x_1 + 4.1551 x_2 + 0.0138 x_3 - 0.0049 x_4 + 0.0220 x_5 - 0.0006 x_6 - 0.0003 x_7$$

ID	x_1 [K]	x_2 []	x_3 [K]	x_4 [°]	x_5 [K]	x_6 [K]	x_7 [m]
H1	293.68 ± 3.00	0.90 ± 0.04	264 ± 12	29 ± 6	296.39 ± 0.40	293.17 ± 2.00	8 ± 3
H2	293.65 ± 3.00	0.90 ± 0.04	264 ± 12	29 ± 6	296.39 ± 0.40	293.17 ± 2.00	8 ± 3
H3	292.01 ± 3.00	0.90 ± 0.04	264 ± 12	29 ± 6	296.39 ± 0.40	293.17 ± 2.00	4 ± 1
H4	293.48 ± 3.00	0.90 ± 0.04	264 ± 12	29 ± 6	296.39 ± 0.40	293.17 ± 2.00	8 ± 3

Table 6.22: Predictor estimates used in the 20jun05G09 parameterized regression model.

ID	Mixed ROI		Cavity ROI	
	Image ΔT [K]	Predicted ΔT [K]	Image ΔT [K]	Predicted ΔT [K]
H1	0.16 ± 1.11	-1.76 ± 1.00	0.84 ± 1.02	-0.79 ± 0.43
H2	1.10 ± 1.10	-1.76 ± 1.00	1.28 ± 1.00	-0.79 ± 0.43
H3	-1.56 ± 1.52	-1.71 ± 1.00	-0.22 ± 1.12	-0.75 ± 0.43
H4	1.21 ± 1.15	-1.76 ± 1.00	1.42 ± 1.03	-0.79 ± 0.43

Table 6.23: Comparison of the actual and predicted temperature errors for the 20jun05G09 image. ROI, atmosphere, and sensor uncertainty is included.

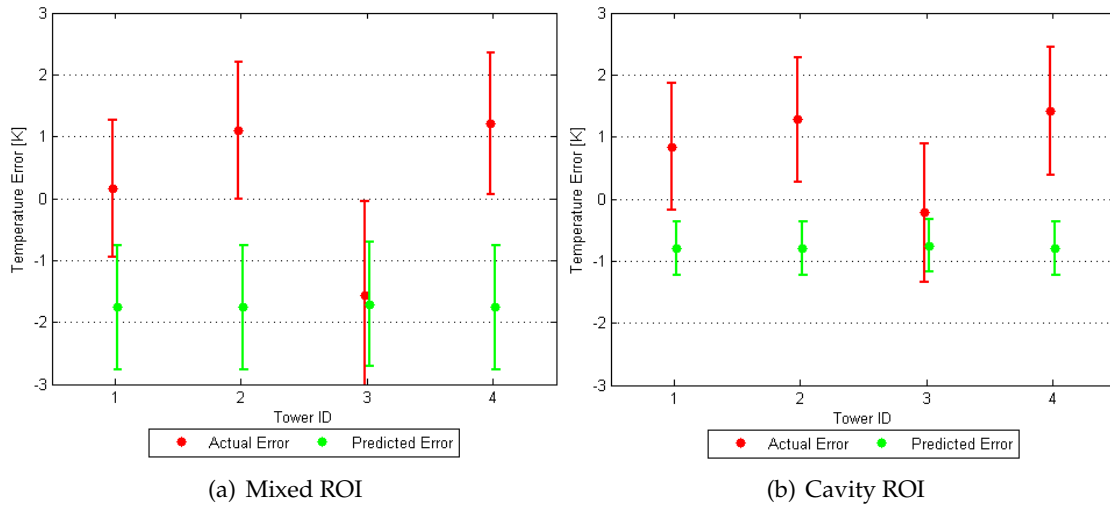


Figure 6.7: The actual and the predicted temperature error with uncertainty ranges for the 20jun05G09 image. ROI, atmosphere, and sensor uncertainty is included in the error bars.

The comparison of the actual temperature error and the predicted temperature error is presented in Figures 6.4 to 6.7. Several statements can be made about the data.

In general, the predicted errors are less than zero for both the mixed and cavity ROIs. The magnitude of the predicted errors are greater than the magnitude of the actual errors for the nadir images (20may04D14, 20may04E02, 20may04E04). The uncertainty ranges overlap for the mixed and cavity ROIs for all the nadir images. Compared to the actual errors, the predicted temperature errors were within ± 1.3 K for the mixed ROIs and within ± 0.7 K for the cavity ROIs.

For the oblique image (20jun05G09), the actual errors vary more from tower to tower than in the nadir images. The uncertainty ranges overlap for two of the four towers for the mixed ROI and overlap for only one tower for the cavity ROI. The predicted temperature errors differed from the actual errors by as much as ± 3 K for the mixed and cavity ROIs. However, the predicted temperature error was within ± 0.5 K for the H3 tower for both ROIs.

These results can be attributed to several factors. First, the the SRNL data set issues discussed in Section 6.3.1 will influence the actual temperature errors. Although uncertainties were assigned to the ground measurements based on expected errors in the temperature sensors, this does not take into account the prospect that the recorded measurement was not the actual measurement desired. The exit air temperature measurement, for example, may not have been the true exit air temperature since the measurement could have been altered by the ambient conditions. The uncertainties are due to the physical process of temperature measurement and are not due to statistical sampling of the temperature. In addition, estimates were made for the uncertainty in the atmospheric compensation and in the sensor measurement. Ideally, these uncertainties would have been understood in detail.

These results may also be attributed to the modeling process. Imperfect information was used in parameterized model. The exact *MDCT external temperature* had to be estimated from the images. The value for the *fan blade emissivity* was estimated based on similar, but not exact, materials. The *effective sky temperature* was estimated from the interpolated atmospheric profile used to atmospherically correct the images. The *sensor view angle* was estimated from the images. Actual sensor orientation data could be used in practice to obtain the value for the view angle. The *ambient air temperature* and *ambient dew point*

temperature measurements were subject to the uncertainties described previously. Finally, the *plume path length* was roughly estimated using a Gaussian plume model. This model yields a time-averaged estimate of the plume path length and is not sensitive to instantaneous changes in the environment around the MDCT. The regression model fit to each sensor LUT was also not a perfect fit to the data. The RMS errors for the regression fits indicated that the parameterized model itself may introduce errors of up to 0.82 K and 0.60 K for the mixed and cavity ROIs, respectively.

Although this demonstration produced mixed results, it did work very well for the nadir images which lends confidence in the use of this methodology and parameterized model for real data sets. The connection between the performance of the parameterized model and the properties of the MDCT units is arbitrary, however. As an example, for the nadir images the parameterized model for the F5 tower performed the best for the mixed ROI. There is nothing unique about this tower. Recall from Section 2.3 that the F1, F4, and F5 units were operating as *water on, fans off* while the F2 and F3 units were *water on, fans on*. The fan status does not appear to be an indication of model performance since there was no correlation between fan status and model performance for the other units. Similarly for the oblique image, the parameterized model performed the best for the H3 tower. This unit was also operating in the *water on, fans off* model while the other units were operating in the *water on, fans on* mode. In this particular case, it appears that the parameterized model was more accurate for the *fans off* unit than for the *fans on* unit. However, no conclusion can be drawn from this observation since it is not consistent with the nadir images.

The poorer performance of the parameterized model predictions for the oblique image might be due to several factors that were not accounted for in the physics model. The oblique viewing geometry means that the emissivity will be different from the nadir viewing geometry due to directional emissivity effects. For external pixels this means that these facets will have a higher reflectance thereby increasing the amount of reflected background radiance. Although the directional emissivity is accounted for in the physics model, the temperature error might be more sensitive to background radiances. The sky was modeled as a uniform radiator. In reality, the skydome radiance will be a function of zenith and azimuth angle depending on the weather conditions. These factors combine to have an increased effect on the sensor-reaching radiance in the oblique case than in the nadir case. Given the physical processes discussed and investigated in Chapters 3 and 5 (*i.e.*, emissivity, atmospheric transmission and path radiance, etc.), the actual temperature errors should be less than zero given the atmospheric information provided. The actual

errors for the oblique image are greater than zero for three of the towers. This suggests that there were errors in the ground-truth measurements or that the physics model did not account for a physical attribute in the scene. For example, an assumption is made that the internal surfaces of the MDCT are the same temperature as the exit air. If this is not true, the measured exit air temperature would be lower than the internal temperature given that the ambient temperature was also less than the internal temperature. In addition, the increased temperature of the gear box associated with the fan mechanical system was not modeled. The high temperature of the gear box for the *fans on* towers might have contributed to the higher apparent temperatures for those towers.

6.3.5 Comparison of Atmospheric Uncertainties

The data presented in Section 6.3.4 included uncertainty ranges that incorporated the suspected errors due to the ROI measurement, the atmospheric compensation, and the sensor measurement along with the uncertainty in the ground measurement (Table 6.10). The total uncertainty for the temperature error was found through equation (6.9). The uncertainties in the ROI temperature and the sensor measurement is fixed for a given sensor. The atmospheric compensation error, however, is dependent on how well atmospheric effects can be removed. This is dependent on knowledge of the atmospheric state. The atmospheric uncertainty was set to ± 0.6 K in Figures 6.4 - 6.7 but this uncertainty in the atmospheric compensation may vary considerable. To demonstrate the effect of this uncertainty, the atmospheric uncertainty was varied between ± 0.1 K, ± 1.1 K, and ± 2.2 K and the corresponding total uncertainty in the image temperature error was calculated for each image. The results are shown in Figures 6.8 - 6.11.

The plots demonstrate the influence of the atmospheric uncertainty on the overall process. As expected, the overall uncertainty increases as the atmospheric uncertainty increases. The overall uncertainty ranges between ± 1.0 K to ± 2.5 K over the atmospheric uncertainty range of ± 0.1 K to ± 2.2 K. This study demonstrates the importance of accurate atmospheric compensation.

SRNL 20may04D14 image

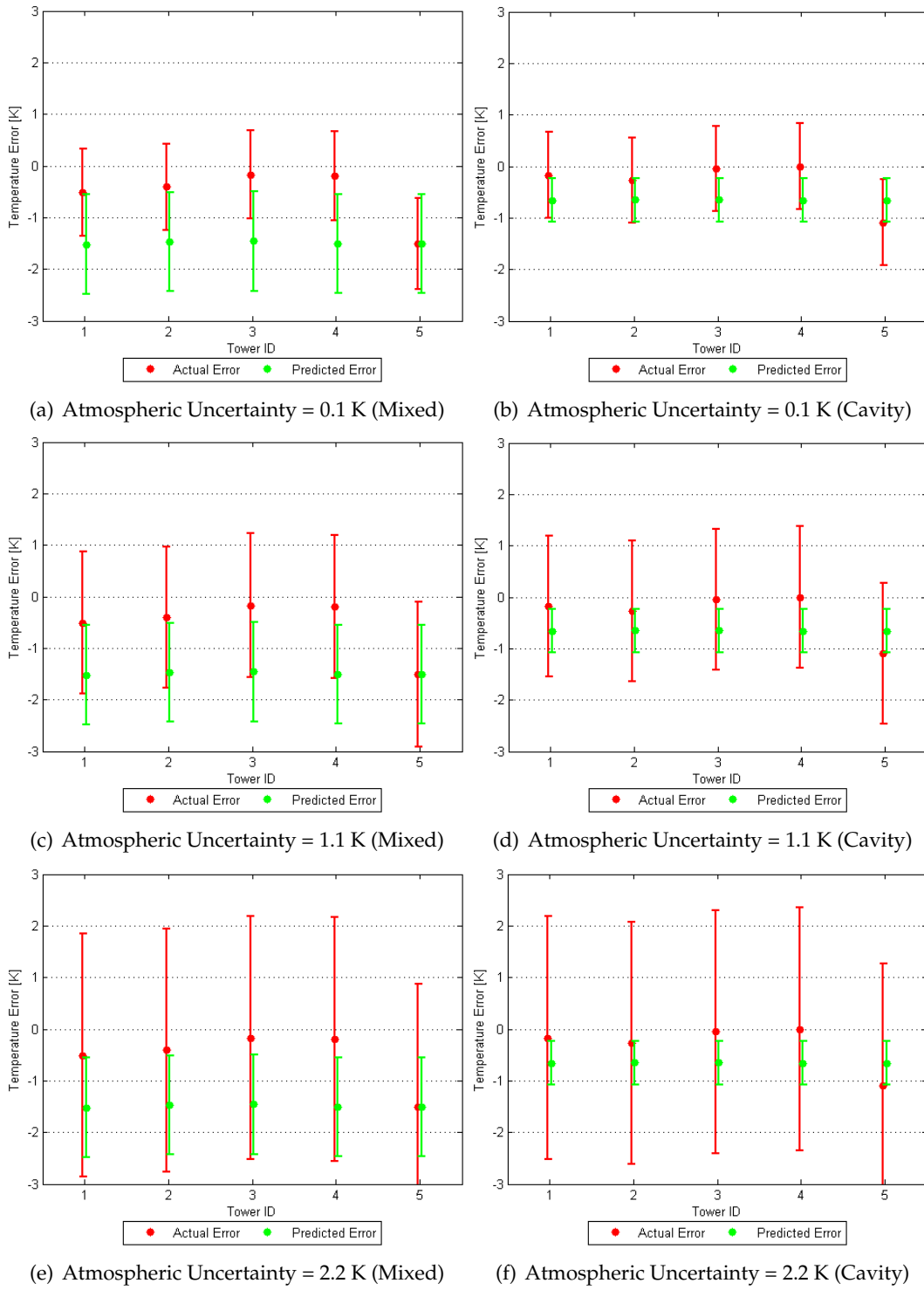


Figure 6.8: The actual and the predicted temperature error with uncertainty ranges for the 20may04D14 image. The uncertainty ranges are for an atmospheric uncertainty of 0.1 K (top), 1.1 K (middle), and 2.2 K (bottom).

SRNL 20may04E02 image

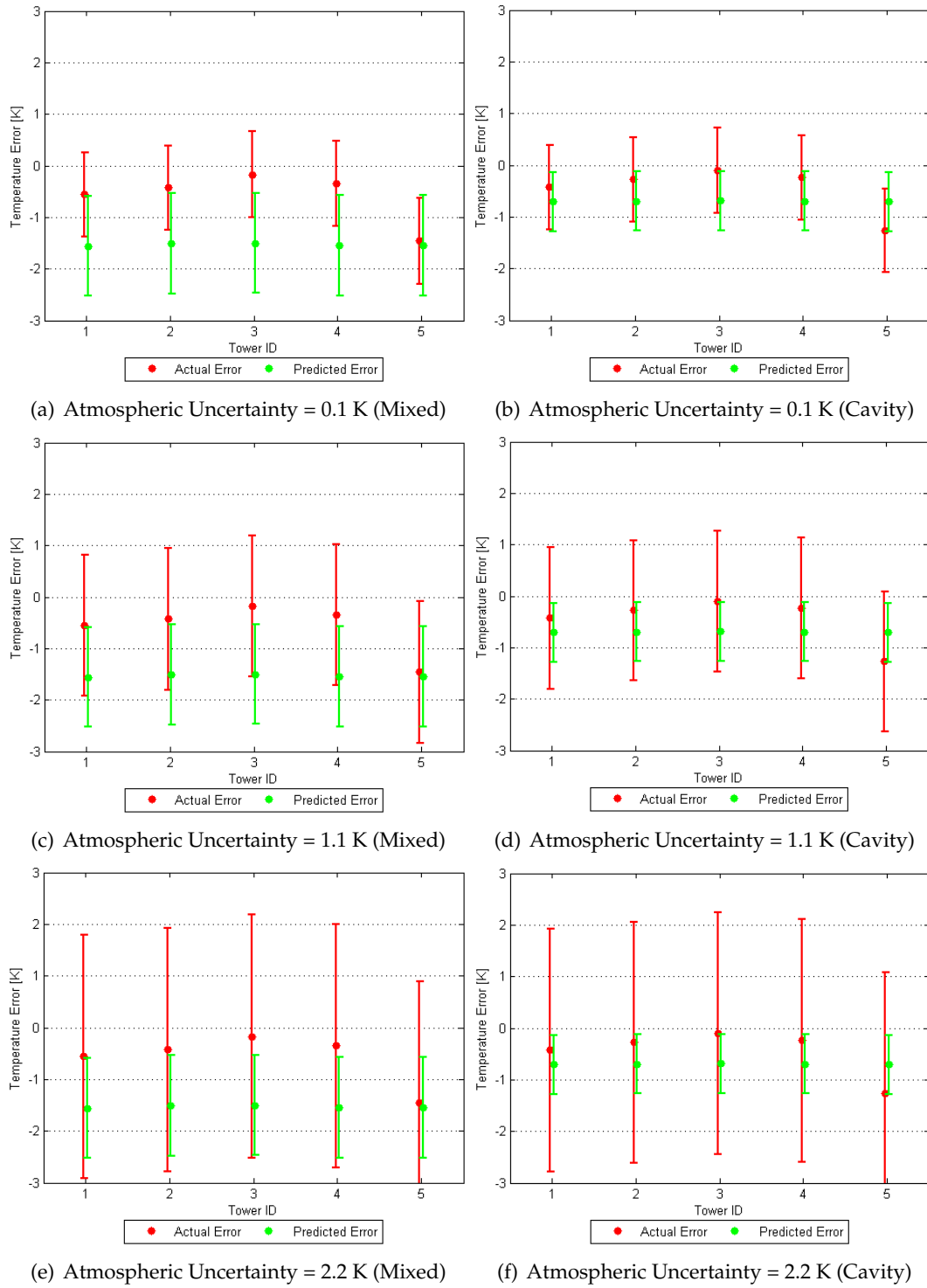


Figure 6.9: The actual and the predicted temperature error with uncertainty ranges for the 20may04E02 image. The uncertainty ranges are for an atmospheric uncertainty of 0.1 K (top), 1.1 K (middle), and 2.2 K (bottom).

SRNL 20may04E04 image

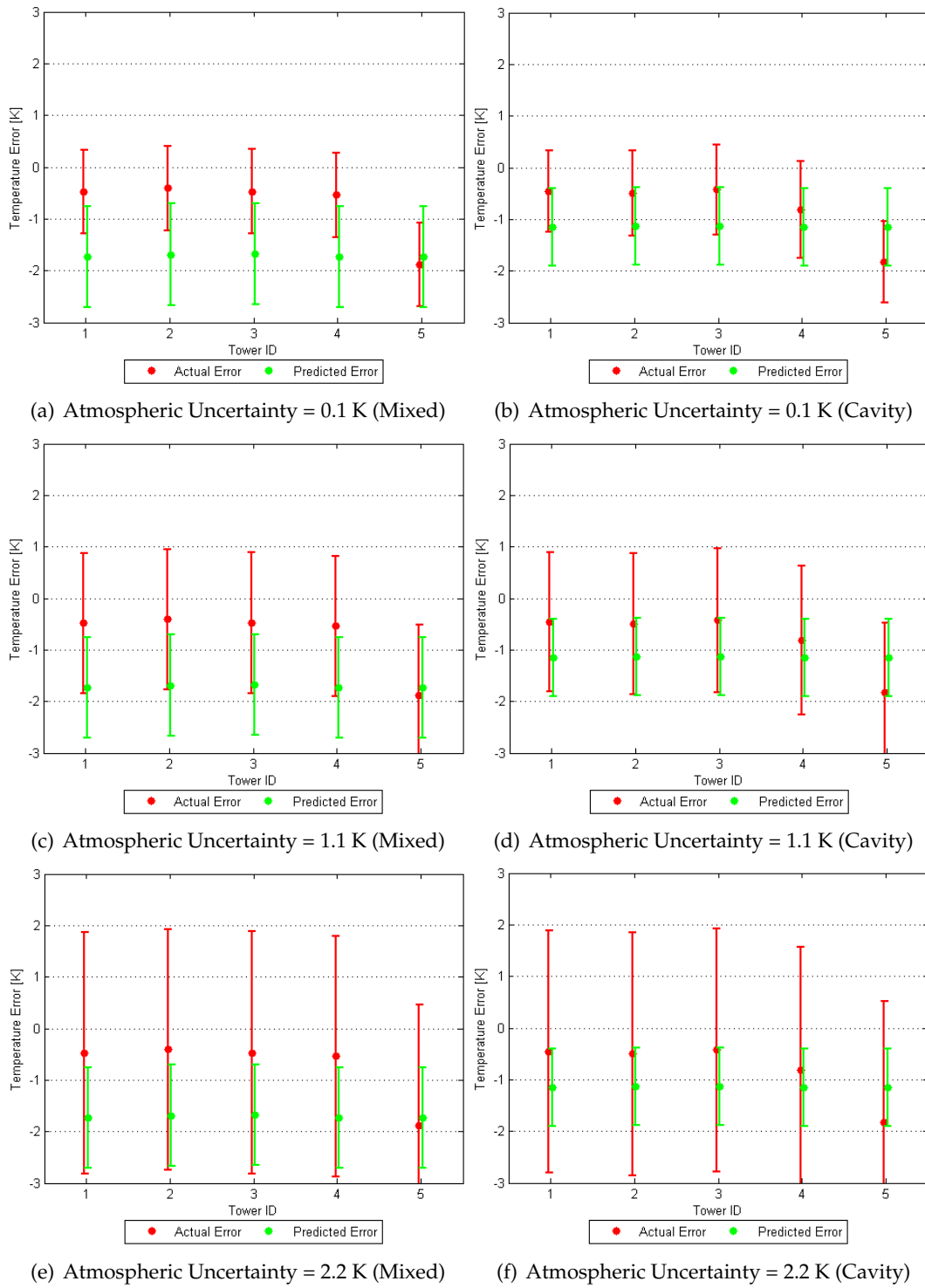
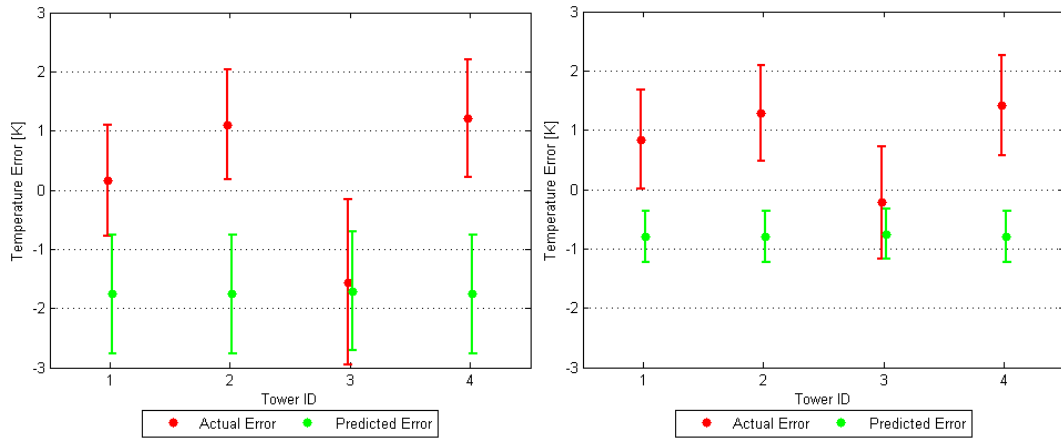


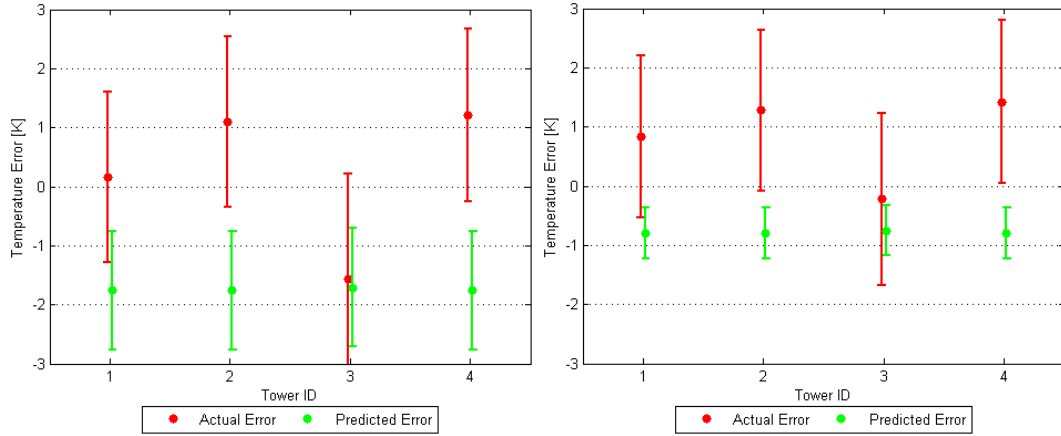
Figure 6.10: The actual and the predicted temperature error with uncertainty ranges for the 20may04E04 image. The uncertainty ranges are for an atmospheric uncertainty of 0.1 K (top), 1.1 K (middle), and 2.2 K (bottom).

SRNL 20jun05G09 image



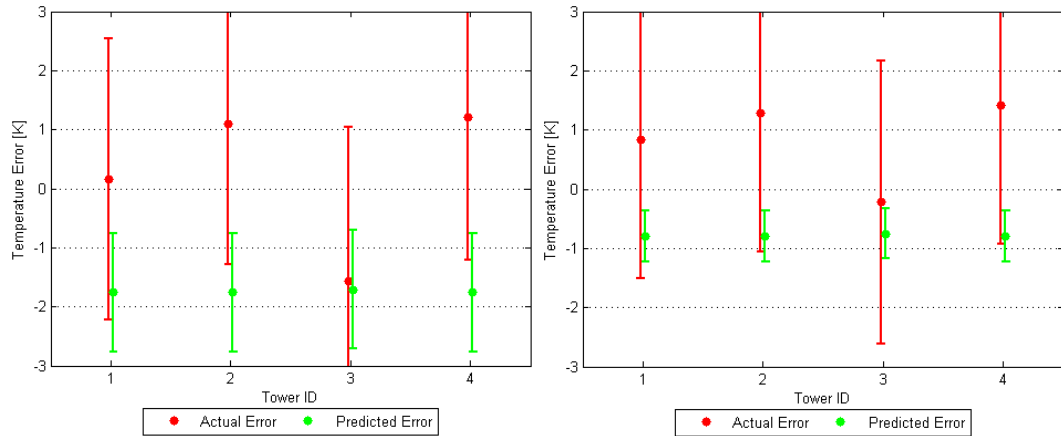
(a) Atmospheric Uncertainty = 0.1 K (Mixed)

(b) Atmospheric Uncertainty = 0.1 K (Cavity)



(c) Atmospheric Uncertainty = 1.1 K (Mixed)

(d) Atmospheric Uncertainty = 1.1 K (Cavity)



(e) Atmospheric Uncertainty = 2.2 K (Mixed)

(f) Atmospheric Uncertainty = 2.2 K (Cavity)

Figure 6.11: The actual and the predicted temperature error with uncertainty ranges for the 20jun05G09 image. The uncertainty ranges are for an atmospheric uncertainty of 0.1 K (top), 1.1 K (middle), and 2.2 K (bottom).

6.3.6 Comparison of Sensor Spectral Response

The sensor model used to generate the target space LUT for the SRNL data set required the spectral response function of the SC 2000 Inframetrics sensor. Recall from Section 6.3.1 that since the exact spectral response was not known, it was approximated by using a flat, unit response between 7.6 and 13.5 μm and zero otherwise.

To investigate the influence of the sensor spectral response function on the predicted temperature error, a realistic spectral response was used in the sensor model to compare the predicted temperature errors to the errors predicted using the flat response. The Long-wave Infrared Camera (LIR) described by Taguchi *et al.* (2007) [46] is a microbolometer array with a LWIR filter to get the desired spectral range of 8 - 12 μm . The design of this sensor is similar to the SC 2000 sensor. Therefore, the spectral response curve of the LIR was modified so that the full spectral width at half its maximum value fell between 7.6 and 13.5 μm while maintaining the same spectral shape. A comparison of this microbolometer spectral response and the flat spectral response is shown in Figure 6.12.

The microbolometer response function is then used in the sensor model in the generation of the LUT of each image. A regression model is fit to the LUT and the predicted temperature errors are compared to the actual temperature errors. The results are shown in Figures 6.13 through 6.16.

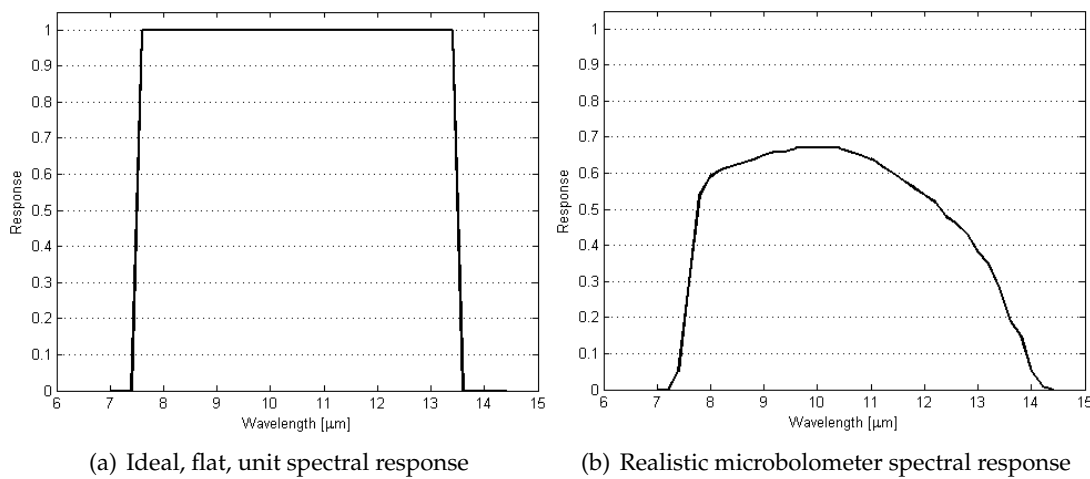


Figure 6.12: Comparison of an ideal, flat, unit spectral response and a realistic microbolometer spectral response in the longwave infrared region.

SRNL 20may04D14 image

02:02 EDT 20 May 2004 at 500 ft (152.5 m) with a GSD of 0.22 m.
(Parameterized Model Prediction - Microbolometer Response)

Mixed ROI: (RMS error = 0.77 K)

$$\hat{y}_1 = -17.0516 - 0.0338 x_1 + 10.8467 x_2 + 0.0345 x_3 - 0.0074 x_4 + 0.0208 x_5 + 0.0015 x_6 + 0.0019 x_7$$

Cavity ROI: (RMS error = 0.22 K)

$$\hat{y}_2 = -2.6939 - 0.0233 x_1 + 2.0021 x_2 + 0.0066 x_3 - 0.0034 x_4 + 0.0204 x_5 - 0.0012 x_6 - 0.0011 x_7$$

ID	x_1 [K]	x_2 []	x_3 [K]	x_4 [°]	x_5 [K]	x_6 [K]	x_7 [m]
F1	293.11 ± 3.00	0.90 ± 0.04	267 ± 9	0 ± 12	292.87 ± 0.40	291.06 ± 2.00	3 ± 1
F2	292.42 ± 3.00	0.90 ± 0.04	267 ± 9	0 ± 12	292.87 ± 0.40	291.06 ± 2.00	15 ± 5
F3	292.46 ± 3.00	0.90 ± 0.04	267 ± 9	0 ± 12	292.87 ± 0.40	291.06 ± 2.00	20 ± 5
F4	292.83 ± 3.00	0.90 ± 0.04	267 ± 9	0 ± 12	292.87 ± 0.40	291.06 ± 2.00	3 ± 1
F5	292.98 ± 3.00	0.90 ± 0.04	267 ± 9	0 ± 12	292.87 ± 0.40	291.06 ± 2.00	3 ± 1

Table 6.24: Predictor estimates used in the 20may04D14 parameterized regression model.

ID	Mixed ROI		Cavity ROI	
	Image ΔT [K]	Predicted ΔT [K]	Image ΔT [K]	Predicted ΔT [K]
F1	-0.51 ± 1.03	-1.45 ± 0.94	-0.17 ± 1.02	-0.34 ± 0.25
F2	-0.41 ± 1.02	-1.40 ± 0.94	-0.27 ± 1.01	-0.34 ± 0.25
F3	-0.17 ± 1.04	-1.39 ± 0.94	-0.06 ± 1.02	-0.34 ± 0.25
F4	-0.19 ± 1.04	-1.44 ± 0.94	0.00 ± 1.03	-0.33 ± 0.25
F5	-1.51 ± 1.06	-1.44 ± 0.94	-1.09 ± 1.02	-0.33 ± 0.25

Table 6.25: Comparison of the actual and predicted temperature errors for the 20may04D14 image using the microbolometer spectral response.

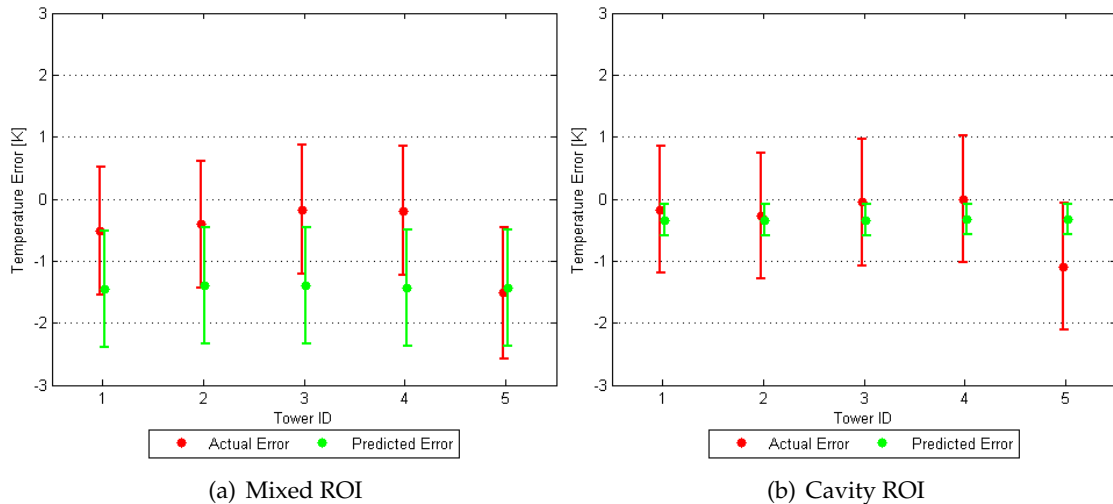


Figure 6.13: The actual and the predicted temperature error with uncertainty ranges for the 20may04D14 image using the microbolometer spectral response.

SRNL 20may04E02 image

02:04 EDT 20 May 2004 at 1000 ft (305.0 m) with a GSD of 0.43 m.
(Parameterized Model Prediction - Microbolometer Response)

Mixed ROI: (RMS error = 0.77 K)

$$\hat{y}_1 = -17.3534 - 0.0338 x_1 + 10.8467 x_2 + 0.0345 x_3 - 0.0074 x_4 + 0.0208 x_5 + 0.0015 x_6 + 0.0019 x_7$$

Cavity ROI: (RMS error = 0.22 K)

$$\hat{y}_2 = -2.6939 - 0.0233 x_1 + 2.0021 x_2 + 0.0066 x_3 - 0.0034 x_4 + 0.0204 x_5 - 0.0012 x_6 - 0.0011 x_7$$

ID	x_1 [K]	x_2 []	x_3 [K]	x_4 [°]	x_5 [K]	x_6 [K]	x_7 [m]
F1	293.11 ± 3.00	0.90 ± 0.04	267 ± 9	0 ± 17	292.87 ± 0.40	291.06 ± 2.00	3 ± 1
F2	292.48 ± 3.00	0.90 ± 0.04	267 ± 9	0 ± 17	292.87 ± 0.40	291.06 ± 2.00	15 ± 5
F3	292.34 ± 3.00	0.90 ± 0.04	267 ± 9	0 ± 17	292.87 ± 0.40	291.06 ± 2.00	20 ± 5
F4	292.76 ± 3.00	0.90 ± 0.04	267 ± 9	0 ± 17	292.87 ± 0.40	291.06 ± 2.00	3 ± 1
F5	292.95 ± 3.00	0.90 ± 0.04	267 ± 9	0 ± 17	292.87 ± 0.40	291.06 ± 2.00	3 ± 1

Table 6.26: Predictor estimates used in the 20may04E02 parameterized regression model.

ID	Mixed ROI		Cavity ROI	
	Image ΔT [K]	Predicted ΔT [K]	Image ΔT [K]	Predicted ΔT [K]
F1	-0.56 ± 1.01	-1.51 ± 0.96	-0.43 ± 1.01	-0.55 ± 0.49
F2	-0.43 ± 1.01	-1.47 ± 0.96	-0.28 ± 1.00	-0.53 ± 0.49
F3	-0.17 ± 1.02	-1.46 ± 0.96	-0.10 ± 1.01	-0.53 ± 0.49
F4	-0.35 ± 1.01	-1.50 ± 0.96	-0.24 ± 1.01	-0.54 ± 0.49
F5	-1.46 ± 1.03	-1.51 ± 0.96	-1.27 ± 1.00	-0.54 ± 0.49

Table 6.27: Comparison of the actual and predicted temperature errors for the 20may04E02 image using the microbolometer spectral response.

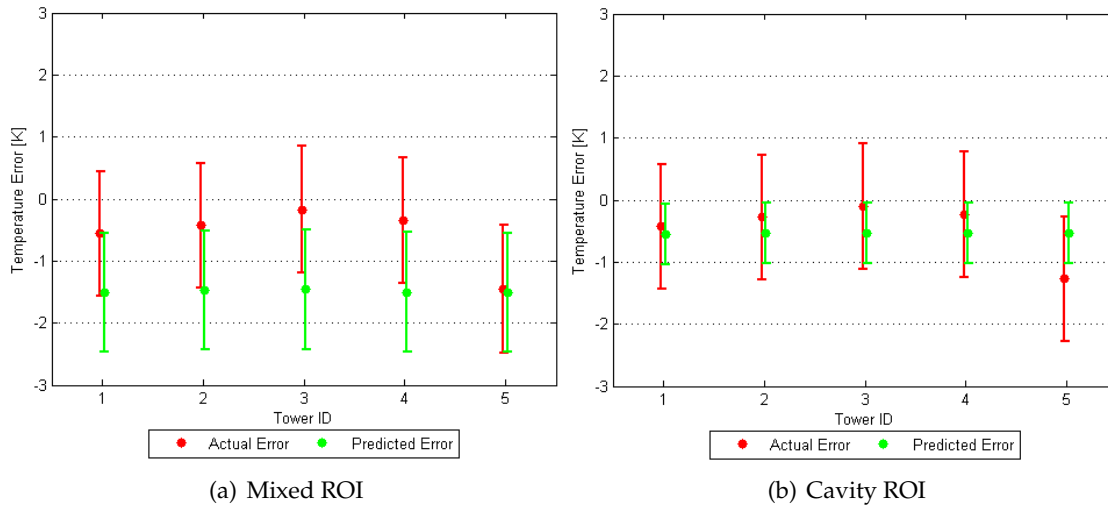


Figure 6.14: The actual and the predicted temperature error with uncertainty ranges for the 20may04E02 image using the microbolometer spectral response.

SRNL 20may04E04 image

02:07 EDT 20 May 2004 at 2000 ft (610.0 m) with a GSD of 0.85 m.
(Parameterized Model Prediction - Microbolometer Response)

Mixed ROI: (RMS error = 0.81 K)

$$\hat{y}_1 = -17.4717 - 0.0327 x_1 + 10.4363 x_2 + 0.0352 x_3 - 0.0048 x_4 + 0.0208 x_5 + 0.0016 x_6 + 0.0020 x_7$$

Cavity ROI: (RMS error = 0.56 K)

$$\hat{y}_2 = -11.3297 - 0.0283 x_1 + 6.9223 x_2 + 0.0232 x_3 - 0.0147 x_4 + 0.0207 x_5 + 0.0004 x_6 + 0.0007 x_7$$

ID	x_1 [K]	x_2 []	x_3 [K]	x_4 [°]	x_5 [K]	x_6 [K]	x_7 [m]
F1	293.18 ± 3.00	0.90 ± 0.04	267 ± 9	0 ± 22	292.87 ± 0.40	291.06 ± 2.00	3 ± 1
F2	292.74 ± 3.00	0.90 ± 0.04	267 ± 9	0 ± 22	292.87 ± 0.40	291.06 ± 2.00	15 ± 5
F3	292.84 ± 3.00	0.90 ± 0.04	267 ± 9	0 ± 22	292.87 ± 0.40	291.06 ± 2.00	20 ± 5
F4	293.19 ± 3.00	0.90 ± 0.04	267 ± 9	0 ± 22	292.87 ± 0.40	291.06 ± 2.00	3 ± 1
F5	293.13 ± 3.00	0.90 ± 0.04	267 ± 9	0 ± 22	292.87 ± 0.40	291.06 ± 2.00	3 ± 1

Table 6.28: Predictor estimates used in the 20may04E04 parameterized regression model.

	Mixed ROI		Cavity ROI	
ID	Image ΔT [K]	Predicted ΔT [K]	Image ΔT [K]	Predicted ΔT [K]
F1	-0.48 ± 1.00	-1.69 ± 0.97	-0.46 ± 0.99	-1.05 ± 0.74
F2	-0.41 ± 0.99	-1.65 ± 0.97	-0.50 ± 1.02	-1.02 ± 0.74
F3	-0.47 ± 1.00	-1.64 ± 0.97	-0.43 ± 1.05	-1.02 ± 0.74
F4	-0.54 ± 0.99	-1.69 ± 0.97	-0.82 ± 1.11	-1.05 ± 0.74
F5	-1.88 ± 0.99	-1.68 ± 0.97	-1.83 ± 0.99	-1.04 ± 0.74

Table 6.29: Comparison of the actual and predicted temperature errors for the 20may04E04 image using the microbolometer spectral response.

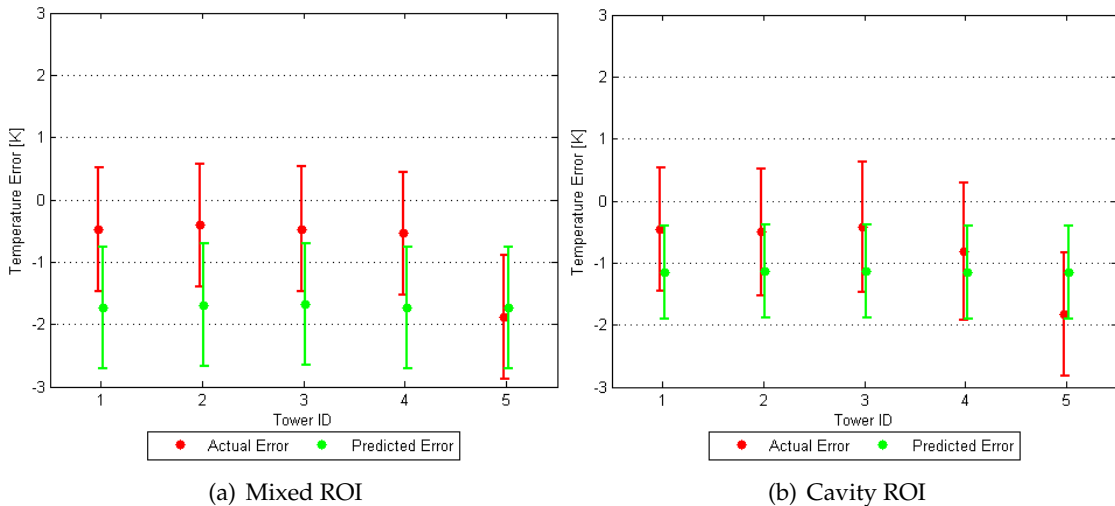


Figure 6.15: The actual and the predicted temperature error with uncertainty ranges for the 20may04E04 image using the microbolometer spectral response.

SRNL 20jun05G09 image

22:17 EDT, 20 June 2005 at 350 ft (106.7 m) with a GSD of 0.15 m.
(Parameterized Model Prediction - Microbolometer Response)

Mixed ROI: (RMS error = 0.76 K)

$$\hat{y}_1 = -17.0723 - 0.0339 x_1 + 10.9377 x_2 + 0.0345 x_3 - 0.0066 x_4 + 0.0208 x_5 + 0.0015 x_6 + 0.0019 x_7$$

Cavity ROI: (RMS error = 0.18 K)

$$\hat{y}_2 = -1.9687 - 0.0228 x_1 + 1.5928 x_2 + 0.0051 x_3 - 0.0007 x_4 + 0.0204 x_5 - 0.0014 x_6 - 0.0013 x_7$$

ID	x_1 [K]	x_2 []	x_3 [K]	x_4 [°]	x_5 [K]	x_6 [K]	x_7 [m]
H1	293.68 ± 3.00	0.90 ± 0.04	264 ± 12	29 ± 6	296.39 ± 0.40	293.17 ± 2.00	8 ± 3
H2	293.65 ± 3.00	0.90 ± 0.04	264 ± 12	29 ± 6	296.39 ± 0.40	293.17 ± 2.00	8 ± 3
H3	292.01 ± 3.00	0.90 ± 0.04	264 ± 12	29 ± 6	296.39 ± 0.40	293.17 ± 2.00	4 ± 1
H4	293.48 ± 3.00	0.90 ± 0.04	264 ± 12	29 ± 6	296.39 ± 0.40	293.17 ± 2.00	8 ± 3

Table 6.30: Predictor estimates used in the 20jun05G09 parameterized regression model.

	Mixed ROI		Cavity ROI	
ID	Image ΔT [K]	Predicted ΔT [K]	Image ΔT [K]	Predicted ΔT [K]
H1	0.16 ± 1.11	-1.47 ± 0.98	0.84 ± 1.02	-0.24 ± 0.21
H2	1.10 ± 1.10	-1.47 ± 0.98	1.28 ± 1.00	-0.24 ± 0.21
H3	-1.56 ± 1.52	-1.42 ± 0.98	-0.22 ± 1.12	-0.20 ± 0.21
H4	1.21 ± 1.15	-1.48 ± 0.98	1.42 ± 1.03	-0.25 ± 0.21

Table 6.31: Comparison of the actual and predicted temperature errors for the 20jun05G09 image using the microbolometer spectral response.

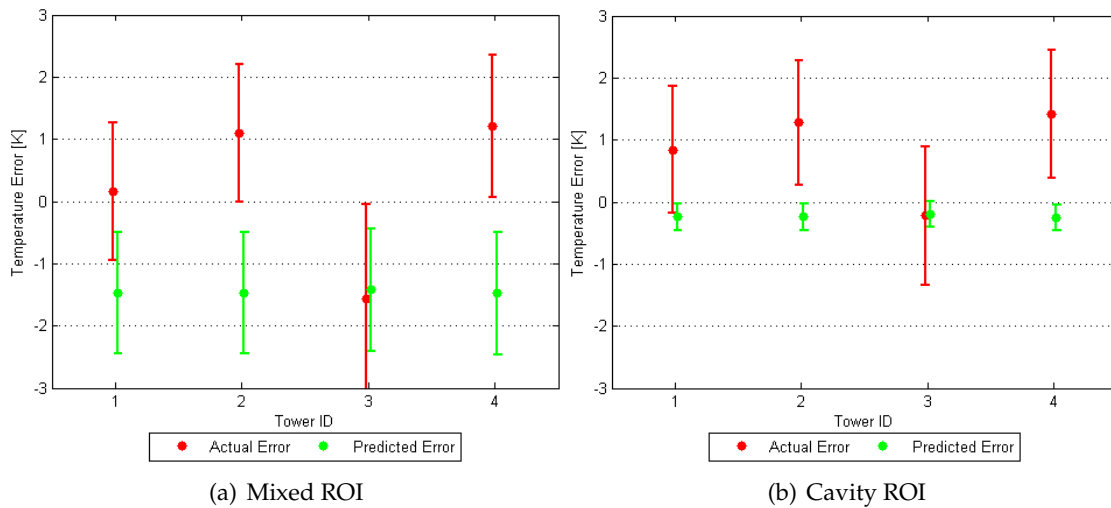


Figure 6.16: The actual and the predicted temperature error with uncertainty ranges for the 20jun05G09 image using the microbolometer spectral response.

The data presented in Figures 6.13 through 6.16 indicate that the spectral response function of the sensor does have a noticeable impact on the predicted temperature errors. The predicted errors are closer to the actual errors for both ROIs for the nadir images. The cavity ROI case shows the largest improvement in the prediction model performance. For the oblique image, the predicted errors moved slightly closer to the actual errors. There is a slight improvement in performance in that the uncertainty ranges now overlap for two of the four towers for the cavity ROI as opposed to just one of the towers for the flat spectral response.

6.3.7 Validity of Parameterized Model

The validity of the parameterized model may be checked to determine if the multiple linear regression model is a good fit to the LUT data. The tests described in Section B.3 were applied to the 20may04D14 data set with the flat spectral response and the mixed ROI to determine if the parameterized model adequately fit the LUT data.

A plot of the standardized residuals versus the fitted responses (predicted temperature errors) is shown in Figure 6.17(a). The data points in this plot should not display any distinct pattern if the regression model was a good fit to the data. Instead, the data points clearly resemble an overall parabolic pattern. This is a visual indication that the regression model is not a good fit to the LUT data.

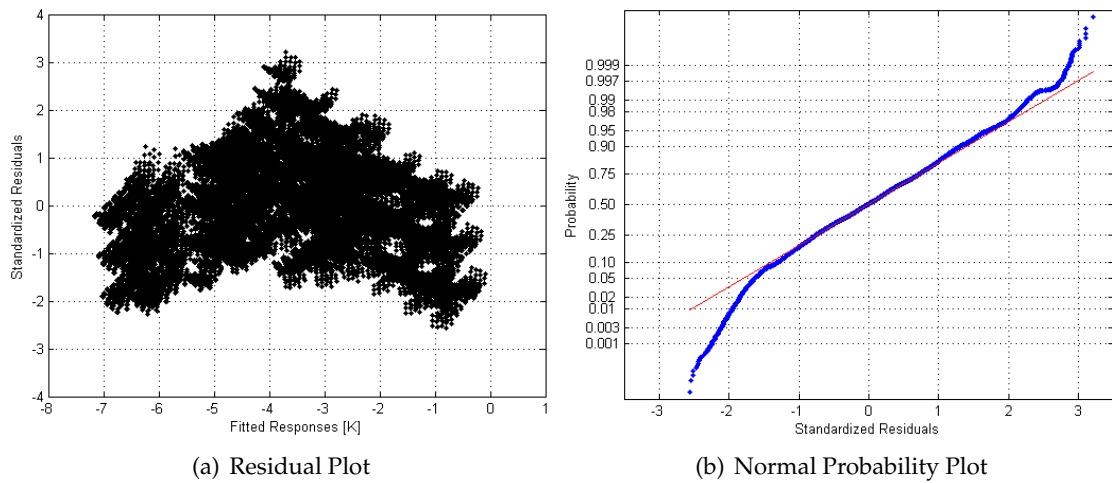


Figure 6.17: Diagnostic plots indicating a lack-of-fit of the multiple linear regression model to the 20may04D14 mixed ROI LUT data.

To get a quantitative understanding of possible lack-of-fit of the regression model, a normal probability plot of the standardized residuals was created (Figure 6.17(b)). The data points should lie on a straight line if the regression model was a good fit to the data. However, the data points exhibit curvature at extreme values. The Ryan-Joiner statistic computed in Minitab yielded a value of 0.9970. The critical value for the Ryan-Joiner test at $\alpha = 0.05$ is greater than 0.9984 [47]. Since the test statistic is below the critical value, the assumption of normality is invalid and therefore the regression model exhibits a lack-of-fit to the LUT data [48].

6.3.8 Look-up Table Interpolation

The analysis in Section 6.3.7 indicated that the multiple linear regression model did not adequately fit the LUT data. Although the parameterized model suffered from lack-of-fit, the errors introduced by the model were taken into account when predicting the temperature errors. The regression equations had an associated RMS error that described how well the regression model fit the look-up table data and these errors were incorporated into the uncertainties reported for the predicted temperature errors. In order to eliminate the error introduced by the regression, the predicted temperature error may be determined from the look-up table data directly without the use of a regression model.

The predicted temperature error is selected from the LUT through a nearest neighbor interpolation using all of the seven predictor parameters. The effectiveness of this LUT search method depends on the sampling resolution of the LUT. A more densely populated LUT should yield a better temperature error prediction.

For each of the SRNL images, the MDCT temperature errors were predicted using the LUT method. The estimated uncertainties in the predicted temperature errors were found from 1944 random physics model runs that were spanned by the LUT. The predicted temperature error for each random run using the LUT nearest neighbor interpolation method was compared to the actual temperature error of the random run. The RMS of all 1944 temperature error residuals was taken as the uncertainty for the LUT method. The results are shown in Figures 6.18 through 6.21.

The predicted temperature errors are similar to the predicted errors from the regression model. For nadir images, the LUT method and the parameterized model predicted temperature errors to within approximately 0.1 K of each other. The estimated uncertainty ranges are approximately one-third to one-half as much as the regression model uncertainties. The uncertainties associated with the LUT table are due to the coarse sampling of the LUT data. These results indicated that the LUT nearest neighbor interpolation method does not show a significant improvement over the parameterized model.

SRNL 20may04D14 image

02:02 EDT 20 May 2004 at 500 ft (152.5 m) with a GSD of 0.22 m.
(LUT Nearest Neighbor Interpolation)

ID	x_1 [K]	x_2 []	x_3 [K]	x_4 [°]	x_5 [K]	x_6 [K]	x_7 [m]
F1	293.11	0.90	267	0	292.87	291.06	3
F2	292.42	0.90	267	0	292.87	291.06	15
F3	292.46	0.90	267	0	292.87	291.06	20
F4	292.83	0.90	267	0	292.87	291.06	3
F5	292.98	0.90	267	0	292.87	291.06	3

Table 6.32: Predictor estimates used in the 20may04D14 LUT nearest neighbor interpolation.

ID	Mixed ROI		Cavity ROI	
	Image ΔT [K]	Predicted ΔT [K]	Image ΔT [K]	Predicted ΔT [K]
F1	-0.51 ± 1.03	-1.56 ± 0.36	-0.17 ± 1.02	-0.69 ± 0.14
F2	-0.41 ± 1.02	-1.54 ± 0.36	-0.27 ± 1.01	-0.69 ± 0.14
F3	-0.17 ± 1.04	-1.53 ± 0.36	-0.06 ± 1.02	-0.69 ± 0.14
F4	-0.19 ± 1.04	-1.56 ± 0.36	0.00 ± 1.03	-0.69 ± 0.14
F5	-1.51 ± 1.06	-1.56 ± 0.36	-1.09 ± 1.02	-0.69 ± 0.14

Table 6.33: Comparison of the actual temperature errors and the predicted temperature errors based on a LUT nearest neighbor interpolation for the 20may04D14 image.

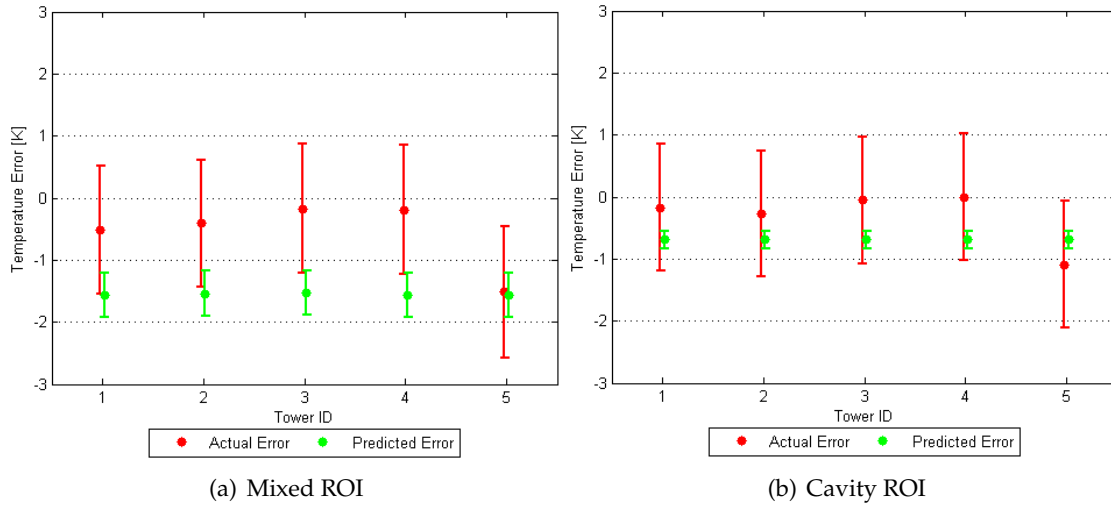


Figure 6.18: The actual temperature errors and the predicted temperature errors based on a LUT nearest neighbor interpolation with uncertainty ranges for the 20may04D14 image.

SRNL 20may04E02 image

02:04 EDT 20 May 2004 at 1000 ft (305.0 m) with a GSD of 0.43 m.
(LUT Nearest Neighbor Interpolation)

ID	x_1 [K]	x_2 []	x_3 [K]	x_4 [°]	x_5 [K]	x_6 [K]	x_7 [m]
F1	293.11	0.90	267	0	292.87	291.06	3
F2	292.48	0.90	267	0	292.87	291.06	15
F3	292.34	0.90	267	0	292.87	291.06	20
F4	292.76	0.90	267	0	292.87	291.06	3
F5	292.95	0.90	267	0	292.87	291.06	3

Table 6.34: Predictor estimates used in the 20may04E02 LUT nearest neighbor interpolation.

ID	Mixed ROI		Cavity ROI	
	Image ΔT [K]	Predicted ΔT [K]	Image ΔT [K]	Predicted ΔT [K]
F1	-0.56 ± 1.01	-1.59 ± 0.37	-0.43 ± 1.01	-0.89 ± 0.24
F2	-0.43 ± 1.01	-1.58 ± 0.37	-0.28 ± 1.00	-0.88 ± 0.24
F3	-0.17 ± 1.02	-1.57 ± 0.37	-0.10 ± 1.01	-0.88 ± 0.24
F4	-0.35 ± 1.01	-1.59 ± 0.37	-0.24 ± 1.01	-0.89 ± 0.24
F5	-1.46 ± 1.03	-1.59 ± 0.37	-1.27 ± 1.00	-0.89 ± 0.24

Table 6.35: Comparison of the actual temperature errors and the predicted temperature errors based on a LUT nearest neighbor interpolation for the 20may04E02 image.

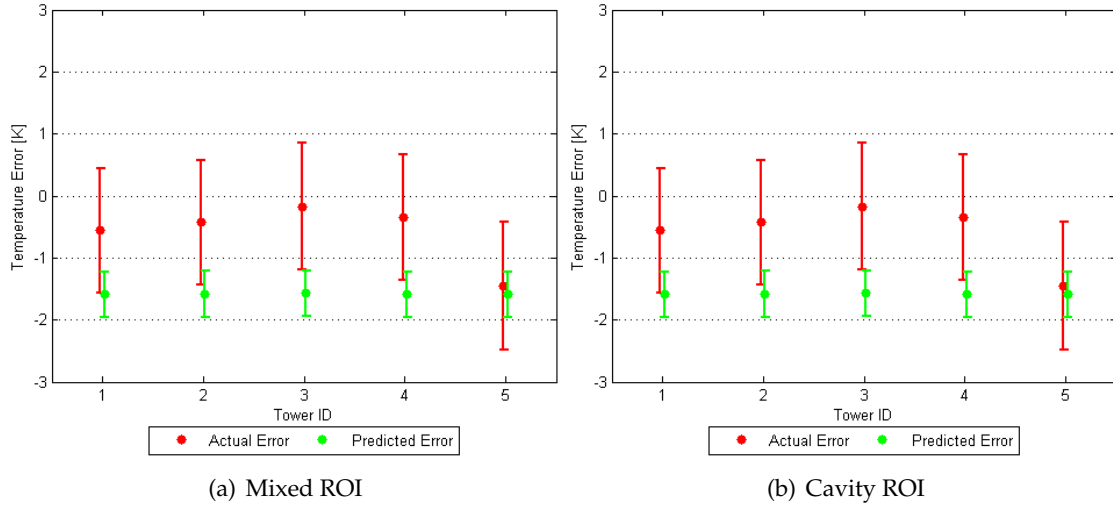


Figure 6.19: The actual temperature errors and the predicted temperature errors based on a LUT nearest neighbor interpolation with uncertainty ranges for the 20may04E02 image.

SRNL 20may04E04 image

02:07 EDT 20 May 2004 at 2000 ft (610.0 m) with a GSD of 0.85 m.
(LUT Nearest Neighbor Interpolation)

ID	x_1 [K]	x_2 []	x_3 [K]	x_4 [°]	x_5 [K]	x_6 [K]	x_7 [m]
F1	293.18	0.90	267	0	292.87	291.06	3
F2	292.74	0.90	267	0	292.87	291.06	15
F3	292.84	0.90	267	0	292.87	291.06	20
F4	293.19	0.90	267	0	292.87	291.06	3
F5	293.13	0.90	267	0	292.87	291.06	3

Table 6.36: Predictor estimates used in the 20may04E04 LUT nearest neighbor interpolation.

ID	Mixed ROI		Cavity ROI	
	Image ΔT [K]	Predicted ΔT [K]	Image ΔT [K]	Predicted ΔT [K]
F1	-0.48 ± 1.00	-1.74 ± 0.38	-0.46 ± 0.99	-1.31 ± 0.25
F2	-0.41 ± 0.99	-1.72 ± 0.38	-0.50 ± 1.02	-1.30 ± 0.25
F3	-0.47 ± 1.00	-1.71 ± 0.38	-0.43 ± 1.05	-1.29 ± 0.25
F4	-0.54 ± 0.99	-1.74 ± 0.38	-0.82 ± 1.11	-1.31 ± 0.25
F5	-1.88 ± 0.99	-1.74 ± 0.38	-1.83 ± 0.99	-1.31 ± 0.25

Table 6.37: Comparison of the actual temperature errors and the predicted temperature errors based on a LUT nearest neighbor interpolation for the 20may04E04 image.

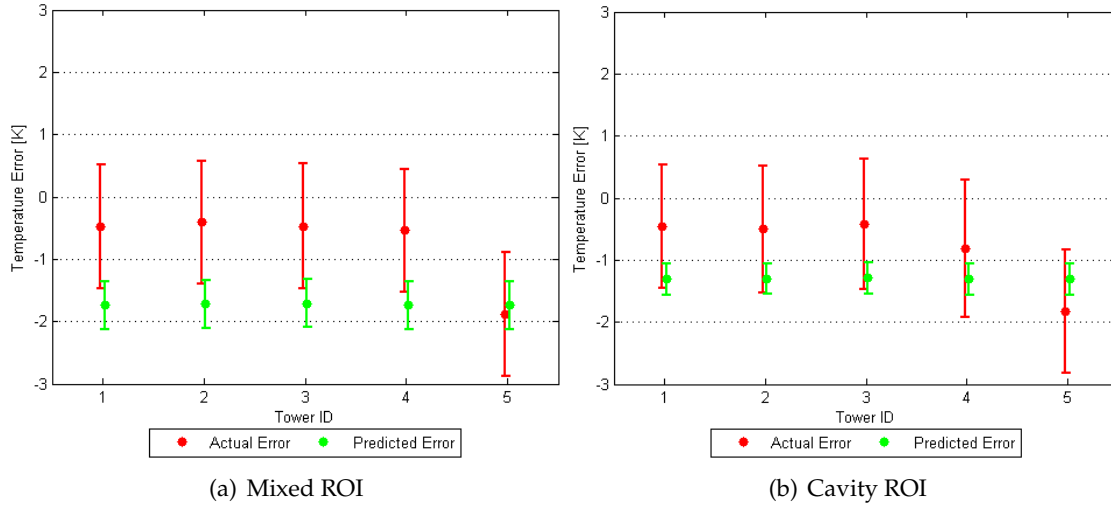


Figure 6.20: The actual temperature errors and the predicted temperature errors based on a LUT nearest neighbor interpolation with uncertainty ranges for the 20may04E04 image.

SRNL 20jun05G09 image

22:17 EDT, 20 June 2005 at 350 ft (106.7 m) with a GSD of 0.15 m.
(LUT Nearest Neighbor Interpolation)

ID	x_1 [K]	x_2 []	x_3 [K]	x_4 [°]	x_5 [K]	x_6 [K]	x_7 [m]
H1	293.68	0.90	264	29	296.39	293.17	8
H2	293.65	0.90	264	29	296.39	293.17	8
H3	292.01	0.90	264	29	296.39	293.17	4
H4	293.48	0.90	264	29	296.39	293.17	8

Table 6.38: Predictor estimates used in the 20jun05G09 LUT nearest neighbor interpolation.

ID	Mixed ROI		Cavity ROI	
	Image ΔT [K]	Predicted ΔT [K]	Image ΔT [K]	Predicted ΔT [K]
H1	0.16 ± 1.11	-1.71 ± 0.36	0.84 ± 1.02	-0.74 ± 0.16
H2	1.10 ± 1.10	-1.71 ± 0.36	1.28 ± 1.00	-0.74 ± 0.16
H3	-1.56 ± 1.52	-1.73 ± 0.36	-0.22 ± 1.12	-0.76 ± 0.16
H4	1.21 ± 1.15	-1.71 ± 0.36	1.42 ± 1.03	-0.74 ± 0.16

Table 6.39: Comparison of the actual temperature errors and the predicted temperature errors based on a LUT nearest neighbor interpolation for the 20jun05G09 image.

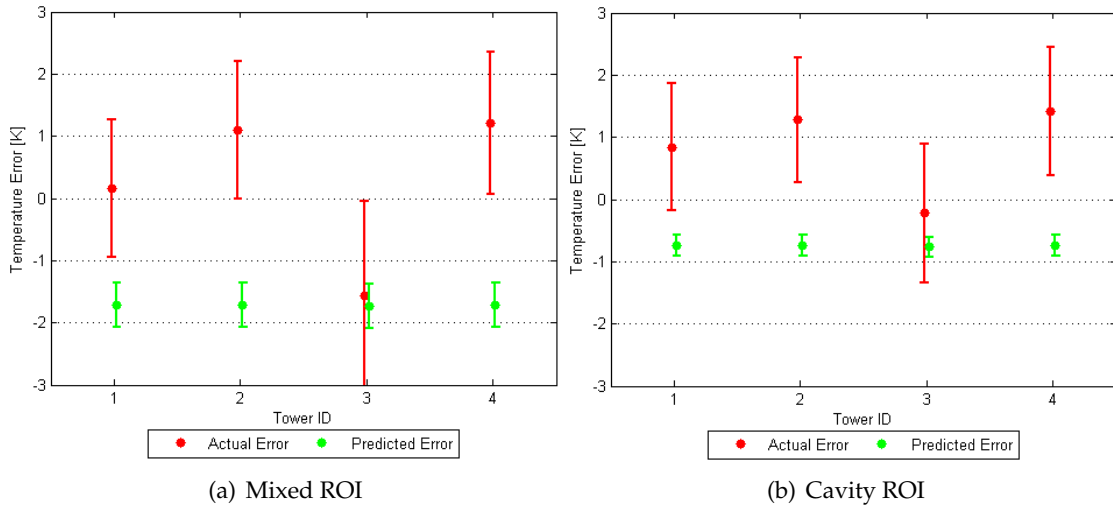


Figure 6.21: The actual temperature errors and the predicted temperature errors based on a LUT nearest neighbor interpolation with uncertainty ranges for the 20jun05G09 image.

6.4 Results Summary

The methodology developed in Chapter 5 was used to generate a parameterized model to predict the temperature error of an MDCT from a thermal image. The physics model parameter values were chosen to cover the range of expected values in the SRNL data set. A parameterized model was generated for the SC 2000 sensor. It was first tested against a simulated data set with 1944 data points. The parameterized model performed well with this random data set producing RMS errors of less than 0.4 K. The model was then used to predict the temperature errors found in the SRNL data set. After taking into account uncertainties in the ground-truth measurements, image ROI temperature, atmospheric compensation, and sensor accuracy, the predicted temperature errors could be compared to the actual temperature errors. The results show that the parameterized model was able to predict the temperature error of the MDCTs to within 1.3 K and 0.7 K of the actual temperature errors for the nadir images for the mixed and cavity ROIs, respectively. For the oblique image, the predicted temperature errors were within 3 K of the actual temperature errors but were as good as 0.5 K in one case. The actual temperature errors are greatly influenced by the amount of error in the atmospheric compensation. The sensitivity of the spectral response of the sensor was also investigated. Using a realistic spectral response function for a microbolometer instead of an ideal flat response, the predicted temperature errors were similar to the previous results for the nadir images. For the oblique image however, the predicted temperature errors with the realistic spectral response improved to within 2.7 K and 1.7 K for the mixed and cavity ROI, respectively. Finally, the predicted temperature errors could also be determined from the LUT data directly through the use of a nearest neighbor interpolation scheme. The resulting predicted temperature errors were similar to those determined from the parameterized regression model. To avoid introducing additional errors due to any lack-of-fit of the parameterized model, the use of the LUT directly to determine the temperature correction factor is recommended.

Chapter 7

Summary and Conclusions

Before I came here I was confused about this subject. Having listened to your lecture I am still confused, but on a higher level.

- Enrico Fermi

Determining the internal temperature of a mechanical draft cooling tower from remotely-sensed thermal imagery is important for many applications that provide input to energy-related process models. Data taken of MDCT units at SRS by the Savannah River National Lab indicated a difference between the measured ground-truth temperature of the cooling towers and the derived apparent temperature from the thermal images. The temperature error was defined as the difference between the apparent temperature of the MDCT in the thermal image and the ground-truth temperature. The objective of this research was to estimate the temperature of the air exiting an MDCT by correlating the temperature of the exit air to the apparent temperature of pixels inside the fan stack of the tower in a thermal image.

The derivation of the absolute temperature of a material surface from remote imagery is a complex process in general. The imaging chain approach was followed from the emission of thermal photons of a material, through their interaction with the radiometric environment, their collection and detection by a sensor, and finally the production of a thermal image. Many methods and tools exist to convert the at-sensor apparent temperature into the absolute temperature of the target material. Each of these methods is specific to a certain set of circumstances. The problem of determining the temperature of an MDCT is unique due to the geometry of the tower and due to the exhausted water vapor plume. Given the existing methods of temperature retrieval and the uniqueness of this problem, a methodology was developed to predict the temperature correction needed to determine the exit air temperature of an MDCT from a thermal image.

The methodology is based on physically modeling the three-dimensional radiometric environment of an MDCT. Studies were performed on the sensitivity of specific aspects of the radiance leaving the fan stack opening of the tower and on the radiance propagating through the exhausted plume. These studies allowed constraints to be placed on several variables in order to assist the creation of the physical model. Conclusions of these studies showed that pixels within the cavity of an MDCT have a unit effective emissivity while pixels from shallow surfaces of an MDCT have an effective emissivity less than unity. Results of the plume studies show that the contribution of the exhausted plume to the temperature error was less than the expected residual error from typical atmospheric compensation techniques.

The approach constructed to predict the MDCT temperature error begins with the physical model. The physics model was used to simulate and predict the radiance reaching the sensor from the MDCT. It consisted of 32,400 parameter value combinations to cover the range of suspected values in the SRNL data set. These runs were processed with an ideal LWIR sensor that consisted of a unit spectral response between 8 - 14 μm and no spatial blurring. A multiple linear regression model was fit to this sensor data set. The RMS error of the regression model was 0.77 K and 0.12 K for the mixed ROI and cavity ROI, respectively.

A sensor model based on specifications from an actual sensor was then used to process the physics model data set. The Inframetrics SC 2000 IR camera was used to collect thermal imagery of MDCT units at SRS. Next, 1944 random physics model data points were produced such that the parameter values were encompassed by the range of values in the physics data set. The random data points were tested with the SC 2000 regression equation. The corresponding RMS values for the mixed ROI and cavity ROI were 0.38 K and 0.22 K, respectively, which indicates a good temperature error prediction by the regression model.

The ultimate test of the regression model was to use it with actual image data. The SRNL data set was first atmospherically compensated using an interpolated radiosonde profile. The actual temperature error is the difference between the ground-truth measurement and the image mean ROI temperature. Uncertainties in the ground measurement, ROI temperature, atmospheric compensation, and sensor temperature measurement were all incorporated to produce an overall temperature error uncertainty. The uncertainty in the atmospheric compensation was found to have a significant impact on the uncertainty in

temperature error. The parameterized regression model was then used to predict the temperature error for the MDCTs in each SRNL image. Values for the seven predictor parameters of the parameterized model were estimated based on actual measurements or on models of the processes occurring in the scene. The uncertainties in the estimates of each predictor value were incorporated into the uncertainty in the overall predicted temperature error. The predicted temperature errors were compared to the actual measured temperature errors in each SRNL image. For some units, the parameterized model was able to predict the error to within less than 0.5 K. Overall, the parameterized model predictions for the nadir images were within 1.3 K and 0.7 K for the mixed and cavity ROIs, respectively. For the oblique image, the parameterized model predictions were within 3 K of the actual temperature errors. The MDCT temperature errors were also determined from the LUT data directly through the use of a nearest neighbor interpolation scheme. The LUT method produced similar results to that of the parameterized model method. Lastly, the spectral response of the sensor was found to have an important influence on the predicted temperature errors. Using a realistic spectral response function, the temperature error prediction showed improved results.

The exit air temperature of a mechanical draft cooling tower can be derived from a remotely-sensed thermal image. The parameterized model produced excellent results with a simulated data set. The model had very good success with the actual SRNL images with a nadir viewing geometry. The performance was less than ideal for the SRNL image with an oblique viewing geometry.

7.1 Recommendations

To rigorously test the methodology, another ground-truth measurement collect is recommended. Atmospheric profile and MDCT measurements should be made as accurately as possible. This would include the use of a radiosonde launched at the time of image acquisition to obtain an accurate atmospheric temperature and humidity profile. Also, multiple temperature measurements of the target from different temperature sensors is highly desirable. These targets would include the exit air temperature of the MDCT at multiple heights in and above the fan stack opening, the decking temperature, the fan blade temperature, the interior fan stack temperature, the drift eliminator temperature, and the ambient temperature and dew point from multiple points around the MDCT perimeter. Emissivity measurements of the fan blades, fan stack shroud, and decking should also be obtained. A thermally stable LWIR camera with a well-known spectral response and

noise characteristics is also recommended to reduce errors in the data collection. The camera should be mounted on a stable platform with accurately measured orientation information. The result of this project emphasized the need for accurate ground truth measurements, atmospheric state knowledge, and sensor design information.

Appendix A

Derivation of the Planck Blackbody Radiation Equation

A blackbody is an object that absorbs all electromagnetic radiation that falls onto it. No light is transmitted through it or reflected off it. Black bodies emit only thermal radiation and the amount is directly related to their temperature. A small opening into a large cavity is considered a blackbody. Any light entering the hole would have to reflect off the walls of the cavity multiple times before it escapes. If the cavity is heated, the spectrum of the hole's radiation will be continuous and will not depend on the material in the cavity. This derivation is adopted from Schroeder (2000) [49].

A.1 Statistical Physics

The key concept in statistical mechanics is the probability of finding a system in a particular microstate when that system is in thermal equilibrium with its environment. The system can be almost anything but here a single particle will be considered as the system of interest. The microstates are the energy levels the particle may exist in. If the particle was completely isolated from the rest of universe then its energy would be fixed and all the microstates associated with that energy would be equally probable. For a particle constantly interacting with its environment, it may still be found in any microstate but some states will be more likely than others depending on the energy of the microstate. The probability of microstate s occurring is

$$P(s) = \frac{1}{Z} e^{-\epsilon(s)/kT}, \quad (\text{A.1})$$

where $\epsilon(s)$ is the energy of the microstate, T is the absolute temperature of the system, and k is Boltzmann's constant ($k = 1.38 \cdot 10^{-23} \text{ J/K}$). The normalization factor, Z , is found

by realizing that the total probability of finding the system in *some* state is unity so

$$1 = \sum_s P(s) = \sum_s \frac{1}{Z} e^{-\epsilon(s)/kT} = \frac{1}{Z} \sum_s e^{-\epsilon(s)/kT}. \quad (\text{A.2})$$

Solving for Z therefore gives

$$Z = \sum_s e^{-\epsilon(s)/kT}. \quad (\text{A.3})$$

The quantity Z is known as the **partition function** and the quantity $e^{-\epsilon(s)/kT}$ is known as the **Boltzmann factor**. The partition function essentially counts how many microstates are accessible to the system. It does not depend on any particular state, s , but does depend on the temperature, T . In words, equation (A.1) gives the probability that the particle will have energy, $\epsilon(s)$, given a temperature, T (probability that the particle will be in state s given temperature, T).

The average value of the particle energies, $\bar{\epsilon}$, at a particular temperature is the sum of the energy of a microstate multiplied by the probability of that state occurring:

$$\bar{\epsilon} = \sum_s \epsilon(s) P(s) = \frac{1}{Z} \sum_s \epsilon(s) e^{-\epsilon(s)/kT} \quad (\text{A.4})$$

The average energy can be rewritten by letting $\beta = 1/kT$ and writing the term inside the summation as a partial derivative:

$$\bar{\epsilon} = \frac{1}{Z} \sum_s \epsilon e^{-\beta\epsilon} = -\frac{1}{Z} \sum_s \frac{\partial}{\partial \beta} e^{-\beta\epsilon} = -\frac{1}{Z} \frac{\partial}{\partial \beta} \left(\sum_s e^{-\beta\epsilon} \right) = -\frac{1}{Z} \frac{\partial Z}{\partial \beta} \quad (\text{A.5})$$

A.2 Planck Distribution

The basic quantum of electromagnetic radiation is known as a photon. Photons have both particle-like properties such as momentum, and wave-like properties such as frequency. The energy of a single photon depends only on its frequency:

$$\epsilon = h\nu \quad (\text{A.6})$$

where ν is the frequency and h is Planck's constant ($h = 6.626 \cdot 10^{-34} \text{ J s}$).

Radiation trapped inside a box can be thought of as a combination of standing wave patterns. Each standing wave acts as a harmonic oscillator with frequency, ν . Planck made

the assertion that each oscillator could take on only certain energy values. The allowed energy states for a quantum oscillator are

$$\epsilon_n = (n + 1/2)h\nu = 1/2h\nu + nh\nu, \quad \text{for } n = 0, 1, 2, \dots \quad (\text{A.7})$$

Considering only the energy with respect to the ground state, the allowed energy levels are

$$\epsilon_n = nh\nu = n\epsilon, \quad \text{for } n = 0, 1, 2, \dots \quad (\text{A.8})$$

The partition function for a single oscillator is then

$$Z = 1 + e^{-h\nu/kT} + e^{-2h\nu/kT} + e^{-3h\nu/kT} + \dots = \frac{1}{1 - e^{-h\nu/kT}}, \quad (\text{A.9})$$

where the geometric series,

$$\frac{1}{1 - q} = 1 + q + q^2 + q^3 + \dots, \quad (\text{A.10})$$

was used with $q = e^{-h\nu/kT}$ to arrive at the result in equation (A.9). The average energy of the photons is calculated from equation (A.5) as

$$\bar{\epsilon} = \frac{\epsilon}{e^{\epsilon/kT} - 1} = \frac{h\nu}{e^{h\nu/kT} - 1}. \quad (\text{A.11})$$

This equation is known as the **Planck distribution** and gives the average energy of the photons at temperature, T .

A.3 Total Energy of the States

For a photon in a box, its wavefunction must vanish at the walls. In a one-dimensional box of length L , the allowed wavelengths of the photon are

$$\lambda = \frac{2L}{n} \quad \text{for } n = 1, 2, 3, \dots \quad (\text{A.12})$$

The energy of a photon is given as

$$\epsilon = pc = \frac{hcn}{2L} \quad (\text{A.13})$$

where de Boglie's relation, $p = h/\lambda$, was used to write the momentum of the photon in terms of its wavelength. In three dimensions the momentum becomes a vector and the

energy is the speed of light times the magnitude of the vector:

$$\epsilon = c\sqrt{p_x^2 + p_y^2 + p_z^2} = \frac{hc}{2L}\sqrt{n_x^2 + n_y^2 + n_z^2} = \frac{hcn}{2L} \quad (\text{A.14})$$

where n is now the magnitude of the \vec{n} vector.

The total energy in all states is the sum of the average energy of the states,

$$U = 2 \sum_{n_x} \sum_{n_y} \sum_{n_z} \bar{\epsilon} = 2 \sum_{n_x} \sum_{n_y} \sum_{n_z} \frac{\epsilon}{e^{\epsilon/kT} - 1} = 2 \sum_{n_x} \sum_{n_y} \sum_{n_z} \frac{hcn}{2L} \frac{1}{e^{hcn/2LkT} - 1}, \quad (\text{A.15})$$

where the factor of two is needed to account for the two polarization states of the photon since both polarization states have the same energy (same frequency). Equations (A.11) and (A.14) were used to express the total energy in terms of n . Since the number of terms is so large, the expression in the sum can be considered continuous. The summations can then be written as integrals. The integration is performed in spherical coordinates over a volume, dV , in n -space as

$$U = \int_{n=0}^{\infty} \int_{\theta=0}^{\pi/2} \int_{\phi=0}^{\pi/2} \frac{hcn}{L} \frac{1}{e^{hcn/2LkT} - 1} n^2 \sin \theta d\theta d\phi dn, \quad (\text{A.16})$$

where $dV = n^2 \sin \theta d\theta d\phi dn$. The angular limits of the θ and ϕ integrals are necessary to take the volume of $1/8$ of a sphere in n -space in order to count only the positive values of n . Evaluating the angular integrals in equation (A.16) reduces the equation to

$$U = \int_{n=0}^{\infty} \frac{hc}{L} \frac{\pi}{2} \frac{n^3}{e^{hcn/2LkT} - 1} dn. \quad (\text{A.17})$$

The total energy can be expressed in terms of the photon energy using equation (A.14) to change variables which results in

$$U = \int_0^{\infty} \frac{8\pi L^3}{h^3 c^3} \frac{\epsilon^3}{e^{\epsilon/kT} - 1} d\epsilon. \quad (\text{A.18})$$

The volume of the box containing the photons is $V = L^3$. The total energy per unit volume can then be expressed as

$$\frac{U}{V} = \int_0^{\infty} \frac{8\pi}{h^3 c^3} \frac{\epsilon^3}{e^{\epsilon/kT} - 1} d\epsilon. \quad (\text{A.19})$$

A.4 Planck Spectral Energy Density

The integrand in equation (A.19) is known as the energy density per unit photon energy,

$$u(\epsilon) = \frac{8\pi}{h^3 c^3} \frac{\epsilon^3}{e^{\epsilon/kT} - 1}. \quad (\text{A.20})$$

This is the Planck equation for the energy density of the photons.

Changing units in equation (A.19) from energy to frequency through the relation, $\epsilon = h\nu$ yields

$$u(\nu) = \frac{8\pi h \nu^3}{c^3} \frac{1}{e^{h\nu/kT} - 1}. \quad (\text{A.21})$$

Changing units in equation (A.19) from energy to wavelength through the relation, $\epsilon = hc/\lambda$ yields

$$u(\lambda) = \frac{8\pi hc}{\lambda^5} \frac{1}{e^{hc/\lambda kT} - 1}. \quad (\text{A.22})$$

A.5 Blackbody Spectral Exitance

The energy density derived in the last section is the energy of the photons in the box per unit volume. Suppose a small hole is cut in the box so photons are allowed to escape. The photons that escape out the hole during time interval dt are from a hemispherical shell of radius R inside the box. The thickness of the shell is $c \cdot dt$. The photons in the shell that escape are those that were traveling towards the hole.

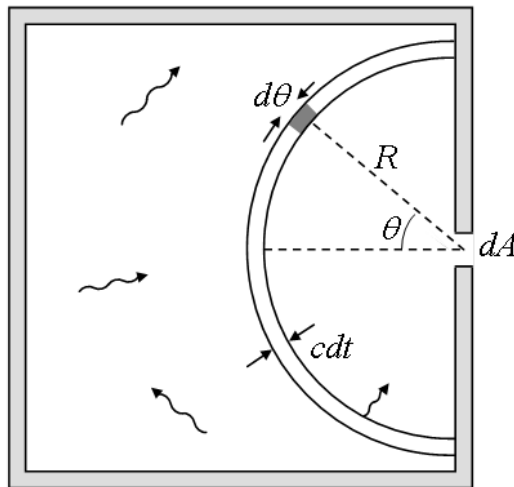


Figure A.1: Photons escaping the cavity from a thin shell inside the cavity [49]

Consider a small volume element in spherical coordinates, $dV = R^2 \sin \theta d\theta d\phi c dt$. Photons in this element are oriented in all directions. The probability of a photon traveling towards the hole is the apparent area of the hole (as viewed from the element) divided by the total area of a sphere of radius R centered on the element. This is written as

$$\text{Probability of escape} = \frac{dA \cos \theta}{4\pi R^2}. \quad (\text{A.23})$$

The energy from the element escaping out the hole is then the energy density times the volume of the element times the probability of the photons escaping:

$$\text{Energy escaping from element} = u(\epsilon) \frac{dA \cos \theta}{4\pi R^2} R^2 \sin \theta d\theta d\phi c dt. \quad (\text{A.24})$$

The total energy escaping from the hole in time dt is the integral over the entire shell:

$$\begin{aligned} U_{\text{exit}} &= u(\epsilon) \frac{dA c dt}{4\pi} \int_{\phi=0}^{2\pi} \int_{\theta=0}^{\pi/2} \cos \theta \sin \theta d\theta d\phi \\ &= \frac{c}{4} dA dt u(\epsilon). \end{aligned} \quad (\text{A.25})$$

The irradiance leaving the hole, or exitance M , is the energy per unit time per unit area and is found by rearranging equation (A.25) as

$$M = \frac{U_{\text{exit}}}{dA dt} = \frac{c}{4} u(\epsilon). \quad (\text{A.26})$$

The blackbody spectral exitance can now be found from the energy density as

$$M_{BB}(\epsilon) = \frac{2\pi}{h^3 c^2} \frac{\epsilon^3}{e^{\epsilon/kT} - 1}, \quad (\text{A.27})$$

or in terms of frequency and wavelength as

$$M_{BB}(\nu, T) = \frac{2\pi h \nu^3}{c^2} \frac{1}{e^{h\nu/kT} - 1} \quad (\text{A.28})$$

$$M_{BB}(\lambda, T) = \frac{2\pi h c^2}{\lambda^5} \frac{1}{e^{hc/\lambda kT} - 1}. \quad (\text{A.29})$$

A.6 Blackbody Spectral Radiance

The radiance, L , is the energy per unit time per unit area emitted per unit solid angle. The relationship between the radiance and the exitance of a material is defined as

$$dM = L \cos \theta d\Omega = L \cos \theta \sin \theta d\theta d\phi. \quad (\text{A.30})$$

The total exitance into the hemisphere above the blackbody is found by integrating both sides over the entire hemisphere:

$$M = \int_{\phi=0}^{2\pi} \int_{\theta=0}^{\pi/2} L \cos \theta \sin \theta d\theta d\phi. \quad (\text{A.31})$$

A blackbody is a Lambertian radiator by definition so the radiance, L , does not depend on angle and may be considered a constant of integration. The result of the integration over the hemisphere is π . The relation between the radiance and exitance of a blackbody is then

$$L = \frac{M}{\pi}. \quad (\text{A.32})$$

The spectral radiance of a blackbody is finally

$$L_{BB}(\epsilon, T) = \frac{2}{h^3 c^2} \frac{\epsilon^3}{e^{\epsilon/kT} - 1}, \quad (\text{A.33})$$

or in terms of frequency and wavelength as

$$L_{BB}(\nu, T) = \frac{2h\nu^3}{c^2} \frac{1}{e^{h\nu/kT} - 1} \quad (\text{A.34})$$

$$L_{BB}(\lambda, T) = \frac{2hc^2}{\lambda^5} \frac{1}{e^{hc/\lambda kT} - 1}. \quad (\text{A.35})$$

A.7 Total Blackbody Radiated Power

The total radiated power of a blackbody can be found by integrating the Planck equation over all wavelengths. Equation (A.29) gives the radiant flux per unit area per unit wavelength and is rewritten here as

$$\frac{\Phi}{dA d\lambda} = \frac{2\pi hc^2}{\lambda^5} \frac{1}{e^{hc/\lambda kT} - 1}. \quad (\text{A.36})$$

The total power is found by rearranging the equation and integrating over all wavelengths as

$$\Phi = dA \int_0^{\infty} \frac{2\pi hc^2}{\lambda^5} \frac{1}{e^{hc/\lambda kT} - 1} d\lambda. \quad (\text{A.37})$$

Substituting $x = hc/\lambda kT$ yields

$$\Phi = dA \frac{2\pi k^4 T^4}{h^3 c^2} \int_0^{\infty} \frac{x^3}{e^x - 1} dx. \quad (\text{A.38})$$

The integral over x evaluates to $\pi^4/15$. Substituting this value yields

$$\Phi = dA \frac{2\pi^5 k^4}{15 h^3 c^2} T^4. \quad (\text{A.39})$$

Grouping the constants and representing the differential area as the radiating surface area, A , the total radiated power of a blackbody of a given area is

$$\Phi = A \sigma T^4. \quad (\text{A.40})$$

The constant σ equals $5.6704 \cdot 10^{-8} \text{ [J/s/m}^2/\text{K}^4\text{]}$ and is known as the *Stefan-Boltzmann* constant. Equation (A.40) is usually referred to as the *Stefan-Boltzmann Law*.

A.8 Wavelength of Maximum Emission

The Planck spectrum is a well-behaved function with a single maximum as indicated in Figure A.2. The wavelength corresponding to the maximum emission can be found by differentiating equation (A.29) and equating it to zero:

$$\frac{\partial L}{\partial \lambda} = \frac{2hc^2}{e^{hc/\lambda kT} - 1} \left[-\frac{5}{\lambda^6} \right] + \frac{2hc^2}{\lambda^5} \left[\frac{e^{hc/\lambda kT}}{(e^{hc/\lambda kT} - 1)^2} \frac{hc}{kT} \frac{1}{\lambda^2} \right] = 0. \quad (\text{A.41})$$

Rearranging equation (A.41) yields

$$\frac{hc}{\lambda kT} \cdot \frac{1}{1 - e^{hc/\lambda kT}} - 5 = 0. \quad (\text{A.42})$$

Let $x = hc/\lambda kT$ and substitute to yield

$$\frac{x}{1 - e^x} - 5 = 0. \quad (\text{A.43})$$

The solution to equation (A.43) is $x = 4.96511423$. Solving for λ yields

$$\lambda = \frac{hc}{xkT}. \quad (\text{A.44})$$

Evaluating the constants yields a relationship between the wavelength associated with the maximum radiance of a blackbody and the temperature of the blackbody:

$$\lambda_{peak} = \frac{2897.768 \text{ } [\mu\text{m K}]}{T} \quad [\mu\text{m}]. \quad (\text{A.45})$$

This relationship is referred to as *Wien's displacement law*.

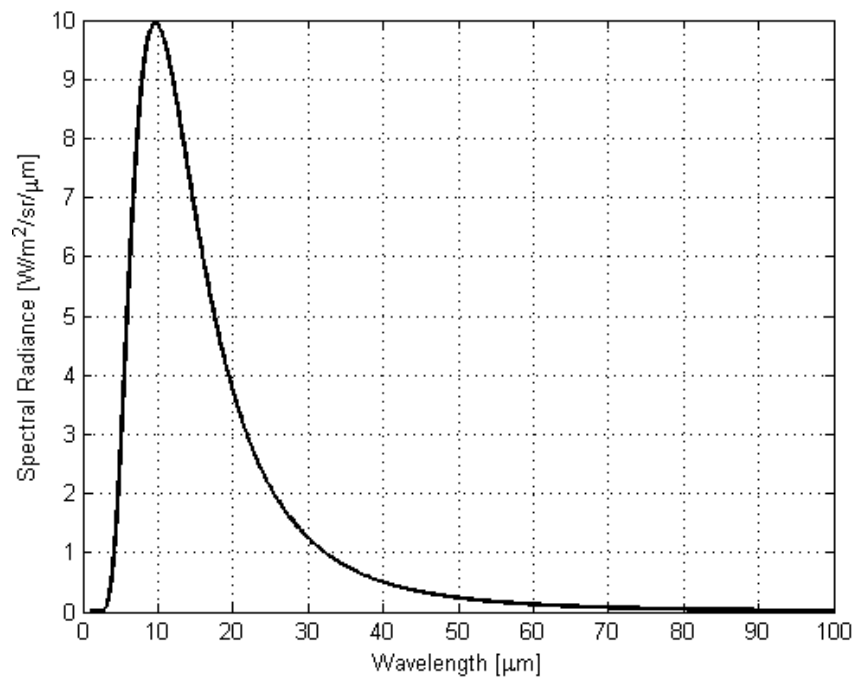


Figure A.2: Spectral radiance for a blackbody at a temperature of 300 Kelvin

Appendix B

Multiple Regression Analysis

Multiple regression analysis seeks to find a relationship between two or more quantitative variables so that one variable can be predicted from the others [43]. The variable to be predicted is known as the response (dependent variable) while the other variables are called predictors (independent variables). Since a perfect relationship between the response and the predictors may not exist, it is desirable to minimize the differences between the predicted values and the actual measured values of the responses. A brief overview of finding a statistical relationship between a dependent variable and multiple independent variables along with ways to test the fit of the model to the data is presented in this chapter.

B.1 Least-Squares Regression

An actual data set may contain a set of independent variables that were varied so that a dependent variable could be observed and measured. For the i^{th} observation, the dependent variable is denoted as Y_i and the independent variables are denoted as $x_{i,1}, x_{i,2}, \dots, x_{i,p-1}$ where $p - 1$ is the number of independent variables.

A linear model can be fit to this data in the form

$$Y_i = \beta_0 + \beta_{i,1} x_{i,1} + \beta_{i,2} x_{i,2} + \dots + \beta_{i,p-1} x_{i,p-1} + \varepsilon_i, \quad (\text{B.1})$$

where ε_i is the error term between the predicted response and the actual response. The error is a random variable and it expected to have a normal distribution with a zero mean [48]. Note that each predictor may be a power or product of other predictors (*i.e.*, $x_3 = x_1 x_2$). Equation (B.1) can be expressed in matrix notation as

$$\mathbf{Y} = \mathbf{X}\boldsymbol{\beta} + \boldsymbol{\varepsilon}, \quad (\text{B.2})$$

where the matrices are

$$\mathbf{Y}_{(nx1)} = \begin{bmatrix} Y_1 \\ Y_2 \\ \vdots \\ Y_n \end{bmatrix}, \quad \mathbf{X}_{(n \times p)} = \begin{bmatrix} 1 & x_{11} & x_{12} & \dots & x_{1,p-1} \\ 1 & x_{21} & x_{22} & \dots & x_{2,p-1} \\ \vdots & \vdots & \vdots & & \vdots \\ 1 & x_{n1} & x_{n2} & \dots & x_{n,p-1} \end{bmatrix}, \quad \boldsymbol{\beta}_{(p \times 1)} = \begin{bmatrix} \beta_0 \\ \beta_1 \\ \vdots \\ \beta_{p-1} \end{bmatrix}, \quad \boldsymbol{\varepsilon}_{(nx1)} = \begin{bmatrix} \varepsilon_1 \\ \varepsilon_2 \\ \vdots \\ \varepsilon_n \end{bmatrix}.$$

Let \mathbf{b} represent the vector of estimated regression coefficients so that the fitted (estimated) response values, \hat{Y} , are represented by

$$\hat{\mathbf{Y}} = \mathbf{X}\mathbf{b}. \quad (\text{B.3})$$

The difference between the observed values and the fitted values is known as the residuals ($\mathbf{e} = \mathbf{Y} - \hat{\mathbf{Y}}$). *Least-squares regression* attempts to choose \mathbf{b} in order to minimize the sum of the square residuals $\mathbf{e}'\mathbf{e}$. The least-squares regression coefficients are calculated by

$$\mathbf{b} = (\mathbf{X}'\mathbf{X})^{-1} \mathbf{X}'\mathbf{Y}. \quad (\text{B.4})$$

B.2 Analysis of Variance

The analysis of variance is based on sums of squares and on degrees of freedom associated with the response, Y [43]. There are several metrics that must be defined.

B.2.1 Sum of Squares

Error Sum of Squares (SSE) is a measure of the variation of the observations around the regression model:

$$SSE = \sum (Y_i - \hat{Y}_i)^2 = \mathbf{e}'\mathbf{e} = \mathbf{Y}'\mathbf{Y} - \mathbf{b}'\mathbf{X}'\mathbf{Y} \quad (\text{B.5})$$

The SSE is the sum of the squared residuals and $SSE = 0$ if the regression model predicted all the observations perfectly.

Regression Sum of Squares (SSR) is the sum of the square deviations between the predicted responses and the mean observed response:

$$SSE = \sum (\hat{Y}_i - \bar{Y})^2 = \mathbf{b}'\mathbf{X}'\mathbf{Y} - n\bar{Y}^2 \quad (\text{B.6})$$

For least-squares regression, the mean of the fitted values equals the mean of the observed responses.

Total Sum of Squares (SSTO) is the sum of the deviations between each response variable, Y_i , and the mean response:

$$SSTO = \sum (Y_i - \bar{Y})^2 = \mathbf{Y}'\mathbf{Y} - n\bar{Y}^2 \quad (\text{B.7})$$

If $SSTO = 0$, then all observations are the same. The total sum of squares is related to the square error and square regression by

$$SSTO = SSE + SSR. \quad (\text{B.8})$$

B.2.2 Mean Squares

A sum of squares divided by its associated degree of freedom is called a mean square [43].

Regression Mean Square (MSR) is the SSR divided by its degrees of freedom:

$$MSR = \frac{SSR}{p-1}. \quad (\text{B.9})$$

Error Mean Square (MSE) is the SSE divided by its degrees of freedom:

$$MSE = \frac{SSE}{n-p}. \quad (\text{B.10})$$

Recall from equation (B.1) that there are p coefficients and $p-1$ independent variables. Note that the degrees of freedom of the SSTO is the sum of the degrees of freedom of the SSR and SSE: $(p-1) + (n-p) = n-1$.

B.2.3 Coefficient of Multiple Determination

The coefficient of multiple determination is used as a goodness of fit of a regression model [44]. The coefficient is defined as

$$R^2 = \frac{SSR}{SSTO} = 1 - \frac{SSE}{SSTO}. \quad (\text{B.11})$$

The value of R^2 lies between 0 and 1. Higher values of R^2 correspond to smaller deviations (a better fit) between the predicted and observed response values.

The coefficient of determination is often adjusted to take into account the number of observations and the number of degrees of freedom [43]. The adjusted coefficient is then defined as,

$$R_a^2 = 1 - \frac{(n-1)}{(n-p)} \frac{SSE}{SSTO}. \quad (\text{B.12})$$

B.2.4 F-Test

It may be useful to test whether there is a statistically significant relation between a dependent variable, Y , and a set of independent variables, x_k . In terms of regression variables, it is possible to simultaneously test whether all $\beta_k = 0$ or alternatively whether at least one $\beta_k \neq 0$. This statement is written as

$$\begin{aligned} H_0 : \quad & \beta_1 = \beta_2 = \dots = \beta_{p-1} = 0 \\ H_1 : \quad & \text{at least one } \beta_k \neq 0. \end{aligned}$$

If all $\beta_k = 0$, then the response function reduces to $\hat{Y} = \beta_0$. Therefore, the predicted value of the response is the same for all x_k values and there is no regression relationship between the response and the independent variables [50]. The test statistic for this case is denoted F^* and is defined as

$$F^* = \frac{MSR}{MSE}. \quad (\text{B.13})$$

The decision as to whether to include a variable in the regression equation or not is defined by,

$$\begin{aligned} H_0 : \quad & F^* \leq F(1 - \alpha; p-1, n-p) \\ H_1 : \quad & F^* > F(1 - \alpha; p-1, n-p), \end{aligned}$$

where $F(\cdot)$ is the F distribution and $(1 - \alpha)100$ is the percentile of the F distribution. F distribution tables are included in many statistics textbooks.

B.3 Aptness of the Fitted Model

Once a model has been fit to the data, it is important to check the fit of the model to determine if the model is appropriate for the given data. A common way to check the fit of a model is through the use of residual diagnostic plots [48]. For these plots, standardized residuals are used. Standardization involves subtracting the mean value from each residual and then dividing by the standard deviation.

B.3.1 Standardized Residuals vs. Fitted Responses

A plot of the standardized residuals, e^* , versus the fitted responses, \hat{y} , provides a visual diagnostic of the fit of the model. The data points in this plot should be randomly distributed about zero, usually with the standardized residuals falling mostly between ± 2 . A good model fit is indicated by the lack of any distinct patterns in the plot [48].

B.3.2 Normal Probability Plot of Standardized Residuals

A normal probability plot of the standardized residuals investigates the assumption that the residuals from a least squares regression model should be normally distributed [48]. If the data points come from a normal distribution, they will fall on an approximately straight line which indicates a good model fit. If the data points come from some alternative distribution, the plot will exhibit some degree of curvature which would indicate a poor model fit.

A Ryan-Joiner test may be performed on the normal probability data to determine if the points fall sufficiently on a line. The Ryan-Joiner statistic is essentially a correlation coefficient of the data points in the normal probability plot. If the Ryan-Joiner statistic is below the critical value, the null hypothesis of a normal distribution is rejected and therefore the model is not a good fit to the data [47]. A Ryan-Joiner test may be computed in statistical analysis software such as Minitab. Some critical values for the Ryan-Joiner test are included in reference [47].

Appendix C

Propagation of Uncertainties

The uncertainty in a response can be calculated from the uncertainties of each predictor. An analytical solution can be derived from random variable statistics. An empirical solution can be found by observing the calculated responses of a large number of predictor distribution values. Both of these methods are based on a weighted sum of random variables to yield a response variable. Let y be a weighted sum of p random variables, x_i , so that

$$y = \alpha_0 + \alpha_1 x_1 + \alpha_2 x_2 + \dots + \alpha_p x_p = \alpha_0 + \sum_{i=1}^p \alpha_i x_i, \quad (\text{C.1})$$

where the α_i are real weighting constants [51].

C.1 Analytical Method

The uncertainty in the response may be derived analytically from equation (C.1). The expected value (mean) of the response, y , is written as

$$E[y] = E\left[\alpha_0 + \sum_{i=1}^p \alpha_i x_i\right] = E[\alpha_0] + E\left[\sum_{i=1}^p \alpha_i x_i\right] = \alpha_0 + \sum_{i=1}^p \alpha_i E[x_i]. \quad (\text{C.2})$$

The interpretation of equation (C.2) is that the mean value of a weighted sum of random variables is the weighted sum of the mean values of the random variables. The difference between the response and the expected value of the response (residual) is written as

$$\begin{aligned} y - E[y] &= \left(\alpha_0 + \sum_{i=1}^p \alpha_i x_i\right) - \left(\alpha_0 + \sum_{i=1}^p \alpha_i E[x_i]\right) \\ &= \sum_{i=1}^p \alpha_i x_i - \sum_{i=1}^p \alpha_i E[x_i] = \sum_{i=1}^p \alpha_i (x_i - E[x_i]). \end{aligned} \quad (\text{C.3})$$

The variance in the response, σ_y^2 , is the expected value of the square of the residual in y written as

$$\begin{aligned}\sigma_y^2 &= E \left[(y - E[y])^2 \right] = E \left[\left(\sum_{i=1}^p \alpha_i (x_i - E[x_i]) \right) \cdot \left(\sum_{i=1}^p \alpha_i (x_i - E[x_i]) \right) \right] \\ &= \sum_{i=1}^p \sum_{j=1}^p \alpha_i \alpha_j E \left[(x_i - E[x_i]) \cdot (x_j - E[x_j]) \right] = \sum_{i=1}^p \sum_{j=1}^p \alpha_i \alpha_j C_{ij},\end{aligned}\quad (C.4)$$

where C_{ij} is the covariance between x_i and x_j .

For the case where the random variables are uncorrelated such that $C_{ij} = \sigma_{x_i}^2$ for $i = j$ and $C_{ij} = 0$ for $i \neq j$, the variance in the response becomes

$$\sigma_y^2 = \sum_{i=1}^p \alpha_i^2 \sigma_{x_i}^2. \quad (C.5)$$

Equation (C.5) means that the variance of a weighted sum of uncorrelated random variables is the weighted sum of the variances of the random variables.

C.2 Empirical Method

The uncertainty in the response may also be found empirically from equation (C.1). For each random variable, a random value is selected based on a Gaussian distribution. The mean of the Gaussian is equal to the expected value of that random variable while the standard deviation is equal to the uncertainty value. A large number of trials ($N \gg p$) of each random variable is generated and then used in equation (C.1) to calculate the associated responses. The mean of these responses equals the expected value of the response and the standard deviation of the responses is equal to the uncertainty in the response.

Appendix D

Calculation of Effective Sky Temperature

The effective temperature of the sky dome in a given spectral band of a sensor can be computed from the DIRSIG `make_adb` utility. The utility uses a user-provided atmospheric profile in the form of a MODTRAN input data file (`tape5`) to calculate the hemispherically-integrated, spectral downwelling radiance. This radiance can then be spectrally sampled by a user-provided sensor spectral response and converted into an apparent temperature.

A MODTRAN input file (`tape5`) is supplied by the user. The file contains the atmospheric profile information (*i.e.*, altitude, pressure, temperature, humidity, etc.) derived from either one of the standard MODTRAN atmospheres or as a custom atmosphere created by the user. The purpose of the `make_adb` utility is to create an atmospheric database for scenes modeled in the DIRSIG environment. The database contains the spectral transmissions and path radiances for the viewing angles of the sensor. It also calculates the spatial distribution of the atmospheric downwelling radiance. To do so, the `make_adb` utility divides the sky hemisphere into discrete samples known as *quads*. The elevation direction is divided into six angles and the azimuth direction is divided into twelve angles. This results in 72 quads covering the hemisphere that are 15° tall in the elevation direction and 30° wide in the azimuth direction. For each point in the center of these quads, the path radiance is computed from MODTRAN using the profile specified by the user and auxiliary scene information (*i.e.*, time of day, location, etc.). In other words, the sensor is placed on the ground and targeted at the center of one of the quads. MODTRAN is run for this geometry and the thermal path radiance is recorded for that direction (quad). A table is built of the zenith and azimuth angle of the sample and the spectral path radiance from the sample. Therefore, the table contains spectral radiances for a total of 72 samples in the hemisphere which represent the spectral downwelling radiances for each of the 72 directions (quads). Finally, these 72 spectral radiances are spatially integrated to produce

a diffuse spectral downwelling radiance. The spatial integration is written as

$$L_d(\lambda) = \int_{2\pi} L(\theta, \phi, \lambda) \cos \theta d\Omega = \int_{\phi=0}^{2\pi} \int_{\theta=0}^{\frac{\pi}{2}} L(\theta, \phi, \lambda) \cos \theta \sin \theta d\theta d\phi \quad \left[\frac{W}{m^2 sr \mu m} \right]. \quad (D.1)$$

This diffuse downwelling spectral radiance is then sampled by the sensor's spectral response function and integrated to arrive at the integrated band radiance. This is written as

$$\hat{L} = \int L_d(\lambda) R'(\lambda) d\lambda \quad \left[\frac{W}{m^2 sr} \right]. \quad (D.2)$$

This integrated band radiance is then converted into an apparent temperature using the methods described in Section 3.6. The apparent temperature is known as the effective sky temperature in the given sensor spectral band.

Appendix E

Estimation of Plume Path Length

The plume length is the line-of-sight path length through the plume between the sensor and the tower throat. To assist the user in estimating the plume length, a simple plume model is considered. The estimated plume length is based on a Gaussian, continuous point-source plume model [52]. In this model, the centerline of the plume at any downrange distance, x , is calculated from knowledge of the wind speed, exhaust velocity, plume temperature and ambient temperature. The plume concentration at any point can also be calculated. The shape of the plume resembles a cone in which diffusion occurs only in the vertical and crosswind directions (z and y directions, respectively). The plume disperses in the vertical and crosswind directions according to a Gaussian distribution with dispersion coefficients σ_z and σ_y .

The plume is assumed to be a continuous point-source. The downwind direction is labeled x and the dispersion of the plume gas occurs only in the crosswind and vertical directions (y and z directions, respectively). The plume therefore has the appearance of a cone with the vertex as the source of emission. This model also assumes that the horizontal wind speed is constant and the mean wind direction is constant. The height of the plume source is H_e .

The centerline of the plume at a downwind distance x is calculated as

$$\Delta h = 1.6 F^{1/3} x^{2/3} u^{-1} \quad [m], \quad (\text{E.1})$$

where Δh is the change in centerline height relative to the height of the emission source, F is the buoyancy flux parameter, x is the downwind distance in meters, and u is the wind speed in meters per second. The buoyancy parameter characterizes the buoyancy of the stack exit gas and can be written as

$$F = g v_s r^2 \frac{T_s - T_a}{T_s} \quad \left[\frac{m^4}{s^3} \right], \quad (\text{E.2})$$

where $g = 9.807 \text{ [m/s]}$ is the acceleration due to gravity at earth's surface, v_s is the exit air velocity from the stack in meters per second, r is the radius of the stack in meters, T_s and T_a are the initial plume temperature as it exits the stack and the ambient air temperature in Kelvin, respectively.

Now that the centerline of the plume has been established, the dispersion in the vertical and crosswind directions may be calculated. The Gaussian dispersion coefficients are calculated by

$$\sigma = (Lx)(1 + Mx)^N \quad [m]. \quad (\text{E.3})$$

The constants L , M , and N are defined in Table E.1.

Stability	For Obtaining σ_z			For Obtaining σ_y		
	L	M	N	L	M	N
A - B	240	1.00	0.50	320	0.40	-0.50
C	200	0.00	0.00	220	0.40	-0.50
D	140	0.30	-0.50	160	0.40	-0.50
E - F	80	1.00	-0.50	110	0.40	-0.50

Table E.1: Constants used in the calculation of the vertical and crosswind dispersion coefficients for the Gaussian plume model in an urban environment [52].

The stability class mentioned in Table E.1 describes the atmospheric stability. The stability is determined by the ambient temperature gradient. The stability classes are listed in Table E.2 along with the average ambient gradient. The ambient temperature gradients are illustrated in Figure E.1.

Stability Class	Avg. Ambient Gradient [$^{\circ}\text{C} / \text{km}$]
A - very unstable	< -18.96
B - unstable	-18.05
C - slightly unstable	-16.04
D - neutral	-10.03
E - slightly stable	5.10
F - stable	> 14.95

Table E.2: Description of the six atmospheric stability classes and the associated ambient temperature gradients [52].

The continuous point-source Gaussian plume can now be described by the centerline (equation E.1) and the vertical and crosswind dispersion coefficients (equation E.3). The dispersion coefficients are the standard deviation of plume gas concentration for the ver-

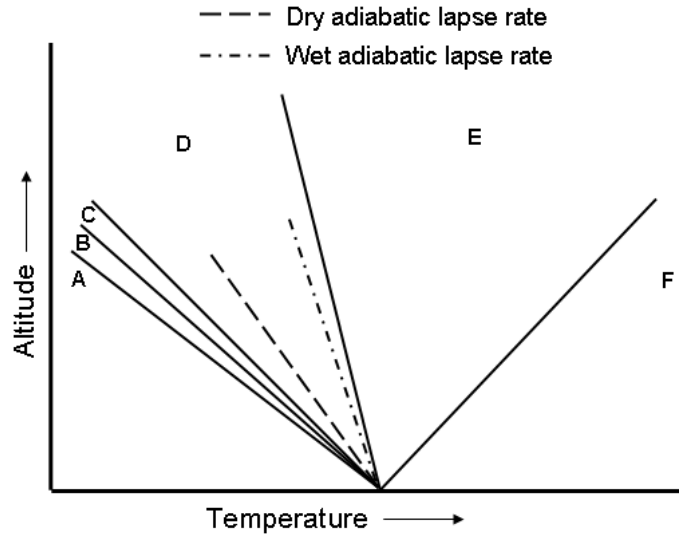


Figure E.1: Comparison of the six atmospheric stability classes using the associated ambient temperature gradients in reference to the dry and wet adiabatic lapse rates [52].

tical and crosswind Gaussian profiles.

The path length through the plume between the fan stack opening and the sensor can be estimated with the Gaussian model and with knowledge of the sensor viewing geometry. The point-source model is modified so that the entire area of the fan stack aperture is the source of emission. First, the coordinates of the centerline trajectory of the plume are computed through equation E.1. For each point along the centerline trajectory, a sphere is drawn whose radius in the vertical and crosswind directions equals the sum of the radius of the stack opening and twice the vertical and crosswind dispersion coefficients, $r + 2\sigma_z$ and $r + 2\sigma_y$, respectively. The radius in the downwind direction x is taken as $r + 2\sigma_y$. In other words, the “edge” of the plume is a distance of two standard deviations from the centerline of the plume in the z and y directions plus the radius of the stack opening. This concept is illustrated from a Matlab rendering in Figure E.2.

The sensor viewing vector is determined from the distance to the stack opening and the sensor zenith and azimuth viewing angles. This vector originates at the center of the stack opening and points in the direction of the sensor. The points on this vector that are within two standard deviations of the plume centerline are considered points contained within the plume. The length of the vector containing these enclosed points equals the path length through the plume.

The necessary user inputs for this model are the stack height $[m]$, the stack radius $[m]$,

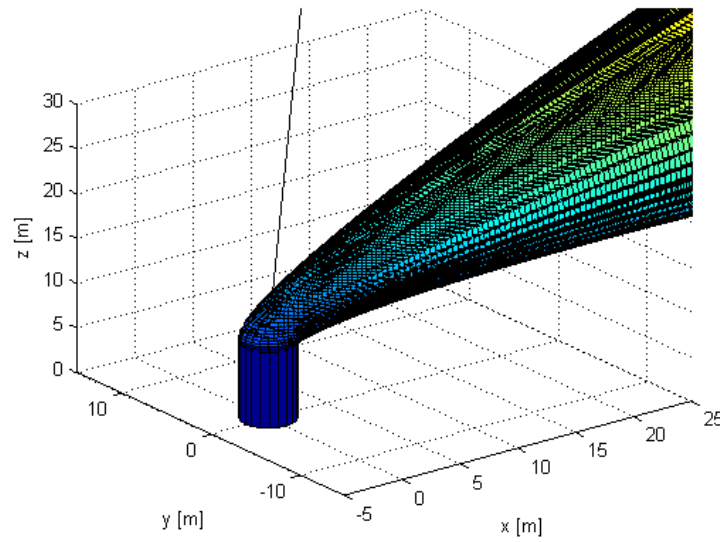


Figure E.2: Gaussian plume model rendered in Matlab. The solid line represents the sensor line-of-sight. The exit air velocity is set to 10 m/s, stack height is 9 m, stack radius is 2 m, wind speed is 0.75 m/s, and the atmospheric stability is slightly unstable. The estimated path length through this plume is 6 m.

the approximate stack gas and ambient air temperatures $[K]$, the wind speed $[m/s]$, the vertical exit gas speed $[m/s]$, and the sensor zenith and azimuth direction angles $[^\circ]$ (the azimuth angle is measured from the downwind direction, x).

Appendix F

Precipitable Water in an Air Column

The atmospheric precipitable water is defined as the total atmospheric water vapor contained in a vertical column of unit cross-sectional area extending between any two specified levels [53]. This concept is commonly expressed in terms of the height to which that water would stand if completely condensed and collected in a vessel of the same unit cross section. The precipitable water, W , can be expressed mathematically as

$$W = \frac{1}{g} \int_{p_1}^{p_2} w(p) dp \quad [mm], \quad (F.1)$$

where p is the atmospheric pressure in Pascals ($Pa = N/m^2$), g is the acceleration due to gravity at the earth's surface ($g = 9.807 m/s^2$), and $w(p)$ is the water vapor mixing ratio. The integral is computed between two pressure levels, p_1 and p_2 . The result has units of millimeters which represents the height of the precipitable water in the air column. The mixing ratio is defined from the pressure and vapor pressure as

$$w(p) = 0.622 \frac{e}{p - e}, \quad (F.2)$$

where e is the water vapor pressure expressed in the same units as the pressure, p (usually in $[mb]$ or $[Pa]$). The vapor pressure can be calculated from the dew point temperature $[K]$ at a given pressure as

$$e = 0.01 \cdot \exp \left[1.391499 - 0.048640239 T_d + (0.41764768 \cdot 10^{-4}) T_d^2 - (0.14452093 \cdot 10^{-7}) T_d^3 + 6.5459673 \log_e (T_d) - 5800.2206 \frac{1}{T_d} \right] \quad [mb]. \quad (F.3)$$

Finally, the dew point can be calculated from the relative humidity [%] and the dry-bulb temperature $[K]$ as

$$T_d = \frac{243.5 \cdot \left[\log_e \left(\frac{RH}{100} \right) + \frac{17.67 (T - 273.15)}{243.5 + (T - 273.15)} \right]}{17.67 - \left[\log_e \left(\frac{RH}{100} \right) + \frac{17.67 (T - 273.15)}{243.5 + (T - 273.15)} \right]} + 273.15 \quad [K]. \quad (F.4)$$

Equations (F.3) and (F.4) were obtained from <http://cires.colorado.edu/~voemel/vp.pro>.

Bibliography

- [1] J. R. Schott, *Remote Sensing: The Image Chain Approach*, Oxford University Press, New York, NY, 1997.
- [2] R. Burger, *Cooling Tower Technology: Maintenance, Upgrading and Rebuilding*, The Fairmont Pres, Inc., Lilburn, GA, third ed., 1995.
- [3] A. Garrett, "Email correspondence." October 2006.
- [4] M. Planck, "On the law of distribution of energy in the normal spectrum," in *Annalen der Physik*, **4**, p. 553, 1901.
- [5] "Nonconventional Exploitation Factors (NEF) Modeling," Tech. Rep. v9.5, April 2005.
- [6] G. J. Ward, "Measuring and modeling anisotropic reflection," in *Computer Graphics*, pp. 265–272, July 1992.
- [7] K. E. Torrance and E. M. Sparrow, "Theory of off-specular reflection from roughened surfaces," in *Journal of the Optical Society of America*, **57**(9), pp. 1105–1114, September 1967.
- [8] R. G. Priest and T. A. Germer, "Polarimetric BRDF in the microfacet model: Theory and measurements," in *Proceedings of the 2000 Meeting of the Military Sensing Symposia Specialty Group on Passive Sensors*, **1**, pp. 169–181, 2002.
- [9] J. R. Maxwell, J. Beard, S. Weiner, D. Ladd, and S. Ladd, "Bidirectional reflectance model validation and utilization," Tech. Rep. AFAL-TR-73-303, Environmental Research Institute of Michigan, Ann Arbor, MI, October 1973.
- [10] J. R. Shell, *Polarimetric Remote Sensing in the Visible to Near Infrared*. PhD thesis, Rochester Institute of Technology, 54 Lomb Memorial Drive, Rochester NY 14623, 2005.
- [11] E. Hecht, *Optics*, Addison-Wesley Publishing Company, Reading, Massachusetts, second ed., 1990.
- [12] J. M. Wallace and P. V. Hobbs, *Atmospheric Science An Introductory Survey*, Academic Press, New York, 1977.

- [13] Air Force Research Laboratory, Hanscom AFB, MA, *MODTRAN User's Manual*, versions 3.7 and 4.0 ed., 1998.
- [14] J. D. Gaskill, *Linear System, Fourier Transforms, and Optics*, John Wiley & Sons, Inc., New York, NY, 1978.
- [15] K. R. Castleman, *Digital Image Processing*, Prentice Hall, Inc., Upper Saddle River, NJ, 1996.
- [16] F. Becker and Z.-L. Li, "Towards a local split window method over land surfaces," in *Groupeement Scientifique de Télédétection Spatial*, pp. 369–393, Laboratoire des Sciences de l'Image et de la Télédétection, 1989.
- [17] F. Sospedra, V. Caselles, and E. Valor, "Effective wavenumber for thermal infrared bands - application to Landsat-TM," in *International Journal of Remote Sensing*, **19**(11), pp. 2105–2117, 1998.
- [18] A. Berk, L. S. Bernstein, and D. C. Robertson, "MODTRAN: A moderate resolution model for LOWTRAN 7," Tech. Rep. GL-TR-89-0122, Spectral Sciences, Inc., Burlington, MA, April 1989.
- [19] Air Force Geophysics Laboratory, Hanscom AFB, MA, *User's Guide to LOWTRAN 7*, afgl-tr-88-0177 ed., August 1988.
- [20] S. Carr, "The aerosol models in MODTRAN: Incorporating selected measurements from northern australia," Tech. Rep. AR-013-545, Defence Science and Technology Organisation, Commonwealth of Australia, December 2005.
- [21] J. R. Schott, S. D. Brown, R. V. Raqueño, H. N. Gross, and G. Robinson, "An advanced synthetic image generation model and its application to multi/hyperspectral algorithm development," in *Canadian Journal of Remote Sensing*, **25**(2), pp. 99–111, 1999.
- [22] Digital Imaging and Remote Sensing Laboratory, Rochester, NY, *The DIRSIG User's Manual*, February 2006.
- [23] P. Dash, F. M. Gottsche, F. S. Olesen, and H. Fischer, "Land surface temperature and emissivity estimation from passive sensor data: Theory and practice - current trends," in *International Journal of Remote Sensing*, **23**(13), pp. 2563–2594, 2002.

- [24] Z. Qin, A. Karnieli, and P. Berliner, "A mono-window algorithm for retrieving land surface temperature from Landsat TM data and its application to the israel-egypt border region," in *International Journal of Remote Sensing*, **22**(18), pp. 3719–3746, 2001.
- [25] K. Mathew, C. M. Nagarani, and A. S. Kirankumar, "Split-window and multi-angle methods of sea surface temperature determination: An analysis," in *International Journal of Remote Sensing*, **22**(16), pp. 3237–3251, 2001.
- [26] A. J. Prata, "Land surface temperatures derived from the advanced very high resolution radiometer and the along-track scanning radiometer: Theory," in *Journal of Geophysical Research*, **98**(D9), pp. 16689–16702, 1993.
- [27] X. Li, W. Pichel, E. Maturi, P. Clemente-Colon, and J. Sapper, "Deriving the operational nonlinear multichannel sea surface temperature algorithm coefficients for NOAA-14 AVHRR/3," in *International Journal of Remote Sensing*, **22**(4), pp. 699–704, 2001.
- [28] J. J. Szymanski and P. G. Weber, "Multispectral thermal imager: Mission and applications overview," in *IEEE Transactions on Geoscience and Remote Sensing*, **43**, pp. 1943 – 1949, IEEE, September 2005.
- [29] C. C. Borel, W. B. Clodius, A. B. Davis, B. W. Smith, J. J. Szymanski, J. Theiler, P. V. Villeneuve, and P. G. Weber, "MTI core science retrieval algorithms," in *Imaging Spectrometry V*, **3753**, pp. 403 – 415, SPIE, (Denver), July 1999.
- [30] W. B. Clodius, C. Borel, L. Balick1, and S. J. Hook, "Validation of the MTI water surface temperature retrieval algorithms," in *Geoscience and Remote Sensing Symposium*, **1**, pp. 30 – 32, IEEE International, June 2002.
- [31] D. Gu, A. R. Gillespie, A. B. Kahle, and F. D. Palluconi, "Autonomous atmospheric compensation (AAC) of high resolution hyperspectral thermal infrared remote-sensing imagery," in *IEEE Transactions on Geoscience and Remote Sensing*, **38**(6), pp. 2557–2570, IEEE, 2000.
- [32] S. J. Young, R. Johnson, and J. A. Hackwell, "An in-scene method for atmospheric compensation of thermal hyperspectral data," in *Journal of Geophysical Research*, **107**(D24), p. 4774, 2002.
- [33] G. Healey and D. Slater, "Models and methods for automated material identification in hyperspectral imagery aquired under unknown illumination and atmospheric

- conditions," in *IEEE Transactions on Geoscience and Remote Sensing*, **37**(6), pp. 2706–2717, IEEE, 1999.
- [34] P. S. Kealy and S. J. Hook, "Separating temperature and emissivity in thermal infrared multispectral scanner data: Implications for recovering land surface temperatures," in *IEEE Transactions on Geoscience and Remote Sensing*, **31**(6), pp. 1155–1164, IEEE, 1993.
- [35] A. Gillespie, S. Rokugawa, T. Matsunaga, J. S. Cothorn, S. Hook, and A. B. Kahle, "A temperature and emissivity separation algorithm for advanced spaceborne thermal emission and reflection radiometer (ASTER) images," in *IEEE Transactions on Geoscience and Remote Sensing*, **36**(4), pp. 1113–1126, IEEE, 1998.
- [36] M. Boonmee, *Land Surface Temperature and Emissivity Retrieval from Thermal Infrared Hyperspectral Imagery*. PhD thesis, Rochester Institute of Technology, 54 Lomb Memorial Drive, Rochester NY 14623, 2007.
- [37] C. C. Borel, "ARTEMIS - an algorithm to retrieve temperature and emissivity from hyper-spectral thermal image data," Tech. Rep. LA-UR-027907, Los Alamos National Laboratory, Tampa, Florida, March - April 2003.
- [38] R. Kaiser and L. Smith, *SOC-400T Field Use Protocol*. DIRS Laboratory, Rochester Institute of Technology, 0.3 ed., July 2004.
- [39] SPX Cooling Technologies, Inc., Overland Park, KS, <http://spxcooling.com/en/>.
- [40] K. Stamnes, S.-C. Tsay, W. Wiscombe, and K. Jayaweera, "Numerically stable algorithm for discrete-ordinate-method radiative transfer in multiple scattering and emitting layered media," in *Applied Optics*, pp. 2502–2509, No. 12, Vol. 27, June 1988.
- [41] G. Anderson, "Email correspondence." August 2007.
- [42] E. J. Ientilucci and J. R. Schott, "Physics based target detection using a hybrid algorithm with an infeasibility metric," in *IEEE International Conference on Acoustics, Speech, and Signal Processing (ICASSP)*, pp. 1193–1196, IEEE ICASSP Vol. 5, (Toulouse, France), May 2006.
- [43] J. Neter and W. Wasserman, *Applied Linear Statistical Models: regression, analysis of variance, and experimental designs*, Richard D. Irwin, Inc., Homewood, Illinois, 1974.

- [44] R. L. Mason, R. F. Gunst, and J. L. Hess, *Statistical Design and Analysis of Experiments with Applications to Engineering and Science*, John Wiley & Sons, Inc., New York, NY, 1989.
- [45] F. P. Padula, "Historic thermal calibration of Landsat 5 TM through an improved physics based approach," Master's thesis, Rochester Institute of Technology, 54 Lomb Memorial Drive, Rochester NY 14623, November 2008.
- [46] M. Taguchi, T. Fukuhara, T. Imamura, M. Nakamura, N. Iwagami, M. Ueno, M. Suzuki, G. Hashimoto, and K. Mitsuyama, "Longwave infrared camera onboard the venus climate orbiter," in *Advances in Space Research*, **40**, p. 861868, COSPAR, Elsevier Ltd., May 2007.
- [47] J. Thomas A. Ryan and B. L. Joiner, "Normal probability plots and tests for normality," tech. rep., The Pennsylvania State University, Statistics Department, 1976.
- [48] J. L. Devore, *Probability and Statistics for Engineering and the Sciences*, Duxbury Thomson Learning, Pacific Grove, CA, fifth ed., 2000.
- [49] D. V. Schroeder, *Introduction to Thermal Physics*, Addison Wesley Longman, New York, NY, 2000.
- [50] J. Neter, W. Wasserman, and G. A. Whitmore, *Applied Statistics*, Allyn and Bacon, Inc., Boston, MA, second ed., 1982.
- [51] J. Peyton Z. Peebles, *Probability, Random Variables and Random Signal Principles*, McGraw-Hill Science/Engineering/Math, 4 ed., July 2000.
- [52] M. R. Beychok, *Fundamentals of Stack Gas Dispersion*, Irvine, CA, third ed., 1994.
- [53] "Glossary of meteorology." <http://amsglossary.allenpress.com/glossary/>, March 2009. Search string: Precipitable Water.